A NANOMEDICINE APPROACH FOR IMMUNE CHECKPOINT INHIBITION: TOWARDS BETTER AND SAFER CANCER IMMUNOTHERAPY

by

Parisa Badiee

Doctor of Pharmacy (PharmD)

A thesis submitted for the degree of

Doctor of Philosophy

(Biomaterials engineering and nanomedicine; IPHD)

Clinical and health sciences



University of South Australia

September 2021

Contents

Contents ..... **ii**
List of Figures ..... **v**
List of Tables ..... **vii**
Glossary ..... **viii**
Summary ..... **xii**
Declaration ..... **xiv**
Acknowledgments ..... **xv**
1 Introduction **2**
1.1 Research hypotheses and aims of the thesis 3
1.2 Thesis structure 5
1.3 Thesis outcomes 7
1.4 References 9
2 Literature review **13**
2.1 Immune checkpoints and their role in field of oncology 13
2.2 Immune checkpoint antibodies 14
2.3 Alternative approaches for ICP inhibition 19
2.3.1 Overview of alternative ICP inhibitors 19
2.3.2 Indoleamine-2,3-dioxygenase inhibitors 20
2.3.3 Glycogen synthase kinase 3 22
2.4 PLGA/PEG-PLGA NPs as a drug delivery system 24
2.5 References 29
3 Intratumoural delivery of anti-PD-1 conjugated PEG-PLGA nanoparticles improves the biodistribution of PD-1 immune checkpoint inhibitor towards safer immunotherapy **46**
3.1 Introduction 46
3.2 Materials and methods 48
3.2.1 Materials 48
3.2.2 Cell culture 48
3.2.3 Preparation of PEG-PLGA NPs 49
3.2.4 Physico-chemical characterization of PEG-PLGA NPs 49
3.2.5 Conjugation of aPD-1 to PEG-PLGA NPs 50
3.2.7 Biodistribution of aPD-1 NPs in orthotopic HNSCC model 51
3.2.8 T-cell isolation and activation 52
3.2.9 PD-1 inhibition by aPD-1 NPs 52
3.2.10 Effects of aPD-1 NPs on T-cells proliferation and viability 52
3.2.11 Effect of aPD-1 NPs on *in vitro* cytotoxicity of T-cells against head and neck cancer cells . 53

3.2.12 Apoptosis 53
3.2.13 Proliferation and cell cycle analysis 54
3.2.14 Cytotoxic cytokine analysis 54
3.2.15 Statistics 55
3.3 Results and discussion 55
3.3.1 Physicochemical characterisation of aPD-1 NPs 55
3.3.2 Enhanced tumour retention and decreased off-target distribution of intratumoural administered aPD-1 NP 56
3.3.3 aPD-1 NPs are biocompatible with T-cells and effectively inhibit PD-1 expression *in vitro* .. 60
3.3.4 Inhibition of PD-1 by aPD-1 NPs enhances *in vitro* cytotoxicity of T-cells against head and neck cancer cells 62
3.4 Conclusion 67
3.5 Supplementary figures 68
3.6 References 74
4 Nanoformulation of the navoximod immune checkpoint inhibitor within PEG-PLGA nanoparticles by hydrophobic ion pair complexation towards improved IDO inhibition 82
4.1 Introduction 82
4.2 Materials and methods 84
4.2.1 Materials 84
4.2.2 Cell culture 84
4.2.3 Preparation of IDOi loaded PEG-PLGA NPs 85
4.2.4 Physicochemical characterization of IDOi NPs 86
4.2.5 IDO enzymatic activity 87
4.2.6 Impact of IDOi NPs on cancer cells metabolic activity 88
4.2.7 T-cell isolation and activation 88
4.2.8 T-cell cytotoxicity modulation by IDOi NPs/aPD-1 88
4.2.9 Cancer cell apoptosis and cell cycle function by IDOi NPs/aPD-1 89
4.2.10 Statistics 90
4.3 Results and discussion 90
4.3.1 Hydrophobic ion pairing improved the physicochemical characteristics of IDOi NP 90
4.3.2 IDOi NPs effectively inhibits IDO activity 93
4.3.3 IDOi NP/aPD-1 significantly reduced the immunosuppressive regulatory T-cells and enhanced the cytotoxicity of T-cells 94
4.3.4 Improved anti-tumour effects by IDOi NP/aPD-1 combination therapy 97
4.4 Conclusion 99
4.5 References 101
5 Development of a Glycogen kinase 3 inhibitor nanoformulation as an alternative strategy to inhibit PD-1 immune checkpoint 108
5.1 Introduction 108
5.2 Materials and method 110
5.2.1 Materials 110

5.2.2 Cell culture 110
5.2.3 Preparation of GSK3i loaded PEG-PLGA NPs 110
5.2.4 Physicochemical characterization of GSK3i NPs 111
5.2.5 GSK3i NPs activity through the Wnt/β-catenin pathway 111
5.2.6 CAR-T cell assay for antigen specific activation of T-cells for PD-1 upregulation 112
5.2.7 PD-1 receptor expression and T-cell proliferation 112
5.2.8 CAR-T cell phenotype characteristics 113
5.2.9 Statistics 113
5.3 Results and discussion 113
5.3.1 Optimized physicochemical properties of GSK3i NP 113
5.3.2 GSK3i NPs efficiently inhibit PD-1 receptor and retain functionality 115
5.3.3 Effect of the GSK3i NPs on the CAR T-cells phenotypes 118
5.4 Conclusion 121
5.5 References 122
6 Microfluidic nanoprecipitation combined with hydrophobic ion pairing enables the preparation of high performance indocyanine green highly tuneable nanoformulations 129
6.1 Introduction 129
6.2 Materials and method 130
6.2.1 Materials 131
6.2.2 PEG-PLGA NPs preparation 131
6.2.3 Preparation of ICG loaded PEG-PLGA NPs 131
6.2.4 Physicochemical characterisation of ICG NPs 132
6.2.5 ICG NP's fluorescence properties 133
6.2.6 Mapping of lymphatic drainage in a large animal swine model 134
6.2.7 Statistics 135
6.3 Results and discussion 135
6.3.1 Size controllable preparation of PEG-PLGA NPs using a 3D printed microfluidic nanoprecipitation device 135
6.3.2 Microfluidic nanoformulation of ICG NPs by hydrophobic ion pairing 137
6.3.3 ICG NP-60 efficiently retains ICG fluorescence for sentinel lymph node detection 143
6.4 Conclusions 146
6.5 References 147
7 Discussion of the research findings and future research recommendations .. 154
7.1 References 160

List of Figures

Figure 1-1 Schematic illustration of project design to address three main aims of the thesis. 5
Figure 2-1 Illustration of PD-1/PD-L1 interaction and aPD-1 site of action at T-cell and cancer cell interface. 15
Figure 2-2 Schematic illustration of PD-1 inhibition effect on IDO pathway. 21
Figure 2-3 GSK3 pathway upstream of PD-1 expression. 24
Figure 2-4 Illustration of two microfluidic chip design used for the nanoprecipitation of NPs. 26
Figure 3-1 Physicochemical characterization of PEG-PLGA aPD-1 NPs. 56
Figure 3-2 *In vivo* biodistribution of aPD-1 NPs and aPD-1 in an orthotopic mouse model of head and neck cancer. 58
Figure 3-3 *Ex vivo* biodistribution of aPD-1 NPs and aPD-1 in an orthotopic mouse model of head and neck cancer. 59
Figure 3-4 *In vitro* primary human T-cells PD-1 receptor inhibition by aPD-1 NPs vs free aPD-1. 61
Figure 3-5 Effects of aPD-1 NPs on proliferation and viability of primary human T-cells. 62
Figure 3-6 Effect of aPD-1 NPs on T-cells cytotoxicity in a co-culture model. 64
Figure 3-7 Effect of aPD-1 NP treated T-cells on UM-SCC1 cells proliferation and cell cycle. 65
Figure 3-8 Effect of aPD-1 NP treatment on T-cells cytotoxic cytokine production in co-culture with UM-SCC1 cells. 66
Figure 3-9 PEG-PLGA NPs physicochemical characterization and stability. 68
Figure 3-10 Establishment of an orthotopic C57BL/6 mouse model of head and neck cancer with the MOC-1 cell line. 69
Figure 3-11 Activated primary human T-cells morphology and PD-1 receptors expression. 70
Figure 3-12 Cancer cell PD-L1 expression and PD-1 inhibition of T-cells in UM-SCC1 co-culture. 71
Figure 3-13 Effect of aPD-1 NPs on T-cells cytotoxicity in co-culture with RFP-SCC47. 72
Figure 3-14 Effect of aPD-1 NP treated T-cells on the UM-SCC47 cell cycle. 73
Figure 4-1 Schematic illustration of IDOi NP preparation using a 3D printed microfluidic nanoprecipitation chip. 86
Figure 4-2 Optimization and physicochemical characterization of the IDOi NPs. 92
Figure 4-3 Inhibition of IDO enzyme and effect on UM-SCC1 metabolic activity. 94
Figure 4-4 Effect of IDOi NPs as single or combination therapy with aPD-1 on immunosuppressive regulatory T-cells. 95
Figure 4-5 Effects of IDOi NPs as a single or combination therapy on the cytotoxic characteristics of T-cells. 96
Figure 4-6 Effect of IDOi NPs as a single or combination therapy with aPD-1 on the activity of T-cells against UM-SCC1 cells. 99
Figure 5-1 Preparation and physicochemical characterization of GSK3i NPs. 115
Figure 5-2 GSK3i NP are functional and efficiently inhibit PD-1 receptor expression. 116
Figure 5-3 GSK3i NPs induce Wnt/β catenin pathway and enhance T-cell proliferation. 117
Figure 5-4 GSK3 inhibition induced changes on CAR T-cell phenotype. 120

Figure 6-1 3D printed herringbone structured microfluidic nanoprecipitation devices for high throughput preparation of PEG-PLGA NPs. 136
Figure 6-2 Physicochemical properties of ICG NPs prepared by hydrophobic ion pairing within the microfluidic device. 138
Figure 6-3 Optical properties of ICG PEG-PLGA nanoformulations. 140
Figure 6-4 Stability of the ICG nanoformulations. 142
Figure 6-5 Relationship between ICG NP-60 concentration and fluorescence intensity. 143
Figure 6-6 SLN mapping in a large animal swine model. 144

List of Tables

Table 2-1 ICP antibodies in the market for cancer immunotherapy. 15
Table 2-2 Clinical outcome of checkmate 141 clinical trial of nivolumab. 16
Table 2-3 Examples of bulk PLGA NPs preparation methods. 24
Table 4-1 Optimization of IDOi NP nanoformulation by hydrophobic ion pairing and nanoprecipitation. 90
Table 5-1 Effect of GSK3 inhibition on the ratios of Tcm/Teff cells. 119
Table 6-1 Physicochemical and optical properties of ICG NPs. 138

Glossary

aCTLA-4	Antibodies against CTLA-4
APC	Antigen presenting cell
aPD-1	Antibodies against PD-1
aPD-1 NP	aPD-1 conjugated NP
aPD-L1	Antibodies against PD-L1
CAR-T	Chimeric antigen receptor expressing T-cells
cHL	Classical Hodgkin lymphoma
CRC	Colorectal cancer
CRISPR/Cas9	Clustered regularly interspaced short palindromic repeats and CRISPR-associated protein 9
CSCC	Cutaneous squamous cell carcinoma
CTLA-4	Cytotoxic T lymphocyte–associated protein 4
DC	Dendritic cell
dMMR	Mismatch repair deficient
EE	Entrapment efficiency
EMA	European medicines agency
ESCC	Esophageal squamous cell carcinoma
FDA	Food and drug administration
Fucci	Fluorescent ubiquitination-based cell cycle indicator
GA	Glycolic acid
GSK3	Glycogen synthase kinase 3
GSK3i	GSK3 inhibitors
GSK3i NP	GSK3i loaded NP

HCC	Hepatocellular carcinoma
HDL	High-density lipoprotein
HNSCC	Head and neck squamous cell carcinoma
HPLC	High-performance liquid chromatography
ICG	Indocyanine green
ICG NP	ICG loaded NP
ICI	ICP inhibitor
ICP	Immune checkpoint
IDO	Indoleamine 2,3-dioxygenase
IDOi	IDO inhibitors
IDOi NP	IDOi loaded NP
IL	Interleukin
INF-γ	Interferon γ
IRAE	Immune related adverse events
LA	Lactic acid
LGR5	Leucine-rich repeat-containing G-protein coupled receptor 5
LN	Lymph node
MCC	Merkel cell carcinoma
MHC	Major histocompatibility complex
MMP-2	Matrix metalloproteinase-2
MSI-H	Microsatellite instability-high
NIR	Near infrared
NP	Nanoparticle
NSCLC	Non-small cell lung cancer

PD-1	Programmed cell death 1
PDI	Polydispersity index
PDMS	Polydimethylsiloxane
PEG-PLGA	Poly(ethylene glycol)-b-poly(lactide-co-glycolide)
PMBCL	Primary mediastinal large B-cell lymphoma
QY	Quantum yield
RCC	Renal cell carcinoma
RFP	Red fluorescent protein
SCLC	Small cell lung cancer
siRNA	Small interfering RNA
SLN	Sentinel lymph node
TAM	Tumour-associated macrophages
Tcm	Central memory T-cell
TCR	T-cell receptor
TDLN	Tumour draining lymph nodes
Teff	Effector T-cell
Tem	Effector memory T-cells
TEM	Transmission electron microscope
TGA	Therapeutic goods administration
TIM-3	T-cell immunoglobulin mucin-3
TME	Tumour microenvironment
Tn	Naïve T-cell
TNBC	Triple-negative breast cancer
TOAB	Tetraoctylammonium bromide

Treg	Regulatory T cell
UC	Urothelial carcinoma

Summary

Immune checkpoint inhibitors (ICIs), including inhibitors against immune checkpoint programmed cell death 1 (PD-1) receptors, have revolutionized the field of oncology owing to their ability to restore the activity of the immune system to fight against the cancer. Although several ICI antibodies have now been approved for clinical use, their success is hampered by limited patients' response rates and high rates of adverse effects. Towards addressing one of the most pressing challenge of the immunotherapy field and considering the pivotal role of ICIs' loco-regional and systemic biodistribution in both their efficacy and off-target toxicity, this PhD thesis aimed to investigate the potential of nanomedicine based ICIs drug delivery systems towards improving both established and emerging ICIs. Specifically, we developed and utilise throughout the research project poly(ethylene glycol)-b-poly(lactide-co-glycolide) (PEG-PLGA) nanoparticles (NPs) prepared using a robust and high throughput 3D printed microfluidic nanoprecipitation device.

First, we endeavoured to investigate the impact of (PD-1) antibodies (aPD-1) nanoformulation on their biodistribution following intratumoural administration. We conjugated aPD-1 to the PEG-PLGA NPs (aPD-1 NPs), and determined their biodistribution after intratumoural administration in an orthoptic mouse model of head and neck cancer (HNC) developed for this project. We also compared the biodistribution of the aPD-1 nanoformulation to that of intratumorally administrated free aPD-1 and systemically administrated free aPD-1 used as the clinical benchmark. We demonstrated that aPD-1 nanoformulation reduced aPD-1 biodistribution in off-target organs. In a comprehensive set of *in vitro* biological assays, we then validated that the aPD-1 remained functional after conjugation to the PEG-PLGA NPs and showed that nanoformulation was associated with high cytotoxicity of T-cells against HNC cells similar to that of the free aPD-1.

In the second part of the project, we developed a delivery system for the indoleamine 2,3-dioxygenase (IDO) inhibitor (IDOi) navoximod using a hydrophobic ion pairing strategy used to dramatically improve the loading of the IDOi within the PEG-PLGA NPs (IDOi NPs). We optimized the physicochemical properties of the navoximod nanoformulation and determined their efficacy to inhibit IDO enzyme of HNC cells. We confirmed the activity of the nanoformulation, both as single therapy and IDOi NPs/ aPD-1 dual therapy,

to enhance the anti-tumour cytotoxicity of T-cells. This nanoformulation of IDOi has potential to overcome acquired resistance to aPD-1 therapy and warrant further preclinical testing.

In the third part, we employed PEG-PLGA NPs and hydrophobic ion pairing to create nanoformulation of a glycogen synthase kinase 3 (GSK3) inhibitor (GSK3i). GSK3 inhibition is a promising alternative approach to inhibit PD-1 expression but the suboptimal bioavailability of small molecule inhibitors remains a challenge. To demonstrate a proof-of-concept, we investigated the efficacy of the GSK3i nanoformulation in a co-culture of chimeric antigen receptor (CAR) T-cells with tumour cells expressing the CAR target. These experiments confirmed that GSK3i NPs efficiently reduced the expression of PD-1 receptors in activated CAR-T cells, prevented their viability loss and induced a central memory T-cell phenotype necessary for long-term immunity.

In the last part, we built on the technological advances delivered through the project to develop a size tuneable indocyanine green (ICG) fluorescent dye loaded PEG-PLGA nanoformulation (ICG NP). The hydrophobic ion pairing was used to improve the loading of the dye within the PEG-PLGA NPs and protect their optical properties. We confirmed that ICG NPs dramatically improved the stability of ICG and prevented quenching at high concentrations. Preliminary results in a large animal swine model suggest that the ICG nanoformulation enables higher retention of ICG in sentinel lymph nodes compared to higher echelon nodes and also preserved fluorescence over at least 10 days. This data warrants further research towards the design of image guided surgery procedures including sentinel lymph node biopsy procedures in deep seated organs.

In summary, this PhD research delivered new knowledge relevant to the rapidly growing field of immunotherapy as well as developed several new nanomedicine approaches aimed at improving immune checkpoint inhibition. It highlighted several significant potential benefits of nanoformulations in alleviating the clinical challenges associated with ICI.

Declaration

This thesis presents work carried out by myself and does not incorporate without acknowledgment any material previously submitted for a degree or diploma in any university; to the best of my knowledge it does not contain any materials previously published or written by another person except where due reference is made in the text; and all substantive contributions by others to the work presented, including jointly authored publications, are clearly acknowledged.



Parisa Badiee

September 2021

Acknowledgments

First and foremost I would like to thank my supervisory panel for their great support. My principal supervisor Professor Benjamin Thierry, for his invaluable support, guidance and generous time throughout my candidature for both my research project and my scientific career. I would like to express my great appreciation to my co-supervisors, Dr Michelle Maritz, for her enthusiastic encouragement and constructive advice, and Dr Nicole Dmochowska for her great support particularly in conducting the animal studies.

I would like to extend my thanks to my REPL, Dr Zlatko Kopecki for his valuable support and all members of Bionanoengineering group, past and present, at the Future Industries Institute, University of South Australia for all their help and support. Particularly, Dr Marnie Winter, Dr Aidan Cousins, Dr Valentina Milanova, Dr Ludivine Delon, Dr Mona Elsemary, Mr Pouya Dehghankelishadi and Mr Edward Cheah.

I would also like to thank Ferronova Pty Ltd for giving me the opportunity to collaborate with them for the animal study in South Australian Health and Medical Research Institute (SAHMRI). I appreciate the help of Carina Biotech and the Simon Barry Lab at the women's and children's hospital for providing me with CAR-T cells.

I would like to express my gratitude to the technical team at Future Industries Institute for providing technical training and assistance, especially Dr Nobuyuki Kawashima, Dr Patrick Sherman, Dr John Denman and Ms Susie Ritch. I would also like to express my appreciation for the help and assistance of the Core Animal Facility's staff at University of South Australia throughout my animal study, and to Dr Briony Gliddon for her assistance in preparing animal ethics application and to Dr Giri Krishnan for his instruction on preparing mouse tumour models.

I wish to acknowledge the financial support of University of South Australia for offering the University of South Australia Presidents Scholarship (UPS), which enabled me to make this work possible.

My special thanks are extended to my beloved family and friends, particularly my parents and my husband Pouya, who have been by my side, believed in me and encouraged me all the time throughout my candidature, and without whom, I would not be able to accomplish my PhD.

Chapter 1

Introduction

1 Introduction

Immune checkpoints (ICPs) are proteins expressed by immune cells, predominately T-cells, and some cancer cells. Their overall function is to suppress the activity of the immune system [1,2]. Induction of immune checkpoints is one of the key means for cancers to evade the immune system and continue to grow. Inhibition of immune checkpoints restores the cytotoxic activity of immune cells to fight against the cancer [2].

Clinical trials led to the US food and drug administration (FDA) and other regulatory bodies approval of several antibodies against ICPs. These immune checkpoint inhibitor (ICI) antibodies block the interactions between ICPs and their ligands, thereby preventing the inhibitory signals towards the immune cells. One of the main class of clinically approved ICIs are antibodies targeting the immune checkpoint programmed cell death 1 (PD-1) receptors, expressed mostly on T-cells. Preclinical and clinical studies have proven that PD-1 blockade is a successful cancer immunotherapy in several cancers [3]. Nevertheless, the therapeutic efficacy of PD-1 antibodies is hampered due to both limited patients' response rates and high rates of adverse events [4,5]. Although the exact mechanisms are yet to be elucidated, limited tumour drug bioavailability, overexpression of alternative immune checkpoints and high off-target distribution are highly involved in the relatively low efficacy and high toxicity of PD-1 antibodies [6,7]. This research tested the hypothesis that intratumoural administration of PD-1 antibodies nanoformulation alters their loco-regional and systemic biodistribution of PD-1 antibodies and may therefore help to alleviate these challenges.

Resistance to immune checkpoints inhibitors by upregulation or interplay of other immune checkpoints is common [7]. Indoleamine-2,3-dioxygenase (IDO) is an immune checkpoint enzyme expressed in many cancer cells and some of immune cells, which is associated to poor prognosis of patients [1]. IDO is also upregulated upon inhibition of PD-1 receptors by PD-1 antibodies [8], implicating a resistance mechanism to PD-1 inhibition. Small molecule inhibitors of the IDO enzyme have been explored in several preclinical and clinical studies, as a single therapy or combined with other anti-cancer therapies. However, the low bioavailability of oral formulations of IDO inhibitors, necessitates the administration of high doses, which is associated with high toxicity and only modest efficacy [9,10]. Therefore, there is need to improve the bioavailability of

IDO inhibitors. To address this issue, we developed and optimised a nanoformulation of navoximod, a potent IDO inhibitor.

Alternative approaches of indirectly targeting immune checkpoints have also been investigated. Glycogen synthase kinase 3 (GSK3) was found to regulate PD-1 gene expression, and hence small molecule inhibitors of GSK3 have been explored as ICIs to reduce PD-1 receptor gene expression in preclinical studies [11]. The role of GSK3 on the regulation of PD-1 led to the identification of GSK3 inhibitors as promising alternatives to PD-1 antibodies with lower manufacturing cost and higher stability [12]. Nonetheless, as small molecules, GSK3 inhibitors demonstrate short half-life and rapid clearance with high distribution in off-target organs [13]. Thereby, improving the biodistribution and delivery of GSK3 inhibitors can potentially address the challenges to improve the efficacy and toxicity.

To address the challenges associated with different approaches of ICP inhibition, it is pivotal to improve the delivery of ICIs. Nanoformulations of ICI have been actively investigated and hold great promise towards improving their delivery. More specifically, poly(ethylene glycol)-b-poly(lactide-co-glycolide) (PEG-PLGA) based nanoparticles (NPs) are versatile, biocompatible and biodegradable nano-carriers that can be employed as drug delivery systems for ICIs [14,15].

1.1 Research hypotheses and aims of the thesis

The overarching aim of this research project was therefore to investigate the potential of nanomedicine-based drug delivery systems to improve ICIs for cancer immunotherapy. On this account, this research investigated PEG-PLGA based NPs as a drug delivery system for three different approaches of immune checkpoint inhibition, namely 1) PD-1 antibodies, 2) an IDO inhibitor and 3) a GSK3 inhibitor. The three main research hypotheses and associated aims of this PhD thesis were:

1) **Hypothesis**

PD-1 antibodies nanoformulation positively alters their loco-regional and systemic biodistribution compared to free antibodies following the intratumoural administration.

Aim

To comprehensively investigate the biodistribution of PD-1 antibodies conjugated or not to PEG-PLGA nanoparticles following intratumoural injection into an orthotopic mouse model of head and neck cancer.

2) **Hypotheses**

2.1) Nanoformulation of the small molecule IDO inhibitor navoximod will advance understanding of the anti-tumour immunological effects of IDO inhibitor and aPD-1 immune checkpoint inhibitor combination therapy.

2.2) Hydrophobic ion pairing is an efficient approach to nanoformulate navoximod within polymeric nanoparticles.

Aims

2.1) Develop and characterise a nanoformulation of navoximod based on hydrophobic ion pairing and PEG-PLGA nanoparticles.

2.2) Investigate an IDO inhibitor and PD-1 immune checkpoint antibodies combination therapy on the anti-tumour immune responses in the context of head and neck cancer.

3) **Hypothesis**

A nanoformulation of the small molecule SB415286 GSK3 inhibitor will provide new insights about its efficacy as an alternative to antibodies for PD-1 inhibition.

Aim

Investigate the potential of a GSK3 inhibitor as an alternative approach to inhibit PD-1 immune checkpoints on CAR T-cells.

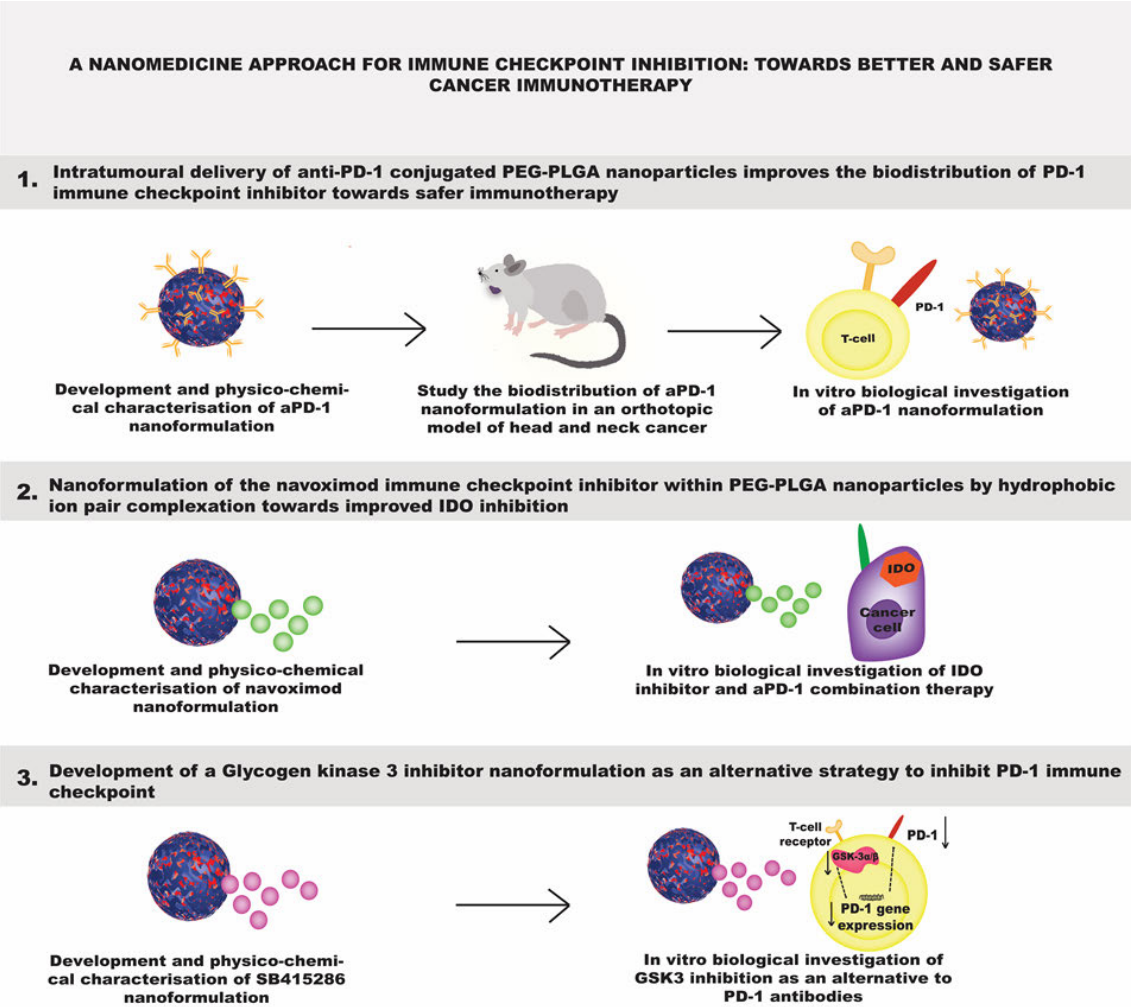

Figure 1-1 Schematic illustration of project design to address three main aims of the thesis.

1.2 Thesis structure

This thesis is entitled 'A Nanomedicine Approach for Immune Checkpoint Inhibition: towards Better and Safer Cancer Immunotherapy'. The thesis is composed of 7 chapters presented in the format of a 'thesis with publications': Chapter 1: Introduction; Chapter 2: Literature review; Chapter 3-6: Results chapters, which are self-contained with their own introduction, methods, results and discussion and conclusion; Chapter 7: Conclusion.

Chapter 1 is an introduction to the thesis, introducing the overall research aims, the thesis structure and the main outcomes.

Chapter 2 reviews the relevant literature regarding immune checkpoint inhibitors for cancer immunotherapy, discussing the existing challenges and the potential of nanomedicine to address these challenges.

Chapter 3 is entitled ‘Intratumoural delivery of anti-PD-1 conjugated PEG-PLGA nanoparticles improves the biodistribution of PD-1 immune checkpoint inhibitor towards safer immunotherapy’. In this study, a PD-1 antibody nanoformulation based on PEG-PLGA NPs was developed towards altering the biodistribution of the antibodies upon intratumoural administration.

Chapter 4 is entitled ‘Nanoformulation of the navoximod immune checkpoint inhibitor within PEG-PLGA nanoparticles by hydrophobic ion pair complexation towards improved IDO inhibition’. In this chapter, we investigate an alternative approach to PD-1 antibodies checkpoint inhibition. Specifically, we demonstrate that the IDO inhibitor navoximod can be efficiently formulated using hydrophobic ion pairing. This approach dramatically improved the loading of navoximod within PEG-PLGA nanoparticles. The efficacy of the navoximod nanoformulation as either a single therapy or in combination with PD-1 antibodies in inhibiting IDO immune checkpoint and enhancing T-cell cytotoxicity against cancer cells was investigated in a comprehensive set of *in vitro* experiments.

Chapter 5 is entitled ‘Development of a Glycogen kinase 3 inhibitor nanoformulation as an alternative strategy to inhibit PD-1 immune checkpoint”. This chapter reports the development of a GSK3 inhibitor nanoformulation within PEG-PLGA NPs using hydrophobic ion pairing. The efficiency of this approach was evaluated *in vitro*, yielding promising evidence of biological activity.

Chapter 6 is entitled ‘Microfluidic nanoprecipitation combined with hydrophobic ion pairing enables the preparation of high performance indocyanine green highly tuneable nanoformulations’. Building on the formulation advances used in chapters 4 and 5, we investigated the use of PEG-PLGA NPs and the hydrophobic ion pairing approach to improve the encapsulation and stability of indocyanine green, a clinically approved fluorescent dye commonly used in image guided cancer surgeries. The physicochemical properties of the ICG nanoformulations could be precisely tuned using a 3D printed high-throughput microfluidic nanoprecipitation device. The potential of the ICG nanoformulation to assist sentinel lymph node biopsy procedure in deep seated organs was assessed in a large animal model (pigs) in collaboration with Ferronova Pty.

Chapter 7 discusses the overall outcomes of this PhD research project and outlines possible future work.

1.3 Thesis outcomes

This PhD research project is anticipated to result in four first author research papers. The details and status of these outcomes are as follow:

1) Badiee P., Maritz M.F, Dmochowska N., Cheah E., Thierry B. Intratumoural delivery of anti-PD-1 conjugated PEG-PLGA nanoparticles improves the biodistribution of PD-1 immune checkpoint inhibitor towards safer immunotherapy. Submitted in September 2021 and under review.

2) Badiee P., Maritz M.F, Dmochowska N., Thierry B. Nanoformulation of the navoximod immune checkpoint inhibitor within PEG-PLGA nanoparticles by hydrophobic ion pair complexation towards improved IDO inhibition. To be submitted in early 2022 after completion of preclinical studies.

3) Badiee P., Maritz M.F, Thierry B. Glycogen Kinase 3 Inhibitor Loaded Nanoparticle, As an Efficient Alternative Strategy to Inhibit PD-1 Immune Checkpoint. To be submitted in December 2021.

4) Badiee P., Cousins A., Cheah E., Thierry B. Microfluidic nanoprecipitation combined with hydrophobic ion pairing enables the preparation of high performance indocyanine green highly tuneable nanoformulations. To be submitted in early 2022. This work has been conducted in collaboration with Ferronova, a cancer diagnostic company, and the technology is presently being evaluated in coordination with Ferronova FerroTrace sentinel lymph node mapping approach.

In addition, this research was presented at the following international conferences:

1) 10th International Nanomedicine Conference, Sydney, Australia, 2019, oral presentation titled: Anti PD-1 Conjugated Nanoparticles: A Promising Delivery System to Inhibit PD-1 Immune Checkpoint.

2) 47th Annual Meeting of the Controlled Release Society, virtual meeting, 2020, poster presentation titled: Anti-PD-1 Decorated PLGA Nanoparticles: A Safer Approach to the Delivery of Immune Checkpoint Inhibitors?

3) 48th Annual Meeting of the Controlled Release Society, virtual meeting, 2021, poster presentation titled: Hydrophobic Ion Pair Complexation Enables Effective Formulation of IDO Inhibitor in PLGA Nanoparticles: A New Delivery System to Improve PD-1 Immune Checkpoint Inhibition.

1.4 References

[1] D.H. Munn, A.L. Mellor, IDO in the Tumor Microenvironment: Inflammation, Counter-Regulation, and Tolerance, Trends Immunol. 37 (2016) 193–207. https://doi.org/10.1016/j.it.2016.01.002.

[2] L. Dyck, K.H.G. Mills, Immune checkpoints and their inhibition in cancer and infectious diseases, Eur. J. Immunol. 47 (2017) 765–779. https://doi.org/10.1002/eji.201646875.

[3] H.T. Lee, S.H. Lee, Y.S. Heo, Molecular interactions of antibody drugs targeting PD-1, PD-L1, and CTLA-4 in immuno-oncology, Molecules. 24 (2019) 1190. https://doi.org/10.3390/molecules24061190.

[4] E. Pérez-Ruiz, I. Melero, J. Kopecka, A.B. Sarmento-Ribeiro, M. García-Aranda, J. De Las Rivas, Cancer immunotherapy resistance based on immune checkpoints inhibitors: Targets, biomarkers, and remedies, Drug Resist. Updat. 53 (2020) 100718. https://doi.org/10.1016/j.drup.2020.100718.

[5] F. Martins, L. Sofiya, G.P. Sykiotis, F. Lamine, M. Maillard, M. Fraga, K. Shabafrouz, C. Ribi, A. Cairoli, Y. Guex-Crosier, T. Kuntzer, O. Michielin, S. Peters, G. Coukos, F. Spertini, J.A. Thompson, M. Obeid, Adverse effects of immune-checkpoint inhibitors: epidemiology, management and surveillance, Nat. Rev. Clin. Oncol. 16 (2019) 563–580. https://doi.org/10.1038/s41571-019-0218-0.

[6] G. Myers, Immune-related adverse events of immune checkpoint inhibitors: A brief review, Curr. Oncol. 25 (2018) 342–347. https://doi.org/10.3747/co.25.4235.

[7] S. Koyama, E.A. Akbay, Y.Y. Li, G.S. Herter-Sprie, K.A. Buczkowski, W.G. Richards, L. Gandhi, A.J. Redig, S.J. Rodig, H. Asahina, R.E. Jones, M.M. Kulkarni, M. Kuraguchi, S. Palakurthi, P.E. Fecci, B.E. Johnson, P.A. Janne, J.A. Engelman, S.P. Gangadharan, D.B. Costa, G.J. Freeman, R. Bueno, F.S. Hodi, G. Dranoff, K.K. Wong, P.S. Hammerman, Adaptive resistance to therapeutic PD-1 blockade is associated with upregulation of alternative immune checkpoints, Nat. Commun. 7 (2016) 1–9. https://doi.org/10.1038/ncomms10501.

[8] X. Wang, F. Wang, M. Zhong, Y. Yarden, L. Fu, The biomarkers of hyperprogressive disease in PD-1/PD-L1 blockage therapy, Mol. Cancer. 19 (2020) 1–15. https://doi.org/10.1186/s12943-020-01200-x.

[9] A. Nayak-Kapoor, Z. Hao, R. Sadek, R. Dobbins, L. Marshall, N.N. Vahanian, W. Jay Ramsey, E. Kennedy, M.R. Mautino, C.J. Link, R.S. Lin, S. Royer-Joo, X. Liang, L. Salphati, K.M. Morrissey, S. Mahrus, B. McCall, A. Pirzkall, D.H. Munn, J.E. Janik, S.N. Khleif, Phase Ia study of the indoleamine 2,3-dioxygenase 1 (IDO1) inhibitor navoximod (GDC-0919) in patients with recurrent advanced solid tumors, J. Immunother. Cancer. 6 (2018) 1–12. https://doi.org/10.1186/s40425-018-0351-9.

[10] K.H. Jung, P. LoRusso, H. Burris, M. Gordon, Y.J. Bang, M.D. Hellmann, A. Cervantes, M. Ochoa de Olza, A. Marabelle, F. Stephen Hodi, M.J. Ahn, L.A. Emens, F. Barlesi, O. Hamid, E. Calvo, D. McDermott, H. Soliman, I. Rhee, R. Lin, T. Pourmohamad, J. Suchomel, A. Tsuhako, K. Morrissey, S. Mahrus, R. Morley, A. Pirzkall, S. Lindsey Davis, Phase I study of the indoleamine 2,3-dioxygenase 1 (IDO1) inhibitor navoximod (GDC-0919) administered with PD-L1 inhibitor (atezolizumab) in advanced solid tumors, Clin. Cancer Res. 25 (2019) 3220–3228. https://doi.org/10.1158/1078-0432.CCR-18-2740.

[11] J. Krueger, C.E. Rudd, A. Taylor, Glycogen synthase 3 (GSK-3) regulation of PD-1 expression and and its therapeutic implications, Semin. Immunol. 42 (2019) 101295. https://doi.org/10.1016/j.smim.2019.101295.

[12] K. Li, H. Tian, Development of small-molecule immune checkpoint inhibitors of PD-1/PD-L1 as a new therapeutic strategy for tumour immunotherapy, J. Drug Target. 27 (2019) 244–256. https://doi.org/10.1080/1061186X.2018.1440400.

[13] S. Lim, J. Park, M.K. Shim, W. Um, H.Y. Yoon, J.H. Ryu, D.K. Lim, K. Kim, Recent advances and challenges of repurposing nanoparticle-based drug delivery systems to enhance cancer immunotherapy, Theranostics. 9 (2019) 7906–7923. https://doi.org/10.7150/thno.38425.

[14] H. Zhong, G. Chan, Y. Hu, H. Hu, D. Ouyang, A comprehensive map of FDA-approved pharmaceutical products, Pharmaceutics. 10 (2018) 263. https://doi.org/10.3390/pharmaceutics10040263.

[15] F. Danhier, E. Ansorena, J.M. Silva, R. Coco, A. Le Breton, V. Préat, PLGA-based nanoparticles: An overview of biomedical applications, J. Control. Release. 161 (2012) 505–522. https://doi.org/10.1016/j.jconrel.2012.01.043.

Chapter 2

Literature Review

2 Literature review

2.1 Immune checkpoints and their role in field of oncology

The harnessing of the immune system as a strategy for cancer treatment was pioneered by Dr William B. Coley in the 1890s [1,2]. More than sixty years later, Paul Ehrlich introduced the concept of immuno-surveillance, which was further developed by Brunet, proposing the role of immune system in cancer formation and growth [2]. This general concept is still true and it is well-established that cancer emerges when the immune system becomes weak and cannot recognize or combat cancer cells [2]. Recognition of immuno-surveillance mechanisms led to the introduction of immunotherapy as a powerful approach that synergize with other cancer therapeutic modalities, such as chemotherapy, radiotherapy and surgery, and shifted the current paradigm of cancer treatment [3].

In cancer immunotherapy, the immune system is stimulated to fight against the cancer, rather than using therapeutics to directly eliminate the cancer. Although cancer immunotherapy has long demonstrated great promises, its application was initially limited to vaccine development or boosting the immune system by inflammatory cytokines such as IL2 [4]. However, in 2013, the Science journal selected cancer immunotherapy as the breakthrough of year, based on the advances of immune checkpoint (ICP) antibodies and chimeric antigen receptor therapy [5].

ICPs are mostly receptors expressed in immune cells, mainly T-cells, that when engaged with their ligand shift T-cells to the exhausted phenotype, which are not proliferative and active against antigens [6]. The cytotoxic T lymphocyte–associated protein 4 (CTLA-4) was first discovered as an intracellular protein, which translocates to the surface of T-cells after T-cell receptor (TCR) engagement [4]. To activate T-cells, antigen presenting cells (APC) present the antigen by major histocompatibility complex (MHC) to interact with TCR on cells. In addition, co-stimulatory receptors of T-cells bind to their receptors to fully activate the T-cells. CTLA-4 outcompetes the CD28 co-stimulatory receptor to bind with CD80/CD86 and induce inhibitory signal into the T-cells [4]. Another immune-inhibitory pathway related to programmed cell death 1 (PD-1; also known as CD279) was soon after discovered. PD-1 is predominantly expressed on T-cells, inducible upon T-cell activation, but it is also expressed on B-cells, natural killer cells, activated monocytes and dendritic cells (DC) [7]. PD-L1 and PD-L2 are PD-1's ligands, the expression of the PD-

L2 is limited, but PD-L1 is expressed on a wide range of both hematopoietic and non-hematopoietic cells and it is upregulated by inflammatory cytokines, such as INFγ [6,7]. Similar to CTLA-4, the interaction of PD-1 with its ligand results in lower T-cell effector functions and induces exhausted T-cells. The PD-1/PD-L1 pathway is involved in central and peripheral tolerance by regulating T-cell priming, as well as T-cell proliferation and cytotoxic functions, such as cytokine production [7].

During cancer formation, immune cells with immunosuppressive phenotype are recruited to induce an immunosuppressive and less immunogenic tumour microenvironment (TME). Immunosuppressive cells include regulatory T-cells (T_{reg}), myeloid-derived suppressor, tumour-associated macrophages (TAM) and tolerogenic DC [8]. The PD-1/PD-L1 pathway has a critical role in mediating immunosuppression and PD-L1 upregulation is found in a wide range of cancers [9]. Interaction of PD-L1 with PD-1 receptors on T-cells hampers T-cell cytotoxicity and induces exhausted T-cells, and is an effective strategy for cancer cells to escape the immune system.

2.2 Immune checkpoint antibodies

About a decade ago, several outstanding clinical trial successes of ICP inhibitors (ICI) revolutionized the field of oncology. These clinical trials led to the US food and drug administration (FDA) approval of several antibodies against ICPs, which block the interaction of ICPs and their ligands, thereby preventing the inhibitory signals toward the immune cells [10] (Figure 2-1). Monoclonal antibodies that block PD-1 (aPD-1), PD-L1 (aPD-L1) and CTLA-4 (aCTLA-4) can restore anti-tumour T-cell activity and increase T-cell activation and proliferation and enhance T-cell tumour infiltration [4,6].

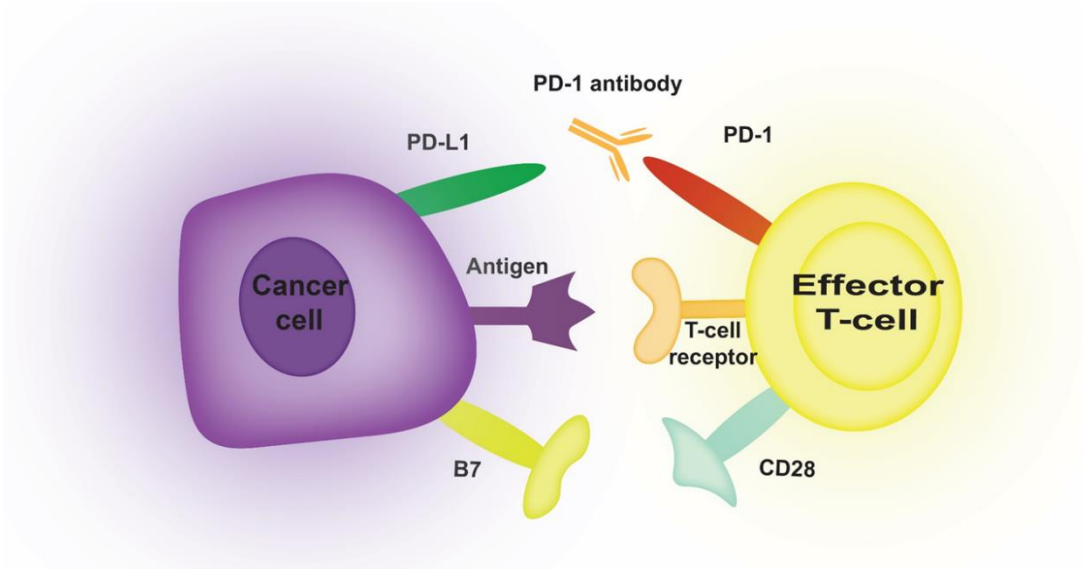

Figure 2-1 Illustration of PD-1/PD-L1 interaction and aPD-1 site of action at T-cell and cancer cell interface.
After transduction of first T-cell activation signal through T-cell receptor, PD-1 co-inhibitory receptor on T-cell competes with CD28 co-stimulatory receptor. Engagement of PD-1 and PD-L1 on cancer cells shifts T-cells to exhausted phenotypes. PD-1 antibodies bind to PD-1 receptors and prevent the co-inhibitory signal and restore T-cell cytotoxic function.

For solid cancers, improved outcomes resulting from ICIs were initially observed in clinical trials of untreated patients at stage III/IV of unresectable melanoma and were then extended to other solid malignancies, including head and neck squamous cell carcinoma (HNSCC), renal cell carcinoma, non-small cell lung cancer [11,12]. These studies resulted in the approval of seven monoclonal antibodies in the market thus far (Table 2-1). For example, nivolumab, an aPD-1 agent, was compared with single-agent systemic therapy (methotrexate, docetaxel, or cetuximab) in a phase 3 trial of HNSCC patients (checkmate141) which demonstrated improved clinical outcome, as shown in table 2-2 [13,14].

Table 2-1 ICP antibodies in the market for cancer immunotherapy.

Antibodies approved/ target	Brand name	Indicated disease	Company/ Year of first approval
Ipilimumab/ CTLA-4 [15]	**Yervoy** ®	Melanoma	Bristol Myers Squibb/ 2011
Nivolumab/ PD-1 [16]	**Opdivo**®	HNSCC, NSCLC, malignant pleural mesothelioma, advanced RCC, cHL, UC, MSI-H, dMMR, metastatic CRC , HCC, ESCC	Bristol Myers Squibb/ 2014
Pembrolizumab/ PD-1 [17]	**Keytruda**®	Melanoma, HNSCC, NSCLC, SCLC, cHL, PMBCL, UC, MSI-H, dMMR, dMMR CRC, ESCC, Gastric Cancer, Cervical Cancer, HCC, MCC, RCC, Endometrial Carcinoma, CSCC, TNBC, tumour mutational burden-high cancer	Merck Sharp Dohme/ 2014
Cemiplimab-rwlc/ PD-1	**Libtayo**®	CSCC	Regeneron pharmaceuticals/ 2018
Atezolizumab/ PD-L1 [18]	**Tecentriq**®	UC, NSCLC, TNBC, SCLC, HCC, melanoma	Genentech Inc/ 2016

Durvalumab/ PD-L1 [19]	**Imfinzi®**	UC, SCLC, NSCLC	Astrazeneca UK Ltd/ 2017
Avelumab/ PD-L1 [20]	**Bavencio®**	MCC, UC, RCC	EMD Serono Inc/ 2017

Table 2-1 abbreviations: Melanoma, head and neck squamous cell carcinoma (HNSCC), non-small cell lung cancer (NSCLC), renal cell carcinoma (RCC), classical Hodgkin lymphoma (cHL), urothelial carcinoma (UC), microsatellite instability-high (MSI-H), mismatch repair deficient (dMMR), colorectal cancer (CRC), hepatocellular carcinoma (HCC), esophageal squamous cell carcinoma (ESCC), small cell lung cancer (SCLC), primary mediastinal large B-cell lymphoma (PMBCL), merkel cell carcinoma (MCC), cutaneous squamous cell carcinoma (CSCC), triple-negative breast cancer (TNBC).

Table 2-2 Clinical outcome of checkmate 141 clinical trial of nivolumab.

	Nivolumab	Standard therapy
Median overall survival (months)	7.7	3.3
Rates of overall survival at 1 year (%)	39.2	15.4
Objective response rate (%)	19.2	11.5
Progression free survival (months)	2.3	2.3
Grade 3-4 treatment-related adverse event (%)	27.5	32

Despite ICIs success in the clinic, only a limited number of patients respond to therapy and a minority of these responding patients achieve complete remission [21]. Analyses of responder and non-responder patients to aPD-1 therapy indicated a combination of predictive criteria [22]. Higher PD-L1 expression levels in tumours are linked to a greater response; however, low PD-L1 burden does not rule out aPD-1 as a choice of treatment [23]. The genetic profile and markers of the tumour, such as type and level of neo-antigens, deficiency of mismatch DNA repair pathway and alterations in leukocyte antigen alleles, all serve as predictive criteria for ICI resistance [4,23]. In some cases, overexpression of alternative ICPs and inhibitory signals are involved in the limited response rate of ICIs. For example, Koyama *et al.*, observed the upregulation of T-cell immunoglobulin mucin-3 (TIM-3) ICP following aPD-1 therapy in two mouse models of lung adenocarcinoma [24]. In addition, overexpression of indoleamine 2,3-dioxygenase (IDO), an inhibitory ICP, is involved in both aCTLA-4 and aPD-1 resistance [25]. Besides

the molecular mechanism of ICI resistance, tumour accumulation of these therapeutic agents is limited and a considerable quantity of antibody is wasted due to the distribution of the ICPs in off-target organs [26,27]. Biodistribution of radio-labelled aPD-L1 in a mouse model of breast cancer showed high accumulation of the antibodies in spleen, thymus, liver and tumour, e.g. the injected dose per gram of tissue was the highest in spleen within the 144 hour of study time frame [26]. Moreover, it was observed that pembrolizumab (aPD-1) has the highest accumulation in liver and spleen of rat and mice models immediately after injection and up until seven days [28].

Another major challenge of ICIs, which limits their application, is that a large population of patients treated with ICP antibodies experience immune related adverse events (IRAE). IRAEs are side effects produced as a consequence of nonspecific immunogenic activation and occur in more than 70 % of patients, often leading to discontinuation of the therapy [29,30]. ICI induced IRAEs are observed in a wide range of organs, but the majority occur in the gastrointestinal tract, endocrine glands, skin and liver, and less often in the central nervous, cardiovascular, pulmonary, musculoskeletal and hematologic systems [31,32]. While IRAEs are more commonly observed following aCTLA-4 treatment compared to aPD-1 and aPD-L1 treatment, it is still one of the major limitations for all approved ICIs [33,34]. The detailed mechanisms of ICI induced IRAEs are yet to be fully elucidated but the inhibition of ICPs in off-target organs, which can then result in activation of immune cells against normal tissues, is directly implicated. For instance, PD-1 receptors function in the maintenance of self-tolerance. Therefore, PD-1 blockade in normal tissues disturbs the balance of immune system and hyper activate the immune cells [35,36]. The inflammatory and autoimmunity nature of the adverse events support this reasoning [35,37]. Once more, the biodistribution of ICIs has an important impact as the presence of ICIs in off-target organs can block the ICPs resulting in active immune cells and cytotoxic cytokines in tissues, other than the tumour.

Ongoing research actively investigates methods to improve ICI therapy. The combination of two ICPs is a strategy that has been shown to enhance the efficacy of ICIs. The co-administration of aPD-1 and aCTLA-4 is currently under investigated in clinical trials [6]. Whilst combination therapy augments the efficacy of immunotherapy, the side effects, especially higher grade IRAEs rise, thereby acting like a double-edged sword [6,38]. Since circulation and accumulation of antibodies in off-target organs contribute to the occurrence of side effects, local delivery of ICIs has also been explored as a more

efficient alternative, as compared to systemic administration. Moreover, intra/peri-tumoural administration of ICIs, such as aPD-1 was shown to be associated with higher bioavailability in tumour and tumour draining lymph nodes (TDLN), which play a central role in priming the immune cells for anti-tumour responses [39,40]. Peri-tumoural administration of aCTLA-4 in a murine model of bladder carcinoma was as effective as systemic administration of higher dose of antibodies in reducing tumour size. In addition, lower levels of circulating antibodies and IL-6 were observed following local administration, potentially reducing the risk of adverse effects [41]. Fransen *et al.,* observed similar results by local injecting of low dose aCTLA-4 in montanide emulsion, as a slow released formulation. The local delivery system was associated with the same efficacy, as systemically administered high dose aCTLA-4, but lower levels of AST and ALT liver enzymes [42]. Nevertheless, two phase 1 clinical trials of intratumoural immuno-modulating antibodies were associated with high rate of adverse effects, suggesting a need for ICIs re-formulation to further improve their biodistribution [43–45].

Nanoparticles (NPs) have been extensively explored as drug delivery systems, although with limited success to date. The capability of NPs to modify the biodistribution of their payloads provides good rationale for using NPs for immunotherapy. Although nano-formulations of ICIs have not found their way to clinical trials yet, they have been investigated in preclinical studies [32]. Chen *et al.,* employed a bio-responsive NPs to co-deliver aPD-1 and anti-CD40 (a phagocytosis stimulating antibody), which enhanced anti-tumour response of T-cells after intratumoural administration in a mouse model of melanoma [46]. Although there is limited information about the biodistribution of nano-formulated ICI after local administration, there are several studies investigating the efficacy and biodistribution of systemically injected formulations. It was shown for example that conjugation of immunostimulatory antibodies to liposomal delivery systems changed the biodistribution of the antibody in a mouse tumour model, which led to a higher accumulation of antibodies in tumour tissue and lower concentration in blood circulation and off-target organs, compared to free antibodies [47]. The modified biodistribution resulted in higher anti-tumour responses and potentially lower side effects in preclinical settings [47]. Zhao *et al*., fabricated NPs by designing a self-assembling fusion protein made of aPD-1 single chain variable fragment and an amphiphilic peptide. The nanoparticulate aPD-1 was as effective as aPD-1 free antibodies in blocking of PD-

1 receptors [27]. To improve the efficacy of ICP inhibition, Mi *et al.*, conjugated aPD-1 and anti-OX-40, an immune-stimulatory antibody, to poly(ethylene glycol)-b-poly(lactide-co-glycolide) (PEG-PLGA) NPs and evaluated the efficacy of this delivery system in murine tumour models. The delivery system improved the anti-tumour response, reducing tumour size, increasing INFγ and inducing anti-tumour memory [48]. In another study, aPD-L1 conjugated to poly-(amidoamine) dendrimers increased the avidity of aPD-L1 to its target with rationale to improve the efficacy. *In vivo* imaging revealed a 2.5 fold increase of tumour targeting by the formulation compared to free antibodies in tumour bearing nude mice [49]. The ongoing research to employ nanoformulations for the delivery of ICIs indicates the strong promise of nanomedicine to improve the efficacy of ICP blockers and reduce their adverse effects. However, there is a limited knowledge of the impact of nanoformulation on their biodistribution, which is a key parameter in the efficacy and side effects of ICIs.

2.3 Alternative approaches for ICP inhibition

2.3.1 Overview of alternative ICP inhibitors

Increased knowledge of gene editing strategies has led to an increased focus on their application for cancer immunotherapy and more specifically, ICP inhibition. Inhibition of ICPs at the genomic level, as opposed to blocking the receptors by antibodies is associated with significant challenges for the gene edition of the immune cells. The majority of successful preclinical studies have utilised *ex vivo* approaches to inhibit ICPs for adoptive cell transfer. Examples of such studies include the electroporation of PD-1 small interfering RNA (siRNA) expressing retrovirus or producing a PD-1:CD28 chimera by viral transfection to activate T-cells, instead of exhaustion upon engagement with PD-L1, which both enhanced the cytotoxicity of T-cells [50,51]. The inhibition of CTLA-4 by clustered regularly interspaced short palindromic repeats (CRISPR) and CRISPR-associated protein 9 (CRISPR/Cas9) expressing lentivirus was also successful in enhancing the anti-tumour responses of T-cells *in vitro* and *in vivo* in colorectal carcinoma mouse model. [52].

The manufacturing complexity of cell-based therapeutics have pushed researchers to investigate *in situ* approaches to genetically modify ICP expression. Hence, NPs, such as lipid coated calcium phosphate, bovine serum albumin coated layered double hydroxide particles have been tested for the delivery of PD-1 and PD-L1 siRNA to T-lymphocytes

[53,54]. The promising results achieved by gene editing of ICPs have improved the cytotoxicity of T-lymphocytes; however, more robust anti-tumour responses are required to translate such approaches clinically.

Another approach applied to ICP inhibition is to employ low molecular weight inhibitors instead of antibodies, which has been mostly explored for PD-1/PD-L1 pathway. The advantages of small molecule inhibitors include lower production costs, higher stability, lower immunogenic side effects and potentially higher penetration in TME [55–57]. Due to the aforementioned benefits, several companies have turned their attention to small molecule inhibitors. There are several peptide-based and non-peptide-based molecules under development, however, only one, a PD-L1 inhibitor (CA-170), has reached the clinical trial phase [58,59]. However, small molecules have a short half-life and high distribution in off-target organs which is associated with high toxicity for immune active drugs [60]. NPs to improve the delivery and biodistribution of small molecules have also been investigated. In this regard, Luo *et al.*, co-loaded anti-PD-1 peptide and hollow gold NPs in PLGA NPs, as a controlled release delivery system. In combination with photothermal ablation, these NPs induced anti-tumour responses *in vitro* and *in vivo* [61]. In addition to targeting the PD-1 or PD-L1 directly, targeting other pathways with already characterised therapeutic agents, which affects the PD-1/PD-L1 pathway offers an alternative approach for immune checkpoint inhibition.

2.3.2 Indoleamine-2,3-dioxygenase inhibitors

Indoleamine-2,3-dioxygenase (IDO) is an inhibitory ICP and consists of two subgroup enzymes, IDO1 and IDO2, which together are referred as IDO. IDO is a deoxygenase enzyme that catabolizes tryptophan to kynurenine and other metabolites [62]. Both depletion of tryptophan and increases of its metabolites are involved in immunosuppressive signals that decrease effector T-cells (T_{eff}) and DCs function, increase T_{reg} differentiation and as a result, mediate immunosuppression. IDO is widely expressed in APCs and many cancer cells and it is upregulated by inflammatory mediators, such as INFγ; and is connected to other ICP pathways [63,64] (Figure 2-2). For example, PD-1 inhibitors increase the function and number of T_{eff} and reduce T_{reg} activity; consequently, T-cells secrete cytotoxic cytokines, such as INFγ, which promote IDO expression. On the other hand, IDO counteracts PD-1 inhibitors and induces immunosuppression.

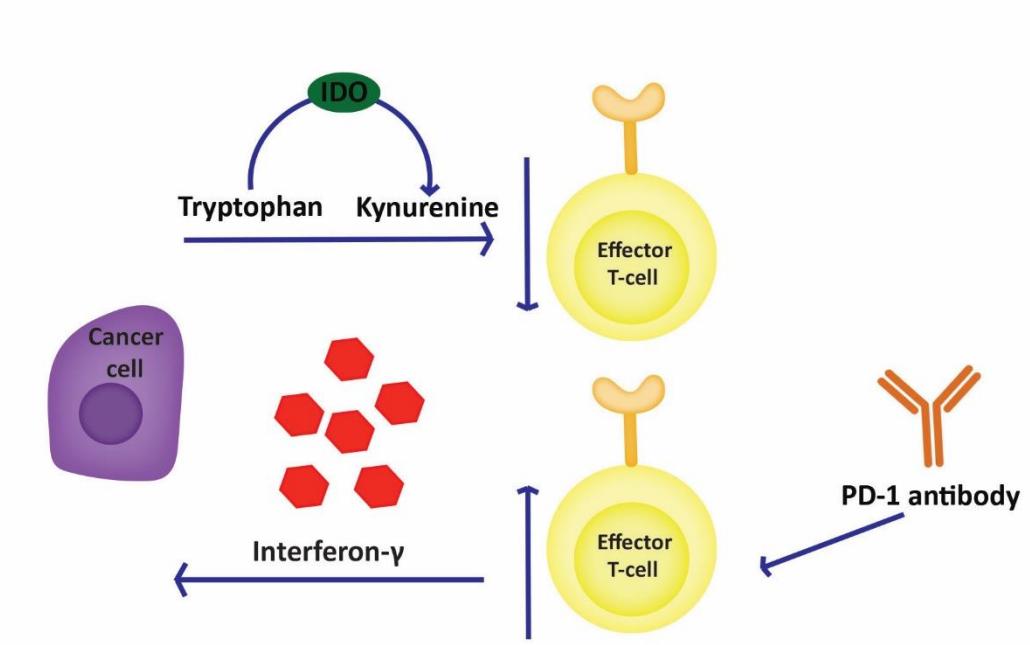

Figure 2-2 Schematic illustration of PD-1 inhibition effect on IDO pathway.
PD-1 inhibition increases the number and cytotoxicity of effector T-cells. As a result, T-cells secrete INFγ cytokine, which is a stimulator of IDO overexpression in cancer cells. IDO catabolizes tryptophan to kynurenine and other metabolites. The reduction of tryptophan and increase of kynurenine reduces the population and function of cytotoxic T-cells.

Several small molecule IDO inhibitors (IDOi) are under development for cancer immunotherapy. IDOis inhibit either IDO1 or IDO2 or both subgroups. Several IDOi, including indoximod, epacadostat, navoximod (NLG919) and BMS-986205 have reached clinical trials and are under investigation as single agents but mostly in combination with other ICIs or chemotherapeutic agents [63,65,66]. There has also been an increased attention of IDOi combination strategies with other oncology therapies. In a hepato-carcinoma preclinical study, IDOi enhanced the anti-tumour efficacy of aCTLA-4 and aPD-1 and overcame the adaptive resistance to ICP inhibitors [67]. A central nervous system penetrating IDOi in combination with aPD-1 and radiation, increased survival in a glioblastoma mouse model [68]. Moreover, it was observed that the anti-tumour response of IDOi was not only directed by IDO inhibition of tumour cells' but also, non-tumour cells were necessary for mediating the cytotoxic responses. Navoximod, in combination with aPD-L1, achieved promising anti-tumour responses in preclinical models [69,70]. Navoximod, as a single intervention administered orally was investigated in a phase 1 clinical trial for patients with advanced or recurrent solid tumours [71]. The most common adverse effects include fatigue, cough, pruritus, nausea and grade ≥ 3 adverse effects were observed in 64 % of total population. The combination of navoximod and atezolizumab (aPD-L1) was appraised in phase 1 clinical trials. Although the anti-

tumour activity was observed in these studies, the studies did not conclusively demonstrate any benefit by adding navoximod to atezolizumab [72,73].

To improve the toxicology profile of IDOi and its efficacy, various nanoparticle strategies have been investigated. Cheng *et al*., encapsulated navoximod in a nano-carrier consisting of self-assembling peptide targeted against PD-L1. This dual delivery system could disassemble in presence of matrix metalloproteinase-2 (MMP-2) of TME and sequentially release its cargo [70]. The self-assembling peptide was also investigated for co-delivery of indoximod and PD-L1 siRNA to enhance the immune cell functions against breast cancer *in vitro* and *in vivo* [74]. Chen *et al*. prepared an amphiphilic pro-drug of navoximod by using PEG polymer, which formed micellar NPs [75]. The micellar navoximod induced anti-tumour responses in preclinical studies and the response was significantly enhanced, when co-delivered with paclitaxel. Feng *et al.,* fabricated NPs by synthesis of PEG conjugated oxaliplatin and homodimer of navoximod [76]. The acidic and reducing properties of the TME was considered to disassemble the NPs and enabled the tumour penetration of the cargos. Also, the immunogenic cell death caused by oxaliplatin triggered the immune system, while IDOi prevented immunosuppression. The same approach of inducing immunogenic cell death and preventing IDO activity was utilized in another study which co-delivered chemotherapeutic agents and lipid tagged indoximod in a liposomal system [77,78]. The anti-tumour immune response of this delivery system was also enhanced when aPD-1 was co-administered in a preclinical model of breast cancer [77]. Dai *et al.,* incorporated navoximod in NPs made of polymer-curcumin conjugate, as a size shrinkable delivery system in TME of melanoma bearing mice model [79]. To improve the delivery of IDOi, drug-peptide conjugates, cyclodextrin and silica NPs have been investigated *in vitro* and in animal models [80–82]. These studies indicate that nanoformulation has a great potential in improving the formulation and delivery of IDOis. However, it is necessary to design the formulations to achieve high potency with a simple and effective formulation to facilitate the clinical translation.

2.3.3 Glycogen synthase kinase 3

Glycogen synthase kinase 3 (GSK3) is a serine/threonine protein kinase that is involved in a variety of physiological functions, such as cell cycle regulation, cell proliferation, and glucose uptake [83]. Due to its important role in different diseases, including cancers, several small molecule inhibitors of GSK3 (GSKi) have been developed as therapeutic agents. In recent years, the effect of GSK3i on PD-1 expression in T-cells was

investigated and it was found that GSK3 is an upstream pathway that controls PD-1 expression [84]. GSK3 is constitutively expressed in resting T-cells and it becomes partially inactive upon T-cell activation; consequently, T-bet transcription increases and this reduces the transcription of PDCD-1 (PD-1 gene) [85] (Figure 2-3). Rudd *et al.*, showed that inhibition of GSK3 was not only beneficial for viral (MHV-68) clearance, but was also as effective as aPD-1 in anti-tumour functions [84,86]. Inhibition of GSK3i by small molecule GSK3i or GSK3 siRNA increased cytotoxic T-cell proliferation, granzyme B and INFγ production of T-cells [84]. Moreover, it was found that GSK3 inhibition substituted CD28 co-stimulatory receptor and also reduced the expression of lymphocyte activation gene-3 (LAG-3) co-inhibitory receptor on T-cells [87,88]. In addition, GSK3i efficiently reduced PD-1 expression in chimeric antigen receptor expressing T-cells (CAR-Ts) and consequently, increased CAR-T cells' proliferation, preventing activated T-cell death and induced memory phenotype of CAR-T cells [89]. Nevertheless, small molecules suffer from short half-life, high off-target distribution and therefore high toxicity and low efficacy [60]. In order to mitigate the toxicity of a GSK3i and improve its biodistribution, Allen *et al.*, encapsulated GSK3i in lipid coated porous silica nanoparticles [90]. By this means, GSK3i tumour accumulation and anti-tumour response increased in a mouse tumour model. GSK3i can potentially serve as a suitable alternative to aPD-1, with lower cost of production and better stability if formulation of GSK3i can improve toxicity profile and efficacy.

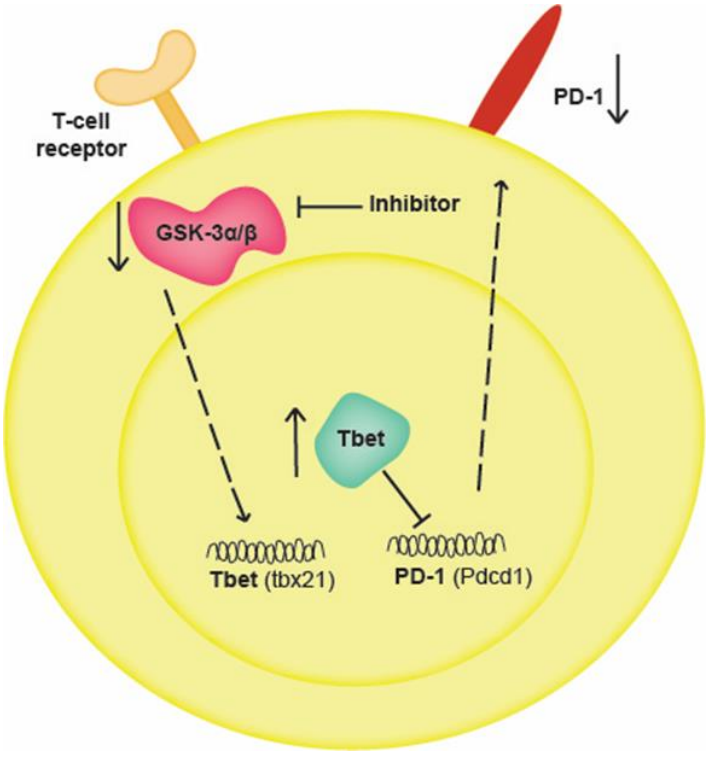

Figure 2-3 GSK3 pathway upstream of PD-1 expression.
GSK3 is an enzyme upstream of Tbet transcription factor and by GSK3 inhibition, the transcription and expression of Tbet increases. Therefore, Tbet will inhibit the transcription of PD-1 gene (pdcd1), which increases T-cells' cytotoxicity.

2.4 PLGA/PEG-PLGA NPs as a drug delivery system

PLGA is a biodegradable co-polymer consisting of lactic acid (LA) and glycolic acid (GA) [91]. PLGA has a long history of safe use in humans. PLGA undergoes ester bond hydrolysis in the body and degrades to monomers, which ultimately metabolize to CO_2 and H_2O compounds and are excreted from the body [92]. The physicochemical properties of PLGA can be modified by using different ratios of LA/GA and different molecular weights of either of these blocks. The biocompatibility as well as the flexibility of PLGA properties have broadened its application in the biomedical sector. FDA approval of PLGA polymer based product in biomedical applications has encouraged scientists to explore its application for several purposes and more than ten biomedical products based on PLGA are currently in the market [93,94].

PLGA has been widely utilized in the field of nanomedicine for a variety of applications, including drug delivery. PLGA NPs are versatile carriers for therapeutic agents with different physicochemical characteristics. When PLGA NPs are administered to the systemic blood circulation, opsonin proteins in the blood attach to the NPs and facilitate phagocytosis by macrophages and the reticuloendothelial system, which clear them from the blood circulation [91]. Opsonisation can be restricted by coating with hydrophilic polymers. PEG is the most common antifouling agent used for PLGA surface coverage [95]. Moreover, PEGylation of PLGA NPs can be used for further surface modifications, such as targeting the delivery system to specific cell subsets or modifying NPs' cellular uptake and internalization using antibodies, peptides, aptamers or chemical small molecules [96–98]. Preparation methods of PLGA NPs are generally based on emulsion and precipitation. Some examples of these methods are summarized in Table 2-3.

Table 2-3 Examples of bulk PLGA NPs preparation methods.

Method of preparation	Advantages	Disadvantages
Single/double emulsion-evaporation [92,99,100]	Suitable for the loading of hydrophobic and hydrophilic drugs	Heat/vacuum requirement, relatively large particle size production, solvent residual, requirement for homogenizer or sonicator

Emulsification-solvent diffusion [99,100]	High encapsulation efficiency, no need for homogenizer	Removal of high volume of water, leakage of hydrophilic drug to the external aqueous phase and low entrapment efficiency
Salting-out [92,99,100]	Suitable method for loading of proteins, DNA and RNA, no heat requirement	Time consuming purification, limitation in scale-up, high speed homogenizer requirement
Nanoprecipitation [92,99]	Single step, relative scalability, small particle size, low energy mixing	Low encapsulation efficacy of hydrophilic drugs, dependence of particles' size distribution on mixing

The conventional preparation of PLGA NPs in bulk batches is highly dependent on several key parameters involved in the procedure, which substantially affects the shape, size, size distribution and batch-to-batch variation. Controlling these parameters in large batches is difficult, which limits the clinical translation of these formulations [101]. Conversely, microfluidic based nanoprecipitation has emerged as an alternative method for reproducible NPs preparation. In a microfluidic chip, nanoprecipitation occurs in small volumes in micron-sized channels. The formulation development and optimization can be adjusted by modifying the precursors' flow rates and polymer concentration [102]. NPs prepared by microfluidics devices usually have very monodisperse size distribution and limited batch-to-batch variation [101]. The NP production rate depends on the design and dimension of the microfluidic chip and with large enough microfluidic channels, high throughput NP production is achievable. Moreover, scale-up of NPs manufacturing can be done using several parallel chips, which in addition to the aforementioned advantages, can facilitate the translation of developed NPs from *in vitro* and preclinical experiments to clinical settings. Different strategies for microfluidic chip-based preparation of NPs have been utilised. The structure of two microfluidic chips developed in our research group for NP preparation are shown in Figure 2-4.

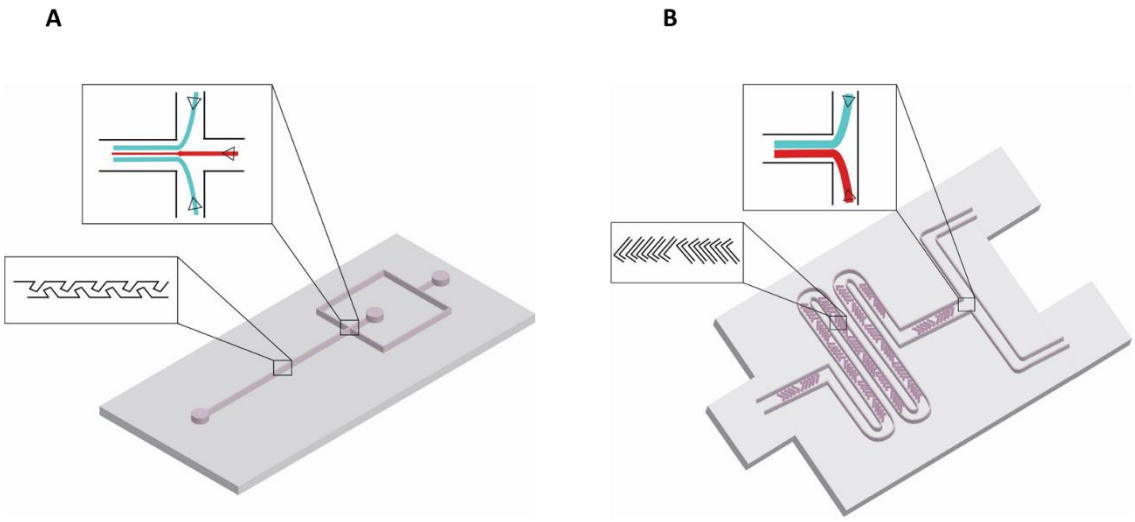

Figure 2-4 Illustration of two microfluidic chip design used for the nanoprecipitation of NPs.
A) A hydrodynamic flow focusing chip fabricated by polydimethylsiloxane (PDMS). The organic phase can be focused in a bollard mixing channel by two streams of aqueous phase. B) 3D printed microfluidic chip that rapidly mixes two immiscible phases in a herringbone structured mixing channel.

A focused-flow microfluidic chip was used for preparing different sizes of PEG-PLGA NPs ranging from micron to nanoscale. Water immiscible solvent and water miscible solvents were used for microparticle and NP preparation, respectively, using continuous phase flow rates 0.3 to 1 mL/min [103]. Similar geometric designs were used in another study to prepare curcumin loaded PLGA NPs [104]. By employing several flow rates and polymer concentration, 30-70 nm NPs were generated. A microfluidic origami chip made of PDMS with three inlets was used for the preparation of doxorubicin loaded PLGA NPs [105]. To decrease the mixing time and NPs size, the chip was manually folded to form either an arc shape or double spiral in the mixing channel, which could reduce the size of NPs to less than 100 nm. Microfluidic chips are also explored for the preparation of hybrid NPs. Lipid-PLGA hybrid NPs were prepared through micro-vortices in a flow-focusing microfluidic chip [106]. By controlling the flow rates and polymer concentration, NPs of 30-170 nm size range were obtained by a productivity rate of about 0.3 g/h. High-density lipoprotein (HDL) mimetic-PLGA NPs were prepared in a microfluidic chip to utilise the natural properties of HDL, while controlling the drug release by PLGA [107]. In this design, polymer and phospholipids were introduced into the central channel in a mixture of acetonitrile and ethanol and ApoA1 protein in PBS was injected from external channels to form a PLGA core and phospholipids shell. Rhee *et al.* fabricated a 3D hydrodynamic flow focusing microfluidic chip having three sequential inlets for inducing vertical focusing of PEG-PLGA phase by acetonitrile and further horizontal focusing of the stream by two aqueous phase streams [108]. Compared to 2D hydrodynamic flow

focusing, microfluidic based preparation and bulk mixing methods, the 3D hydrodynamic flow focusing chip resulted in more monodispersed and size-tuneable NPs.

The flexibility in controlling NPs size afforded by microfluidic method has critical application in the field of oncology and drug delivery. The impact of NP properties, including size, on NPs cellular uptake, pharmacokinetic and biodistribution and tumour accumulation is well-studied [109]. For example, the penetration and uptake of polystyrene NPs of three different sizes (30, 50 and 100 nm) were assessed in a spheroid model of colorectal cancer [110]. Smaller sized NPs (30 and 50 nm), could penetrate deeper than the larger ones, towards the core of spheroid. Also, cellular uptake profiles differed between different NP sizes, indicating more efficient uptake with the smaller ones. The effect of polymeric NPs' size and surface charge were investigated in a study by He *et al.* [111]. Carboxymethyl chitosan grafted and chitosan hydrochloride grafted NPs were used as the model of negatively and positively charged NPs with 150-500 nm size range, respectively. Phagocytosis in murine macrophages was highest for the highly charged lager NPs. In addition, slightly charged 150 nm NPs had more efficient tumour accumulation and the lowest distribution in off-target organs such as liver, lung and spleen in heterotopic mouse model of breast cancer. The size dependent uptake of mesoporous silica NPs was studied by Lu *et al.*, using NPs in the range of 30-280 nm [112]. In this range, 50 nm NPs had the highest cell uptake in HeLa cell lines followed by 30, 110, 280 and 170 nm NPs. NPs' size can demonstrate different properties depending on the context of application. For example, PEG coated and transferrin coated gold NPs were used as models of passive targeting and active targeting carriers, respectively [113]. Although tumour accumulation in an orthotopic mouse model was faster and higher for 60 nm NPs, no significant difference was observed for the 15, 30 and 100 nm NPs. A similar range of NPs size (30-120 nm) was used to investigate the effect of polyvinylpyrrolidone coated iron oxide NPs on magnetic resonance imaging of hepatic lesions [114]. NPs with the core size of 37 nm and hydrodynamic particle size of 100 nm had the highest cellular uptake and greatest contrast enhancement in imaging liver lesions. Two sizes of 50 nm and 75 nm PEGylated liposomes were prepared by Dong *et al*, to determine the effect of liposomes' size on cell penetration and biodistribution [115]. Liposomes of 50 nm and 75 nm showed similar cellular uptake profiles and biodistribution; but smaller liposomes extravasated further than larger ones, which is an important step for tissue distribution. As reviewed above, optimization of NPs size in

addition to other physico-chemical properties can extensively affect the NPs biodistribution, tumour uptake, extravasation, cellular endocytosis and off-target distribution.

Nevertheless, nanoprecipitation, which is the main mechanism of PLGA NPs formation within the microfluidic chips, has limitation in loading some drugs, typically small molecules that are not hydrophobic enough for efficient encapsulation [92]. In this regard, different strategies can be employed to overcome the difficulty of loading therapeutics. For example, preparation of a prodrug that chemically modifies the structure of the drug molecule and change its physicochemical properties has been broadly explored [116,117]. As an alternative approach, hydrophobic ion pairing has been successfully investigated by different researchers and even pharmaceutical companies [118]. In this approach, the drug molecule is paired with a counter ion, which has an opposite ionic charge to the drug molecule, without making any chemical modification to the structure of drug [119]. In addition to the shielding the ionic charge of drug, the hydrophobicity of drug further increases by hydrophobic group of counter ion, which eventually increases the encapsulation of drug [119]. The simplicity and efficacy of hydrophobic ion pairing provide a promising solution to enhance the drug loading of nanoprecipitated NPs.

The development of better strategies to overcome the challenges associated with ICIs is ongoing. The development of high performance carriers by scalable preparation methods are crucial for the translation of delivery systems. In this body of work, we developed and applied simple nanomedicine approaches to improve the delivery of immune checkpoint inhibitors and investigated the potential benefits of using such nanoformulations. A greater understanding of the effects of pairing nanomedicine with ICIs has strong potential to address some of the challenges of ICI formulations.

2.5 References

[1] I. Mellman, G. Coukos, G. Dranoff, Cancer immunotherapy comes of age, Nature. 480 (2011) 480–489. https://doi.org/10.1038/nature10673.

[2] P. Sharma, S. Hu-Lieskovan, J.A. Wargo, A. Ribas, Primary, Adaptive, and Acquired Resistance to Cancer Immunotherapy, Cell. 168 (2017) 707–723. https://doi.org/10.1016/j.cell.2017.01.017.

[3] J. Borst, T. Ahrends, N. Bąbała, C.J.M. Melief, W. Kastenmüller, CD4+ T cell help in cancer immunology and immunotherapy, Nat. Rev. Immunol. 18 (2018) 635–647. https://doi.org/10.1038/s41577-018-0044-0.

[4] A. Ribas, J.D. Wolchok, Cancer immunotherapy using checkpoint blockade, Science (80-.). 359 (2018) 1350–1355. https://doi.org/10.1126/science.aar4060.

[5] J. Couzin-Frankel, Cancer immunotherapy, Science (80-.). 342 (2013) 1432–1433. https://doi.org/10.1126/science.342.6165.1432.

[6] E.I. Buchbinder, A. Desai, CTLA-4 and PD-1 pathways similarities, differences, and implications of their inhibition, Am. J. Clin. Oncol. Cancer Clin. Trials. 39 (2016) 98–106. https://doi.org/10.1097/COC.0000000000000239.

[7] M.E. Keir, M.J. Butte, G.J. Freeman, A.H. Sharpe, PD-1 and its ligands in tolerance and immunity, Annu. Rev. Immunol. 26 (2008) 677–704. https://doi.org/10.1146/annurev.immunol.26.021607.090331.

[8] Y. Kondo, T. Ohno, N. Nishii, K. Harada, H. Yagita, M. Azuma, Differential contribution of three immune checkpoint (VISTA, CTLA-4, PD-1) pathways to antitumor responses against squamous cell carcinoma, Oral Oncol. 57 (2016) 54–60. https://doi.org/10.1016/j.oraloncology.2016.04.005.

[9] S.P. Patel, R. Kurzrock, PD-L1 expression as a predictive biomarker in cancer immunotherapy, Mol. Cancer Ther. 14 (2015) 847–856. https://doi.org/10.1158/1535-7163.MCT-14-0983.

[10] L. Galluzzi, G. Kroemer, A. Eggermont, Novel immune checkpoint blocker approved for the treatment of advanced melanoma, Oncoimmunology. 3 (2014) e967147.

[11] J.A. Seidel, A. Otsuka, K. Kabashima, Anti-PD-1 and anti-CTLA-4 therapies in cancer: Mechanisms of action, efficacy, and limitations, Front. Oncol. 8 (2018) 86. https://doi.org/10.3389/fonc.2018.00086.

[12] J. Larkin, V. Chiarion-Sileni, R. Gonzalez, J.J. Grob, C.L. Cowey, C.D. Lao, D. Schadendorf, R. Dummer, M. Smylie, P. Rutkowski, P.F. Ferrucci, A. Hill, J. Wagstaff, M.S. Carlino, J.B. Haanen, M. Maio, I. Marquez-Rodas, G.A. McArthur, P.A. Ascierto, G. V. Long, M.K. Callahan, M.A. Postow, K. Grossmann, M. Sznol, B. Dreno, L. Bastholt, A. Yang, L.M. Rollin, C. Horak, F.S. Hodi, J.D. Wolchok, Combined Nivolumab and Ipilimumab or Monotherapy in Untreated Melanoma, N. Engl. J. Med. 373 (2015) 23–34. https://doi.org/10.1056/nejmoa1504030.

[13] R.L. Ferris, G. Blumenschein, J. Fayette, J. Guigay, A.D. Colevas, L. Licitra, K. Harrington, S. Kasper, E.E. Vokes, C. Even, F. Worden, N.F. Saba, L.C. Iglesias Docampo, R. Haddad, T. Rordorf, N. Kiyota, M. Tahara, M. Monga, M. Lynch, W.J. Geese, J. Kopit, J.W. Shaw, M.L. Gillison, Nivolumab for Recurrent Squamous-Cell Carcinoma of the Head and Neck, N. Engl. J. Med. 375 (2016) 1856–1867. https://doi.org/10.1056/nejmoa1602252.

[14] M.L. Gillison, G. Blumenschein, J. Fayette, J. Guigay, A.D. Colevas, L. Licitra, K.J. Harrington, S. Kasper, E.E. Vokes, C. Even, F. Worden, N.F. Saba, L.C. Iglesias Docampo, R. Haddad, T. Rordorf, N. Kiyota, M. Tahara, M. Monga, M. Lynch, L. Li, R.L. Ferris, CheckMate 141: 1-Year Update and Subgroup Analysis of Nivolumab as First-Line Therapy in Patients with Recurrent/Metastatic Head and Neck Cancer, Oncologist. 23 (2018) 1079. https://doi.org/10.1634/theoncologist.2017-0674.

[15] Purple Book: Database of Licensed Biological Products, (2011). https://purplebooksearch.fda.gov/results?query=ipilimumab&title=Yervoy (accessed January 11, 2021).

[16] Purple Book: Database of Licensed Biological Products, (2014). https://purplebooksearch.fda.gov/results?query=nivolumab&title=Opdivo (accessed January 11, 2021).

[17] Purple Book: Database of Licensed Biological Products, (2014). https://purplebooksearch.fda.gov/results?query=pembrolizumab&title=Keytruda

(accessed January 11, 2021).

[18] Purple Book: Database of Licensed Biological Products, (2016). https://purplebooksearch.fda.gov/results?query=atezolizumab&title=Tecentriq (accessed January 11, 2021).

[19] Purple Book: Database of Licensed Biological Products, (2017). https://purplebooksearch.fda.gov/results?query=durvalumab&title=Imfinzi (accessed January 11, 2021).

[20] Purple Book: Database of Licensed Biological Products, (2017). https://purplebooksearch.fda.gov/results?query=avelumab&title=Bavencio (accessed January 11, 2021).

[21] R.M. Wong, R.B. Cameron, Immune Checkpoint Blockade and Adaptive Immune Resistance in Cancer, in: Immunother. - Myth. Reality, Ideas, Futur., 2017: pp. 47–61. https://doi.org/10.5772/66494.

[22] E. Pérez-Ruiz, I. Melero, J. Kopecka, A.B. Sarmento-Ribeiro, M. García-Aranda, J. De Las Rivas, Cancer immunotherapy resistance based on immune checkpoints inhibitors: Targets, biomarkers, and remedies, Drug Resist. Updat. 53 (2020) 100718. https://doi.org/10.1016/j.drup.2020.100718.

[23] D. Liu, R.W. Jenkins, R.J. Sullivan, Mechanisms of resistance to immune checkpoint blockade, Am. J. Clin. Dermatol. 20 (2019) 41–54.

[24] S. Koyama, E.A. Akbay, Y.Y. Li, G.S. Herter-Sprie, K.A. Buczkowski, W.G. Richards, L. Gandhi, A.J. Redig, S.J. Rodig, H. Asahina, R.E. Jones, M.M. Kulkarni, M. Kuraguchi, S. Palakurthi, P.E. Fecci, B.E. Johnson, P.A. Janne, J.A. Engelman, S.P. Gangadharan, D.B. Costa, G.J. Freeman, R. Bueno, F.S. Hodi, G. Dranoff, K.K. Wong, P.S. Hammerman, Adaptive resistance to therapeutic PD-1 blockade is associated with upregulation of alternative immune checkpoints, Nat. Commun. 7 (2016) 1–9. https://doi.org/10.1038/ncomms10501.

[25] D.H. Munn, A.L. Mellor, IDO in the Tumor Microenvironment: Inflammation, Counter-Regulation, and Tolerance, Trends Immunol. 37 (2016) 193–207. https://doi.org/10.1016/j.it.2016.01.002.

[26] A. Josefsson, J.R. Nedrow, S. Park, S.R. Banerjee, A. Rittenbach, F. Jammes, B. Tsui, G. Sgouros, Imaging, biodistribution, and dosimetry of radionuclide-labeled PD-L1 antibody in an immunocompetent mouse model of breast cancer, Cancer Res. 76 (2016) 472–479. https://doi.org/10.1158/0008-5472.CAN-15-2141.

[27] P. Zhao, D. Atanackovic, S. Dong, H. Yagita, X. He, M. Chen, An Anti-Programmed Death-1 Antibody (αPD-1) Fusion Protein That Self-Assembles into a Multivalent and Functional αPD-1 Nanoparticle, Mol. Pharm. 4 (2017) 1494–1500. https://doi.org/10.1021/acs.molpharmaceut.6b01021.

[28] C.G. England, E.B. Ehlerding, R. Hernandez, B.T. Rekoske, S.A. Graves, H. Sun, G. Liu, D.G. McNeel, T.E. Barnhart, W. Cai, Preclinical pharmacokinetics and biodistribution studies of 89Zr-Labeled Pembrolizumab, J. Nucl. Med. 58 (2017) 162–168. https://doi.org/10.2967/jnumed.116.177857.

[29] M.A. Postow, M.K. Callahan, J.D. Wolchok, Immune checkpoint blockade in cancer therapy, J. Clin. Oncol. 33 (2015) 1974. https://doi.org/10.1200/JCO.2014.59.4358.

[30] M.E. Suarez-Almazor, S.T. Kim, N. Abdel-Wahab, A. Diab, Review: Immune-Related Adverse Events With Use of Checkpoint Inhibitors for Immunotherapy of Cancer, Arthritis Rheumatol. 69 (2017) 687–699. https://doi.org/10.1002/art.40043.

[31] M.A. Postow, R. Sidlow, M.D. Hellmann, Immune-Related Adverse Events Associated with Immune Checkpoint Blockade, N. Engl. J. Med. 378 (2018) 158–168. https://doi.org/10.1056/nejmra1703481.

[32] M.J. Sanaei, A. Pourbagheri-Sigaroodi, V. Kaveh, S.A. Sheikholeslami, S. Salari, D. Bashash, The application of nano-medicine to overcome the challenges related to immune checkpoint blockades in cancer immunotherapy: Recent advances and opportunities, Crit. Rev. Oncol. Hematol. 157 (2021) 103160. https://doi.org/10.1016/j.critrevonc.2020.103160.

[33] S.L. Topalian, F.S. Hodi, J.R. Brahmer, S.N. Gettinger, D.C. Smith, D.F. McDermott, J.D. Powderly, R.D. Carvajal, J.A. Sosman, M.B. Atkins, P.D. Leming, D.R. Spigel, S.J. Antonia, L. Horn, C.G. Drake, D.M. Pardoll, L. Chen,

W.H. Sharfman, R.A. Anders, J.M. Taube, T.L. McMiller, H. Xu, A.J. Korman, M. Jure-Kunkel, S. Agrawal, D. McDonald, G.D. Kollia, A. Gupta, J.M. Wigginton, M. Sznol, Safety, Activity, and Immune Correlates of Anti–PD-1 Antibody in Cancer, N. Engl. J. Med. 366 (2012) 2443–2454. https://doi.org/10.1056/nejmoa1200690.

[34] J.R. Brahmer, S.S. Tykodi, L.Q.M. Chow, W.-J. Hwu, S.L. Topalian, P. Hwu, C.G. Drake, L.H. Camacho, J. Kauh, K. Odunsi, H.C. Pitot, O. Hamid, S. Bhatia, R. Martins, K. Eaton, S. Chen, T.M. Salay, S. Alaparthy, J.F. Grosso, A.J. Korman, S.M. Parker, S. Agrawal, S.M. Goldberg, D.M. Pardoll, A. Gupta, J.M. Wigginton, Safety and Activity of Anti–PD-L1 Antibody in Patients with Advanced Cancer, N. Engl. J. Med. 366 (2012) 2455–2465. https://doi.org/10.1056/nejmoa1200694.

[35] T. Alissafi, A. Hatzioannou, A.I. Legaki, A. Varveri, P. Verginis, Balancing cancer immunotherapy and immune-related adverse events: The emerging role of regulatory T cells, J. Autoimmun. 104 (2019) 102310. https://doi.org/10.1016/j.jaut.2019.102310.

[36] G. Myers, Immune-related adverse events of immune checkpoint inhibitors: A brief review, Curr. Oncol. 25 (2018) 342–347. https://doi.org/10.3747/co.25.4235.

[37] H. Nishimura, M. Nose, H. Hiai, N. Minato, T. Honjo, Development of lupus-like autoimmune diseases by disruption of the PD-1 gene encoding an ITIM motif-carrying immunoreceptor, Immunity. 11 (1999) 141–151. https://doi.org/10.1016/S1074-7613(00)80089-8.

[38] J. Liu, S.J. Blake, M.J. Smyth, M.W.L. Teng, Improved mouse models to assess tumour immunity and irAEs after combination cancer immunotherapies, Clin. Transl. Immunol. 3 (2014) e22. https://doi.org/10.1038/cti.2014.18.

[39] D.M. Francis, M.P. Manspeaker, A. Schudel, L.F. Sestito, M.J. O'Melia, H.T. Kissick, B.P. Pollack, E.K. Waller, S.N. Thomas, Blockade of immune checkpoints in lymph nodes through locoregional delivery augments cancer immunotherapy, Sci. Transl. Med. 12 (2020) eaay3575. https://doi.org/10.1126/scitranslmed.aay3575.

[40] M.F. Fransen, M. Schoonderwoerd, P. Knopf, M.G. Camps, L.J. Hawinkels, M.

Kneilling, T. van Hall, F. Ossendorp, Tumor-draining lymph nodes are pivotal in PD-1/PD-L1 checkpoint therapy, JCI Insight. 3 (2018) e124507. https://doi.org/10.1172/jci.insight.124507.

[41] L. van Hooren, L.C. Sandin, I. Moskalev, P. Ellmark, A. Dimberg, P. Black, T.H. Tötterman, S.M. Mangsbo, Local checkpoint inhibition of CTLA-4 as a monotherapy or in combination with anti-PD1 prevents the growth of murine bladder cancer, Eur. J. Immunol. 47 (2017) 385–393. https://doi.org/10.1002/eji.201646583.

[42] M.F. Fransen, T.C. Van Der Sluis, F. Ossendorp, R. Arens, C.J.M. Melief, Controlled local delivery of CTLA-4 blocking antibody induces CD8 + T-cell-dependent tumor eradication and decreases risk of toxic side effects, Clin. Cancer Res. 19 (2013) 5381–5389. https://doi.org/10.1158/1078-0432.CCR-12-0781.

[43] A. Ray, M.A. Williams, S.M. Meek, R.C. Bowen, K.F. Grossmann, R.H.I. Andtbacka, T.L. Bowles, J.R. Hyngstrom, S.A. Leachman, D. Grossman, G.M. Bowen, S.L. Holmen, M.W. VanBrocklin, G. Suneja, H.T. Khong, A phase I study of intratumoral ipilimumab and interleukin-2 in patients with advanced melanoma, Oncotarget. 7 (2016) 64390. https://doi.org/10.18632/oncotarget.10453.

[44] S.M.M. Irenaeus, D. Nielsen, P. Ellmark, J. Yachnin, A. Deronic, A. Nilsson, P. Norlén, N. Veitonmäki, C.S. Wennersten, G.J. Ullenhag, First-in-human study with intratumoral administration of a CD40 agonistic antibody, ADC-1013, in advanced solid malignancies, Int. J. Cancer. 145 (2019) 1189–1199. https://doi.org/10.1002/ijc.32141.

[45] C.Y.X. Chua, J. Ho, A. Susnjar, G. Lolli, N. Di Trani, F. Pesaresi, M. Zhang, E. Nance, A. Grattoni, Intratumoral Nanofluidic System for Enhancing Tumor Biodistribution of Agonist CD40 Antibody, Adv. Ther. 3 (2020) 2000055. https://doi.org/10.1002/adtp.202000055.

[46] Q. Chen, G. Chen, J. Chen, J. Shen, X. Zhang, J. Wang, A. Chan, Z. Gu, Bioresponsive Protein Complex of aPD1 and aCD47 Antibodies for Enhanced Immunotherapy, Nano Lett. 19 (2019) 4879–4889. https://doi.org/10.1021/acs.nanolett.9b00584.

[47] Y. Zhang, N. Li, H. Suh, D.J. Irvine, Nanoparticle anchoring targets immune agonists to tumors enabling anti-cancer immunity without systemic toxicity, Nat. Commun. 9 (2018) 1–15. https://doi.org/10.1038/s41467-017-02251-3.

[48] Y. Mi, C.C. Smith, F. Yang, Y. Qi, K.C. Roche, J.S. Serody, B.G. Vincent, A.Z. Wang, A Dual Immunotherapy Nanoparticle Improves T-Cell Activation and Cancer Immunotherapy, Adv. Mater. 30 (2018) 1706098. https://doi.org/10.1002/adma.201706098.

[49] J. Bu, A. Nair, M. Iida, W.J. Jeong, M.J. Poellmann, K. Mudd, L.J. Kubiatowicz, E.W. Liu, D.L. Wheeler, S. Hong, An Avidity-Based PD-L1 Antagonist Using Nanoparticle-Antibody Conjugates for Enhanced Immunotherapy, Nano Lett. 20 (2020) 4901–4909. https://doi.org/10.1021/acs.nanolett.0c00953.

[50] L. Borkner, A. Kaiser, W. Van De Kasteele, R. Andreesen, A. MacKensen, J.B. Haanen, T.N. Schumacher, C. Blank, RNA interference targeting programmed death receptor-1 improves immune functions of tumor-specific T cells, Cancer Immunol. Immunother. 59 (2010) 1173–1183. https://doi.org/10.1007/s00262-010-0842-0.

[51] M.E. Prosser, C.E. Brown, A.F. Shami, S.J. Forman, M.C. Jensen, Tumor PD-L1 co-stimulates primary human CD8+ cytotoxic T cells modified to express a PD1: CD28 chimeric receptor, Mol. Immunol. 51 (2012) 263–272. https://doi.org/10.1016/j.molimm.2012.03.023.

[52] L. Shi, T. Meng, Z. Zhao, J. Han, W. Zhang, F. Gao, J. Cai, CRISPR knock out CTLA-4 enhances the anti-tumor activity of cytotoxic T lymphocytes, Gene. 636 (2017) 36–41. https://doi.org/10.1016/j.gene.2017.09.010.

[53] Y. Wu, W. Gu, L. Li, C. Chen, Z.P. Xu, Enhancing PD-1 gene silence in T lymphocytes by comparing the delivery performance of two inorganic nanoparticle platforms, Nanomaterials. 9 (2019) 159. https://doi.org/10.3390/nano9020159.

[54] Y. Wu, W. Gu, J. Li, C. Chen, Z.P. Xu, Silencing PD-1 and PD-L1 with nanoparticle-delivered small interfering RNA increases cytotoxicity of tumor-infiltrating lymphocytes, Nanomedicine. 14 (2019) 955–967. https://doi.org/10.2217/nnm-2018-0237.

[55] K. Li, H. Tian, Development of small-molecule immune checkpoint inhibitors of PD-1/PD-L1 as a new therapeutic strategy for tumour immunotherapy, J. Drug Target. 27 (2019) 244–256. https://doi.org/10.1080/1061186X.2018.1440400.

[56] L. Skalniak, K.M. Zak, K. Guzik, K. Magiera, B. Musielak, M. Pachota, B. Szelazek, J. Kocik, P. Grudnik, M. Tomala, S. Krzanik, K. Pyrc, A. Dömling, G. Dubin, T.A. Holak, Small-molecule inhibitors of PD-1/PD-L1 immune checkpoint alleviate the PD-L1-induced exhaustion of T-cells, Oncotarget. 8 (2017) 72167. https://doi.org/10.18632/oncotarget.20050.

[57] P. Sasikumar, R. Shrimali, S. Adurthi, R. Ramachandra, L. Satyam, A. Dhudashiya, D. Samiulla, K.B. Sunilkumar, M. Ramachandra, A novel peptide therapeutic targeting PD1 immune checkpoint with equipotent antagonism of both ligands and a potential for better management of immune-related adverse events, J. Immunother. Cancer. 1 (2013) O24. https://doi.org/10.1186/2051-1426-1-s1-o24.

[58] X. Lin, X. Lu, G. Luo, H. Xiang, Progress in PD-1/PD-L1 pathway inhibitors: From biomacromolecules to small molecules, Eur. J. Med. Chem. 186 (2020) 111876. https://doi.org/10.1016/j.ejmech.2019.111876.

[59] Q. Wu, L. Jiang, S. cheng Li, Q. jun He, B. Yang, J. Cao, Small molecule inhibitors targeting the PD-1/PD-L1 signaling pathway, Acta Pharmacol. Sin. 42 (2021) 1–9. https://doi.org/10.1038/s41401-020-0366-x.

[60] S. Lim, J. Park, M.K. Shim, W. Um, H.Y. Yoon, J.H. Ryu, D.K. Lim, K. Kim, Recent advances and challenges of repurposing nanoparticle-based drug delivery systems to enhance cancer immunotherapy, Theranostics. 9 (2019) 7906–7923. https://doi.org/10.7150/thno.38425.

[61] L. Luo, J. Yang, C. Zhu, M. Jiang, X. Guo, W. Li, X. Yin, H. Yin, B. Qin, X. Yuan, Q. Li, Y. Du, J. You, Sustained release of anti-PD-1 peptide for perdurable immunotherapy together with photothermal ablation against primary and distant tumors, J. Control. Release. 278 (2018) 87–99. https://doi.org/10.1016/j.jconrel.2018.04.002.

[62] J.L. Adams, J. Smothers, R. Srinivasan, A. Hoos, Big opportunities for small

molecules in immuno-oncology, Nat. Rev. Drug Discov. 14 (2015) 603–622. https://doi.org/10.1038/nrd4596.

[63] G.C. Prendergast, W.P. Malachowski, J.B. DuHadaway, A.J. Muller, Discovery of IDO1 Inhibitors: From bench to bedside, Cancer Res. 77 (2017) 6795–6811. https://doi.org/10.1158/0008-5472.CAN-17-2285.

[64] X. Wang, F. Wang, M. Zhong, Y. Yarden, L. Fu, The biomarkers of hyperprogressive disease in PD-1/PD-L1 blockage therapy, Mol. Cancer. 19 (2020) 1–15. https://doi.org/10.1186/s12943-020-01200-x.

[65] X. Meng, G. Du, L. Ye, S. Sun, Q. Liu, H. Wang, W. Wang, Z. Wu, J. Tian, Combinatorial antitumor effects of indoleamine 2,3-dioxygenase inhibitor NLG919 and paclitaxel in a murine B16-F10 melanoma model, Int. J. Immunopathol. Pharmacol. 30 (2017) 215–226. https://doi.org/10.1177/0394632017714696.

[66] T. Komiya, C.H. Huang, Updates in the clinical development of Epacadostat and other indoleamine 2,3-dioxygenase 1 inhibitors (IDO1) for human cancers, Front. Oncol. 8 (2018) 423. https://doi.org/10.3389/fonc.2018.00423.

[67] Z.J. Brown, S.J. Yu, B. Heinrich, C. Ma, Q. Fu, M. Sandhu, D. Agdashian, Q. Zhang, F. Korangy, T.F. Greten, Indoleamine 2,3-dioxygenase provides adaptive resistance to immune checkpoint inhibitors in hepatocellular carcinoma, Cancer Immunol. Immunother. 67 (2018) 1305–1315. https://doi.org/10.1007/s00262-018-2190-4.

[68] E. Ladomersky, L. Zhai, A. Lenzen, K.L. Lauing, J. Qian, D.M. Scholtens, G. Gritsina, X. Sun, Y. Liu, F. Yu, W. Gong, Y. Liu, B. Jiang, T. Tang, R. Patel, L.C. Platanias, C. David James, R. Stupp, R. V. Lukas, D.C. Binder, D.A. Wainwright, IDO1 inhibition synergizes with radiation and PD-1 blockade to durably increase survival against advanced glioblastoma, Clin. Cancer Res. 24 (2018) 2559–2573. https://doi.org/10.1158/1078-0432.CCR-17-3573.

[69] J. Spahn, J. Peng, E. Lorenzana, D. Kan, T. Hunsaker, E. Segal, M. Mautino, E. Brincks, A. Pirzkall, S. Kelley, S. Mahrus, L. Liu, S. Dale, C. Quiason, E. Jones, Y. Liu, S. Latham, L. Salphati, K. DeMent, M. Merchant, G. Hatzivassiliou,

Improved anti-tumor immunity and efficacy upon combination of the IDO1 inhibitor GDC-0919 with anti-PD-l1 blockade versus anti-PD-l1 alone in preclinical tumor models, J. Immunother. Cancer. 3 (2015) 303. https://doi.org/10.1186/2051-1426-3-s2-p303.

[70] K. Cheng, Y. Ding, Y. Zhao, S. Ye, X. Zhao, Y. Zhang, T. Ji, H. Wu, B. Wang, G.J. Anderson, L. Ren, G. Nie, Sequentially Responsive Therapeutic Peptide Assembling Nanoparticles for Dual-Targeted Cancer Immunotherapy, Nano Lett. 18 (2018) 3250–3258. https://doi.org/10.1021/acs.nanolett.8b01071.

[71] A. Nayak-Kapoor, Z. Hao, R. Sadek, R. Dobbins, L. Marshall, N.N. Vahanian, W. Jay Ramsey, E. Kennedy, M.R. Mautino, C.J. Link, R.S. Lin, S. Royer-Joo, X. Liang, L. Salphati, K.M. Morrissey, S. Mahrus, B. McCall, A. Pirzkall, D.H. Munn, J.E. Janik, S.N. Khleif, Phase Ia study of the indoleamine 2,3-dioxygenase 1 (IDO1) inhibitor navoximod (GDC-0919) in patients with recurrent advanced solid tumors, J. Immunother. Cancer. 6 (2018) 1–12. https://doi.org/10.1186/s40425-018-0351-9.

[72] K.H. Jung, P. LoRusso, H. Burris, M. Gordon, Y.J. Bang, M.D. Hellmann, A. Cervantes, M. Ochoa de Olza, A. Marabelle, F. Stephen Hodi, M.J. Ahn, L.A. Emens, F. Barlesi, O. Hamid, E. Calvo, D. McDermott, H. Soliman, I. Rhee, R. Lin, T. Pourmohamad, J. Suchomel, A. Tsuhako, K. Morrissey, S. Mahrus, R. Morley, A. Pirzkall, S. Lindsey Davis, Phase I study of the indoleamine 2,3-dioxygenase 1 (IDO1) inhibitor navoximod (GDC-0919) administered with PD-L1 inhibitor (atezolizumab) in advanced solid tumors, Clin. Cancer Res. 25 (2019) 3220–3228. https://doi.org/10.1158/1078-0432.CCR-18-2740.

[73] T. Ebata, T. Shimizu, Y. Fujiwara, K. Tamura, S. Kondo, S. Iwasa, K. Yonemori, A. Shimomura, S. Kitano, T. Koyama, N. Sato, K. Nakai, M. Inatani, N. Yamamoto, Phase I study of the indoleamine 2,3-dioxygenase 1 inhibitor navoximod (GDC-0919) as monotherapy and in combination with the PD-L1 inhibitor atezolizumab in Japanese patients with advanced solid tumours, Invest. New Drugs. 38 (2020) 468–477. https://doi.org/10.1007/s10637-019-00787-3.

[74] G. Li, Y. Gao, C. Gong, Z. Han, L. Qiang, Z. Tai, J. Tian, S. Gao, Dual-Blockade Immune Checkpoint for Breast Cancer Treatment Based on a Tumor-Penetrating

Peptide Assembling Nanoparticle, ACS Appl. Mater. Interfaces. 11 (2019) 39513–39524. https://doi.org/10.1021/acsami.9b13354.

[75] Y. Chen, R. Xia, Y. Huang, W. Zhao, J. Li, X. Zhang, P. Wang, R. Venkataramanan, J. Fan, W. Xie, X. Ma, B. Lu, S. Li, An immunostimulatory dual-functional nanocarrier that improves cancer immunochemotherapy, Nat. Commun. 7 (2016) 1–12. https://doi.org/10.1038/ncomms13443.

[76] B. Feng, F. Zhou, B. Hou, D. Wang, T. Wang, Y. Fu, Y. Ma, H. Yu, Y. Li, Binary Cooperative Prodrug Nanoparticles Improve Immunotherapy by Synergistically Modulating Immune Tumor Microenvironment, Adv. Mater. 30 (2018) 1803001. https://doi.org/10.1002/adma.201803001.

[77] J. Lu, X. Liu, Y.P. Liao, X. Wang, A. Ahmed, W. Jiang, Y. Ji, H. Meng, A.E. Nel, Breast Cancer Chemo-immunotherapy through Liposomal Delivery of an Immunogenic Cell Death Stimulus Plus Interference in the IDO-1 Pathway, ACS Nano. 12 (2018) 11041–11061. https://doi.org/10.1021/acsnano.8b05189.

[78] A.E. Nel, H. Meng, K.C. Mei, Y.P. Liao, J. Jiang, M. Chiang, M. Khazaieli, X. Liu, X. Wang, Q. Liu, C. Hyun Chang, X. Zhang, J. Li, Y. Ji, B. Melano, D. Telesca, T. Xia, Liposomal delivery of mitoxantrone and a cholesteryl indoximod prodrug provides effective chemo-immunotherapy in multiple solid tumors, ACS Nano. 14 (2020) 13343–13366. https://doi.org/10.1021/acsnano.0c05194.

[79] J.J. Sun, Y.C. Chen, Y.X. Huang, W.C. Zhao, Y.H. Liu, R. Venkataramanan, B.F. Lu, S. Li, Programmable co-delivery of the immune checkpoint inhibitor NLG919 and chemotherapeutic doxorubicin via a redox-responsive immunostimulatory polymeric prodrug carrier, Acta Pharmacol. Sin. 38 (2017) 823–834. https://doi.org/10.1038/aps.2017.44.

[80] X. Han, K. Cheng, Y. Xu, Y. Wang, H. Min, Y. Zhang, X. Zhao, R. Zhao, G.J. Anderson, L. Ren, G. Nie, Y. Li, Modularly Designed Peptide Nanoprodrug Augments Antitumor Immunity of PD-L1 Checkpoint Blockade by Targeting Indoleamine 2,3-Dioxygenase, J. Am. Chem. Soc. 142 (2020) 2490–2496. https://doi.org/10.1021/jacs.9b12232.

[81] J. Xu, X. Ren, T. Guo, X. Sun, X. Chen, L.H. Patterson, H. Li, J. Zhang,

NLG919/cyclodextrin complexation and anti-cancer therapeutic benefit as a potential immunotherapy in combination with paclitaxel, Eur. J. Pharm. Sci. 138 (2019) 105034. https://doi.org/10.1016/j.ejps.2019.105034.

[82] Q. Li, J. Liu, H. Fan, L. Shi, Y. Deng, L. Zhao, M. Xiang, Y. Xu, X. Jiang, G. Wang, L. Wang, Z. Wang, IDO-inhibitor potentiated immunogenic chemotherapy abolishes primary tumor growth and eradicates metastatic lesions by targeting distinct compartments within tumor microenvironment, Biomaterials. 269 (2020) 120388. https://doi.org/10.1016/j.biomaterials.2020.120388.

[83] J.G. Pizarro, J. Folch, J.L. Esparza, J. Jordan, M. Pallàs, A. Camins, A molecular study of pathways involved in the inhibition of cell proliferation in neuroblastoma B65 cells by the GSK-3 inhibitors lithium and SB-415286, J. Cell. Mol. Med. 13 (2009) 3906–3917. https://doi.org/10.1111/j.1582-4934.2008.00389.x.

[84] A. Taylor, J.A. Harker, K. Chanthong, P.G. Stevenson, E.I. Zuniga, C.E. Rudd, Glycogen Synthase Kinase 3 Inactivation Drives T-bet-Mediated Downregulation of Co-receptor PD-to Enhance CD8+ Cytolytic T Cell Responses, Immunity. 44 (2016) 274–286. https://doi.org/10.1016/j.immuni.2016.01.018.

[85] A. Taylor, C. Rudd, Commentary: Small Molecule Inhibition of PD-1 Transcription is an Effective Alternative to Antibody Blockade in Cancer Therapy, J. Immunol. Sci. 3 (2019) 9. https://doi.org/10.29245/2578-3009/2019/1.1167.

[86] A. Taylor, D. Rothstein, C.E. Rudd, Small-molecule inhibition of pd-1 transcription is an effective alternative to antibody blockade in cancer therapy, Cancer Res. 78 (2018) 706–717. https://doi.org/10.1158/0008-5472.CAN-17-0491.

[87] C.E. Rudd, K. Chanthong, A. Taylor, Small Molecule Inhibition of GSK-3 Specifically Inhibits the Transcription of Inhibitory Co-receptor LAG-3 for Enhanced Anti-tumor Immunity, Cell Rep. 30 (2020) 2075–2082. https://doi.org/10.1016/j.celrep.2020.01.076.

[88] A. Taylor, C.E. Rudd, Glycogen synthase kinase 3 inactivation compensates for the lack of CD28 in the priming of CD8+ cytotoxic T-cells: Implications for anti-PD-1 immunotherapy, Front. Immunol. 8 (2017) 1653.

https://doi.org/10.3389/fimmu.2017.01653.

[89] S. Sengupta, S.C. Katz, S. Sengupta, P. Sampath, Glycogen synthase kinase 3 inhibition lowers PD-1 expression, promotes long-term survival and memory generation in antigen-specific CAR-T cells, Cancer Lett. 433 (2018) 131–139. https://doi.org/10.1016/j.canlet.2018.06.035.

[90] S.D. Allen, X. Liu, J. Jiang, Y.-P. Liao, C.H. Chang, A.E. Nel, H. Meng, Immune Checkpoint Inhibition in Syngeneic Mouse Cancer Models by a Silicasome Nanocarrier Delivering a GSK3 Inhibitor, Biomaterials. 269 (2021) 120635. https://doi.org/10.1016/j.biomaterials.2020.120635.

[91] F. Danhier, E. Ansorena, J.M. Silva, R. Coco, A. Le Breton, V. Préat, PLGA-based nanoparticles: An overview of biomedical applications, J. Control. Release. 161 (2012) 505–522. https://doi.org/10.1016/j.jconrel.2012.01.043.

[92] S. Rezvantalab, N.I. Drude, M.K. Moraveji, N. Güvener, E.K. Koons, Y. Shi, T. Lammers, F. Kiessling, PLGA-based nanoparticles in cancer treatment, Front. Pharmacol. 9 (2018) 1260. https://doi.org/10.3389/fphar.2018.01260.

[93] H. Zhong, G. Chan, Y. Hu, H. Hu, D. Ouyang, A comprehensive map of FDA-approved pharmaceutical products, Pharmaceutics. 10 (2018) 263. https://doi.org/10.3390/pharmaceutics10040263.

[94] Y. Wang, W. Qu, S.H. Choi, FDA's regulatory science program for generic PLA/PLGA-based drug products, Am. Pharm. Rev. 19 (2017) 5–9.

[95] I. Banerjee, R.C. Pangule, R.S. Kane, Antifouling coatings: Recent developments in the design of surfaces that prevent fouling by proteins, bacteria, and marine organisms, Adv. Mater. 23 (2011) 690–718. https://doi.org/10.1002/adma.201001215.

[96] B. Yu, Y. Pu, J. Liu, J. Liao, K. Chen, J. Zhang, W. Zhong, Y. Hu, X.Q. Wang, B. Liu, H. Liu, W. Tan, Targeted delivery of emodin to adipocytes by aptamer-functionalized PEG-PLGA nanoparticles in vitro, J. Drug Deliv. Sci. Technol. 57 (2020) 101739. https://doi.org/10.1016/j.jddst.2020.101739.

[97] X. Nie, Y. Liu, M. Li, X. Yu, W. Yuan, S. Huang, D. Ren, Y. Wang, Y. Wang,

SP94 Peptide-Functionalized PEG-PLGA Nanoparticle Loading with Cryptotanshinone for Targeting Therapy of Hepatocellular Carcinoma, AAPS PharmSciTech. 21 (2020) 1–11. https://doi.org/10.1208/s12249-020-01655-7.

[98] W.J. McDaid, M.K. Greene, M.C. Johnston, E. Pollheimer, P. Smyth, K. McLaughlin, S. Van Schaeybroeck, R.M. Straubinger, D.B. Longley, C.J. Scott, Repurposing of Cetuximab in antibody-directed chemotherapy-loaded nanoparticles in EGFR therapy-resistant pancreatic tumours, Nanoscale. 11 (2019) 20261–20273. https://doi.org/10.1039/c9nr07257h.

[99] F.S.T. Mirakabad, K. Nejati-Koshki, A. Akbarzadeh, M.R. Yamchi, M. Milani, N. Zarghami, V. Zeighamian, A. Rahimzadeh, S. Alimohammadi, Y. Hanifehpour, S.W. Joo, PLGA-based nanoparticles as cancer drug delivery systems, Asian Pacific J. Cancer Prev. 15 (2014) 517–535. https://doi.org/10.7314/APJCP.2014.15.2.517.

[100] C.E. Astete, C.M. Sabliov, Synthesis and characterization of PLGA nanoparticles, J. Biomater. Sci. Polym. Ed. 17 (2006) 247–289. https://doi.org/10.1163/156856206775997322.

[101] X. Li, X. Jiang, Microfluidics for producing poly (lactic-co-glycolic acid)-based pharmaceutical nanoparticles, Adv. Drug Deliv. Rev. 128 (2018) 101–114. https://doi.org/10.1016/j.addr.2017.12.015.

[102] R. Karnik, F. Gu, P. Basto, C. Cannizzaro, L. Dean, W. Kyei-Manu, R. Langer, O.C. Farokhzad, Microfluidic platform for controlled synthesis of polymeric nanoparticles, Nano Lett. 8 (2008) 2906–2912. https://doi.org/10.1021/nl801736q.

[103] B. Amoyav, O. Benny, Controlled and tunable polymer particles' production using a single microfluidic device, Appl. Nanosci. 8 (2018) 905–914. https://doi.org/10.1007/s13204-018-0790-0.

[104] M.H.M. Leung, A.Q. Shen, Microfluidic Assisted Nanoprecipitation of PLGA Nanoparticles for Curcumin Delivery to Leukemia Jurkat Cells, Langmuir. 34 (2018) 3961–3970. https://doi.org/10.1021/acs.langmuir.7b04335.

[105] J. Sun, Y. Xianyu, M. Li, W. Liu, L. Zhang, D. Liu, C. Liu, G. Hu, X. Jiang, A microfluidic origami chip for synthesis of functionalized polymeric nanoparticles,

Nanoscale. 5 (2013) 5262–5265. https://doi.org/10.1039/c3nr01289a.

[106] Y. Kim, B. Lee Chung, M. Ma, W.J.M. Mulder, Z.A. Fayad, O.C. Farokhzad, R. Langer, Mass production and size control of lipid-polymer hybrid nanoparticles through controlled microvortices, Nano Lett. 12 (2012) 3587–3591. https://doi.org/10.1021/nl301253v.

[107] B.L. Sanchez-Gaytan, F. Fay, M.E. Lobatto, J. Tang, M. Ouimet, Y. Kim, S.E.M. Van Der Staay, S.M. Van Rijs, B. Priem, L. Zhang, E.A. Fisher, K.J. Moore, R. Langer, Z.A. Fayad, W.J.M. Mulder, HDL-Mimetic PLGA Nanoparticle To Target Atherosclerosis Plaque Macrophages, Bioconjug. Chem. 26 (2015) 443–451. https://doi.org/10.1021/bc500517k.

[108] M. Rhee, P.M. Valencia, M.I. Rodriguez, R. Langer, O.C. Farokhzad, R. Karnik, Synthesis of size-tunable polymeric nanoparticles enabled by 3D hydrodynamic flow focusing in single-layer microchannels, Adv. Mater. 23 (2011) H79–H83. https://doi.org/10.1002/adma.201004333.

[109] N. Hoshyar, S. Gray, H. Han, G. Bao, The effect of nanoparticle size on in vivo pharmacokinetics and cellular interaction, Nanomedicine. 11 (2016) 673–692. https://doi.org/10.2217/nnm.16.5.

[110] A. Tchoryk, V. Taresco, R.H. Argent, M. Ashford, P.R. Gellert, S. Stolnik, A. Grabowska, M.C. Garnett, Penetration and uptake of nanoparticles in 3D tumor spheroids, Bioconjug. Chem. 30 (2019) 1371–1384. https://doi.org/10.1021/acs.bioconjchem.9b00136.

[111] C. He, Y. Hu, L. Yin, C. Tang, C. Yin, Effects of particle size and surface charge on cellular uptake and biodistribution of polymeric nanoparticles, Biomaterials. 31 (2010) 3657–3666. https://doi.org/10.1016/j.biomaterials.2010.01.065.

[112] F. Lu, S.H. Wu, Y. Hung, C.Y. Mou, Size effect on cell uptake in well-suspended, uniform mesoporous silica nanoparticles, Small. 5 (2009) 1408–1413. https://doi.org/10.1002/smll.200900005.

[113] E.A. Sykes, J. Chen, G. Zheng, W.C.W. Chan, Investigating the impact of nanoparticle size on active and passive tumor targeting efficiency, ACS Nano. 8 (2014) 5696–5706. https://doi.org/10.1021/nn500299p.

[114] J. Huang, L. Bu, J. Xie, K. Chen, Z. Cheng, X. Li, X. Chen, Effects of nanoparticle size on cellular uptake and liver MRI with polyvinylpyrrolidone-coated iron oxide nanoparticles, ACS Nano. 4 (2010) 7151–7160. https://doi.org/10.1021/nn101643u.

[115] Y. Da Dong, E. Tchung, C. Nowell, S. Kaga, N. Leong, D. Mehta, L.M. Kaminskas, B.J. Boyd, Microfluidic preparation of drug-loaded PEGylated liposomes, and the impact of liposome size on tumour retention and penetration, J. Liposome Res. 29 (2019) 1–9. https://doi.org/10.1080/08982104.2017.1391285.

[116] A. Nguyen, R. Böttger, S.-D. Li, Recent trends in bioresponsive linker technologies of Prodrug-Based Self-Assembling nanomaterials, Biomaterials. 275 (2021) 120955. https://doi.org/10.1016/j.biomaterials.2021.120955.

[117] K.-J. Chen, A.J. Plaunt, F.G. Leifer, J.Y. Kang, D. Cipolla, Recent advances in prodrug-based nanoparticle therapeutics, Eur. J. Pharm. Biopharm. 165 (2021) 219–243. https://doi.org/10.1016/j.ejpb.2021.04.025.

[118] S. Ashton, Y.H. Song, J. Nolan, E. Cadogan, J. Murray, R. Odedra, J. Foster, P.A. Hall, S. Low, P. Taylor, R. Ellston, U.M. Polanska, J. Wilson, C. Howes, A. Smith, R.J.A. Goodwin, J.G. Swales, N. Strittmatter, Z. Takáts, A. Nilsson, P. Andren, D. Trueman, M. Walker, C.L. Reimer, G. Troiano, D. Parsons, D. De Witt, M. Ashford, J. Hrkach, S. Zale, P.J. Jewsbury, S.T. Barry, Aurora kinase inhibitor nanoparticles target tumors with favorable therapeutic index in vivo, Sci. Transl. Med. 8 (2016) 325ra17. https://doi.org/10.1126/scitranslmed.aad2355.

[119] K.D. Ristroph, R.K. Prud'homme, Hydrophobic ion pairing: Encapsulating small molecules, peptides, and proteins into nanocarriers, Nanoscale Adv. 1 (2019) 4207–4237. https://doi.org/10.1039/c9na00308h.

Chapter 3

Intratumoural Delivery of Anti-PD-1 Conjugated PEG-PLGA Nanoparticles Improves the Biodistribution of PD-1 Immune Checkpoint Inhibitor towards Safer Immunotherapy

3 Intratumoural delivery of anti-PD-1 conjugated PEG-PLGA nanoparticles improves the biodistribution of PD-1 immune checkpoint inhibitor towards safer immunotherapy

3.1 Introduction

Immune checkpoint inhibition has emerged as a frontline cancer immunotherapy, and several antibodies have already been approved by regulatory bodies for several cancers [1,2]. Programmed cell death-1 (PD-1) targeting antibodies (aPD-1) are one of these approved immune checkpoint inhibitors. PD-1 is an immune-inhibitory receptor overexpressed on immune cells, predominantly T-cells, upon activation and exhaustion [3,4]. PD-1 blockade by aPD-1s restores T-cell cytotoxicity against cancer cells [3–5]. Nevertheless, aPD-1 immunotherapy is hampered by both limited patient response rates and high rates of immune related adverse effects that can lead to the discontinuation of therapy [6–9]. The mechanisms underlying the adverse effects and low response rates have not been fully elucidated. However, studies suggest that aPD-1 accumulation in tumour tissues is suboptimal and that conversely, aPD-1 is also distributed to off-target organs, which not only reduces the available therapeutic dose in tumours, but also blocks PD-1 receptors of non-targeted cells and consequently interferes with patients' immune system's self-tolerance [10–13].

Local administration of anti-cancer drugs aimed at direct delivery of the therapeutics to the tumour is being actively investigated as an alternative to conventional parental administration towards reducing off-target drug concentration and therefore toxicity, increasing tumour bioavailability and potentially reducing administered doses and/or frequency of injection. Although logistically more complex than systemic administration in the case of deep-seated organs, intratumoural administration is feasible in most cases under contemporary image guidance [14,15]. Local administration of immunomodulatory agents, including immune checkpoint inhibitors is especially promising and has been investigated in preclinical and even clinical trials, driven by the importance of the tumour microenvironment and tumour draining lymph nodes for priming the immune cells and inducing tumour specific immune responses [16–20]. Francis *et al.* compared loco-regional administration of aPD-1 vs systemic (intraperitoneal) injection in a melanoma mouse model, and observed higher accumulation of antibodies in tumour and tumour draining lymph nodes (TDLNs) following intratumoural administration, which also led

to improved anti-tumour efficacy [19]. However, no significant difference in antibodies biodistribution in off-target organs was observed between systemic and intratumoural injections. Local injection of immune checkpoint CTLA-4 antibodies resulted in lower serum level of antibodies and liver enzymes in a mouse model [21]. Moreover, intratumoural injection of CTLA-4 antibodies alone or in combination with aPD-1 resulted in lower systemic concentration of antibodies; while providing efficient responses in a mouse model of bladder cancer [22]. However, these promising preclinical results have not translated clinically. Intratumoural injection of IL-2 and ipilimumab, a CTLA-4 immune checkpoint inhibitor, did not significantly diminish off-target toxicity compared to systemic administration as grade III adverse effects were observed in a phase 1 clinical trial [23]. Similarly, intratumoural administration of CD40 agonistic antibodies was also associated with high rate of side effects in a phase 1 clinical trial [18].

Conversely, the conjugation of antibodies to nanoparticles (NPs) substantially modifies their biodistribution and bioavailability upon systemic administration and several NPs have been investigated as delivery systems for immunotherapy antibodies, including dendrimers, liposomes and polymeric NPs [10,24–26]. Among these, poly(ethylene glycol)-b-poly(lactide-co-glycolide) (PEG-PLGA) nanoparticles present notable advantages. First, PEG-PLGA is a biodegradable polymer with a well-established safety profile. Second, the preparation of PEG-PLGA NPs is simple, scalable, and their physicochemical properties can be easily adjusted [27,28]. PEG-PLGA NPs conjugated with aPD-1 and aOX-40 yielded enhanced anti-tumour efficacies after systemic administration in mice models [29,30]. A general limitation of this approach is that NPs typically display limited tumour uptake following systemic administration. On the other hand, NPs are efficiently retained within tumour tissues and transported to draining lymph nodes upon local administration, two highly desirable features for immunotherapeutic agent [31].

However, to the best of our knowledge, the impact of aPD-1 nanoformulation on their loco-regional and systemic biodistribution following intratumoural administration has not been comprehensively studied. More surprisingly, only limited insight about the impact of intratumoural vs systemic administration of free aPD-1 on their biodistribution is available [19]. To address this knowledge gap, we designed and comprehensively characterized aPD-1 conjugated PEG-PLGA NPs (aPD-1 NPs) and investigated their biodistribution upon intratumoural administration. Our overarching goal was to

determine whether nanoformulation could improve aPD-1 tumour bioavailability and/or reduce off-target systemic distribution following intratumoural administration compared to free aPD-1 administered either intratumorally or systemically.

The PEG-PLGA NPs were prepared using microfluidics based nanoprecipitation, which is a simple, highly reproducible and easy to scale-up method of preparation of monodispersed NPs [27,32]. The benefits of microfluidic-based NP preparation have recently come to the fore in the preparation of mRNA vaccine. We used an orthotopic mouse model of head and neck squamous cell carcinoma (HNSCC) to investigate the biodistribution of aPD-1 after intratumoural administration of aPD-1 NP or free aPD-1, and compared it with systemic aPD-1, the gold standard of anti-PD-1 therapy. Finally, based on the promising *in vivo* data and towards fully validating the potential of this novel approach, we used a comprehensive set of *in vitro* analyses to confirm the functionality and efficacy of the aPD-1 NPs to inhibit T-cells PD-1 receptors and induce the cytotoxicity of T-cells against head and neck cancer cells.

3.2 Materials and methods

3.2.1 Materials

PLGA (25 KDa), PLGA-PEG-COOH (17-3.4 KDa) and methoxy-PEG-PLGA (mPEG-PLGA) (2-15 KDa) were purchased from PoliSciTech (USA). Acetonitrile, N-(3-Dimethylaminopropyl)-N′-ethylcarbodiimide hydrochloride (EDC) and N-hydroxysuccinimide (NHS) were supplied from Sigma Aldrich (USA). GoInVivo™ Purified anti-human PD-1 antibody (clone EH12.2H7) and Ultra-LEAF™ Purified anti-mouse PD-1 antibody (clone 29F.1A12) were obtained from Biolegend (USA). Anti-human CD28 antibody (clone CD28.2) and anti-human CD3 (clone OK3) were supplied from ThermoFisher scientific (USA). Recombinant human interleukin-2 (IL-2) was purchased from Peprotech (USA).

3.2.2 Cell culture

The squamous cell carcinoma cell lines UM-SCC1 and UM-SCC47 (EMD Millipore, USA) were used as the *in vitro* HNSCC model and co-cultured with T-cells for cytotoxicity assays. UM-SCC1 and UM-SCC47 cells stably expressing red fluorescent protein (RFP) (RFP-SCC1, RFP-SCC47, respectively) were generated as previously described [33] and used for the apoptosis assay. UM-SCC1 and UM-SCC47 cells stably

expressing the fluorescent ubiquitination-based cell cycle indicator (fucci) system (Fucci-SCC1 or Fucci-SCC47), were generated as previously described [34] and used for cell cycle analysis. Fucci cells express red fluorescence in G1 and green fluorescence in S-G2 phases [34]. The fucci and the RFP constructs were obtained from RIKEN BRC through the National Bio-Resources Project of the MEXT/AMED, Japan [33,34]. The cells were cultured in complete RPMI media, (Gibco, UK) supplemented with 10% fetal bovine serum (FBS) (Gibco, UK), 1% streptomycin/penicillin (Gibco, UK) and 1% L-glutamine (Gibco, UK).

The mouse oral carcinoma (MOC)-1 cell line used to establish an orthotopic mouse model of HNSCC was obtained from Kerafast cell bank repository (USA). These cells were cultured in 2:1 IMDM to Ham's F12 nutrient mixture (ThermoFisher scientific, USA), supplemented with 5% FBS (GE healthcare, USA), 1% streptomycin/penicillin, 5 mg/L insulin (Sigma Aldrich, USA), 40 µg/L hydrocortisone (Sigma Aldrich, USA), and 5 µg/L epidermal growth factor (EMD Millipore, USA). All cells were maintained in humidifying incubator (90% humidity and 5% CO_2) at 37˚C. Cells were subcultured by 0.25% trypsin-EDTA at 80% confleuncy.

3.2.3 Preparation of PEG-PLGA NPs

PEG-PLGA NPs were prepared by nanoprecipitation in a custom made 3D printed microfluidic chip (Figure 3-1-A). The microfluidic chip was fabricated by a MiiCraft 3D printer with channel dimensions of 0.6 mm in width and 1.1 mm in height. It has two inlets, which mix two streams of liquid in a herringbone structured mixing channel. The herringbone pattern is depicted in Figure 3-1-A. For NP preparation, a polymer mixture composed of 50% PLGA, 25% mPEG-PLGA and 25% PLGA-PEG-COOH at a concentration of 5 mg/mL in acetonitrile was introduced into one of the inlet and Milli-Q® water was introduced into the other inlet. The flow rates of aqueous and organic phases were 3 and 1 mL/min, respectively, which was controlled by syringe pumps (Chemyx fusion 200). The prepared PEG-PLGA NPs were collected from the outlet and washed by centrifugation at 24000 g for 10 min at 4 °C and redispersed in Milli-Q® water for further characterization/use.

3.2.4 Physico-chemical characterization of PEG-PLGA NPs

The hydrodynamic size of PEG-PLGA NPs dispersed in Milli-Q® water was measured by dynamic light scattering (DLS) using a Zetasizer 3000 HS (Malvern Instruments Ltd).

Nanoparticle Tracking Analysis was also used to confirm the size and distribution of the NPs using a Nanosight NS300 (Malvern Instruments Ltd). The zeta potentials of the NPs were measured via the Zetasizer. The morphology of the NPs was determined using a JEOL JEM-2100F-HR transmission electron microscope (TEM) (Jeol, Japan) after negative staining with 2% phosphotungstic acid. The stability of the NPs in terms of size, size polydispersity index (PDI) and zeta potential was determined over one month by storing the NPs at room temperature in 1x Phosphate-Buffered Saline (PBS) or Milli-Q® water.

3.2.5 Conjugation of aPD-1 to PEG-PLGA NPs

To conjugate aPD-1 to PEG-PLGA NPs, the blank NPs were resuspended in Milli-Q® water and EDC (10 Mm) and NHS (25 mM) were added to the NPs, to activate the carboxylate groups in the PLGA-PEG-COOH polymers. After 10 min, the NPs were washed twice with 1x Dulbecco's PBS (DPBS) (ThermoFisher Scientific, USA) and aPD-1 was added to the NPs at the concentration of 0.6 mg/mL. The conjugation mixture was shaken for 2 h and then incubated at room temperature overnight. Unconjugated antibodies were separated from conjugated NPs by centrifugation and the supernatant was collected to measure the concentration of unbound antibodies by NanoDrop™ 2000/2000c Spectrophotometers (Thermo Fisher scientific Inc.). The conjugation efficiency (CE) was determined by the following equation:

$$\text{CE}\ (\%) = \frac{\text{Initial mass of antibodies} - \text{ mass of unbound antibodies}}{\text{Initial mass of antibodies}} \times 100$$

The conjugation of aPD-1 to NPs was also confirmed by x-ray photoelectron spectroscopy and the size of aPD-1 NPs was measured by zetasizer.

3.2.6 Orthotopic HNSCC preclinical model

Six-week old C57BL/6J mice of either sex were used. The animal work was conducted following approval and monitoring of University of South Australia (UniSA) animal ethics committee (ethics number U10-21). The animals were kept under the guideline of UniSA and their weight and clinical signs were monitored regularly. The data were analysed by one-way ANOVA and P value of < 0.05 considered significant. To establish the orthotopic mouse HNSCC model, the MOC-1 cell line was used. The MOC-1 line is

originally derived from a primary tumour of the oral cavity in wild type C57BL/6 mice [35]. 300,000 MOC-1 cells were resuspended in 1X DPBS and mixed with matrigel® basement membrane matrix (Corning, USA), 50 % (V/V). The cells were injected into the floor of mouth of C57BL/6 mice by using an insulin syringe (BD, USA). Tumour growth was monitored by measuring their volume using digital callipers to measure two perpendicular diameters. The volume was calculated as volume = 0.5 x length x width^2.

3.2.7 Biodistribution of aPD-1 NPs in orthotopic HNSCC model

To conduct the biodistribution study, mouse specific aPD-1 were labelled with NHS tagged IRDye® 800 CW fluorescent dye (Li-COR, USA). This dye has near IR excitation and emission and therefore provides suitable imaging depth and low background noise. The labelling was optimised to yield approximately 3-5 dyes per antibody. Fluorescent aPD-1 were then used to prepare the aPD-1 NPs. One week before imaging, the animals' standard diet was changed to a non-autofluorescence special diet (cat no: SF19-107, SpecialtyFeeds, Australia) to minimise the background auto-fluorescence. When the tumour reached about 50 mm^3, the animals' fur was removed by depilatory cream to prevent light scattering for imaging. Animals were randomly divided in four groups, namely aPD-1 NPs (local injection), aPD-1 (local injection), aPD-1 (systemic injection) and saline control group (N=4/group). For local injections, a dose of 0.625 mg/Kg of aPD-1 for either the free aPD-1 or aPD-1 NPs was dispersed in saline and injected into the tumour tissue in three divided injections. For systemic injections, 2.5 mg/Kg of aPD-1 was injected into the animals' lateral tail veins. Equal volume of saline was injected to the fourth group of animals to control for background fluorescence in data analysis. At 6 h, 24 h and 48 h after injection, blood was collected from tail vein (0.05 % body weight) into a Microvette® 100 K3 EDTA capillary blood collection tube and whole-body images were taken using an IVIS Lumina S5 (Perkinelmer, USA) at excitation of 700 nm and emission of 790 nm. At 48 h, the animals were euthanized and the tumours, tumour draining lymph nodes (TDLNs), livers, spleens, hearts, lungs and kidneys were dissected, weighed and imaged *ex vivo*. The images were analysed with the Living image software 4.7.2. To quantify the fluorescence in the *ex vivo* images, the region of interest was selected for each organ and the total radiant efficiency was calculated by the software. After subtracting the mean of background signals of the control cohort, the data was normalized to tissue's weight. For the detection of antibodies in the blood circulation, the collected blood was diluted by 1X DPBS and centrifuged at 500 G for 5 min. The

separated serum was collected to measure the fluorescence intensity using a Cary Eclipse Fluorescence Spectrophotometer (Agilent, US) using a 785 nm excitation filter and a 790-850 nm emission.

3.2.8 T-cell isolation and activation

Primary T-cells were isolated from peripheral blood collected from healthy volunteers in accordance with the UniSA Human Research Ethics Committee (approval number 201726) using RosetterSep™ human T-cell enrichment kit (Stemcell), according to the manufacturer's protocol. The isolated T-cells (10^6 cells/mL) were activated for 2 days using an anti-CD3 (5 µg/mL) coated well-plate in presence of 4 µg/mL anti-CD28 and 500 U/mL IL-2. After two days, the activation of T-cells was assessed by monitoring of the cells' microscopic morphological changes and expression of the CD69 activation marker and PD-1 receptors which were quantified by flow cytometry. For flow cytometric analyses, cells were harvested and washed with 1X DPBS. Cells (10^5) were washed twice with DPBS after a 30 min staining antibodies incubation in 0.5% BSA/DPBS. The following immune-staining antibody panel from Biolegend (USA) were used: BV421-CD3, PE-PD-1, FITC-CD4, PerCP Cy5.5-CD8, PE-CD69. Data was collected using an imaging flow cytometer Image Stream X (AMNIS, USA). The IDEAS® 6.2 (EMD Millipore, USA) and FlowJo V10 (FlowJo, USA) software were used for data analysis.

3.2.9 PD-1 inhibition by aPD-1 NPs

To investigate the efficiency of the aPD-1 NPs to inhibit PD-1 receptors, activated T-cells were seeded in a 96-well plate at a density of 10^5 cells/well in complete RPMI supplemented with 10 U/mL IL-2. T-cells were treated for two hours with different concentrations of free aPD-1 (ranging from 0.166 µg/mL to 10 µg/mL) or equivalent doses of aPD-1 NPs or nonspecific IgG conjugated NPs (IgG NPs) or unconjugated NPs. Untreated cells were used as negative control. After treatment, the cells were harvested and washed to remove unbound aPD-1 or aPD-1 NPs and immune-staining was performed to quantify the PD-1 receptors' fluorescence signal by imaging flow cytometry.

3.2.10 Effects of aPD-1 NPs on T-cells proliferation and viability

To determine the effect of PEG-PLGA NPs on the viability of T-cells, T-cells were labelled by CellTrace™ CFSE Cell Proliferation Kit (Thermo Fisher Scientific, USA). CFSE dilution by cell proliferation is a robust method to study T-cells proliferation [36].

In this assay, reduction in CFSE fluorescence intensity defines as CFSE dilution that occurs by the division of cells. After two days activation, T-cells were treated with 5 µg/mL aPD-1, aPD-1 NPs or equal amounts of unconjugated NPs. T-cells were harvested after three days and stained with the BV421-CD3 antibody and T-cell proliferation was determined from CFSE intensities by imaging flow cytometry. To determine the effect of NPs on T-cell metabolism, the RealTime-Glo™ MT cell viability assay (Promega, US) was used, according to the manufacturers' protocol. The cells were treated as described above and the luminescence of metabolically active T-cells was quantified after two days using a FLUOstar OPTIMA plate reader (BMG Labtech, USA) equipped with a 590 nm emission filter.

3.2.11 Effect of aPD-1 NPs on *in vitro* cytotoxicity of T-cells against head and neck cancer cells

Prior to the cytotoxic assays, PD-L1 expressions in UM-SCC1 and UM-SCC47 cells were determined. For PD-L1 expression, cells were trypsinized, washed with PBS and stained with human PE-PD-L1 antibodies (Biolegend, USA) and analysed by imaging flow cytometry. To investigate the effect of aPD-1 NPs on the cytotoxicity of T-cells against HNSCC cells, UM-SCC1 and UM-SCC47 cells and T-cells were co-cultured *in vitro*. HNSCC cells were seeded at densities of 10^4 cells/well with complete RPMI media and incubated overnight. The next day, the media was changed and activated T-cells (10^5 cells/well) in complete RPMI supplemented with 10 U/mL IL-2 were added and the cytotoxicity were determined using the following assays.

3.2.12 Apoptosis

Activated T-cells were co-cultured with RFP-SCC1 or RFP-SCC47 in a 48-well plate. The cells were treated with 5 ug/mL of free aPD-1 or aPD-1 NPs or unconjugated NPs or left without treatment as a control. Unstimulated T-cells were co-cultured with cancer cells and treated by aPD-1 NPs to serve as a control due to the basal expression of PD-1 in unstimulated T-cells. Apoptosis was measured 3 h, 18 h and 24 h after treatment, using the CellEvent™ Caspase-3/7 Green Detection Reagent (ThermoFisher scientific, USA) as per the manufacturer's protocol. The reagent is a nucleic acid binding dye conjugated to DEVD peptide. In apoptotic cells, caspase 3/7 becomes active and cleaves the DEVD-dye conjugate and the dye binds the DNA to become fluorescent. Cells were imaged by a Nikon TiE fluorescence microscope (Nikon, Japan), using 10x objective in FITC and Texas Red channels. The caspase 3/7 activated cells were quantified by NIS-Elements

software (Nikon, Japan). Apoptosis was also evaluated following the co-culture of the parental UM-SCC1 with T-cells and the same treatment as mentioned above, using CellEvent™ Caspase-3/7 Green Detection Reagent. After 24h, the cells were harvested by Accutase® (Biolegend, US) and stained by human AF660-EpCAM antibodies to label the cancer cells and apoptotic cancer cells were quantified by imaging flow cytometry.

3.2.13 Proliferation and cell cycle analysis

Fucci-SCC1 and Fucci-SCC47 cells were seeded 1 X 10^4 cells per well in ibiTreat µ-Slide 8 Well (Ibidi GmbH, Germany) and co-cultured with activated T-cells and treated as described above. 24 h and 48 h after treatment, the samples were imaged by Confocal Laser Scanning Microscopy (710, Carl Zeiss, Germany), using objective 10x and FITC and Texas red channels. The numbers of red and green cells were counted by NIS-Elements software (Nikon, Japan).

Additionally, Ki67 positive cells, a marker of cell proliferation, were determined using immuno-staining. UM-SCC1 cells were co-cultured with activated T-cells in ibiTreat µ-Slide 8 well and treated as described in the above section. After 24h, cells were washed twice by DPBS and fixed by 4% formalin for 30 min and washed again by DPBS. The cells were then permeabilized by 0.1% triton X-100 for 5 min and washed by DPBS. The samples were incubated with 1/250 diluted human specific anti-Ki67 rabbit antibodies (Abcam, USA) for 2 h. After washing with DPBS, the samples were stained by 2 ug/mL Alexa Fluor® 647 (AF-647) goat anti-rabbit secondary antibodies for 1 h and the nucleus was stained by 100 ng/mL DAPI for 5 min. The samples were washed twice by DPBS and imaged by Confocal Laser Scanning Microscope 710 (Zeiss, Germany), by objective 10x using DAPI and AF-647 channels. The $Ki67^+$ cells were quantified by NIS-Elements software (Nikon, Japan).

3.2.14 Cytotoxic cytokine analysis

ELISAs were used to determine the effect of aPD-1 NPs treatment on T-cells' cytotoxic cytokine secretion. The cell culture media of co-cultured UM-SCC1 and T-cells was collected 24 h and 48 h after treatment by 5 ug/mL of free aPD-1 or aPD-1 NPs or unconjugated NPs or no treatment control. The samples were centrifuged for 5 min at 500 G and the supernatant was collected and stored at -80°C. Levels of TNF-α and INF-γ cytokines in the samples were determined by using human IFN-γ and TNF-α Standard TMB ELISA Development Kit (Peprotech, USA) according to the manufacturer's

protocol. Optical densities were measured using a FLUOstar OPTIMA plate reader (BMG Labtech, USA) at 450 nm.

3.2.15 Statistics

All *in vitro* experiments were repeated at least twice. Data was analysed by one-way ANOVA and Tukey post hoc test using GraphPad Prism 7 (GraphPad Software, Inc., USA). Statistical significance is indicated as *P<0.05, **P < 0.01, ***P ≤ 0.001 and ****P ≤ 0.0001. Ns indicates no significant differences. The data is represented as average ± standard error of mean.

3.3 Results and discussion

3.3.1 Physicochemical characterisation of aPD-1 NPs

Monodispersed spherical PEG-PLGA NPs were reproducibly prepared using nanoprecipitation induced by chaotic mixing within a microfluidic device. In a typical preparation, NPs with an optimized hydrodynamic size of approx. 91.3 ± 2 nm were generated as measured by DLS (Figure 3-1-B) with very monodispersed size distribution and average zeta potential of -27.6 ± 0.35 mV (Figure 3-1-C). Nanoparticle tracking analysis also indicated a mean size of 86.2 ± 0.4 nm (supplementary Figure 3-9-A). TEM confirmed the spherical morphology of the NPs and were in agreement with DLS size measurement (Figure 3-1-D). NPs were stable in terms of zeta potential, size and size polydispersity index in both water and PBS over at least one month (supplementary figure 3-9-B, C, D). Microfluidic preparation of nanoparticles present several advantages over conventional bulk methods, including excellent flexibility to adjust the size of the NPs and minimize the variation between different batches [37]. The 3D printed microfluidic micromixer device enabled us to consistently generate highly monodisperse PEG-PLGA NPs with hydrodynamic diameters in the range of ~90 nm, which has been commonly used for targeted drug delivery in the literature [29,38]. The features and dimensions of the 3D printed microfluidic device also allowed the use of relatively high flow rates and therefore the efficient preparation of large amounts of PEG-PLGA NPs. This is an important consideration that facilitates scale-up and translation of NPs for preclinical and clinical investigations [32,39].

aPD-1 were conjugated using carbodiimide chemistry to the terminal carboxylate groups of the PEG-PLGA polymers. The conjugation efficiency was determined to be 30.3 ± 3.7

%, which is consistent with reported efficiency in literature [40]. There was a slight increase (about 23.9 nm) in the hydrodynamic size of NPs after conjugation as measured by DLS but the absence of broadening confirmed that no NP aggregation occurred (Figure 3-1-E). Based on the size of the NPs and amounts of conjugated antibodies, we estimated that an average of 10 aPD-1 are attached to each NP.

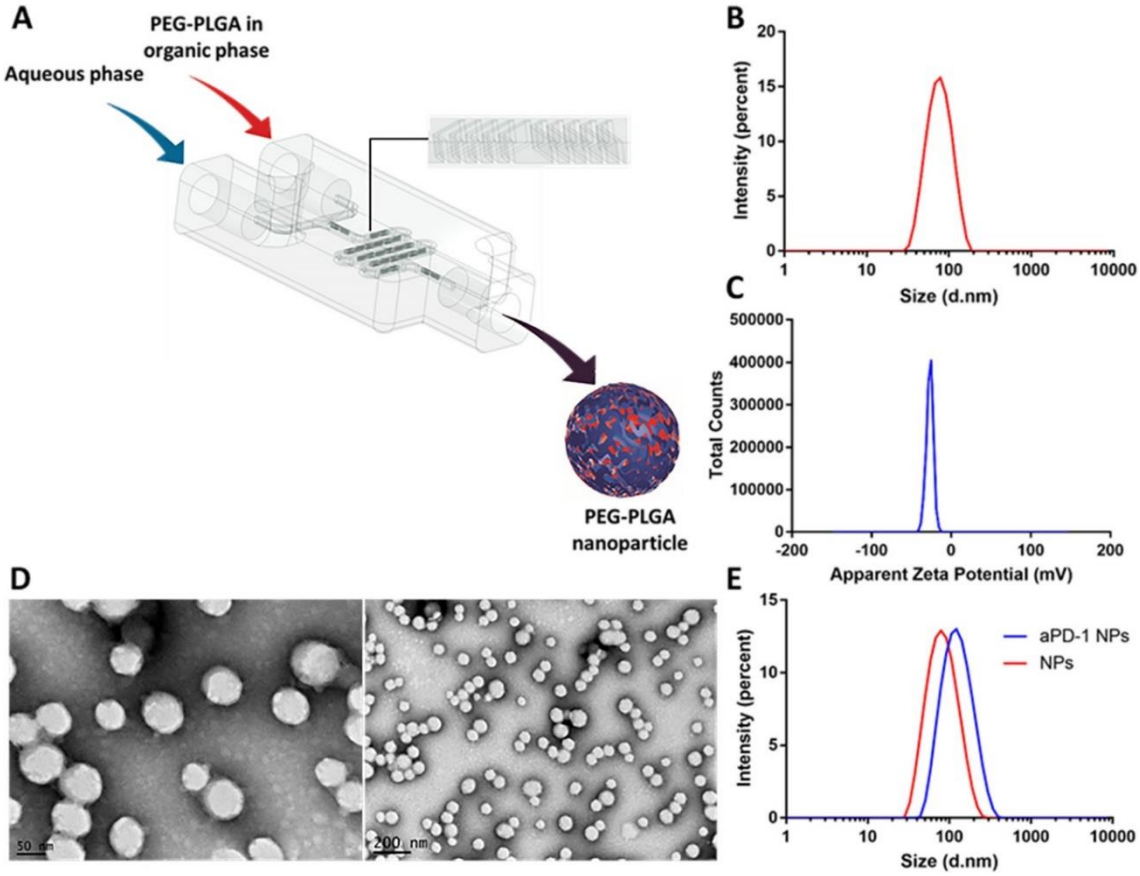

Figure 3-1 Physicochemical characterization of PEG-PLGA aPD-1 NPs.
A) Schematic illustration of NP preparation using a 3D printed microfluidic nanoprecipitation device. PEG-PLGA in organic phase and MQ water are introduced in the two inlets of the device and the two phases are mixed in a herringbone structured mixing channel where nanoprecipitation of the NP occurs. B) NP hydrodynamic diameter distribution and C) zeta potential as measured by dynamic light scattering. D) NP images by transmission electron microscopy; scale bar 50 nm (left), 200 nm (right). E) NP hydrodynamic diameters before and after aPD-1 conjugation (aPD-1 NP).

3.3.2 Enhanced tumour retention and decreased off-target distribution of intratumoural administered aPD-1 NP

The location of tumours is important in biodistribution studies, especially in the case of local administration. Therefore, to improve the physiological relevance of the data, we first developed an orthotopic C57BL/6 mouse model of HNSCC. Head and neck mouse cancer MOC1 cells were injected into the floor of mouth, and the formation of a palpable tumours was monitored from 10 days after injection. Tumours typically established within four weeks after injection and were characterised by steady growth rates. Animals

were otherwise healthy and gained weight during tumour establishment (supplementary Figure 3-10-A, B, C).

To investigate the impact of aPD-1 nanoformulation on the biodistribution of aPD-1 antibodies after local (intratumoural) administration, we compared locally administered aPD-1 NPs to free aPD-1 as well as intravenously injected (systemic) free aPD-1 used as the "gold-standard" reference. Tumour bearing mice were injected with fluorescent IRDye CW800 tagged aPD-1 / aPD-1 NPs and the respective biodistribution were determined by *in vivo* whole-body fluorescence imaging over 48 h (Figure 3-2-A). 6 h after injection, both locally administered aPD-1 NPs and aPD-1 groups showed strong fluorescent signals in the area surrounding the tumour, which persisted over 48 h, indicating tumour accumulation. However, the fluorescent signal in the abdominal area was significantly lower for the aPD-1 NPs (local) group than for the free aPD-1 group (local). Fluorescence in the abdomen was undetectable after 24 h in the case of aPD-1 NPs whereas aPD-1 showed persistent fluorescence in the abdomen until 48 h after intratumoural administration. Conversely the systemic administration aPD-1 group showed very high fluorescence in abdominal areas while tumour areas only displayed minor fluorescence. While the total fluorescence decreased over 48 h in all 3 treatment groups, the systemic aPD-1 group showed substantially higher fluorescence in the abdomen and lower fluorescence in the floor of mouth tumours than that observed for both aPD-1 NPs and aPD-1 locally injected groups at all time-points.

To gain more quantitative insights on the systemic distribution of the aPD-1, the serum fluorescence was measured and used to assess the amounts of aPD-1 (Figure 3-2-B). After 6 h, no fluorescent signal was detectable in the serum of aPD-1 NPs group. However, a strong fluorescent signal was detected in the systemic aPD-1 group and, to a much lower extent, in the local aPD-1 group, representing 2.4 % of the fluorescence intensity measured in the systemic aPD-1 group. The fluorescent signal was undetectable in the serum of all groups after 24 h confirming the clearance of the aPD-1 antibodies.

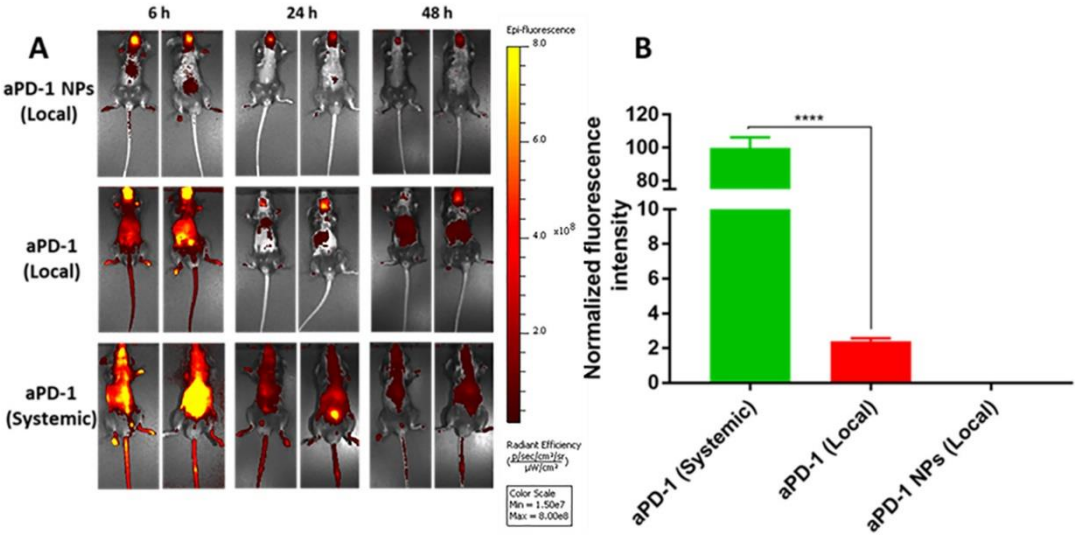

Figure 3-2 *In vivo* biodistribution of aPD-1 NPs and aPD-1 in an orthotopic mouse model of head and neck cancer.

In vivo biodistribution of aPD-1 NPs and aPD-1 in an orthotopic mouse model of head and neck cancer. A) Representative whole-body fluorescence images of tumour bearing mice over 48 h for the 3 tested groups. Mice were injected intratumorally with equal doses (0.625 mg/kg) of IRDye CW800 tagged aPD-1 either as free antibody (aPD-1) or nanoformulation (aPD-1 NPs). 2.5 mg/Kg aPD-1 was injected by IV route and used as a benchmark for standard administration. (N=4/group). B) Normalized fluorescence intensity of IRDye CW800 in the serum of mice collected 6 h after injection as described in (A). **** indicates $P \leq 0.0001$ by one-way ANOVA and Tukey post-hoc test.

Next, to more precisely quantify the biodistribution of aPD-1 antibodies in the tumours and off-target organs, tumours, TDLNs, livers, spleens, hearts, lungs and kidneys were resected 48 h after injection and imaged by IVIS (Figure 3-3-A). This *ex vivo* biodistribution analysis, using weight normalized radiant efficiency of the resected organs/tissues demonstrated that the amounts of antibodies in tumours were comparable for locally administered aPD-1 and aPD-1 NPs. However, the amounts of antibodies in the TDLNs for the free aPD-1 (local) group was higher (Figure 3-3-B) than in the case of aPD-1 NPs. In contrast, antibody accumulation was lower in all measured off-target organs for the aPD-1 NPs group compared to the aPD-1 (local) group, particularly in the kidneys and liver by 0.5 and 0.54 times, respectively (Figure 3-3-B). Amounts of aPD-1 in tumour and TDLNs were significantly higher (more than five times) after intratumoural injection vs systemic IV injection of the free aPD-1. This data is somewhat in agreement with a previous study by Francis *et al.*, which reported that intratumoural administration of aPD-1 antibodies yielded increased tumour and TDLN accumulation compared with intraperitoneal (systemic) injection. However, no significant difference was observed in this study in off-target organs [19]. Previous biodistribution investigation of free aPD-1 showed significant accumulation of the antibodies in liver, kidney, spleen and lung, which

is consistent with our data [13,41,42]. In our study, however, aPD-1 accumulation was significantly lower in the kidneys and liver following intratumoural injection. Remarkably, intratumorally administrated aPD-1 NPs yielded dramatically lower accumulation of aPD-1 in the lung, spleen, kidneys and liver compared to aPD-1 systemic administration (Figure 3-3-B) and the ratios of fluorescence at 48 h for aPD-1 NPs/ systemic aPD-1 in the lung, spleen, kidneys and liver were 0.14, 0.29, 0.21 and 0.09, respectively.

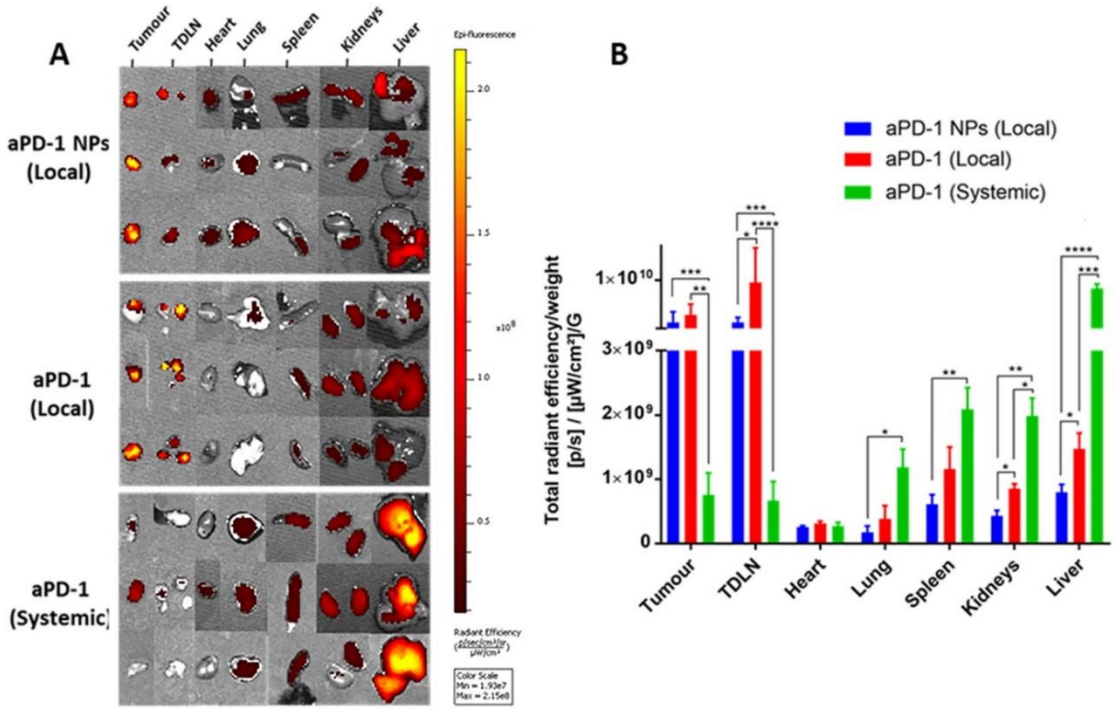

Figure 3-3 *Ex vivo* biodistribution of aPD-1 NPs and aPD-1 in an orthotopic mouse model of head and neck cancer.
A) Representative *ex vivo* fluorescence imaging of tumours and key organs at 48 h after injection. B) Quantification of *ex vivo* fluorescence images using total radiant efficiency normalized to the tissue weight after background subtraction. Asterisks indicate statistical significance by two-way ANOVA and Tukey post-hoc test *P<0.05, **P < 0.01, ***P ≤ 0.001 and ****P ≤ 0.0001.

The results from this biodistribution study demonstrate that intratumoural injection of aPD-1 NPs yielded better retention of the aPD-1 antibodies in tumour tissues and reduced the amounts of antibodies in the systemic circulation and in off-target organs compared to intratumoural administration of the free antibodies. The data also demonstrate that, in comparison with systemic administration of the aPD-1 antibodies which is the current clinical gold standard method of aPD-1 checkpoint inhibition, intratumoural administration significantly enhanced tumour bioavailability and decreased off-target systemic distribution. Our data supports the growing interest in local administration of

immunotherapeutic agents, as illustrated by several clinical studies investigating the safety and feasibility of intratumoural injection in a wide range of cancers [43]. Several preclinical studies also reported improved anti-tumour efficacy of aPD-1 administered locally. For example, both Fransen *et al*. [44] and Hooren *et al*. [45] observed tumour size reduction and increased survival rates upon local aPD-1 administration. The efficacy of intratumoural delivery of PD-1 antibodies was also shown preclinically using a microneedle patch that locally delivered dextran NPs loaded with aPD-1 in a melanoma mouse model, yielding better anti-tumour responses compared to free intratumoural or systemic administrated aPD-1 [46].

While intratumoural delivery of immune checkpoint inhibitors is therefore a promising approach towards harnessing the therapeutic benefits of immunotherapy while minimizing off-target toxicities, little attention has been paid to date to the biodistribution of locally administered antibodies. In addition, the biodistribution of immune checkpoint inhibitor nanoformulations has not been fully characterized despite the obvious opportunity to alter transport to tumour draining lymph nodes, systemic distribution and consequently toxicity profiles. The detailed biodistribution of systemically vs locally administered aPD-1 and nanoformulated aPD-1 reported in this study provides insight into the important parameters contributing to not only aPD-1 efficacy but also toxicity. Encouraged by these results, we next endeavoured to confirm the biological activity and efficacy of aPD-1 nanoformulation.

3.3.3 aPD-1 NPs are biocompatible with T-cells and effectively inhibit PD-1 expression *in vitro*

To confirm the biological functionality of aPD-1 NPs, we next carried out a comprehensive *in vitro* study of their biological activity. To determine the ability of aPD-1 NPs to inhibit PD-1 receptors in activated T-cells, human primary T-cells were isolated from peripheral blood and activated through CD3/CD28 signalling for two days. Upon activation, T-cells formed clusters while unstimulated T-cells did not (supplementary Figure 3-11-A), which confirmed effective activation of T-cells by T-cell receptors [47]. Staining for PD-1 and CD3 receptors at this time point revealed significant upregulation of PD-1 expression (56.3 ± 8.1 % vs 20.9 ± 2.9 %) (Figure 3-4-A, and supplementary Figure 3-11-B). Activation was further confirmed by overexpression of the activation marker CD69 (Figure 3-4-B) [48]. To determine the efficiency of aPD-1 NPs to inhibit PD-1 receptors, activated T-cells were treated with a range of doses (from 0.166 µg/mL

to 10 µg/mL aPD-1) of either aPD-1 NPs or free aPD-1 following a standard *in vitro* protocol [49] and then stained with PD-1 and CD3 antibodies. A dose-dependent reduction in PD-1 signal was observed up to 5 µg/mL for the aPD-1 NPs. No further inhibition was observed between 5 µg/mL to 10 µg/mL. Free aPD-1 were more efficient than aPD-1 NPs in the lower concentration range but inhibition rapidly plateaued from 0.833 µg/mL at ~57 % (vs ~42 % inhibition for PD-1 NPs at 5 µg/mL and above, Figure 3-4-C). Moreover, while a 5 µg/mL dose of aPD-1 NPs resulted in 42 % specific PD-1 inhibition, controls NPs conjugated with an irrelevant antibody or unconjugated yielded at the same equivalent NP concentrations, fluorescent signals similar to that of the untreated control group. This confirmed the specificity of aPD-1 NP inhibition (Figure 3-4-D).

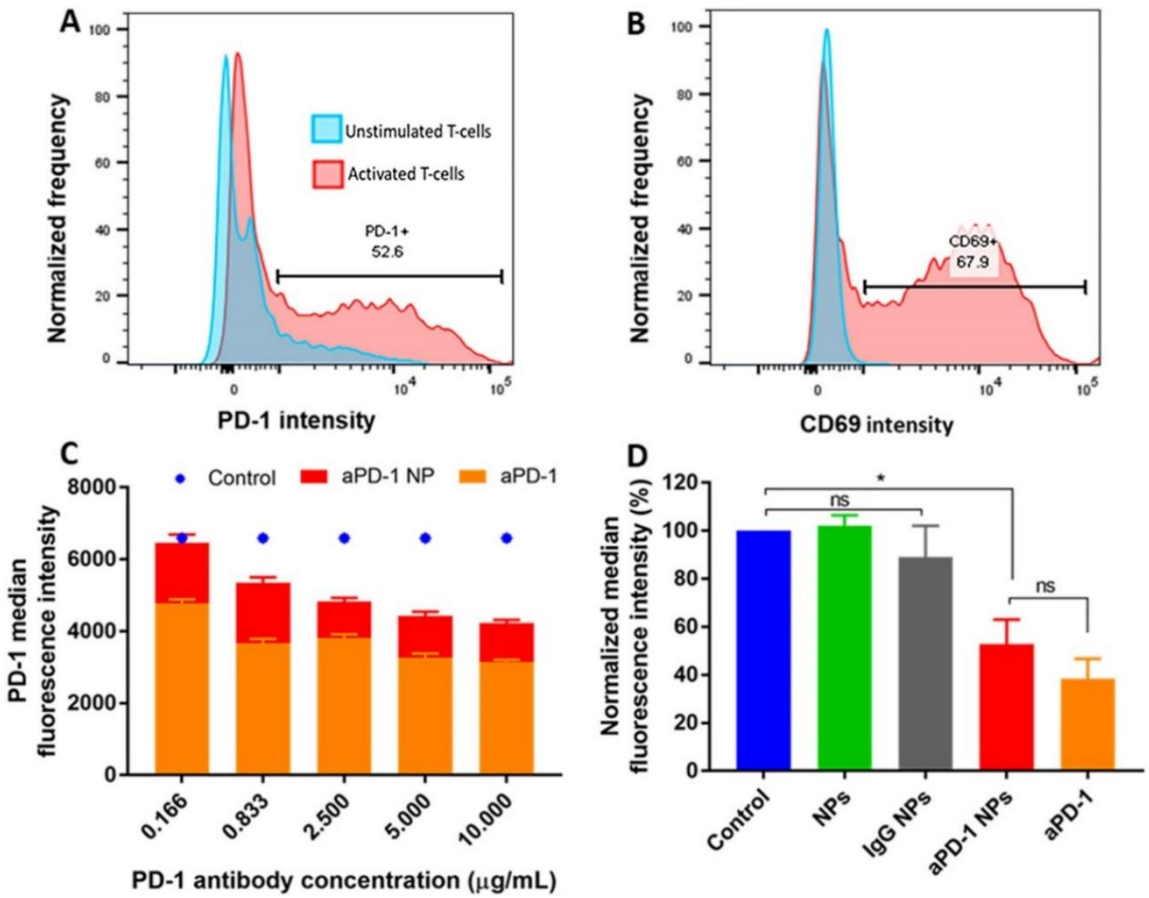

Figure 3-4 *In vitro* primary human T-cells PD-1 receptor inhibition by aPD-1 NPs vs free aPD-1.
A) PD-1 and B) CD69 expression two days after T-cells activation. C) Representative graph of PD-1 receptors inhibition in activated T-cells after 2 h incubation with 0.166, 0.833, 2.5, 5 and 10 µg/mL of aPD-1 or aPD-1 NPs. D) Specific PD-1 inhibition at 5 µg/mL for activated T cells treated for 2 h with aPD-1 NPs, aPD-1, IgG NPs, unconjugated PEG-PLGA NP vs untreated cells (N=3). Asterisks indicate statistical significance by one-way ANOVA and Tukey post-hoc test: *P<0.05.

The effect of the aPD-1 nanoformulation on T-cell proliferation was then investigated using CFSE dilution three days after treatment. aPD-1 NPs had no adverse effect on the proliferation of T-cells, as indicated by similar CFSE intensity for the aPD-1 NPs treated cells compared to the untreated control. Unconjugated PEG-PLGA NPs also had no effects on proliferation (Figure 3-5-A). The absence of toxicity was further confirmed in a cell viability assay using the Real Time-Glo™ MT cell viability assay. No changes in viability were measured two days after treatment by aPD-1 NPs or unconjugated NPs compared to the untreated control group (Figure 3-5-B).

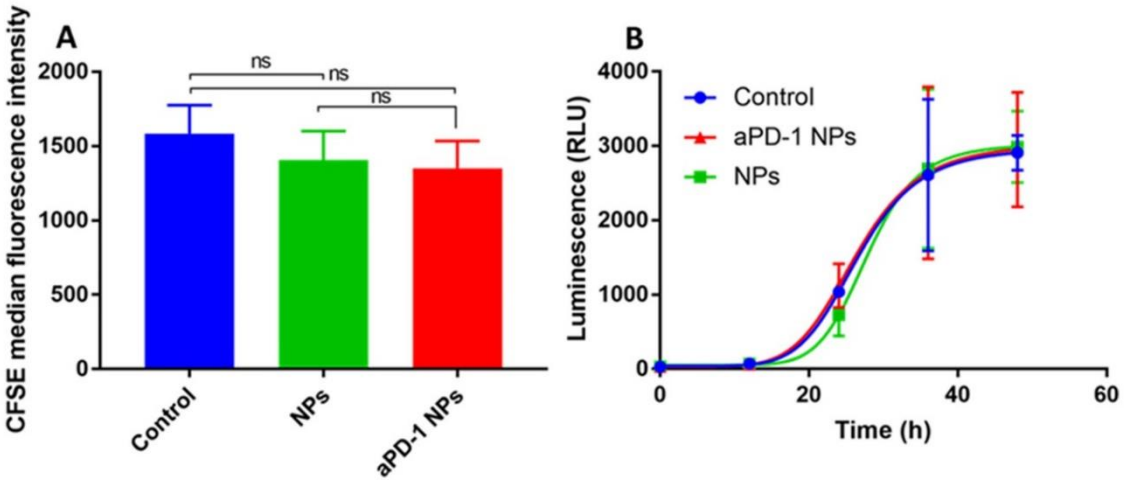

Figure 3-5 Effects of aPD-1 NPs on proliferation and viability of primary human T-cells.
A) Fluorescence intensity of CellTrace™ CFSE labelled T-cells three days after treatment with 5 µg/mL of aPD-1 NP or aPD-1, measured by imaging flow cytometry. B) Luminescence of metabolically active T-cells two days after treatment by 5 µg/mL of aPD-1 NP or aPD-1, using RealTime-Glo™ MT cell viability assay and measured at 490 nm by plate reader. Ns indicates not significant by one-way ANOVA and Tukey post-hoc test.

3.3.4 Inhibition of PD-1 by aPD-1 NPs enhances *in vitro* cytotoxicity of T-cells against head and neck cancer cells

We next investigated the cytotoxicity of aPD-1-NPs vs free aPD-1 treated T-cells against HNSCC cell lines using a standard T-cell/cancer cell co-culture protocol. The human papilloma virus (HPV) negative UM-SCC1 cells and the HPV positive UM-SCC47 cells were used as models of HNSCC. Imaging flow cytometry confirmed high expression of PD-L1 in both UM-SCC1 and UM-SCC47 (supplementary Figure 3-12-A), confirming their suitability for cytotoxicity studies targeting PD-1 inhibition. Next, we also confirmed the PD-1 inhibitory efficacy of aPD-1 NPs in the UM-SCC1/T-cells co-culture conditions. Consistent with the assay conducted with activated T cells mono-culture, aPD-1 NPs inhibited ~ 53 % of the PD-1 receptors in co-culture condition, which was comparable with the inhibition obtained with the free aPD-1 (50 %, supplementary Figure

3-12-B). T-cells treatment with the negative control (unconjugated NPs) had no effect on PD-1 fluorescent intensity. In addition, expression of PD-1 in unstimulated T-cells remained at basal levels upon aPD-1 NPs treatment, validating the accuracy of the assay.

We then investigated the efficacy of aPD-1 NPs to increase T-cell cytotoxicity against the two HNSCC cell lines by assessing apoptosis in the co-culture. Apoptosis is induced as part of T-cells' cytotoxic function [50] and was determined by measuring caspase 3/7. The number of green fluorescence caspase 3/7 activated cancer cells were quantified for the RFP expressing cancer cells 3 h, 18 h and 24 h after co-culture with treated or control T-cells by fluorescence microscopy (Figure 3-6-A, B and C). The longitudinal analysis demonstrated a significant increase in the percentage of apoptotic cancer cells. After 24 h of co-culture, PD-1-NPs increased caspase 3/7 activation in RFP-SCC1 cells three-fold (67.4 ± 10.2 %) as compared to control untreated cells (22.4 ± 3.2 %), yielding similar activity to the free aPD-1 (61.7 ± 4.8 %) (Figure 3-6-A, B and C). Apoptosis at 24 h was also assessed using imaging flow cytometry. A significantly increased percentage of UM-SCC1 cells were apoptotic following co-culture with T-cells treated with either aPD-1 NPs (85 ± 8 %) or free aPD-1 (75.8 ± 8 %) in comparison to co-culture with untreated T cells (40.5 ± 8.4 %) and T cells treated with unconjugated NPs (42.3 ± 10.2 %) (Figure 3-6-D). Similar biological activity was measured in RFP-SCC47 cells (supplementary Figure 3-13-A, B and C).

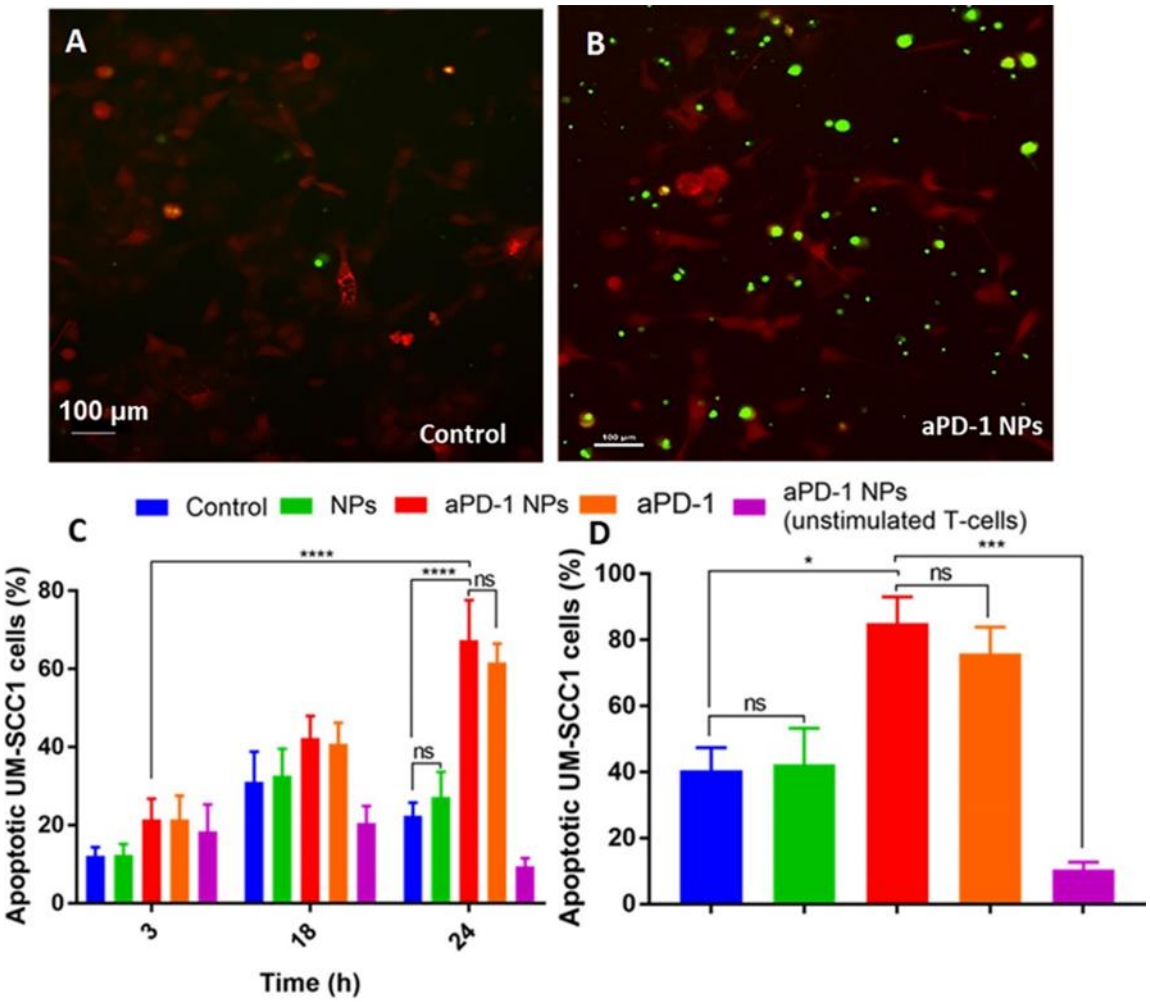

Figure 3-6 Effect of aPD-1 NPs on T-cells cytotoxicity in a co-culture model.
Representative fluorescence microscopy images of caspase 3/7 activated RFP-SCC1 cells 24 h after co-culture with activated T-cells (A) untreated and (B) treated with 5 µg/mL of aPD-1 NPs. Green: Caspase 3/7 activated cells; Red: RFP-SCC1 (scale bar 100 µm). C) Percentage of apoptotic UM-SCC1 cells by fluorescence microscopy after co-culture for 3 h, 18 h and 24 h with T-cells treated with 5 µg/mL of aPD-1 NPs, free aPD-1, unconjugated NPs, and untreated. (D) Percentage of apoptotic UM-SCC1 cells by imaging flow cytometry 24 h after co-culture (n=3). The statistical analysis was by two-way ANOVA (C) and one-way ANOVA (D) and Tukey post-hoc test. Statistical significance is indicated by asterisk as *P<0.05, **P < 0.01, ***P ≤ 0.001 and ****P ≤ 0.0001 and ns is not significant.

We further investigated the activity of the aPD-1 NPs compared to that of free aPD-1 on the cytotoxicity of T-cells on cancer by measuring effects on cell proliferation and cell cycle. Expression levels of the proliferative marker Ki-67 were determined in UM-SCC1 cells by Confocal Laser Scanning Microscopy 24 h after co-culture with T cells (Figure 3-7-A). aPD-1 NPs treated T cells significantly decreased the percentage of Ki-67^{+} cancer cells from 73.3 ± 5.6 % in the control group to 51.9 ± 2.7 % (Figure 3-7-C). Similar effect was measured for T cells treated by the free aPD-1 (50.1 ± 0.9 %). Cell cycle effects were investigated using HNSCC cells expressing the fluorescent based cell cycle indicator (fucci) system [33,34]. After 24 h of co-culture with T-cells, a significant decrease in the

S-G2 cells/G1 fucci-SCC1 cells ratio was measured from 1.2 ± 0.1 to 0.3 ± 0.05. T-cells treated with aPD-1 NPs and aPD-1 reduced the S-G2 cells/G1 fucci-SCC1 cells ratio even further to 0.09 ± 0.004 and 0.09 ± 0.008, respectively (Figure 3-7-B, D). After 48 h, aPD-1 NPs and aPD-1 treatment impaired the time dependent cell cycle progression back into the S-G2 phase, as indicated by the lower ratio of S-G2 cells/G1 cells for aPD-1 NPs treated T-cell group (0.85 ± 0.02 and 0.82 ± 0.06, respectively) compared to the control untreated T-cells and unconjugated NP treated T-cells groups (1.75 ± 0.030 and 1.6 ± 0.05, respectively) (Figure 3-7-E). No significant difference was measured between the aPD-1 nanoformulation and the free aPD-1 antibodies. Similar effects were measured for the fucci-SCC47 cells (supplementary Figure 3-14), where aPD-1 NPs treatment decreased S-G2 fucci-SCC1 cells/G1 cells ratio to 0.18 ± 0.012 from 0.29 ± 0.017 in the control group (supplementary Figure 3-14-A and B). However, T cell induction of G1 cell cycle arrest in the UM-SCC47 cells was less effective compared to the UM-SCC1 cells, possibly owing to the p53 inactivation in UM-SCC47 cells [51,52]. These results show that PD-1 inhibition by aPD-1 NP treatment of T cells induced cell cycle arrest in HNSCC cells over time.

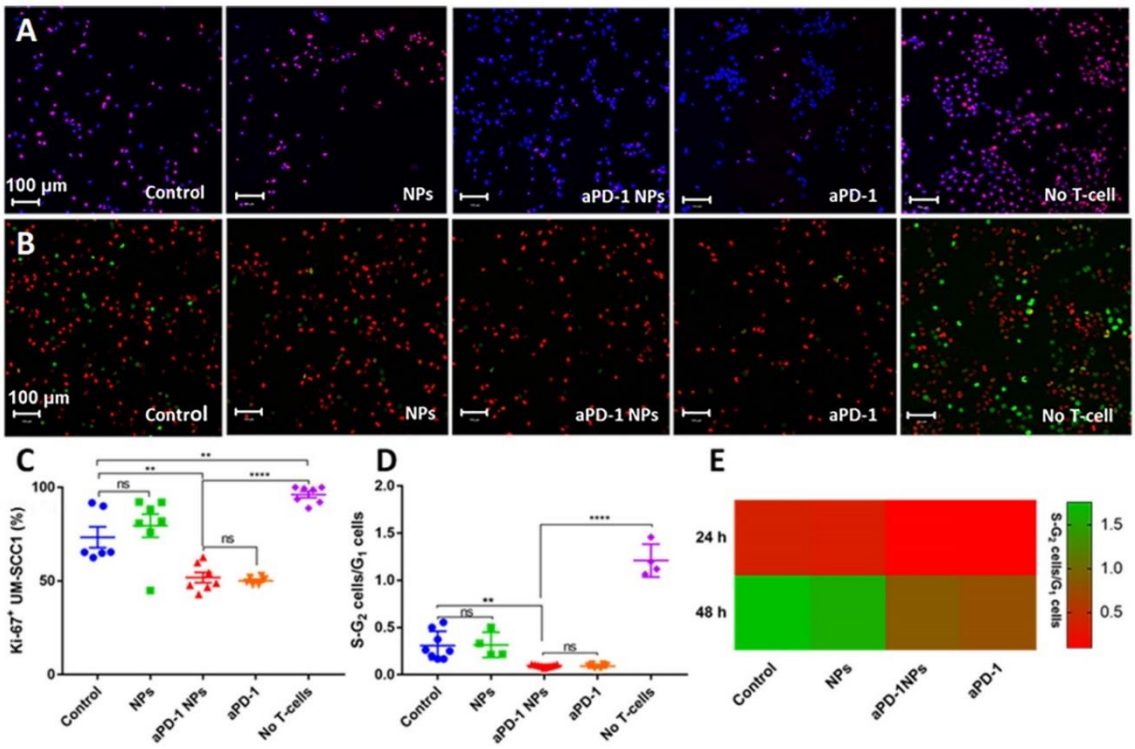

Figure 3-7 Effect of aPD-1 NP treated T-cells on UM-SCC1 cells proliferation and cell cycle.
A) Representative confocal microscopy images of Ki-67$^+$ UM-SCC1 cells and (B) fucci-SCC1 cells 24 h after treatment with T-cells treated with 5 µg/mL of aPD-1 NPs, aPD-1, and unconjugated NPs. UM-SCC1 cells exposed to untreated T-cells or no T cells were used as control. Blue: DAPI; magenta: Ki-67$^+$ cells. Green: cells in S-G2 phase; red: cells in G1 phase. C) Percentage of Ki-67$^+$ UM-SCC7 cells and (D) ratio of fucci-SCC1 cells in S-G2 vs cells in G1 phase 24 h after T-cell treatment, obtained by quantification of

images. E) Fucci-SCC1 cell cycle change 24 h and 48 h after T-cell treatment obtained by quantification of microscopy images. Statistical significance by one-way ANOVA and Tuckey post-hoc test is indicated by asterisk *P<0.05, **P < 0.01, ***P ≤ 0.001 and ****P ≤ 0.0001. Ns is not significant. Scale bar is 100 µm in all images.

Finally, we endeavour to confirm that aPD-1 NPs treatment supports the cytotoxic function of T-cells by measuring secretion of the inflammatory cytokines INFγ and TNFα. Both cytokines mediate the recruitment of more cytotoxic immune cells and consequently lead to increased T-cell anti-cancer cytotoxicity. To further confirm the enhanced T-cells cytotoxicity against HNSCC cells upon treatment with aPD-1 NPs and compared to free aPD-1 antibodies, levels of INFγ and TNFα cytokines were determined by ELISA following T-cell co-culture with UM-SCC1 cells. As shown in Figure 3-8-A and B, levels of these two cytokines dramatically increased at 24 h following aPD-1 NP and aPD-1 treatment of T cells and co-culture. This effect was also significant 48 h after treatment. The observed increase in INFγ and TNFα cytokines confirmed the enhanced anti-cancer cytotoxicity of T-cells following aPD-1 inhibition.

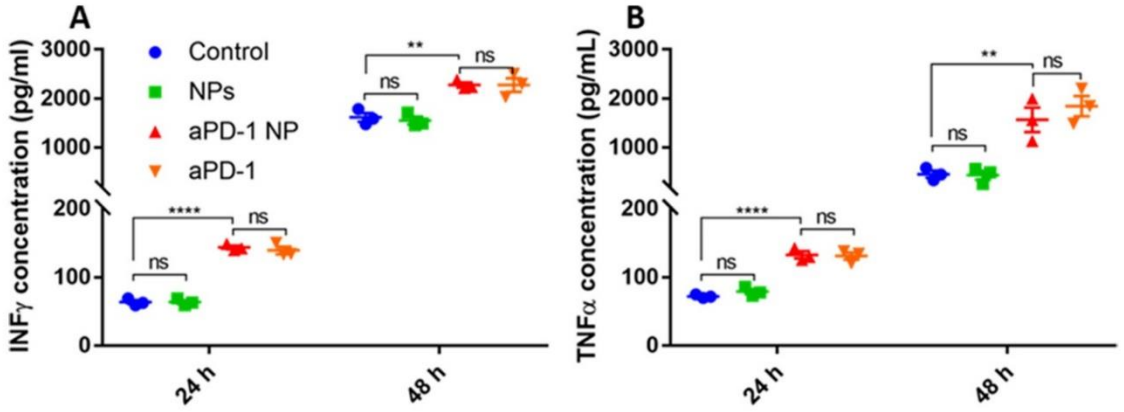

Figure 3-8 Effect of aPD-1 NP treatment on T-cells cytotoxic cytokine production in co-culture with UM-SCC1 cells.
Levels of INFγ (A) and TNFα (B) secreted in the media of T-cells and UM-SCC1 co-culture, 24 h and 48 h after treatment with 5 µg/mL aPD-1 NPs, aPD-1, and an equivalent amount of unconjugated NPs (n=3). Statistical significance by one-way ANOVA and Tuckey post-hoc test is indicated by asterisk as *P<0.05, **P < 0.01, ***P ≤ 0.001 and ****P ≤ 0.0001. Ns is not significant.

Taken together, the high level of these cytotoxic cytokines, and enhanced cytotoxicity effects of T-cells on the apoptosis, G1 cell cycle arrest and lower proliferation of UM-SCC1 and UM-SCC47 are consistent with the expected T-cells function upon immune checkpoint inhibition. These results validate that nanoformulation of aPD-1 by conjugation to PEG-PLGA NPs does not alter the biological efficacy of the aPD-1 antibodies. It should also be noted that the role of HPV status in HNSCC resistance to immune checkpoint inhibitors is not fully elucidated. While several studies reported

higher anti-tumour response rate in HPV^+ cancer cells vs HPV^-, other studies have observed higher resistance to immune checkpoint inhibitors such as aPD-L1 in HPV^+ cells [53–55]. In this study, we therefore included both the HPV^- UM-SCC1 and HPV^+ UMSCC-47 cell lines to shed additional light on this question. No significant differences between the two cell lines were observed in their response to T cells, suggesting that immune checkpoint inhibition with either free aPD-1 antibodies or aPD-1 NPs is effective in inducing anti-tumour responses for both HPV^- and HPV^+ cells.

3.4 Conclusion

Intratumoural administration of aPD-1 conjugated PEG-PLGA NPs resulted in favourable biodistribution with reduced off-target biodistribution of the antibodies compared to intratumoural administration of free aPD-1. Intratumoural administration also led to significantly higher tumour accumulation and decreased distribution in off-target organs and systemic circulation compared to systemic (IV) injection of free aPD-1. A comprehensive characterisation of the aPD-1 nanoformulation demonstrated equivalent immune checkpoint inhibition activity to the free PD-1 antibodies. Altogether, our data warrant further preclinical investigation of intratumoural administration of immune checkpoint inhibitor nanoformulation towards reducing off-target biodistribution and associated toxicity while maintaining the oncological control afforded by this state-of-the art cancer immunotherapy.

3.5 Supplementary figures

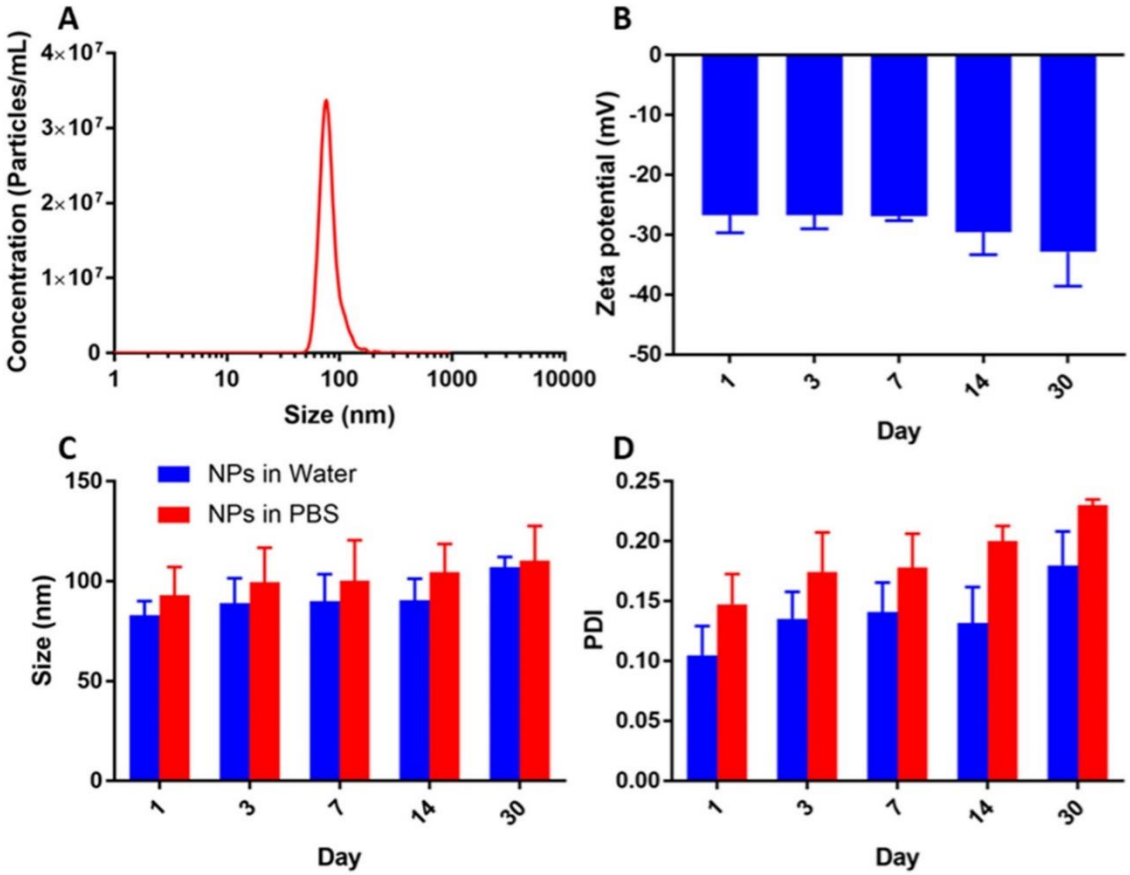

Figure 3-9 PEG-PLGA NPs physicochemical characterization and stability.
A) Nanoparticle tracking analysis of PEG-PLGA NPs dispersed in Milli-Q® water. B, C, D) Stability of PEG-PLGA NPs' zetapotential, size and size PDI stored in Milli-Q® water or 1x PBS for 30 days, measured by dynamic light scattering (n=3).

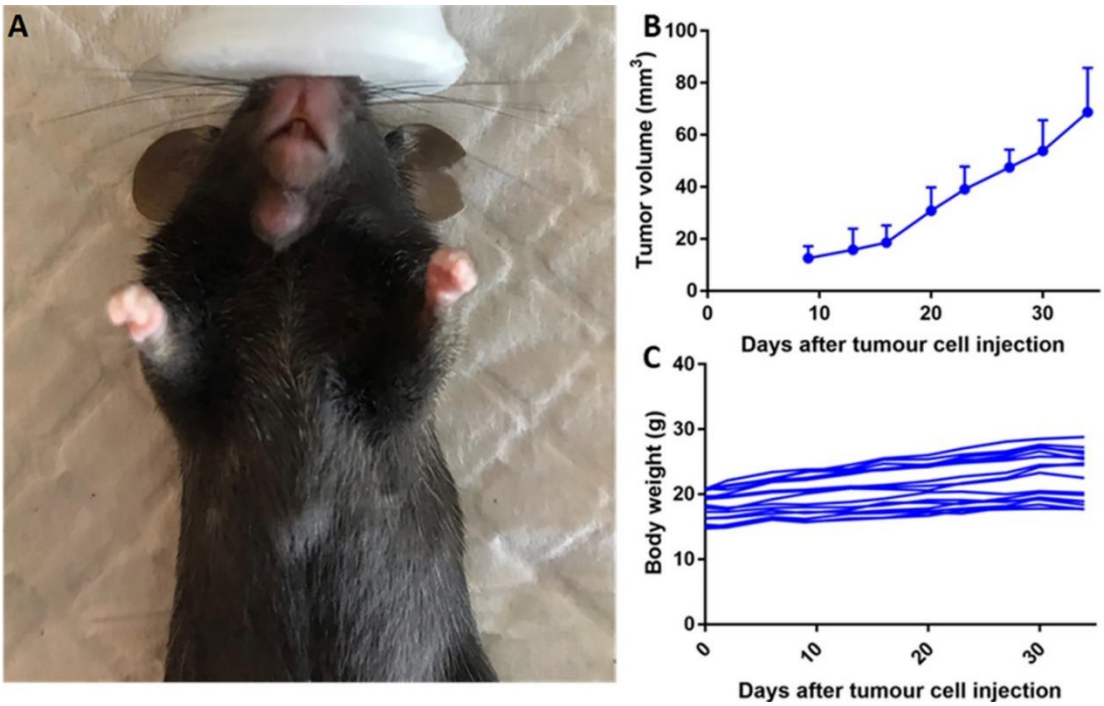

Figure 3-10 Establishment of an orthotopic C57BL/6 mouse model of head and neck cancer with the MOC-1 cell line.
A) A representative photo of C57BL/6 mice bearing orthotopic head and neck tumour in the floor of mouth. B) Tumour growth rate after detection of a palpable tumour until end of study. C) C57BL/6 mice body weights vs time after MOC-1 cells injection.

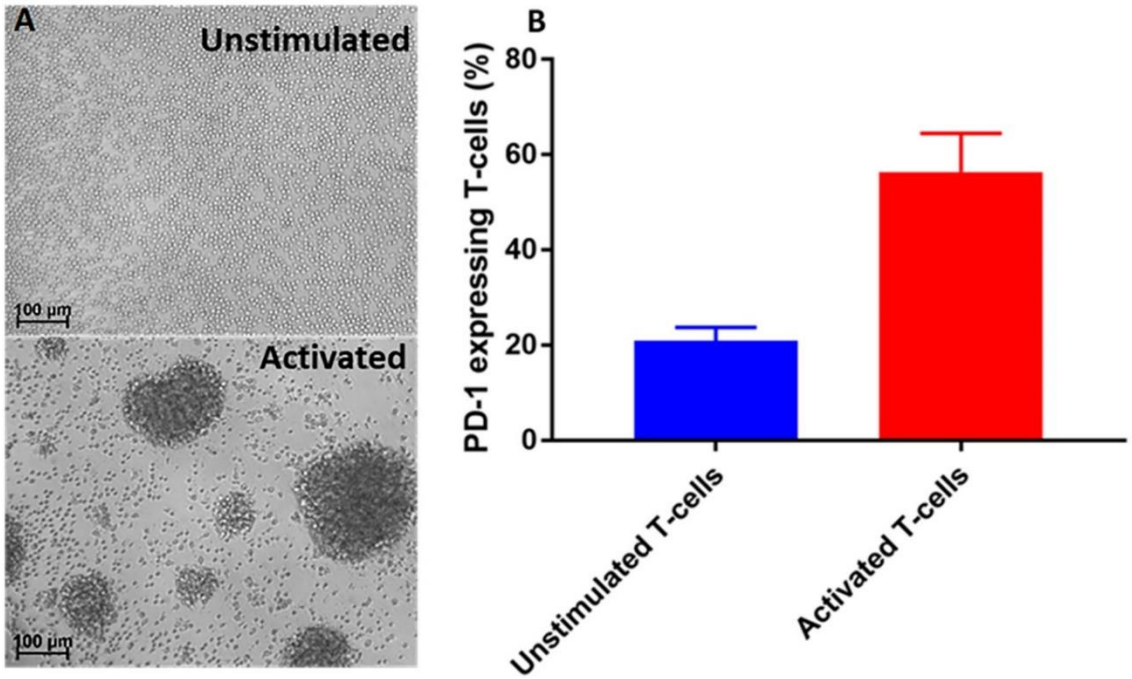

Figure 3-11 Activated primary human T-cells morphology and PD-1 receptors expression.
A) Unstimulated T-cells two days after isolation from peripheral blood under microscope vs cluster formed for activated T-cells by anti-CD3/CD28, scale bar 100 µm. B) Percentage of PD-1 expressing T-cells before and after 2 days activation (n=8).

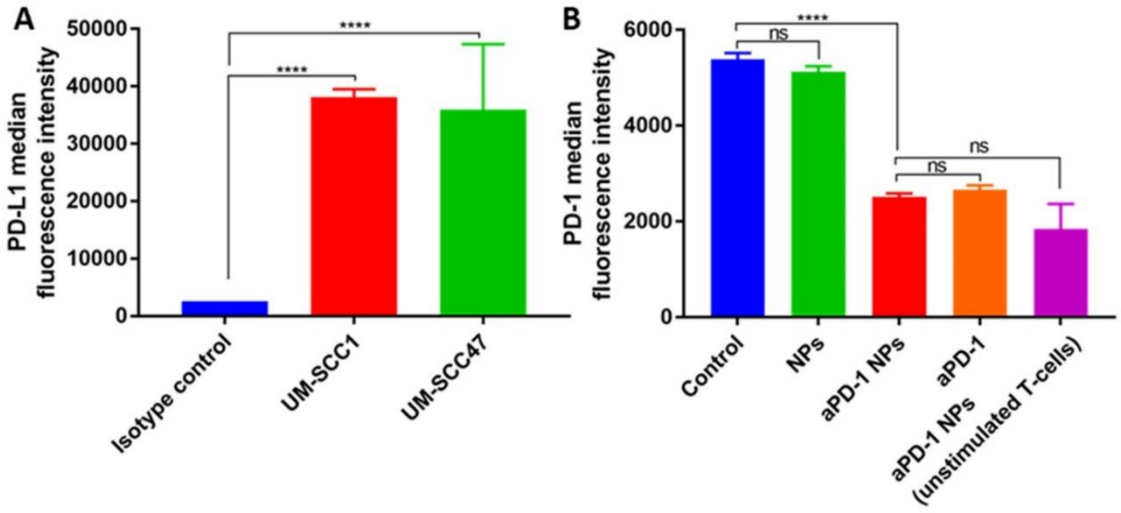

Figure 3-12 Cancer cell PD-L1 expression and PD-1 inhibition of T-cells in UM-SCC1 co-culture. A) PD-L1 expression by UM-SCC1 and UM-SCC47 cells. B) PD-1 inhibition 24 h after 5 µg/mL treatment of aPD-1 NPs, aPD-1 and unconjugated NPs in a co-culture of T-cells and UM-SCC1. Asterisk indicates statistical significance by one-way ANOVA and Tuckey post-hoc test:****$P \leq 0.0001$ and ns indicates not significant.

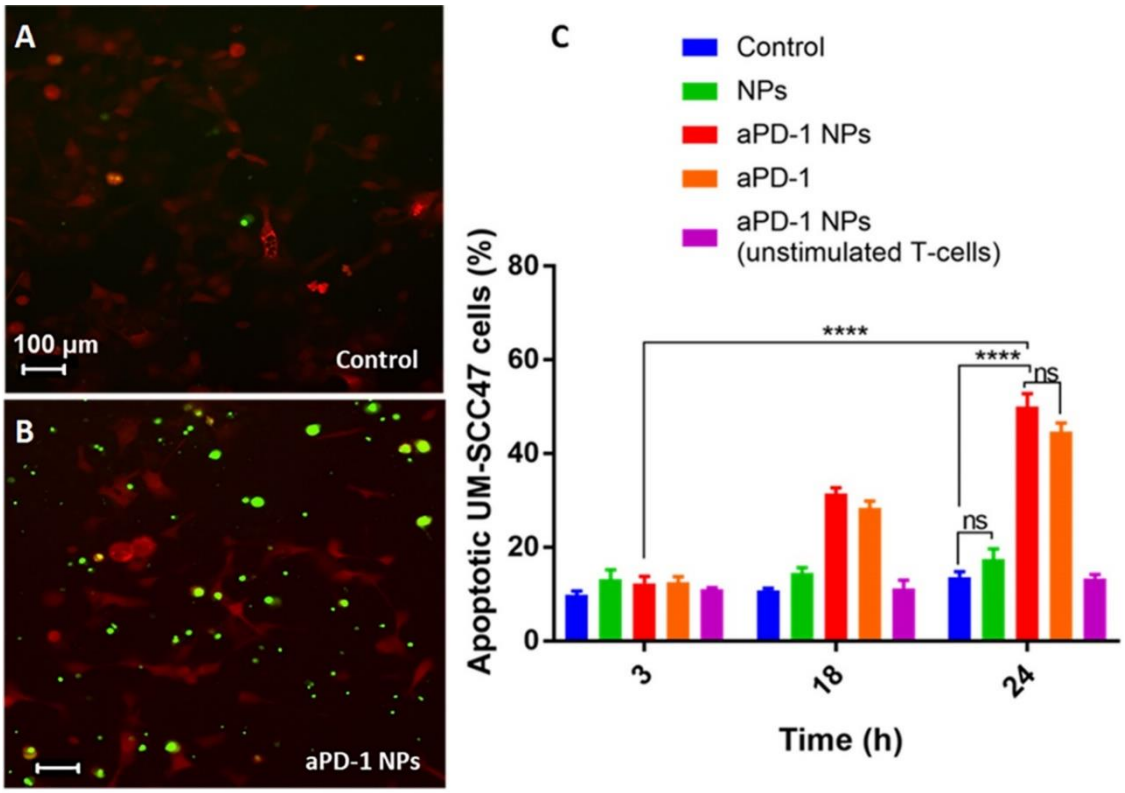

Figure 3-13 Effect of aPD-1 NPs on T-cells cytotoxicity in co-culture with RFP-SCC47.
Representative fluorescence images of caspase 3/7 activated RFP-SCC47 cells 24 h after co-culture with activated T-cells (A) untreated and (B) treated with 5 µg/mL of aPD-1 NPs. Green: caspase 3/7 activated cells; Red: RFP-SCC1 (scale bar 100 µm). C) Percentage of apoptotic UM-SCC47 cells by fluorescence microscopy after co-culture for 3 h, 18 h and 24 h with T-cells treated with 5 µg/mL of aPD-1 NPs, aPD-1, unconjugated NPs, and untreated. The statistical analysis was by one-way ANOVA and Tuckey post-hoc test. Asterisk indicates ****$P \leq 0.0001$ and ns is not significant.

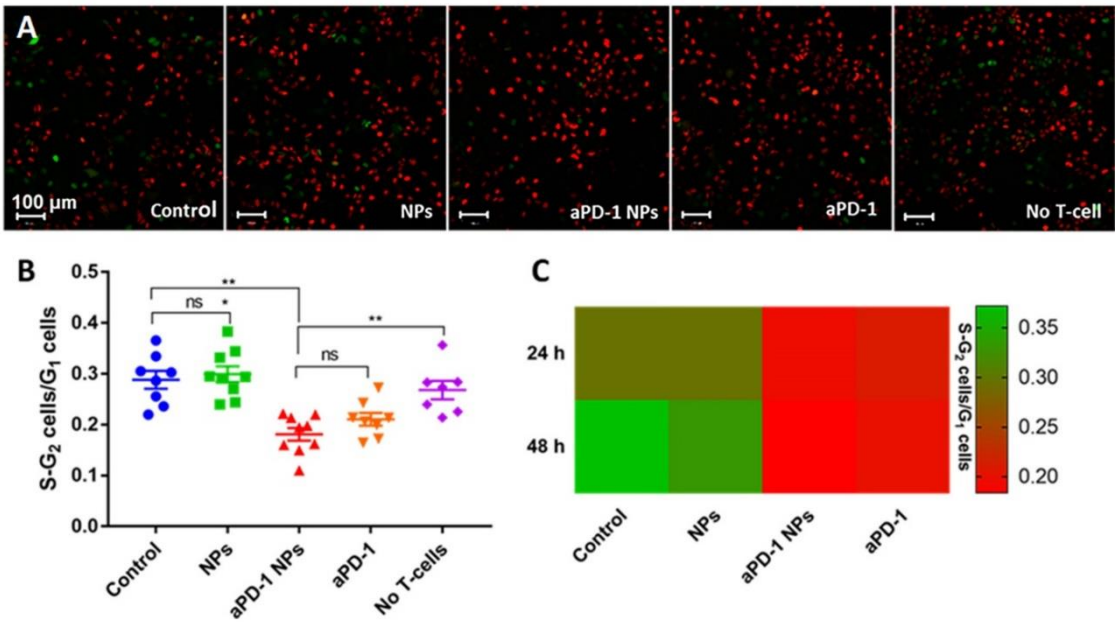

Figure 3-14 Effect of aPD-1 NP treated T-cells on the UM-SCC47 cell cycle.
A) Representative confocal microscopy images of fucci-SCC47 24 h after co-culture with T-cells treated with 5 µg/mL of aPD-1 NPs, aPD-1, and unconjugated NPs. Fucci-SCC47 cells exposed to untreated T cells or no T cells were used as control. Green: cells in S-G2 phase; red: cells in G1 phase (Scale bar: 100 µm). B) Ratio of fucci-SCC47 cells in S-G2 vs cells in G1 phase 24 h after T-cell treatment, obtained by quantification of images. C) Fucci-SCC1 cell cycle change 24 h and 48 h after T-cell treatment obtained by quantification of microscopy images. Statistical significance by one-way ANOVA and Tuckey post-hoc test is indicated by asterisk *P<0.05, **P < 0.01, ***P ≤ 0.001 and ****P ≤ 0.0001. Ns is not significant.

3.6 References

[1] Purple Book: Database of Licensed Biological Products, (2014). https://purplebooksearch.fda.gov/results?query=pembrolizumab&title=Keytruda (accessed January 11, 2021).

[2] Purple Book: Database of Licensed Biological Products, (2014). https://purplebooksearch.fda.gov/results?query=nivolumab&title=Opdivo (accessed January 11, 2021).

[3] E.I. Buchbinder, A. Desai, CTLA-4 and PD-1 pathways similarities, differences, and implications of their inhibition, Am. J. Clin. Oncol. Cancer Clin. Trials. 39 (2016) 98–106. https://doi.org/10.1097/COC.0000000000000239.

[4] A. Ribas, J.D. Wolchok, Cancer immunotherapy using checkpoint blockade, Science (80-.). 359 (2018) 1350–1355. https://doi.org/10.1126/science.aar4060.

[5] J.A. Seidel, A. Otsuka, K. Kabashima, Anti-PD-1 and anti-CTLA-4 therapies in cancer: Mechanisms of action, efficacy, and limitations, Front. Oncol. 8 (2018) 86. https://doi.org/10.3389/fonc.2018.00086.

[6] M.E. Suarez-Almazor, S.T. Kim, N. Abdel-Wahab, A. Diab, Review: Immune-Related Adverse Events With Use of Checkpoint Inhibitors for Immunotherapy of Cancer, Arthritis Rheumatol. 69 (2017) 687–699. https://doi.org/10.1002/art.40043.

[7] M.A. Postow, R. Sidlow, M.D. Hellmann, Immune-Related Adverse Events Associated with Immune Checkpoint Blockade, N. Engl. J. Med. 378 (2018) 158–168. https://doi.org/10.1056/nejmra1703481.

[8] M.A. Postow, M.K. Callahan, J.D. Wolchok, Immune checkpoint blockade in cancer therapy, J. Clin. Oncol. 33 (2015) 1974. https://doi.org/10.1200/JCO.2014.59.4358.

[9] R.M. Wong, R.B. Cameron, Immune Checkpoint Blockade and Adaptive Immune Resistance in Cancer, in: Immunother. Reality, Ideas, Futur., InTech, Rijeka, 2017: pp. 47–61.

[10] P. Zhao, D. Atanackovic, S. Dong, H. Yagita, X. He, M. Chen, An Anti-Programmed Death-1 Antibody (αPD-1) Fusion Protein That Self-Assembles into a

Multivalent and Functional αPD-1 Nanoparticle, Mol. Pharm. 14 (2017) 1494–1500. https://doi.org/10.1021/acs.molpharmaceut.6b01021.

[11] G. Myers, Immune-related adverse events of immune checkpoint inhibitors: A brief review, Curr. Oncol. 25 (2018) 342–347. https://doi.org/10.3747/co.25.4235.

[12] S.P. Arlauckas, C.S. Garris, R.H. Kohler, M. Kitaoka, M.F. Cuccarese, K.S. Yang, M.A. Miller, J.C. Carlson, G.J. Freeman, R.M. Anthony, R. Weissleder, M.J. Pittet, In vivo imaging reveals a tumor-associated macrophage-mediated resistance pathway in anti-PD-1 therapy, Sci. Transl. Med. 9 (2017) eaal3604. https://doi.org/10.1126/scitranslmed.aal3604.

[13] A. Natarajan, A.T. Mayer, L. Xu, R.E. Reeves, J. Gano, S.S. Gambhir, Novel Radiotracer for ImmunoPET Imaging of PD-1 Checkpoint Expression on Tumor Infiltrating Lymphocytes, Bioconjug. Chem. 26 (2015) 2062–2069. https://doi.org/10.1021/acs.bioconjchem.5b00318.

[14] M. Kwon, H. Jung, G.H. Nam, I.S. Kim, The right Timing, right combination, right sequence, and right delivery for Cancer immunotherapy, J. Control. Release. 331 (2021) 321–334. https://doi.org/10.1016/j.jconrel.2021.01.009.

[15] E. De Lombaerde, O. De Wever, B.G. De Geest, Delivery routes matter: Safety and efficacy of intratumoral immunotherapy, Biochim. Biophys. Acta - Rev. Cancer. 1875 (2021) 188526. https://doi.org/10.1016/j.bbcan.2021.188526.

[16] M.A. Aznar, N. Tinari, A.J. Rullán, A.R. Sánchez-Paulete, M.E. Rodriguez-Ruiz, I. Melero, Intratumoral Delivery of Immunotherapy—Act Locally, Think Globally, J. Immunol. 198 (2017) 31–39. https://doi.org/10.4049/jimmunol.1601145.

[17] D.H. Johnson, S.E. Bentebibel, S. Lecagoonporn, C. Bernatchez, C.L. Haymaker, R. Murthy, A. Tam, C. Yee, R.N. Amaria, S.P. Patel, H.A.-H. Tawbi, I.C. Glitza, M.A. Davies, W.-J. Hwu, P. Hwu, W.W. Overwijk, A. Diab, Phase I/II dose escalation and expansion cohort safety and efficacy study of image guided intratumoral CD40 agonistic monoclonal antibody APX005M in combination with systemic pembrolizumab for treatment naive metastatic melanoma., J. Clin. Oncol. 36 (2018) TPS3133. https://doi.org/10.1200/jco.2018.36.15_suppl.tps3133.

[18] S.M.M. Irenaeus, D. Nielsen, P. Ellmark, J. Yachnin, A. Deronic, A. Nilsson, P. Norlén, N. Veitonmäki, C.S. Wennersten, G.J. Ullenhag, First-in-human study with intratumoral administration of a CD40 agonistic antibody, ADC-1013, in advanced solid malignancies, Int. J. Cancer. 145 (2019) 1189–1199. https://doi.org/10.1002/ijc.32141.

[19] D.M. Francis, M.P. Manspeaker, A. Schudel, L.F. Sestito, M.J. O'Melia, H.T. Kissick, B.P. Pollack, E.K. Waller, S.N. Thomas, Blockade of immune checkpoints in lymph nodes through locoregional delivery augments cancer immunotherapy, Sci. Transl. Med. 12 (2020) eaay3575. https://doi.org/10.1126/scitranslmed.aay3575.

[20] W.X. Hong, S. Haebe, A.S. Lee, C. Benedikt Westphalen, J.A. Norton, W. Jiang, R. Levy, Intratumoral immunotherapy for early-stage solid tumors, Clin. Cancer Res. 26 (2020) 3091–3099. https://doi.org/10.1158/1078-0432.CCR-19-3642.

[21] M.F. Fransen, T.C. Van Der Sluis, F. Ossendorp, R. Arens, C.J.M. Melief, Controlled local delivery of CTLA-4 blocking antibody induces CD8 + T-cell-dependent tumor eradication and decreases risk of toxic side effects, Clin. Cancer Res. 19 (2013) 5381–5389. https://doi.org/10.1158/1078-0432.CCR-12-0781.

[22] L. van Hooren, L.C. Sandin, I. Moskalev, P. Ellmark, A. Dimberg, P. Black, T.H. Tötterman, S.M. Mangsbo, Local checkpoint inhibition of CTLA-4 as a monotherapy or in combination with anti-PD1 prevents the growth of murine bladder cancer, Eur. J. Immunol. 47 (2017) 385–393. https://doi.org/10.1002/eji.201646583.

[23] A. Ray, M.A. Williams, S.M. Meek, R.C. Bowen, K.F. Grossmann, R.H.I. Andtbacka, T.L. Bowles, J.R. Hyngstrom, S.A. Leachman, D. Grossman, G.M. Bowen, S.L. Holmen, M.W. VanBrocklin, G. Suneja, H.T. Khong, A phase I study of intratumoral ipilimumab and interleukin-2 in patients with advanced melanoma, Oncotarget. 7 (2016) 64390. https://doi.org/10.18632/oncotarget.10453.

[24] J. Bu, A. Nair, M. Iida, W.J. Jeong, M.J. Poellmann, K. Mudd, L.J. Kubiatowicz, E.W. Liu, D.L. Wheeler, S. Hong, An Avidity-Based PD-L1 Antagonist Using Nanoparticle-Antibody Conjugates for Enhanced Immunotherapy, Nano Lett. 20 (2020) 4901–4909. https://doi.org/10.1021/acs.nanolett.0c00953.

[25] Y. Zhang, N. Li, H. Suh, D.J. Irvine, Nanoparticle anchoring targets immune agonists to tumors enabling anti-cancer immunity without systemic toxicity, Nat. Commun. 9 (2018) 1–15. https://doi.org/10.1038/s41467-017-02251-3.

[26] C. Cremolini, E. Vitale, R. Rastaldo, C. Giachino, Advanced nanotechnology for enhancing immune checkpoint blockade therapy, Nanomaterials. 11 (2021) 661. https://doi.org/10.3390/nano11030661.

[27] H.A. Almoustafa, M.A. Alshawsh, Z. Chik, Technical aspects of preparing PEG-PLGA nanoparticles as carrier for chemotherapeutic agents by nanoprecipitation method, Int. J. Pharm. 533 (2017) 275–284. https://doi.org/10.1016/j.ijpharm.2017.09.054.

[28] C.E. Astete, C.M. Sabliov, Synthesis and characterization of PLGA nanoparticles, J. Biomater. Sci. Polym. Ed. 17 (2006) 247–289. https://doi.org/10.1163/156856206775997322.

[29] Y. Mi, C.C. Smith, F. Yang, Y. Qi, K.C. Roche, J.S. Serody, B.G. Vincent, A.Z. Wang, A Dual Immunotherapy Nanoparticle Improves T-Cell Activation and Cancer Immunotherapy, Adv. Mater. 30 (2018) 1706098. https://doi.org/10.1002/adma.201706098.

[30] M. Chen, H. Ouyang, S. Zhou, J. Li, Y. Ye, PLGA-nanoparticle mediated delivery of anti-OX40 monoclonal antibody enhances anti-tumor cytotoxic T cell responses, Cell. Immunol. 287 (2014) 91–99. https://doi.org/10.1016/j.cellimm.2014.01.003.

[31] C.J.H. Porter, N.L. Trevaskis, Targeting immune cells within lymph nodes, Nat. Nanotechnol. 15 (2020) 423–425. https://doi.org/10.1038/s41565-020-0663-z.

[32] J.P. Martins, G. Torrieri, H.A. Santos, The importance of microfluidics for the preparation of nanoparticles as advanced drug delivery systems, Expert Opin. Drug Deliv. 15 (2018) 469–479. https://doi.org/10.1080/17425247.2018.1446936.

[33] N.C. Shaner, R.E. Campbell, P.A. Steinbach, B.N.G. Giepmans, A.E. Palmer, R.Y. Tsien, Improved monomeric red, orange and yellow fluorescent proteins derived from Discosoma sp. red fluorescent protein, Nat. Biotechnol. 22 (2004) 1567–1572. https://doi.org/10.1038/nbt1037.

[34] A. Sakaue-Sawano, T. Kobayashi, K. Ohtawa, A. Miyawaki, Drug-induced cell cycle modulation leading to cell-cycle arrest, nuclear mis-segregation, or endoreplication, BMC Cell Biol. 12 (2011) 1–12. https://doi.org/10.1186/1471-2121-12-2.

[35] N.P. Judd, A.E. Winkler, O. Murillo-Sauca, J.J. Brotman, J.H. Law, J.S. Lewis, G.P. Dunn, J.D. Bui, J.B. Sunwoo, R. Uppaluri, ERK1/2 regulation of CD44 modulates oral cancer aggressiveness, Cancer Res. 72 (2012) 365–374.

[36] I. Terrén, A. Orrantia, J. Vitallé, O. Zenarruzabeitia, F. Borrego, CFSE dilution to study human T and NK cell proliferation in vitro, in: Methods Enzymol., 2020: pp. 239–255. https://doi.org/10.1016/bs.mie.2019.05.020.

[37] B. Amoyav, O. Benny, Controlled and tunable polymer particles' production using a single microfluidic device, Appl. Nanosci. 8 (2018) 905–914. https://doi.org/10.1007/s13204-018-0790-0.

[38] J. Guo, X. Gao, L. Su, H. Xia, G. Gu, Z. Pang, X. Jiang, L. Yao, J. Chen, H. Chen, Aptamer-functionalized PEG-PLGA nanoparticles for enhanced anti-glioma drug delivery, Biomaterials. 32 (2011) 8010–8020. https://doi.org/10.1016/j.biomaterials.2011.07.004.

[39] W. Li, L. Zhang, X. Ge, B. Xu, W. Zhang, L. Qu, C.H. Choi, J. Xu, A. Zhang, H. Lee, D.A. Weitz, Microfluidic fabrication of microparticles for biomedical applications, Chem. Soc. Rev. 47 (2018) 5646–5683. https://doi.org/10.1039/c7cs00263g.

[40] P. Kocbek, N. Obermajer, M. Cegnar, J. Kos, J. Kristl, Targeting cancer cells using PLGA nanoparticles surface modified with monoclonal antibody, J. Control. Release. 120 (2007) 18–26. https://doi.org/10.1016/j.jconrel.2007.03.012.

[41] S.P. Arlauckas, C.S. Garris, R.H. Kohler, M. Kitaoka, M.F. Cuccarese, K.S. Yang, M.A. Miller, J.C. Carlson, G.J. Freeman, R.M. Anthony, In vivo imaging reveals a tumor-associated macrophage–mediated resistance pathway in anti–PD-1 therapy, Sci. Transl. Med. 9 (2017) eaal3604.

[42] M.E. Suarez-Almazor, S.T. Kim, N. Abdel-Wahab, A. Diab, Review: Immune-Related Adverse Events With Use of Checkpoint Inhibitors for Immunotherapy of Cancer. Arthritis Rheumatol. 2017; 69: 687–99, (n.d.).

[43] R.A. Sheth, R. Murthy, D.S. Hong, S. Patel, M.J. Overman, A. Diab, P. Hwu, A. Tam, Assessment of Image-Guided Intratumoral Delivery of Immunotherapeutics in Patients with Cancer, JAMA Netw. Open. 3 (2020) e207911. https://doi.org/10.1001/jamanetworkopen.2020.7911.

[44] M.F. Fransen, M. Schoonderwoerd, P. Knopf, M.G. Camps, L.J. Hawinkels, M. Kneilling, T. van Hall, F. Ossendorp, Tumor-draining lymph nodes are pivotal in PD-1/PD-L1 checkpoint therapy, JCI Insight. 3 (2018) e124507. https://doi.org/10.1172/jci.insight.124507.

[45] L. van Hooren, L.C. Sandin, I. Moskalev, P. Ellmark, A. Dimberg, P. Black, T.H. Tötterman, S.M. Mangsbo, Local checkpoint inhibition of CTLA-4 as a monotherapy or in combination with anti-PD1 prevents the growth of murine bladder cancer, Eur. J. Immunol. 47 (2017) 385–393. https://doi.org/10.1002/eji.201646583.

[46] C. Wang, Y. Ye, G.M. Hochu, H. Sadeghifar, Z. Gu, Enhanced Cancer Immunotherapy by Microneedle Patch-Assisted Delivery of Anti-PD1 Antibody, Nano Lett. 16 (2016) 2334–2340. https://doi.org/10.1021/acs.nanolett.5b05030.

[47] T.A. Potter, K. Grebe, B. Freiberg, A. Kupfer, Formation of supramolecular activation clusters on fresh ex vivo CD8+ T cells after engagement of the T cell antigen receptor and CD8 by antigen-presenting cells, Proc. Natl. Acad. Sci. U. S. A. 98 (2001) 12624–12629. https://doi.org/10.1073/pnas.221458898.

[48] D. Cibrián, F. Sánchez-Madrid, CD69: from activation marker to metabolic gatekeeper, Eur. J. Immunol. 47 (2017) 946–953. https://doi.org/10.1002/eji.201646837.

[49] C. Wang, K.B. Thudium, M. Han, X.T. Wang, H. Huang, D. Feingersh, C. Garcia, Y. Wu, M. Kuhne, M. Srinivasan, S. Singh, S. Wong, N. Garner, H. Leblanc, R.T. Bunch, D. Blanset, M.J. Selby, A.J. Korman, In vitro characterization of the anti-PD-1 antibody nivolumab, BMS-936558, and in vivo toxicology in non-human primates, Cancer Immunol. Res. 2 (2014) 846–856. https://doi.org/10.1158/2326-6066.CIR-14-0040.

[50] B. Farhood, M. Najafi, K. Mortezaee, CD8+ cytotoxic T lymphocytes in cancer immunotherapy: A review, J. Cell. Physiol. 234 (2019) 8509–8521. https://doi.org/10.1002/jcp.27782.

[51] C.R. Bradford, S. Zhu, H. Ogawa, T. Ogawa, M. Ubell, A. Narayan, G. Johnson, G.T. Wolf, S.G. Fisher, T.E. Carey, p53 mutation correlates with cisplatin sensitivity in head and neck squamous cell carcinoma lines, Head Neck. 25 (2003) 654–661. https://doi.org/10.1002/hed.10274.

[52] G.L. Clayman, T.J. Liu, S.M. Overholt, S.R. Mobley, M. Wang, F. Janot, H. Goepfert, Gene therapy for head and neck cancer: Comparing the tumor suppressor gene p53 and a cell cycle regulator WAF1/CIP1 (p21), Arch. Otolaryngol. - Head Neck Surg. 122 (1996) 489–493. https://doi.org/10.1001/archotol.1996.01890170025006.

[53] M.D. Forster, M.J. Devlin, Immune checkpoint inhibition in head and neck cancer, Front. Oncol. 8 (2018) 310. https://doi.org/10.3389/fonc.2018.00310.

[54] E.L. Göttgens, C. Ostheimer, P.N. Span, J. Bussink, E.M. Hammond, HPv, hypoxia and radiation response in head and neck cancer, Br. J. Radiol. 92 (2018) 20180047. https://doi.org/10.1259/bjr.20180047.

[55] S. Miyauchi, P.D. Sanders, K. Guram, S.S. Kim, F. Paolini, A. Venuti, E.E.W. Cohen, J.S. Gutkind, J.A. Califano, A.B. Sharabi, HPV16 E5 mediates resistance to PD-L1 blockade and can be targeted with rimantadine in head and neck cancer, Cancer Res. 80 (2020) 732–746. https://doi.org/10.1158/0008-5472.CAN-19-1771.

Chapter 4

Nanoformulation of the Navoximod Immune Checkpoint Inhibitor within PEG-PLGA Nanoparticles by Hydrophobic Ion Pair Complexation towards Improved IDO Inhibition

4 Nanoformulation of the navoximod immune checkpoint inhibitor within PEG-PLGA nanoparticles by hydrophobic ion pair complexation towards improved IDO inhibition

4.1 Introduction

The use of immunotherapies in oncology has rapidly increased following the demonstration of the therapeutic activity of immune checkpoint (ICP) inhibitors [1]. One of the leading class of ICP inhibitors are programmed cell death-1 (PD-1) antibodies (aPD-1) that target PD-1 receptors expressed on immune cells, such as T-cells. PD-1 receptors are upregulated upon activation of T-cells and interactions with their ligands (such as PD-L1) lead to T-cell exhaustion [2]. This pathway of T-cell exhaustion occurs in many cancer types and is mediated through the overexpression of PD-L1 in cancer cells and immunosuppressive immune cells [3]. Treatment with aPD-1 has been shown to restore the cytotoxic activity of the immune system by blocking the PD-1/PD-L1 pathway, increasing the function and proliferation of T-cells [4,5].

However, the patient response rates to PD-1/PD-L1 inhibitors is low, which is largely due to the development of resistance [6]. Although the precise mechanisms of resistance to PD-1/PD-L1 inhibitors are yet to be elucidated, it is likely that the overexpression of other ICPs is a contributing factor [7]. In this regard, inhibitors of indoleamine 2, 3-dioxygenase (IDO) are under clinical investigation, particularly in combination with PD-1/PD-L1 inhibitors [8,9]. IDO is an enzyme that catabolizes tryptophan to kynurenine and other metabolites [10]. The depletion of tryptophan, and the subsequent increase of its metabolites, decreases the proliferation and activity of immune cells, leading to immune cell suppression [10]. Since the upregulation of IDO in cancer cells and some of immune cells is mediated by inflammatory cytokines such as interferon (INF)-γ, aPD-1 therapy can also increase the expression of IDO due to the increased secretion of INF-γ by restored cytotoxic T-cells, which counteract the therapeutic benefit of aPD-1 therapy. [11]

Navoximod (NLG-919, GDC-0919) is a potent IDO inhibitor (IDOi) which has been evaluated either as a single therapy or in combination with other cancer therapies in preclinical and clinical studies [12,13]. As a small molecule, navoximod has a short half-life and high off-target biodistribution, which is usually associated with resistance and side effects [14]. In addition, due to its low oral bioavailability, navoximod is typically

administered at high doses, resulting in high rates of adverse effects [15]. Finally, navoximod either as a single or dual therapy with PD-L1 antibodies yielded only modest efficacy in clinical trials, despite the high potency of navoximod in priming anti-tumour immune activity, highlighting the insufficient tumour delivery of this potent molecule [13,16].

Several preclinical studies have shown that nanoparticle (NP) IDOi formulations have improved tumour accumulation. However, the loading of intact navoximod and other IDOi within NPs is challenging due to IDOi physicochemical properties, such as hydrophobicity and solubility [17–19]. To address this issue, it has been shown that the delivery of navoximod using self-assembling peptides targeting PD-L1 can efficiently increase the anti-tumour activity of immune cells and reduce tumour size in a murine model of melanoma [15]. Chen *et al.*, prepared a prodrug of navoximod using poly(ethylene glycol) (PEG) and self-assembling micelles to improve the loading of navoximod [18]. A similar approach was used by Liu *et al.*, who PEGylated IDOi with a peptide linker and co-delivered IDOi and a photosensitizer using NPs [17]. In another study, a homodimer of navoximod was prepared through the addition of a disulfide bond, which was subsequently incorporated into PEGylated oxaliplatin for sequential release in the acidic tumour microenvironment [20]. Moreover, lipid tagged or gelatin conjugated IDOi were employed for delivery by liposomes or mesoporous silica NPs, respectively [21–23]. These nanoformulations all demonstrated increased efficacy of IDOi in comparison to unformulated IDOi.

While these previous reports establish the potential of IDOi nanoformulation, the reliance on chemical alteration of the molecule itself not only adds to the complexity to the synthesis, it can also affect the activity of the inhibitors [24]. In view of its clinical implementation, a drug delivery system should ideally be amenable to large scale reproducible manufacture. Moreover, the loading of therapeutics into the carrier should be efficient enough to reach to the site of action, while preserving its stability and activity. Poly(ethylene glycol)-b-poly(lactide-co-glycolide) (PEG-PLGA) is a biodegradable polymer extensively used in the synthesis of NPs. PEG-PLGA nanocarriers have a well established safety profile including clinically [25,26]. In addition, microfluidic-based nanoprecipitation enables simpler and more reproducible manufacturing of PEG-PLGA nanocarriers compared to conventional bulk mixing methods [27]. However, efficient loading of challenging molecules into the PLGA or PEG-PLGA NPs is suboptimal [28].

A promising strategy to improve the drug loading and stability of low molecular weight bioactive is hydrophobic ion pairing [29]. In hydrophobic ion pairing, a drug molecule which is not intrinsically hydrophobic enough to be efficiently loaded into polymeric NPs is complexed with a counter ion molecule to shield its ionic charge. The counter ion also has a hydrophobic group that increases the hydrophobicity of the drug upon formation of the complex, consequently improving the loading within the NP core [29]. Unlike the synthesis of prodrugs, this approach does not permanently modify the drug chemically and therefore preserves its biological activity.

In this study, we developed a simple yet efficient PEG-PLGA nanoformulation of navoximod (IDOi NP) using hydrophobic ion pairing. We validated the efficacy of the nanformulation in inhibiting IDO in head and neck cancer cells. We also demonstrate that in combination with aPD-1, IDOi NPs can overcome resistance to aPD-1 and improve the anti-tumour activity of T-cells.

4.2 Materials and methods

4.2.1 Materials

PLGA (15-25 KDa) and methoxy-PEG-PLGA (mPEG-PLGA) (2-15 KDa) were obtained from PoliSciTech (USA). Acetonitrile, dimethyl sulfoxide (DMSO) and sodium deoxycholate were purchased from Sigma Aldrich (USA). Navoximod was from MedChemExpress (USA). Recombinant human interferon γ (INF-γ) and interleukin-2 (IL-2) were purchased from Peprotech (USA). GoInVivo™ Purified anti-human PD-1 antibody (clone EH12.2H7) was obtained from Biolegend (USA). Anti-human CD28 antibody (clone CD28.2) and anti-human CD3 (clone OK3) were supplied from ThermoFisher scientific (USA).

4.2.2 Cell culture

The head and neck cancer squamous cell carcinoma (HNSCC) cell line UM-SCC1 (Merck Millipore, USA) was used for the *in vitro* biological investigation and co-cultured with T-cells for cytotoxicity assays. UM-SCC1 cells stably expressing the fluorescent ubiquitination-based cell cycle indicator (fucci) system (fucci-SCC1) were prepared as previously reported (see chapter 3) and used for cell cycle analysis. The fucci construct was obtained from RIKEN BRC through the National Bio-Resources Project of the MEXT/AMED, Japan [30]. The fucci cells express red fluorescence in G1 and green

fluorescence in S-G2 phases. The UM-SCC1 cells were cultured in complete RPMI media, (Gibco, UK) supplemented with 10% FBS (Gibco, UK), 1% streptomycin/penicillin (Gibco, UK) and 1% L-glutamine (Gibco, UK) and maintained in a humidified incubator (90% humidity and 5% CO_2) at 37˚C. Cells were subcultured using 0.25% trypsin-EDTA at 80% confluency.

4.2.3 Preparation of IDOi loaded PEG-PLGA NPs

PEG-PLGA NPs were prepared using a 3D printed microfluidic-based mixing chip (Figure 4-1). The chip was fabricated using a MiiCraft 3D printer (Rays Optics, Canada) with channel dimensions of 0.6 mm and 1.1 mm for width and height, respectively. Aqueous and polymer phases were introduced via two inlets and mixed in a herringbone structured mixing channel to nano-precipitate the polymer. To prepare the IDOi NPs, a sodium deoxycholate solution in DMSO and navoximod in ethanol were premixed at different molar ratios as indicated in table 4-1. To optimise the IDOi loading, the IDOi/ sodium deoxycholate mixture was added to 10 mg/mL of polymer mixture in DMSO with various IDOi/polymer weight ratios (table 4-1). The polymer mixture was comprised of 50 % PLGA and 50 % PEG-PLGA, and Milli-Q® water was used as the aqueous phase. The flow rates of water and DMSO were controlled by two syringe pumps (Chemyx fusion 200). A range of flow rates was tested to optimize the physicochemical properties of the NPs. The IDOi NPs were collected from the outlet of the device and centrifuged and washed at 24000 g for 15 minutes at 4°C and redispersed in Milli-Q® water for further characterization. For the small sized NPs, the sample was washed and collected using Amicon® Ultra-4 Centrifugal Filters with a 10 KDa cut-off (Merck Millipore, USA) instead of centrifugation.

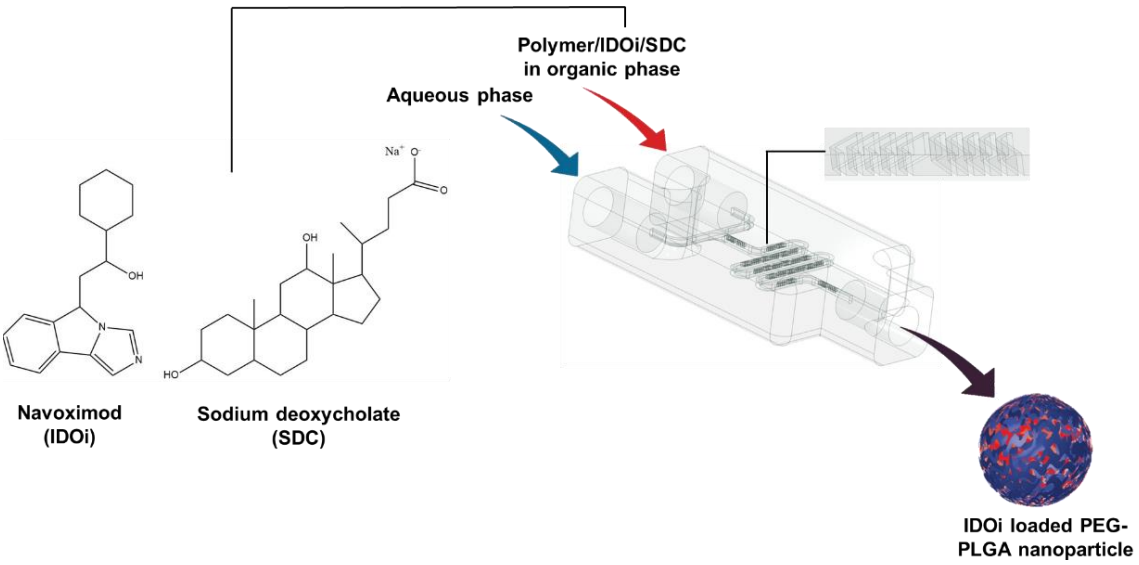

Figure 4-1 Schematic illustration of IDOi NP preparation using a 3D printed microfluidic nanoprecipitation chip.
The IDOi navoximod was loaded by hydrophobic ion pairing using sodium deoxycholate (SDC) as the counter ion. In this procedure, a mixture of PLGA, PEG-PLGA, IDOi and sodium deoxycholate in DMSO is introduced into one inlet and rapidly mixed with the aqueous phase in a herringbone structured microfluidic channel to nanoprecipitate the polymer and load IDOi/SDC complex.

4.2.4 Physicochemical characterization of IDOi NPs

The hydrodynamic size of IDOi NPs dispersed in Milli-Q® water was measured by dynamic light scattering using a Zetasizer 3000 HS (Malvern Instruments Ltd, UK). The zeta potential of the NPs was also measured using the Zetasizer 3000 HS (in Milli-Q® water). The morphology of the IDOi NPs was observed using a JEOL JEM-2100F-HR transmission electron microscope (TEM) (Jeol, Japan) after negative staining with 2% phosphotungstic acid in water.

Reversed phase high-performance liquid chromatography (HPLC) was used to quantify the IDOi loading using an Agilent 1200 HPLC system and Eclipse Plus C18 column (4.6 x 100 mm, 3.5 µm) (Agilent Technologies, USA). After centrifugation, pelleted IDOi NPs were dissolved in acetonitrile prior to injection into the HPLC system. A gradient mobile phase of water and HPLC grade methanol with 0.1 % formic acid (Sigma, USA) was used. The mobile phase was pumped at a flow rate of 2 mL/minute with 10 % methanol/90 % water, which was changed to 90 % methanol/10 % water over 8 minutes. Subsequently, the drug peak was detected by DAD UV-Vis spectroscopy at 262 nm. To quantify the sample, a standard curve of IDOi in acetonitrile (0.5 µg/mL to 100 µg/mL) was prepared. The drug loading was calculated using the following equation.

$\text{Drug loading (\%)} = \frac{\text{Mass of loaded IDOi}}{\text{Mass of IDOi NPs}} \times 100$. The mass of IDOi NPs was measured after freeze drying by Modulyo® freeze dryer (Thermo Fisher Scientific Inc., USA).

The release profile of the IDOi NPs was measured using dialysis. 0.3 mL of IDOi NP (equal to 0.6 mg/mL of IDOi) suspension in 1x Dulbecco's PBS (DPBS) (Thermo Fisher Scientific, USA) was transferred into a Membra-cel® MD34 14X100 CLR dialysis tube (Sigma Aldrich, USA). The dialysis bag was placed into a beaker of 20 mL DPBS as the releasing medium, while stirring at 100 rpm. The release study was performed at both room temperature and 37°C to simulate storage at shelf temperature and *in vivo* temperature, respectively. The volume of sample and releasing medium were adjusted based on the solubility of navoximod to mimic the sink condition and prevent the saturation of dissolution. At 0.5, 1, 2, 4, 6, 8 and 24 h time-points, 1 mL of the releasing media was collected to quantify the released drug, after which, the medium was replaced with 20 mL of fresh DPBS to maintain the sink condition. The collected sample was centrifuged at 24000 g for 15 minutes at 4 °C and the supernatant was analysed by HPLC.

4.2.5 IDO enzymatic activity

To determine the efficacy of the IDOi NPs to inhibit IDO activity, UM-SCC1 cells were seeded in a 96-well plate ($5x10^3$ cells per well). After overnight incubation, the cell culture media was replaced with complete RPMI supplemented with 400 ng/mL INF-γ to stimulate IDO expression. The cells were treated with different concentrations of IDOi NPs or free IDOi ranging from 0.001 µM to 20 µM. After 72 h of treatment, 150 µL of supernatant was collected from each well and incubated with 75 µL trichloroacetic acid (30 %) at 50 °C for 30 minutes to hydrolyse N-formylkynurenine to kynurenine. The samples were then centrifuged for 5 minutes at 5000 g and 100 µL of the supernatant was transferred to a 96-well plate and incubated with an equal volume of Ehrlich's reagent (2% *p*-dimethylamino-benzaldehyde w/v in glacial acetic acid) to develop yellow colour. Various concentrations of kynurenine (0 - 240 µM) were used to generate a standard curve for quantification of kynurenine in the samples. The absorbances of the samples were measured at 490 nm using a FLUOstar OPTIMA plate reader (BMG Labtech, USA).

4.2.6 Impact of IDOi NPs on cancer cells metabolic activity

The effect of IDOi NPs or blank NPs on metabolic activity of UM-SCC1 cells was determined based on the reduction of 3-(4,5-dimethylthiazol-2-yl)-2,5-diphenyltetrazolium bromide (MTT) salt (Sigma Aldrich, USA). UM-SCC1 cells were seeded in a 96-well-plate ($7.5x10^3$ cells per well). After overnight incubation, the cell culture media was changed and the cells were treated with various concentrations of IDOi NPs or equal doses of blank NPs (IDOi doses ranging from 0 – 100 µM). After 48 h, the cell culture media was discarded, and the cells were incubated in 60 µL complete RPMI and 40 µL MTT solution (5 mg/mL). After 4 h, the MTT solution was replaced with 100 µL DMSO to solubilize formazan as the product of MTT reduction. The developed colour was measured at 540 nm using a FLUOstar OPTIMA plate reader (BMG Labtech, USA).

4.2.7 T-cell isolation and activation

Primary T-cells were isolated from peripheral blood collected from healthy volunteers in accordance with the UniSA Human Research Ethics Committee (approval number 201726). T-cells were enriched by RosetterSep^{TM} human T-cell enrichment kit (Stemcell) according to the manufacturer's protocol. The isolated T-cells (10^6 cells/mL) were activated for 2 days using an anti-CD3 (5 µg/mL) coated well-plate in presence of 4 µg/mL anti-CD28 and 500 U/mL IL-2.

4.2.8 T-cell cytotoxicity modulation by IDOi NPs/aPD-1

UM-SCC1 cells (10^5) were seeded in a 24-well plate and incubated in complete RPMI media supplemented with 400 ng/mL INF-γ. After an overnight, the cell culture medium was changed to complete RPMI supplemented with 10 U/mL IL-2 and 50 ng/mL INF-γ and the cancer cells were co-cultured with $2x10^5$ activated T-cells. The cells were then treated with 10 µM IDOi NPs or 5 µg/mL aPD-1 or a combination of IDOi NPs/ aPD-1 or left without treatment which was used as the control.

Imaging flow cytometry was used to determine the expression of various T-cell markers. Co-cultured T-cells were harvested and washed twice with DPBS and centrifuged at 500 g for 5 minutes. The cells were stained for 30 minutes with specific fluorophore conjugated antibodies in 0.5% bovine serum albumin in DPBS. After staining, the cells were washed twice with DPBS and analysed by imaging flow cytometry Image Stream X (AMNIS, USA). Imaging flow cytometry data was analysed using IDEAS 6.2 (EMD Millipore, USA) and FlowJo V10 (FlowJo, USA). The following human antibodies were

used for immune-staining: FITC CD3(ThermoFisher Scientific, USA), BV421 CD3, PE PD-1, FITC CD4, PerCP Cy5.5 CD8, AF647 Ki67, AF647 foxP3 (BioLegend, USA) and BV421 granzyme B (BD bioscience, USA). Ki67, foxP3 and granzyme B were detected after intracellular staining using eBioscience Foxp3 / Transcription Factor Staining Buffer kit (ThermoFisher Scientific, USA), according to the manufacturer's protocol.

The population of immunosuppressive regulatory T-cells (T_{reg}), was determined 48 h after treatment of co-cultures by imaging flow cytometry and following immunostaining for CD3, CD4 and foxP3.

The effect of IDOi NPs or IDOi NPs/aPD-1 on T-cell proliferation was assessed by CellTrace™ CFSE Cell Proliferation Kit (Thermo Fisher Scientific, USA). Activated T-cells were labelled with CellTrace™ CFSE Cell Proliferation Kit according to the manufacturer's conditions and co-cultured with UM-SCC1 cells. Two days after treatment, the T-cells were harvested and the CFSE intensity was quantified by imaging flow cytometry after gating for $CD3^+$ single cells. In this method, CFSE dilution indicates T-cell proliferation. T-cell proliferation was further investigated by examining Ki67 expression. One day after treatment, $Ki67^+$ T-cells were quantified by imaging flow cytometry after staining with Ki67 and CD3 antibodies.

The efficacy of IDOi NPs or IDOi NPs/aPD-1 on inhibiting PD-1 receptors as a marker of T-cell exhaustion and granzyme B as a marker of T-cell cytotoxicity was determined by quantifying $PD\text{-}1^+$ $CD3^+$ cells 48 h after treatment and granzyme B^+ $CD3^+$ T-cells, 24 h after treatment by imaging flow cytometry.

4.2.9 Cancer cell apoptosis and cell cycle function by IDOi NPs/aPD-1

UM-SCC1 cells were seeded in ibiTreat µ-Slide 8 Well (Ibidi GmbH, Germany), 2 x 10^4 cells/ well and co-cultured with 4 x 10^4/ well activated T-cells. The cells were treated for 24 h with 10 µM IDOi NP or 5 µg/mL aPD-1 or combination of IDOi NP/ aPD-1 or left without treatment, as the control. The same dose of free IDOi was also used as the positive control. To determine the rate of cancer cells apoptosis, CellEvent™ Caspase-3/7 Green Detection Reagent (ThermoFisher Scientific, USA) was used as per the manufacturer's protocol. This reagent is a DNA binding fluorescent dye conjugated to a DEVD peptide. The peptide is cleaved by activated caspase 3/7, allowing the dye to bind to DNA and show fluorescence. The cells were imaged with a Confocal Laser Scanning Microscope

710 (Zeiss, Germany) using objective 10x and the FITC channel. The number of apoptotic cells were quantified using NIS-Elements software (Nikon, Japan).

Fucci-SCC1 cells were used in the co-culture system to determine the effects of T-cells on the cancer cell cycle after treatment with IDOi NPs or IDOi NPs/ aPD-1 as described above. The cells were imaged by Confocal Laser Scanning Microscope 710 (Zeiss, Germany) using objective 10x and in the FITC and Texas red channels. The number of red and green cells were counted using NIS-Elements software (Nikon, Japan), as the indicator of G1 and S-G2 cell cycle, respectively, and the green/red cells ratio calculated.

4.2.10 Statistics

All experiments were repeated independently at least two times. Data was analysed by one-way ANOVA with Tukey post hoc test using GraphPad Prism 7 (GraphPad Software, Inc., USA). Statistical significance was indicated by asterisk as *P<0.05, **P < 0.01, ***P ≤ 0.001, ****P ≤ 0.0001 and ns indicates not significant. The data is represented as average ± standard error of mean.

4.3 Results and discussion

4.3.1 Hydrophobic ion pairing improved the physicochemical characteristics of IDOi NP

Our initial attempts at loading the navoximod IDOi within PEG-PLGA NPs yielded very low efficiency (Table 4-1). We therefore employed hydrophobic ion pairing to increase the compatibility between the drug and the hydrophobic core of the PEG-PLGA NPs. Sodium deoxycholate was used as the counter ion. To optimize the drug loading and physicochemical properties of the NPs, key formulation parameters namely the ratios of IDOi/polymer (w/w), sodium deoxycholate/IDOi (mol/mol) and flow rate of aqueous/solvent phases were optimized. The details of each tested condition and their effects on drug loading and the NPs' hydrodynamic size are summarized in table 4-1.

Table 4-1 Optimization of IDOi NP nanoformulation by hydrophobic ion pairing and nanoprecipitation.

IDOi/polymer ratio (W/W %)	Sodium deoxycholate/ IDOi (mol/mol)	Aqueous/Solvent flow rate (mL/min)	Drug loading (W/W %, mean ± SD)	Hydrodynamic diameter (nm, mean ± SD)
20	0	3/1	0.8 ± 0.1	43.5 ± 8.7
10	3/1	3/1	1 ± 0.3	52.5 ± 1.4
10	5/1	3/1	0.8 ± 0.1	66 ± 7.8
10	10/1	3/1	1.8 ± 0.9	76.8 ± 6.7

20	2/1	3/1	5.7 ± 3.1	63.5 ± 2.1
20	3/1	3/1	5.8 ± 2.1	78 ± 0.7
20	4/1	3/1	9.7 ± 0.2	83.5 ± 2.5
20	5/1	3/1	10.1 ± 0.4	80.8 ± 5.0
20	7/1	3/1	7.2 ± 0.3	96 ± 2.8
20	10/1	3/1	6.0 ± 3.1	109 ± 12.7
20	5/1	8/1	5.2 ± 2.2	51.4 ± 1.3
20	5/1	15/3	1.5 ± 0.1	36.9 ± 0.7

By increasing the weight ratio of IDOi/polymer without changing any other parameters, the drug loading increased, with a 20 % ratio yielding the highest loading. As shown in figure 4-2-A, at 20 % IDOi/polymer, the loading was further enhanced by increasing the sodium deoxycholate/IDOi ratio up to 5/1. Further increase of the sodium deoxycholate /IDOi ratio was associated with a decrease in loading of IDOi. To optimize the NPs' size, various aqueous/solvent flow rates were tested. The microfluidic nanoprecipitation device made it possible to easily adjust the NPs size by adjusting the flow rates without changing the polymer composition or concentration. Keeping constant both the drug/polymer (20 %) and sodium deoxycholate /IDOi (5/1) ratios, very small PEG-PLGA NPs could be reliably prepared at high flow rate, but this was associated with significant reduction of the drug loading (Figure 4-2-B). The highest drug loading was achieved at ratios of 20 % drug/polymer, 5/1 sodium deoxycholate /IDOi and 3/1 aqueous/solvent flow rate. The drug loading and NPs' size at these optimized parameters were 10.1 ± 0.4 % and 80.8 ± 5 nm, respectively. Nanoformulations within this hydrodynamic diameter range have been commonly used for cancer immunotherapy [31], and these conditions were therefore selected and used for subsequent studies. The data demonstrates the remarkable efficiency of hydrophobic ion pairing as it improved the loading of navoximod from less than 1 % to above 10 %. The optimized IDOi nanoformulation was highly monodispersed with a narrow hydrodynamic size distribution and a zeta potential of -23.1 ± 0.5 mV, which might be due to the carboxylate end cap of the polymer (Figure 4-2-C, D). TEM confirmed the monodispersity and spherical morphology of the IDOi NPs (Figure 4-2-E) as well as the size, (71.9 ± 1.6 nm obtained by measuring the size of 60 NPs in ten TEM images).

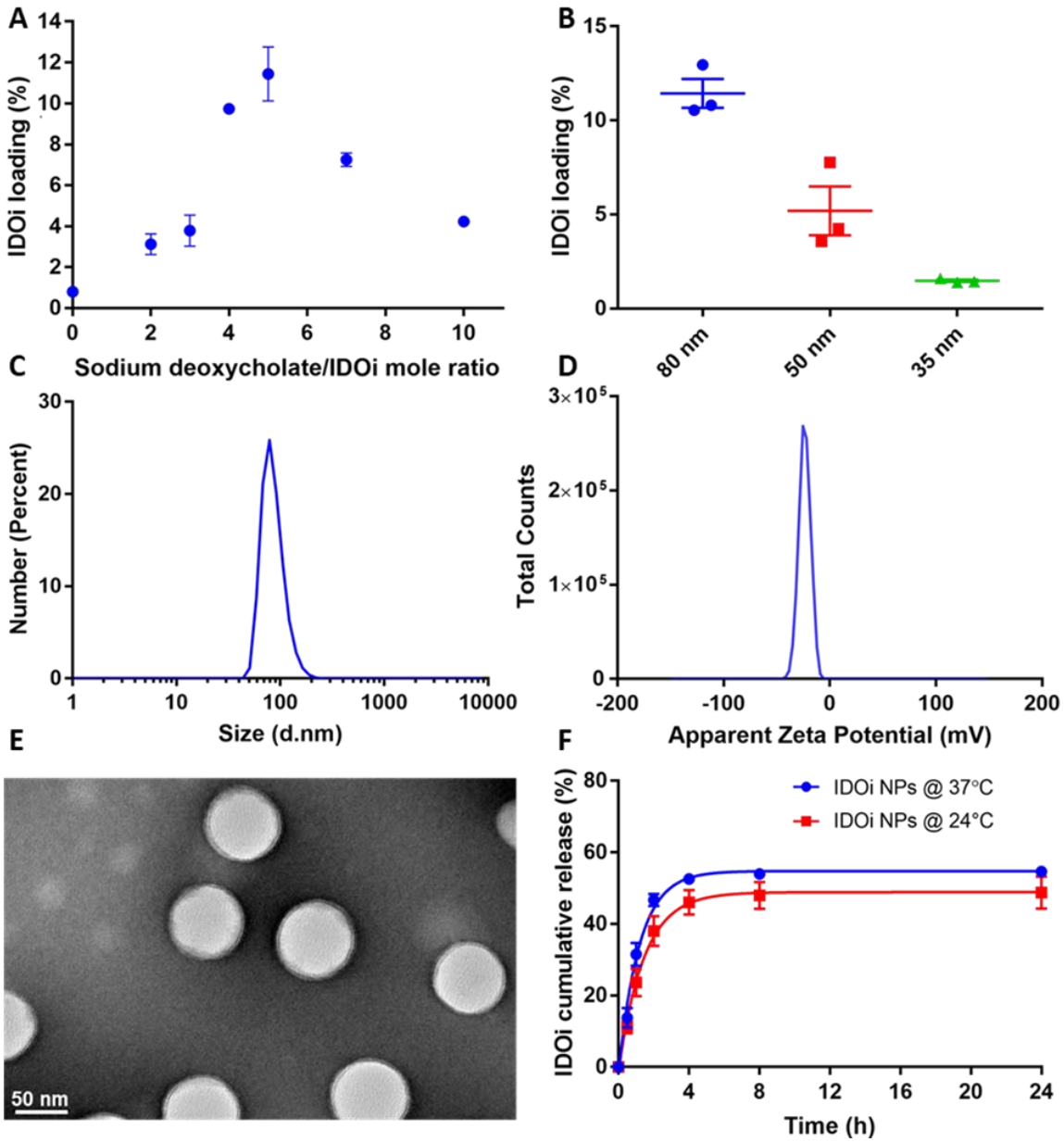

Figure 4-2 Optimization and physicochemical characterization of the IDOi NPs.
Effect of (A) sodium deoxycholate /IDOi molar ratio and (B) NPs' size on IDOi loading. (C) Hydrodynamic diameter and (D) zeta potential of the optimised IDOi nanoformulation. (E) Representative TEM image of the IDOi nanoformulation (scale bar is 50 nm). (F) Cumulative release profile of IDOi nanoformulation over 24 h at 24 °C and 37 °C.

Next, the release of the IDOi from the nanoformulation was determined under sink condition and at temperatures of 37°C and 24°C. As expected the IDOi NPs displayed a biphasic release profile at both temperatures, where a high rate release was observed over the first two hours of the study followed by a slower release phase (Figure 4-2-F). At the 2 h time-point 48.4 % (at 37°C) and 33.8 % (at 24°C) of the drug was released, which can be attributed to the drugs adsorbed on the surface of NPs or were close to the surface [32]. Subsequent time points demonstrated a sustained drug release, where 54.6 % (at 37°C)

and 48.8 % (at 24°C) of drug was released over 24 h. The IDOi NPs demonstrated faster release rate at 37°C compared to 24°C. This can be due to higher diffusion rate of the drug at higher temperatures, which is the main mechanism of drug release in the initial release phase [32].

Altogether, the data validated the use of hydrophobic ion pairing and microfluidic nanoprecipitation towards the preparation of high quality navoximod nanoformulations. Hydrophobic ion pairing is actively being applied for the nanoformulation of small molecule drugs and has been shown to improve drug loading, stability and release profiles [24,33]. In our hand, hydrophobic ion pairing of navoximod with sodium deoxycholate as the pairing agent dramatically improved its loading within the PEG-PLGA NPs. While a variety of approaches have been successfully explored for the formulation of IDO inhibitors, including drug dimerization and conjugation of the drug to polymer or lipid [18,20–22,34], the chemical modification of the IDOi molecules increase the overall complexity of the formulation. The combination of hydrophobic ion pairing and microfluidic nanoprecipitation is therefore promising towards the manufacturing of high quality nanoformulations, especially considering the recent development of GMP compatible microfluidic nanoprecipitation technology.

4.3.2 IDOi NPs effectively inhibits IDO activity

To confirm the efficiency of the IDOi NPs to inhibit the IDO enzyme, an IDO activity assay was performed in the UM-SCC1 cell line used as model of human HNSCC. UM-SCC1 cells were treated with different concentrations of IDOi NP or free IDOi (as a control) and the concentration of kynurenine produced by IDO activity was measured. IDOi NPs efficiently inhibited the activity of IDO with an IC50 of 3.33 µM compared to an IC50 of 6.66 µM for the free IDOi (Figure 4-3-A). This assay also provided an insight into the minimum dose required for *in vitro* biological assays. It also demonstrated that navoximod loading by hydrophobic ion pairing with sodium deoxycholate did not affect its function. This is not surprising as the counter ion interacts with the drug molecule only physically [29]. Likewise, when navoximod was nanoformulated within cyclodexterin, the activity of the drug was not altered compared to the free drug [19]. On the other hand, chemical modification of navoximod was previously shown to be associated with reduction of IDO inhibition [18]. In addition, the effect of the IDOi NPs on the metabolic activity of UM-SCC1 cells was measured by a MTT assay and compared to that of the blank NPs. No changes in the metabolic activity was observed up to 10 µM of IDOi NPs

(Figure 4-3-B). Therefore, 10 µM IDOi NPs was selected as it is above the observed IC50 for inhibition of the IDO activity but did not affect the cancer cell's metabolic activity.

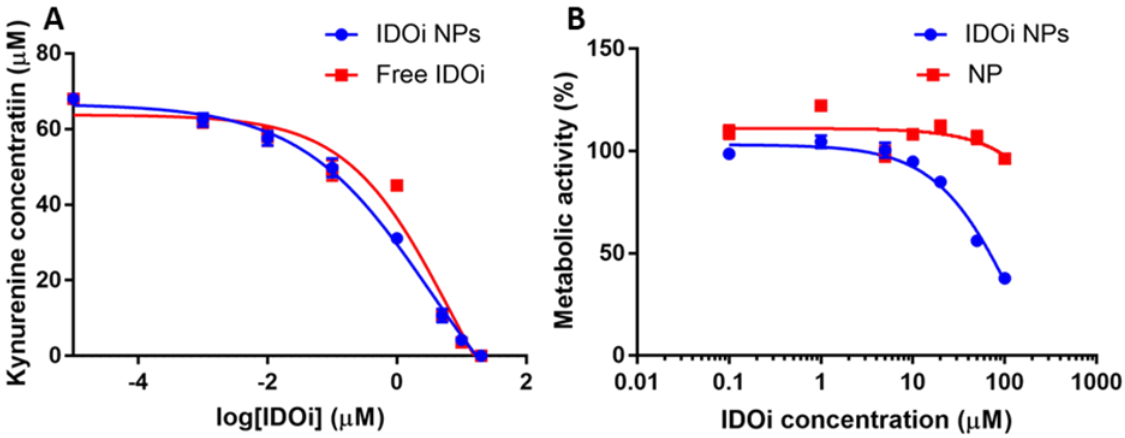

Figure 4-3 Inhibition of IDO enzyme and effect on UM-SCC1 metabolic activity.
A) The effect of IDOi NPs and free navoximod on the inhibition of IDO enzyme in UM-SCC1 cells. (N=5/navoximod concentration. (B) The effect of IDOi NPs and blank NPs on the metabolic activity of UM-SCC1 by MTT assay.

4.3.3 IDOi NP/aPD-1 significantly reduced the immunosuppressive regulatory T-cells and enhanced the cytotoxicity of T-cells

The biological effects of the IDOi nanoformulation as either a single therapy or in combination with aPD-1 to promote ICP inhibitors was next investigated. The main role of IDO inhibition is to reduce the immunosuppressive Treg population. IDO mediated increase of Treg expression is involved in low survivals both in preclinical tumour models and cancer patients [35–38]. Reduction in the number of Treg cells was observed in a preclinical mouse model of pancreatic cancer co-treated by PD-L1 antibodies and self-assembled peptide conjugated navoximod [39]. To investigate the IDOi nanoformulation, the Treg population was analysed by imaging flow cytometry in a T-cells/UM-SCC1 co-culture after IDOi NP treatment. As shown in Figure 4-4-A, blockade of PD-1 receptors by aPD-1, significantly increased the mean fluorescence intensity of Treg cells by 42.7 %. IDOi NPs as a single treatment dramatically decreased the mean fluorescence intensity of Treg cells population by 91.9 %. Similarly, treatment of the co-culture with IDOi NPs in combination with aPD-1 reduced the Treg cells' mean fluorescence intensity by 82.8 % compared to the control (no treatment). This data demonstrates that IDOi NPs efficiently overcome the aPD-1 induced increase in Treg cells. Cytotoxic CD8 T-cells and the ratio of CD8 T-cells/Treg cells are also critical to the anti-tumour activity of the immune system. Treatment with the IDOi NPs alone or in combination with aPD-1

increased the population of CD8 T-cells, which led to higher ratios of CD8 T-cells/Treg cells relative to the no treatment control group (Figure 4-4-B). CD8 T-cells/Treg cells ratios increased to 2.2 and 2.5 upon IDOi NPs and IDOi NPs/aPD-1 treatment, respectively, compared to the ratios of no treatment control (1) and aPD-1 (0.7). These results demonstrate that the combination of IDOi NPs and aPD-1 treatment efficiently mitigated the aPD-1 induced increase of Tregs and increased the ratio of Treg/CD8 cytotoxic T-cells, implicating a role for IDO upregulation. The connection between the PD-1 and IDO pathways is reported to contribute towards resistance to aPD-1 therapy [40].

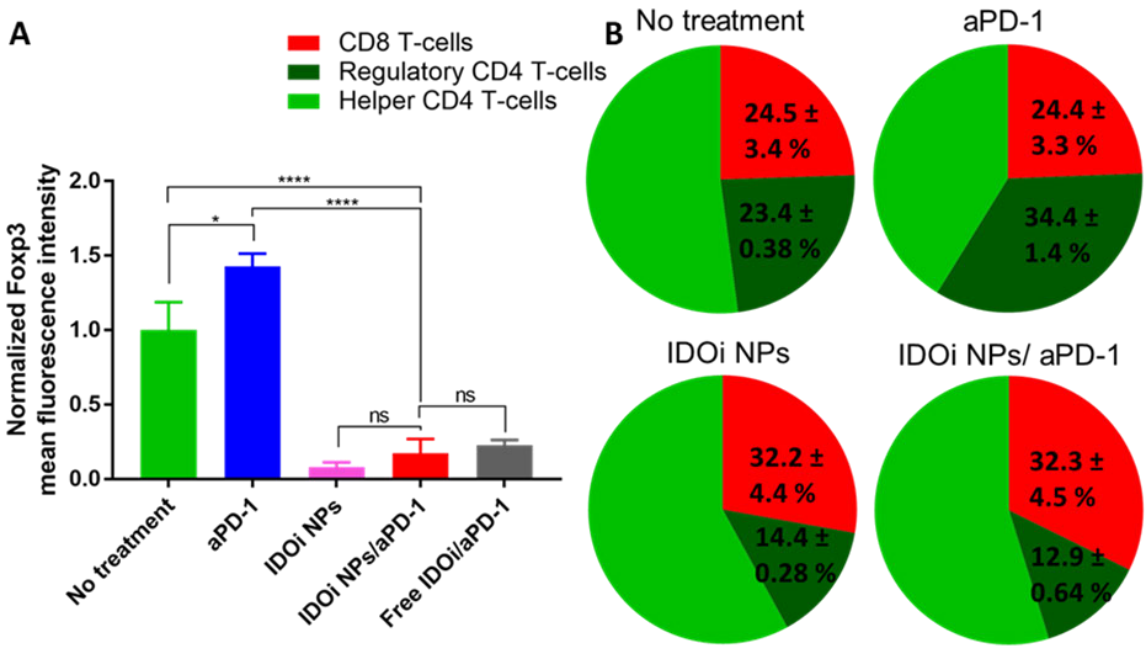

Figure 4-4 Effect of IDOi NPs as single or combination therapy with aPD-1 on immunosuppressive regulatory T-cells.
A) Effect of treatment of co-cultures of activated T-cells and UM-SCC1 cancer cells with aPD-1 (5 µg/mL), IDOi NPs (10 µM), IDOi NPs combined with aPD-1 (10 µM and 5 µg/mL), and free navoximod combined with aPD-1 (10 µM and 5 µg/mL) on regulatory T-cells ($CD3^+CD4^+FoxP3^+$ T-cells). B) Effect of treatment on the populations of cytotoxic CD8 T-cells ($CD3^+CD8^+$ T-cells), regulatory T-cells ($CD3^+CD4^+FoxP3^+$ T-cells) and helper CD4 T-cells ($CD3^+CD4^+FoXP3^-$ T-cells). The cellular markers were measured by imaging flow cytometry after gating for $CD3^+$ single cells. Statistical significance by one-way ANOVA with Tukey post hoc test is indicated as *P<0.05, **P < 0.01, ***P ≤ 0.001 and ****P ≤ 0.0001 and ns indicates not significant.

To investigate the impact of treatment with IDOi NPs and IDOi NP/aPD-1 on T-cell proliferation, T-cells were labelled with the proliferation marker CFSE. aPD-1 treatment decreased proliferation, as observed by a modest increase in the CFSE median fluorescence intensity compared to the untreated cells (4%). This might be due to upregulation of IDO enzyme upon aPD-1 treatment. Consistent with our results, a

previous study observed that aPD-1 treatment increases the Treg cells, which consequently reduced the proliferation of CD8 T-cells [41]. On the other hand, IDO inhibition by the IDOi NPs significantly deceased the T cell CFSE fluorescence intensity (7%, compared to untreated cells), indicating increased T-cell proliferation (Figure 4-5-A). T-cell proliferation was further significantly increased in the case of the dual IDOi NP/aPD-1 therapy (11% vs 7%, $p<0.05$).

In line with the reduced CFSE proliferation result, Ki67 used as a marker of T-cells' proliferation was quantified by imaging flow cytometry. This confirmed that aPD-1 treatment reduced the proliferation of T-cells compared to the untreated cells by decrease of Ki67 median fluorescence intensity (18 % Figure 4-5-B). Although IDOi NPs had no significant effect on fluorescence intensity of Ki67 in T-cells, the IDOi NP/aPD-1 combination therapy significantly increased median fluorescence intensity of Ki67 in T cells by 19 % compared to untreated T-cells, confirming the higher T-cell proliferation observed in the CFSE assay.

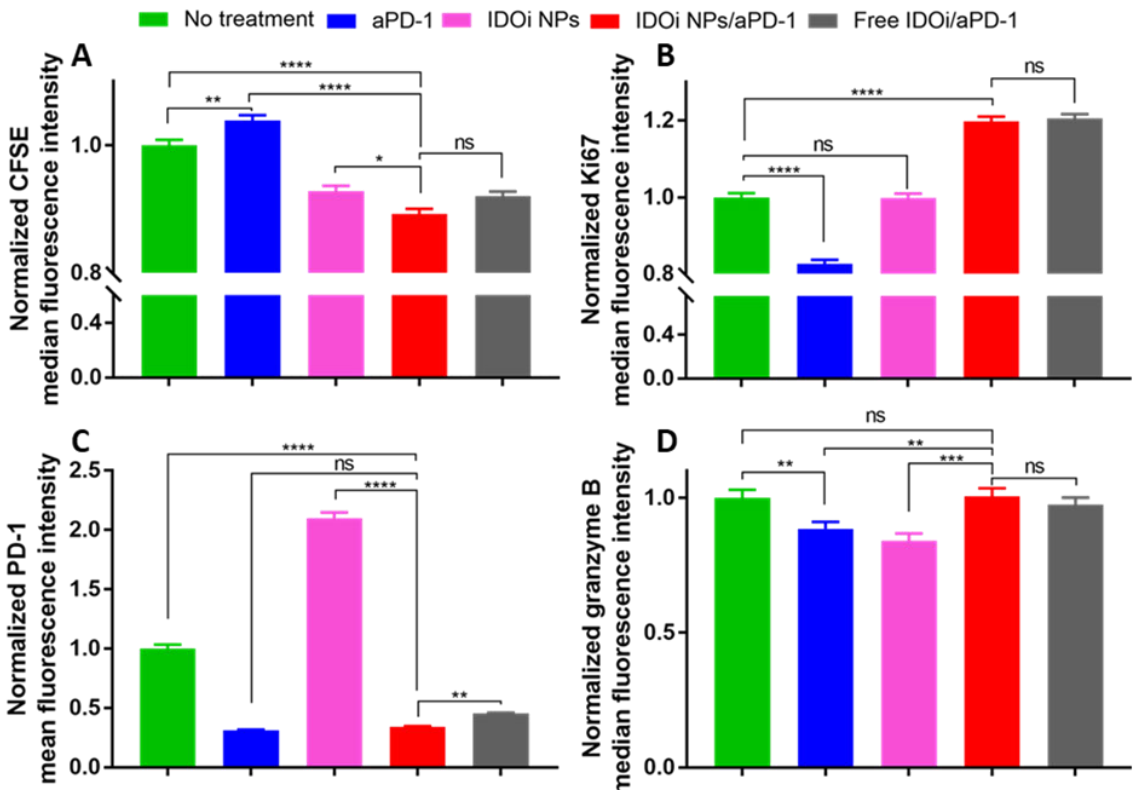

Figure 4-5 Effects of IDOi NPs as a single or combination therapy on the cytotoxic characteristics of T-cells.
A) Proliferation of CFSE labelled T-cells in co-culture of activated T-cells and UM-SCC1 cancer cells treated with aPD-1 (5 µg/mL), IDOi NPs (10 µM), IDOi NPs combined with aPD-1 (10 µM and 5 µg/mL), and free navoximod combined with aPD-1 (10 µM and 5 µg/mL) (48 h after treatment). B) Ki67 expression measured 24 h after treatment. C) Expression of PD-1 receptors in treated T-cells 48 h after treatment. D) Impact of treatment on granzyme B production by T-cells 24 h after treatment. The cellular markers were measured by imaging flow cytometry after gating for $CD3^+$ cells. Statistical significance by one-way

ANOVA with Tukey post hoc test is indicated by *P<0.05, **P < 0.01, ***P ≤ 0.001 and ****P ≤ 0.0001 and ns indicates not significant.

PD-1 receptor expression was next quantified as a marker of T-cell exhaustion. As expected, treatment with aPD-1 effectively inhibited PD-1 receptors and decreased the mean fluorescence intensity of PD-1 receptors by ~69 % (Figure 4-5-C). Interestingly, IDOi NP treatment resulted in a two-fold greater increase in the PD-1 mean fluorescence intensity, demonstrating overexpression of PD-1 receptors, due to increased T-cells cytotoxicity upon IDO inhibition. This observed increase of PD-1 receptors can also implicate the resistance to IDO inhibition single therapy. However, addition of aPD-1 to IDOi NP treatment efficiently inhibited PD-1 receptors, as comparable to aPD-1 single therapy.

Secretion of Granzyme B, which is required for cell lysis and apoptosis is a well-established marker of T cell cytotoxicity [42]. Single treatment with aPD-1 or IDOi NPs induced lower levels of granzyme B^+ T-cells, suggesting overexpression of the alternative ICP following inhibition with either single therapy (Figure 4-5-D). The combination of IDOi NPs and aPD-1 however successfully restored the level of granzyme B^+ T-cells and the cytotoxicity of T-cells (Figure 4-5-D).

It is noteworthy that in all these experiments, the efficacy of IDOi NPs was comparable with that of the free navoximod, confirming that the nanoformulation of the IDOi using hydrophobic ionic pairing had no effect on the stability and activity of the drug.

4.3.4 Improved anti-tumour effects by IDOi NP/aPD-1 combination therapy

To determine the anti-tumour activity of T-cells treated with the IDOi nanoformulation, the apoptosis of the UM-SCC1 cancer cells in the co-culture was investigated by staining for caspase 3/7 (Figure 4-6-A). Treatment of cells by aPD-1 or IDOi NPs as a single therapy increased the population of apoptotic cancer cells by 2 and 2.2 fold respectively, indicating the efficacy of both single treatments to enhance the anti-tumour effects of T-cells (Figure 4-6-B). Remarkably, a synergistic effect was observed in the IDOi NP/ aPD-1combination therapy, which led to a 6.5-fold increase in the number of apoptotic UM-SCC1 cells. Combined treatment with free navoximod and aPD-1 also increased the number of apoptotic UM-SCC1 cells by 5.7-fold (Figure 4-6-B).

We finally investigated the effect of the IDOi nanoformulation on the cell cycle of the UM-SCC1 cells in co-culture with T cells. The shift of cancer cells from the S-G2 to the G1 phase of the cell cycle indicates the efficiency of T-cells therapy in reducing cancer cell proliferation [43]. The cell cycle response of the cancer cells was evaluated by imaging fucci-SCC1 after treatments (Figure 4-6-C, D). Representative images of fucci-SCC1 cells 24 h after treatment are shown, where red cells represent cells in the G1 phase and green cells represent the S-G2 phase of the cell cycle. Upon aPD-1 treatment, the ratio of cells in S-G2/G1 reduced to 0.157 ± 0.018 compared to 0.217 ± 0.016 in the no treatment control group, indicating G1 cell cycle arrest. IDOi NPs had no significant effect on the cell cycle. On the other hand, IDOi NPs/aPD-1 combination therapy significantly reduced the ratio of S-G2 cells/G1 cells to 0.128 ± 0.015 comparable to what was measured for treatment with free navoximod and aPD-1 (0.136 ± 0.011). Although the effect of T-cell on cancer cell cycle arrest was improved by combined IDOi NP/aPD-1 treatment compared to aPD-1 single therapy, the difference was not statistically significant.

The observed increase in T-cell proliferation, and cancer cell apoptosis and cell cycle arrest indicates the efficiency of the combined IDOi NPs/aPD-1 therapy in enhancing T-cell cytotoxicity against cancer cells. Combination therapy of IDOi and inhibitors of the PD-1/PD-L1 pathway was associated with improved anti-tumour responses in several studies, which led to investigation of this approach in several clinical trials. However, dual therapies were associated with only modest and therefore unsatisfactory results [38]. We anticipate that improving the biodistribution of IDOi through the use of a nanoformulation with high navoximod payload will increase oncological control as well as improve toxicity profile [44].

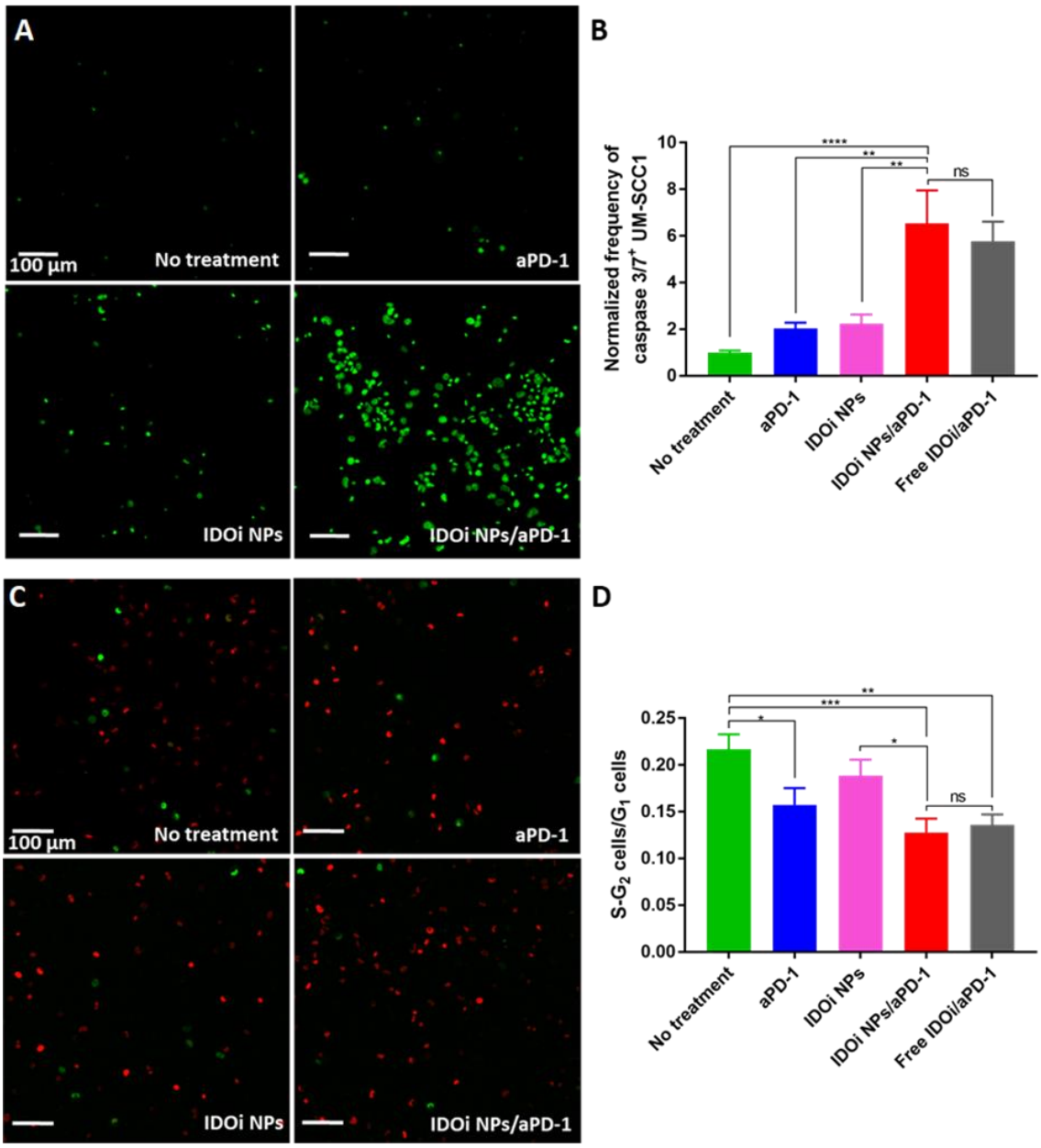

Figure 4-6 Effect of IDOi NPs as a single or combination therapy with aPD-1 on the activity of T-cells against UM-SCC1 cells.
A) Representative images and (B) quantification of caspase 3/7 activated UM-SCC1 cells co-cultured for 24 h with T cells after treatment with aPD-1 (5 µg/mL), IDOi NPs (10 µM), IDOi NPs combined with aPD-1 (10 µM and 5 µg/mL), and free navoximod combined with aPD-1 (10 µM and 5 µg/mL). C) Representative images and (D) quantification of fucci-SCC1 cell cycle after treatment. Red cells are in the G1 phase / green cells are in the S /G2 phase. In all images the scale bar is 100 µm. Cell population were quantified by counting 10 images/group taken from different areas of well plate by NIS-Elements software (Nikon, Japan). Statistical significance is indicated by asterisk as *P<0.05, **P < 0.01, ***P ≤ 0.001 and ****P ≤ 0.0001 and ns indicates not significant.

4.4 Conclusion

A navoximod nanoformulation was developed towards addressing the biodistribution limitation of current approach. Hydrophobic ion pairing of the IDOi with sodium deoxycholate efficiently overcome the difficulty of loading the drug within PEG-PLGA NPs prepared using a 3D printed high throughput nanoprecipitation microfluidic device.

This combined approach enabled the reproducible preparation of PEG-PLGA nanoparticles with remarkably high navoximod loading (>10%) and hydrodynamic diameters ~80 nm. The navoximod nanoformulation efficiently inhibited the IDO enzyme in a HNSCC cell line and, in combination with aPD-1, significantly enhanced the cytotoxicity and anti-tumour effects of T-cells. Based on this promising *in vitro* assessment of the IDOi NPs, further studies are underway to determine the efficacy of nanoformulation in an orthotopic murine model of head and neck cancer.

4.5 References

[1] J. Couzin-Frankel, Cancer immunotherapy, Science (80-.). 342 (2013) 1432–1433. https://doi.org/10.1126/science.342.6165.1432.

[2] M.A. Postow, M.K. Callahan, J.D. Wolchok, Immune checkpoint blockade in cancer therapy, J. Clin. Oncol. 33 (2015) 1974. https://doi.org/10.1200/JCO.2014.59.4358.

[3] K.M. Mahoney, G.J. Freeman, D.F. McDermott, The next immune-checkpoint inhibitors: Pd-1/pd-l1 blockade in melanoma, Clin. Ther. (2015). https://doi.org/10.1016/j.clinthera.2015.02.018.

[4] A. Ribas, J.D. Wolchok, Cancer immunotherapy using checkpoint blockade, Science (80-.). 359 (2018) 1350–1355. https://doi.org/10.1126/science.aar4060.

[5] E.I. Buchbinder, A. Desai, CTLA-4 and PD-1 pathways similarities, differences, and implications of their inhibition, Am. J. Clin. Oncol. Cancer Clin. Trials. 39 (2016) 98–106. https://doi.org/10.1097/COC.0000000000000239.

[6] R.M. Wong, R.B. Cameron, Immune Checkpoint Blockade and Adaptive Immune Resistance in Cancer, in: Immunother. - Myth. Reality, Ideas, Futur., 2017: pp. 47–61. https://doi.org/10.5772/66494.

[7] D.H. Munn, A.L. Mellor, IDO in the Tumor Microenvironment: Inflammation, Counter-Regulation, and Tolerance, Trends Immunol. 37 (2016) 193–207. https://doi.org/10.1016/j.it.2016.01.002.

[8] Q. Ye, C. Wang, J. Xian, M. Zhang, Y. Cao, Y. Cao, Expression of programmed cell death protein 1 (PD-1) and indoleamine 2,3-dioxygenase (IDO) in the tumor microenvironment and in tumor-draining lymph nodes of breast cancer, Hum. Pathol. 75 (2018) 81–90. https://doi.org/10.1016/j.humpath.2018.02.004.

[9] A. Botticelli, B. Cerbelli, L. Lionetto, I. Zizzari, M. Salati, A. Pisano, M. Federica, M. Simmaco, M. Nuti, P. Marchetti, Can IDO activity predict primary resistance to anti-PD-1 treatment in NSCLC?, J. Transl. Med. 16 (2018) 1–6. https://doi.org/10.1186/s12967-018-1595-3.

[10] J.L. Adams, J. Smothers, R. Srinivasan, A. Hoos, Big opportunities for small molecules in immuno-oncology, Nat. Rev. Drug Discov. 14 (2015) 603–622. https://doi.org/10.1038/nrd4596.

[11] G.C. Prendergast, W.P. Malachowski, J.B. DuHadaway, A.J. Muller, Discovery of IDO1 Inhibitors: From bench to bedside, Cancer Res. 77 (2017) 6795–6811. https://doi.org/10.1158/0008-5472.CAN-17-2285.

[12] A. Nayak, Z. Hao, R. Sadek, N. Vahanian, W. Ramsey, E. Kennedy, M. Mautino, C. Link, P. Bourbo, R. Dobbins, K. Adams, A. Diamond, L. Marshall, D.H. Munn, J. Janik, S.N. Khleif, A Phase I study of NLG919 for adult patients with recurrent advanced solid tumors, J. Immunother. Cancer. 2 (2014) P250. https://doi.org/10.1186/2051-1426-2-s3-p250.

[13] T. Ebata, T. Shimizu, Y. Fujiwara, K. Tamura, S. Kondo, S. Iwasa, K. Yonemori, A. Shimomura, S. Kitano, T. Koyama, N. Sato, K. Nakai, M. Inatani, N. Yamamoto, Phase I study of the indoleamine 2,3-dioxygenase 1 inhibitor navoximod (GDC-0919) as monotherapy and in combination with the PD-L1 inhibitor atezolizumab in Japanese patients with advanced solid tumours, Invest. New Drugs. 38 (2020) 468–477. https://doi.org/10.1007/s10637-019-00787-3.

[14] Z. Zeng, C. Zhang, J. Li, D. Cui, Y. Jiang, K. Pu, Activatable Polymer Nanoenzymes for Photodynamic Immunometabolic Cancer Therapy, Adv. Mater. 33 (2021) 2007247. https://doi.org/10.1002/adma.202007247.

[15] K. Cheng, Y. Ding, Y. Zhao, S. Ye, X. Zhao, Y. Zhang, T. Ji, H. Wu, B. Wang, G.J. Anderson, L. Ren, G. Nie, Sequentially Responsive Therapeutic Peptide Assembling Nanoparticles for Dual-Targeted Cancer Immunotherapy, Nano Lett. 18 (2018) 3250–3258. https://doi.org/10.1021/acs.nanolett.8b01071.

[16] K.H. Jung, P. LoRusso, H. Burris, M. Gordon, Y.J. Bang, M.D. Hellmann, A. Cervantes, M. Ochoa de Olza, A. Marabelle, F. Stephen Hodi, M.J. Ahn, L.A. Emens, F. Barlesi, O. Hamid, E. Calvo, D. McDermott, H. Soliman, I. Rhee, R. Lin, T. Pourmohamad, J. Suchomel, A. Tsuhako, K. Morrissey, S. Mahrus, R. Morley, A. Pirzkall, S. Lindsey Davis, Phase I study of the indoleamine 2,3-dioxygenase 1 (IDO1) inhibitor navoximod (GDC-0919) administered with PD-L1 inhibitor (atezolizumab) in

advanced solid tumors, Clin. Cancer Res. 25 (2019) 3220–3228. https://doi.org/10.1158/1078-0432.CCR-18-2740.

[17] Y. Liu, Y. Lu, X. Zhu, C. Li, M. Yan, J. Pan, G. Ma, Tumor microenvironment-responsive prodrug nanoplatform via co-self-assembly of photothermal agent and IDO inhibitor for enhanced tumor penetration and cancer immunotherapy, Biomaterials. 242 (2020) 119933. https://doi.org/10.1016/j.biomaterials.2020.119933.

[18] Y. Chen, R. Xia, Y. Huang, W. Zhao, J. Li, X. Zhang, P. Wang, R. Venkataramanan, J. Fan, W. Xie, X. Ma, B. Lu, S. Li, An immunostimulatory dual-functional nanocarrier that improves cancer immunochemotherapy, Nat. Commun. 7 (2016) 1–12. https://doi.org/10.1038/ncomms13443.

[19] J. Xu, X. Ren, T. Guo, X. Sun, X. Chen, L.H. Patterson, H. Li, J. Zhang, NLG919/cyclodextrin complexation and anti-cancer therapeutic benefit as a potential immunotherapy in combination with paclitaxel, Eur. J. Pharm. Sci. 138 (2019) 105034. https://doi.org/10.1016/j.ejps.2019.105034.

[20] B. Feng, F. Zhou, B. Hou, D. Wang, T. Wang, Y. Fu, Y. Ma, H. Yu, Y. Li, Binary Cooperative Prodrug Nanoparticles Improve Immunotherapy by Synergistically Modulating Immune Tumor Microenvironment, Adv. Mater. 30 (2018) 1803001. https://doi.org/10.1002/adma.201803001.

[21] J. Lu, X. Liu, Y.P. Liao, X. Wang, A. Ahmed, W. Jiang, Y. Ji, H. Meng, A.E. Nel, Breast Cancer Chemo-immunotherapy through Liposomal Delivery of an Immunogenic Cell Death Stimulus Plus Interference in the IDO-1 Pathway, ACS Nano. 12 (2018) 11041–11061. https://doi.org/10.1021/acsnano.8b05189.

[22] A.E. Nel, H. Meng, K.C. Mei, Y.P. Liao, J. Jiang, M. Chiang, M. Khazaieli, X. Liu, X. Wang, Q. Liu, C. Hyun Chang, X. Zhang, J. Li, Y. Ji, B. Melano, D. Telesca, T. Xia, Liposomal delivery of mitoxantrone and a cholesteryl indoximod prodrug provides effective chemo-immunotherapy in multiple solid tumors, ACS Nano. 14 (2020) 13343–13366. https://doi.org/10.1021/acsnano.0c05194.

[23] Q. Li, J. Liu, H. Fan, L. Shi, Y. Deng, L. Zhao, M. Xiang, Y. Xu, X. Jiang, G. Wang, L. Wang, Z. Wang, IDO-inhibitor potentiated immunogenic chemotherapy abolishes primary tumor growth and eradicates metastatic lesions by targeting distinct

compartments within tumor microenvironment, Biomaterials. 269 (2020) 120388. https://doi.org/10.1016/j.biomaterials.2020.120388.

[24] Y.H. Song, E. Shin, H. Wang, J. Nolan, S. Low, D. Parsons, S. Zale, S. Ashton, M. Ashford, M. Ali, D. Thrasher, N. Boylan, G. Troiano, A novel in situ hydrophobic ion paring (HIP) formulation strategy for clinical product selection of a nanoparticle drug delivery system, J. Control. Release. 229 (2016) 106–119. https://doi.org/10.1016/j.jconrel.2016.03.026.

[25] F. Danhier, E. Ansorena, J.M. Silva, R. Coco, A. Le Breton, V. Préat, PLGA-based nanoparticles: An overview of biomedical applications, J. Control. Release. 161 (2012) 505–522. https://doi.org/10.1016/j.jconrel.2012.01.043.

[26] F.S.T. Mirakabad, K. Nejati-Koshki, A. Akbarzadeh, M.R. Yamchi, M. Milani, N. Zarghami, V. Zeighamian, A. Rahimzadeh, S. Alimohammadi, Y. Hanifehpour, S.W. Joo, PLGA-based nanoparticles as cancer drug delivery systems, Asian Pacific J. Cancer Prev. 15 (2014) 517–535. https://doi.org/10.7314/APJCP.2014.15.2.517.

[27] X. Li, X. Jiang, Microfluidics for producing poly (lactic-co-glycolic acid)-based pharmaceutical nanoparticles, Adv. Drug Deliv. Rev. 128 (2018) 101–114. https://doi.org/10.1016/j.addr.2017.12.015.

[28] S. Rezvantalab, N.I. Drude, M.K. Moraveji, N. Güvener, E.K. Koons, Y. Shi, T. Lammers, F. Kiessling, PLGA-based nanoparticles in cancer treatment, Front. Pharmacol. 9 (2018) 1260. https://doi.org/10.3389/fphar.2018.01260.

[29] K.D. Ristroph, R.K. Prud'homme, Hydrophobic ion pairing: Encapsulating small molecules, peptides, and proteins into nanocarriers, Nanoscale Adv. 1 (2019) 4207–4237. https://doi.org/10.1039/c9na00308h.

[30] A. Sakaue-Sawano, T. Kobayashi, K. Ohtawa, A. Miyawaki, Drug-induced cell cycle modulation leading to cell-cycle arrest, nuclear mis-segregation, or endoreplication, BMC Cell Biol. 12 (2011) 1–12. https://doi.org/10.1186/1471-2121-12-2.

[31] M. Yang, J. Li, P. Gu, X. Fan, The application of nanoparticles in cancer immunotherapy: Targeting tumor microenvironment, Bioact. Mater. 6 (2021) 1973–1987. https://doi.org/10.1016/j.bioactmat.2020.12.010.

[32] S. Fredenberg, M. Wahlgren, M. Reslow, A. Axelsson, The mechanisms of drug release in poly(lactic-co-glycolic acid)-based drug delivery systems - A review, Int. J. Pharm. 415 (2011) 34–52. https://doi.org/10.1016/j.ijpharm.2011.05.049.

[33] S. Ashton, Y.H. Song, J. Nolan, E. Cadogan, J. Murray, R. Odedra, J. Foster, P.A. Hall, S. Low, P. Taylor, R. Ellston, U.M. Polanska, J. Wilson, C. Howes, A. Smith, R.J.A. Goodwin, J.G. Swales, N. Strittmatter, Z. Takáts, A. Nilsson, P. Andren, D. Trueman, M. Walker, C.L. Reimer, G. Troiano, D. Parsons, D. De Witt, M. Ashford, J. Hrkach, S. Zale, P.J. Jewsbury, S.T. Barry, Aurora kinase inhibitor nanoparticles target tumors with favorable therapeutic index in vivo, Sci. Transl. Med. 8 (2016) 325ra17. https://doi.org/10.1126/scitranslmed.aad2355.

[34] S. Yu, C. Wang, J. Yu, J. Wang, Y. Lu, Y. Zhang, X. Zhang, Q. Hu, W. Sun, C. He, X. Chen, Z. Gu, Injectable Bioresponsive Gel Depot for Enhanced Immune Checkpoint Blockade, Adv. Mater. 30 (2018) 1801527. https://doi.org/10.1002/adma.201801527.

[35] D.A. Wainwright, I. V. Balyasnikova, A.L. Chang, A.U. Ahmed, K.S. Moon, B. Auffinger, A.L. Tobias, Y. Han, M.S. Lesniak, IDO expression in brain tumors increases the recruitment of regulatory T cells and negatively impacts survival, Clin. Cancer Res. 18 (2012) 6110–6121. https://doi.org/10.1158/1078-0432.CCR-12-2130.

[36] J.R. Brody, C.L. Costantino, A.C. Berger, T. Sato, M.P. Lisanti, C.J. Yeo, R. V. Emmons, A.K. Witkiewicz, Expression of indoleamine 2,3-dioxygenase in metastatic malignant melanoma recruits regulatory T cells to avoid immune detection and affects survival, Cell Cycle. 8 (2009) 1930–1934. https://doi.org/10.4161/cc.8.12.8745.

[37] S. Salmi, A. Lin, B. Hirschovits-Gerz, M. Valkonen, N. Aaltonen, R. Sironen, H. Siiskonen, S. Pasonen-Seppänen, The role of FoxP3+ regulatory T cells and IDO+ immune and tumor cells in malignant melanoma – an immunohistochemical study, BMC Cancer. 21 (2021) 1–13. https://doi.org/10.1186/s12885-021-08385-4.

[38] Y. Yao, H. Liang, X. Fang, S. Zhang, Z. Xing, L. Shi, C. Kuang, B. Seliger, Q. Yang, What is the prospect of indoleamine 2,3-dioxygenase 1 inhibition in cancer? Extrapolation from the past, J. Exp. Clin. Cancer Res. (2021) 1–14. https://doi.org/10.1186/s13046-021-01847-4.

[39] X. Han, K. Cheng, Y. Xu, Y. Wang, H. Min, Y. Zhang, X. Zhao, R. Zhao, G.J. Anderson, L. Ren, G. Nie, Y. Li, Modularly Designed Peptide Nanoprodrug Augments Antitumor Immunity of PD-L1 Checkpoint Blockade by Targeting Indoleamine 2,3-Dioxygenase, J. Am. Chem. Soc. 142 (2020) 2490–2496. https://doi.org/10.1021/jacs.9b12232.

[40] J. Cai, Q. Qi, X. Qian, J. Han, X. Zhu, Q. Zhang, R. Xia, The role of PD-1/PD-L1 axis and macrophage in the progression and treatment of cancer, J. Cancer Res. Clin. Oncol. 145 (2019) 1377–1385. https://doi.org/10.1007/s00432-019-02879-2.

[41] T. Kamada, Y. Togashi, C. Tay, D. Ha, A. Sasaki, Y. Nakamura, E. Sato, S. Fukuoka, Y. Tada, A. Tanaka, H. Morikawa, A. Kawazoe, T. Kinoshita, K. Shitara, S. Sakaguchi, H. Nishikawa, PD-1+ regulatory T cells amplified by PD-1 blockade promote hyperprogression of cancer, Proc. Natl. Acad. Sci. U. S. A. 116 (2019) 9999–10008. https://doi.org/10.1073/pnas.1822001116.

[42] X. Qian, Z. Shi, H. Qi, M. Zhao, K. Huang, D. Han, J. Zhou, C. Liu, Y. Liu, Y. Lu, X. Yuan, J. Zhao, C. Kang, A novel Granzyme B nanoparticle delivery system simulates immune cell functions for suppression of solid tumors, Theranostics. 9 (2019) 7616. https://doi.org/10.7150/thno.35900.

[43] J.L. Bandura, B.R. Calvi, Duplication of the genome in normal and cancer cell cycles, Cancer Biol. Ther. 1 (2002) 8–13. https://doi.org/10.4161/cbt.1.1.31.

[44] Y. Guo, Y. Liu, W. Wu, D. Ling, Q. Zhang, P. Zhao, X. Hu, Indoleamine 2, 3-dioxygenase (Ido) inhibitors and their nanomedicines for cancer immunotherapy, Biomaterials. 276 (2021) 121018. https://doi.org/10.1016/j.biomaterials.2021.121018.

Chapter 5

Development of a Glycogen Kinase 3 Inhibitor Nanoformulation as an Alternative Strategy to Inhibit PD-1 Immune Checkpoint

5 Development of a Glycogen kinase 3 inhibitor nanoformulation as an alternative strategy to inhibit PD-1 immune checkpoint

5.1 Introduction

Immune checkpoint (ICP) inhibitors, such as programmed death-1 (PD-1) antibodies (aPD-1) have changed the paradigm of cancer therapy by improving the anti-tumour activity of immune cells, leading to durable responses [1]. However, limited response rates and high off-target toxicity have hampered clinical application of aPD-1 immunotherapy [2–4]. A possible mechanism for the relative lack of efficiency is that tumour associated macrophages recognize the Fc region of the aPD-1 antibodies and uptake them after administration, thus reducing the effective tumour antibody dose [5]. The Fc antibody region is not only involved in clearance of aPD-1, it can also increase immunogenic adverse effects [6]. Small molecule inhibitors of the PD-1 pathway have emerged as promising alternatives to antibodies on the bases of lower costs of production, increased formulation stability, lower immunogenicity, and potentially higher tumour penetration [7–9].

Glycogen synthase kinase 3 (GSK3) is a serine/threonine protein kinase involved in several cellular pathways including cell cycle, proliferation and apoptosis [10]. GSK3 is constitutively expressed in resting T-cells but becomes inactivated upon T-cell activation, leading to clonal expansion of cytotoxic T-lymphocytes [11,12]. However, this clonal expansion of activated T-cells is transient and associated with rapid cytokine loss and activated T-cell death. The pivotal role of GSK3 as an upstream regulator of PD-1 gene expression has been appraised in recent years [12]. Inhibitors of GSK3 (GSK3i) have therefore been investigated as substitutes for aPD-1 [10]. The GSK3i SB415286 was shown to upregulate the transcription of T-bet gene (Tbx-21), resulting in the downregulation of Pdcd1 transcription and PD-1 expression. Conversely, GSK3 inhibition efficiently lowered PD-1 expression, increased cytotoxic T-cells proliferation and survival, and induced long-term memory in T-cells [13].

Nevertheless, the delivery of small molecule drugs is challenging due to their short half-life and high distribution in off-target organs, which can lead to significant off-target toxicities, as observed in clinical trials of GSK3i for Alzheimer's disease [14,15]. Nanoparticles (NPs) have been actively explored to improve the biodistribution and

tumour accumulation of small molecules. Lipid coated mesoporous silica NPs were used to encapsulate the GSK3i AZD1080. This nanoformulation improved the tumour concentration of GSK3i and increased the anti-tumour responses, reducing tumour size and enhancing the number of cytotoxic T-cells in colon, pancreas and lung tumour models [16]. Among nanocarriers under investigation for the delivery of drugs to solid tumours, poly(ethylene glycol)-poly(lactide-co-glycolide) (PEG-PLGA) NPs have been extensively investigated including in early stage clinical trials [17–19]. PEG-PLGA NPs have been shown to increase the circulation time and tumour accumulation of several small molecules in pre-clinical models [20,21]. PEG-PLGA based drug nanocarriers present several significant advantageous features. First, both PEG and PLGA have a long history of safe use in humans. Second, PEG-PLGA NPs with acceptably high drug payload can be readily prepared using nanoprecipitation of the copolymers.

Straightforward and highly reproducible nanocarrier manufacturing processes compatible with large-scale production is required towards their routine implementation, which is an often-underestimated challenge in the nanomedicine field. Microfluidic based nanoprecipitation approaches have emerged as substitutes for conventional bulk mixing strategies, enabling the continuous and reproducible preparation of monodispersed NPs including PEG-PLGA based NPs [22]. Different microfluidic designs have been proposed and validated for the preparation of several types of NPs [23,24].

Another important consideration towards the design of a successful delivery system is the ability to both efficiently encapsulate the bioactive payload and minimise its burst release. However, the physicochemical properties of therapeutics, such as the hydrophobicity and molecular weight, are not always suitable for their efficient loading within nanocarriers formed by nanoprecipitation. To address this challenge, innovative strategies such as hydrophobic ion pairing are being increasingly used. The hydrophobic ion pairing of small molecular drug with suitable pairing agent increases its hydrophobicity and therefore affinity with the polymeric core of the nanoprecipitated carriers, and have been successfully employed to improve loading, stability and release [25,26].

Towards the development of a high performance GSK3i nanoformulation, we optimised the loading of SB415286 within PEG-PLGA NPs using the hydrophobic ion pairing strategy and a 3D printed microfluidic nanoprecipitation device. To demonstrate its biological activity, we investigated the efficacy of the nanoformulation in inhibiting the

PD-1 expression of chimeric antigen receptor (CAR)-T cells and in inducing memory response against human colorectal carcinoma cells.

5.2 Materials and method

5.2.1 Materials

PLGA (10-15 KDa) and methoxy-PEG-PLGA (PEG-PLGA) (2-15 KDa) were purchased from PoliSciTech (USA). Acetonitrile and sodium deoxycholate were obtained from Sigma Aldrich (USA). SB415286 was purchased from MedChemExpress (USA). Recombinant human IL-15, IL-7 IL-2 were purchased from Peprotech (USA).

5.2.2 Cell culture

Leucine-rich repeat-containing G-protein coupled receptor 5 (LGR5) targeting human CAR-T cells were generously provided by Carina Biotech (Australia). These cells were cultured in X-VIVO^{TM} 15 media (Lonza biosciences, USA) supplemented by 5 % heat inactivated human serum (Sigma, USA), 1 ng/mL IL-15 and 5 ng/mL IL-7. The human colorectal carcinoma LIM1215 cell line was obtained from the Ludwig Institute for Cancer Research (Australia). LIM1215 cells were cultured in complete RPMI media (Gibco, UK), supplemented with 10% FBS, 1% streptomycin/penicillin (Gibco, UK (Gibco, UK) and 1% L-glutamine (Gibco, UK). The Lenti-TCF-NL-UBC-FL transduced HEK293T cells, which constitutively express firefly luciferase and express NanoLuc® by induction of Wnt, [27] were supplied by Dr Susan Woods (The University of Adelaide). The HEK293T cells were cultured in complete DMEM media (Gibco, UK) supplemented with 10% FBS, 1% streptomycin/penicillin and 1% L-glutamine. Cells were subcultured at 80 % confluency by 0.25% trypsin-EDTA (Gibco, UK). All cells were maintained in a humidifying incubator (90% humidity and 5% CO2) at 37˚C.

5.2.3 Preparation of GSK3i loaded PEG-PLGA NPs

PEG-PLGA NPs were prepared using a 3D printed microfluidic-based mixing device (Figure 5-1-A). The chip was fabricated using a MiiCraft 3D printer (Rays Optics, Canada) with width and height of 0.6 mm and 1.1 mm, respectively. The nanoprecipitation device design enable the introduction of both aqueous and polymer solvent phases via two inlets, which are mixed in a herringbone structured mixing channel to nano-precipitate the polymers/drugs and form the nanocarriers in highly reproducible conditions. To prepare GSK3i NPs, sodium deoxycholate and GSK3i solutions in ethanol

were premixed with a two to one molar ratio (sodium deoxycholate to GSK3i) and added to 10 mg/mL of the polymer mixture in acetonitrile (50 % PLGA and 50 % PEG-PLGA). A 20 % (w/w) SB415286 / polymer was used. The flow rates of the aqueous and solvent phases were controlled by two syringe pumps (Chemyx fusion 200, USA) and kept at 3/1 mL/min. The GSK3i NPs were centrifuged and washed at 24000 g for 15 min at 4 °C and redispersed in Milli-Q® water for further characterization.

5.2.4 Physicochemical characterization of GSK3i NPs

The hydrodynamic size of the GSK3i NPs dispersed in Milli-Q® water was measured using dynamic light scattering with a Zetasizer 3000 HS, Malvern Instruments Ltd. Particle size stability when stored at room temperature in 1x Phosphate-Buffered Saline (PBS) or Milli-Q® water was monitored over two weeks. The zeta potential of the NPs was also measured via the zetasizer in Milli-Q® water. The NPs morphology was observed using a JEM-2100F-HR transmission electron microscope (TEM) (JEOL, Japan) after negative staining with 2% phosphotungstic acid in water.

The GSK3i loading within the NPs was determined by a reversed phase high-performance liquid chromatography (HPLC) method on an Agilent 1200 HPLC system (Agilent Technologies, USA). GSK3i NPs were centrifuged and the pellet was dissolved in acetonitrile and injected into the system. The Eclipse Plus C18 column of 4.6 x 100 mm, 3.5 µm and a gradient method for the mobile phase, consisting of water and HPLC grade methanol with 0.1 % formic acid (Sigma, USA) were used. A gradient of mobile phase was pumped at a flow rate of 2 mL/min and initiated with 90 % water and 10 % methanol which changed to 10 % water and 90 % methanol over 10 min. The drug absorbance was detected by DAD UV-Vis detector at 391 nm. To quantify the sample, a standard curve of GSK3i in acetonitrile (0.5 µg/mL to 50 µg/mL) was prepared. The drug loading was calculated using the following equation. $\text{Drug loading} = \frac{\text{Mass of loaded GSK3i}}{\text{Mass of GSK3i NPs}} \times 100$. The mass of GSK3i NP was measured after freeze drying the NPs by Modulyo® freeze dryer (Thermo Fisher Scientific Inc., USA).

5.2.5 GSK3i NPs activity through the Wnt/β-catenin pathway

GSK3i NPs function on the Wnt/β-catenin pathway was assessed using the lenti-TCF-NL-UBC-FL HEK293T reporter cells, which constitutively express firefly luciferase and express NanoLuc® by induction of Wnt/β-catenin pathway [27]. Cells ($5x10^4$) were seeded in a 48-well plate and incubated overnight. Cells were then treated in triplicate by

an equivalent dose of 20 µM SB415286 with the GSK3i NPs or free SB415286 or left untreated as control. After 24h, the cell culture media was removed and the cells were lysed by addition of 50 µL passive lysis buffer (Promega, USA). The Nano-Glo® Dual-Luciferase® Reporter Assay (Promega) was used to measure the luminescence of induced NanoLuc® luciferase using a FLUOstar OPTIMA plate reader (BMG Labtech, USA), as per the manufacturers protocol. The luminescence of firefly luciferase was measured as the internal control and the ratio of NanoLuc® luciferase/ firefly luciferase (NLuc/FLuc) was determined.

5.2.6 CAR-T cell assay for antigen specific activation of T-cells for PD-1 upregulation

Co-cultures of LGR5 specific CAR-T cells (Carina biotech) and human colorectal carcinoma cell line LIM1215, which overexpress LGR5 [28] were utilised to stimulate T-cells for PD-1 upregulation. LGR5 is a protein overexpressed on many cancers especially colorectal carcinoma which is associated with poor patients' prognosis [29]. LIM1215 cells were seeded at 250,000 cells/well in 24-well plates in complete RPMI media and incubated overnight. The cell culture media was changed to complete RPMI supplemented with 1 ng/mL IL-15 and 5 ng/mL IL-7, and CAR-T cells were added at 500,000 cells/well (2:1 ratio T-cells to cancer cells). The basal level of PD-1 expression was determined by seeding the CAR-T cells without LIM1215 cells. Untransduced human T-cells (from Carina Biotech) were used as a control to validate the antigen specific activation of the CAR-T cells and seeded with/without LIM1215 cells. Cells were co-cultured for two days, after which, the T-cells were harvested and stained for CD3 and PD-1 markers (BV421 CD3 and PE PD-1 human antibodies, BioLegend, USA) and analysed by an imaging flow cytometer, Image Stream X (AMNIS, USA). The IDEAS® 6.2 (EMD Millipore, USA) and FlowJo V10 (FlowJo, USA) software were used for data analysis.

5.2.7 PD-1 receptor expression and T-cell proliferation

Co-cultures of CAR-T cells and LIM1215 cells as described above were treated with 20 µM GSK3i NPs or free GSK3i (as a positive control), and PD-1 expression was measured, two days after treatment. CAR-T cells were harvested and washed by PBS and stained using BV421 CD3, PE PD-1, FITC CD4 and PerCP Cy5.5 CD8 human antibodies (BioLegend, USA) and analysed by imaging flow cytometry. The percentages of viable

CAR-T cells were quantified by counting the cells on a Bright-Line™ hemocytometer (Sigma, USA) by trypan blue exclusion assay (Sigma, USA).

5.2.8 CAR-T cell phenotype characteristics

The distribution of the CAR-T cells phenotype subsets, namely naïve $CCR7^+$ $CD45RO^-$ T-cells (Tn), effector $CCR7^-$ $CD45RO^-$ T-cells (Teff), central memory $CCR7^+$ $CD45RO^+$ T-cells (Tcm) and effector memory $CCR7^-$ $CD45RO^+$ T-cells (Tem) was investigated following the co-culture of the CAR-T cells and LIM1215 cells as described above. Co-cultures of CAR-T cells and LIM1215 cells were treated at an equivalent dose of 20 µM SB415286 with the GSK3i NPs or free SB415286 or left untreated as control. CAR-T cells were also cultured without LIM1215 to determine their primary phenotype. Six days after treatment, T-cells were stained by FITC CD4, PerCP Cy5.5 CD8, PE CD45RO (BioLegend, USA) and BV421 CCR7 (BD Biosciences, USA) human antibodies and analysed by imaging flow cytometry. T-cells were gated on the $CD4^+$ or $CD8^+$ cells and the Tn, Teff, Tcm and Tem positive subpopulations were determined.

5.2.9 Statistics

Data was analysed using one-way ANOVA and with the Tukey post hoc test using GraphPad Prism 7 (GraphPad Software, Inc., USA). Statistical significance was indicated by asterisk as *P<0.05, **P < 0.01, ***P ≤ 0.001 and ****P ≤ 0.0001 and ns indicates not significant. The data is represented as average ± standard error of mean.

5.3 Results and discussion

5.3.1 Optimized physicochemical properties of GSK3i NP

The preparation of the GSK3i NPs was optimized using the 3D-printed microfluidic chip (Figure 5-1-A) and hydrophobic ion pairing to obtain monodispersed and reproducible nanoformulations. In a typical formulation, the optimized PEG-PLGA NPs displayed a hydrodynamic average size of 86 ± 3.7 nm with a narrow size distribution and a negative zeta potential of -30 ± 0.3 (Figure 5-1-B, C). Nanocarriers in this medium size range are commonly used in immunotherapy studies as they are large enough not to be cleared by kidneys and not too large to stimulate the reticuloendothelial system for rapid clearance [30]. The TEM images confirmed the NP size measured by dynamic light scattering and the expected spherical morphology (Figure 5-1D). The NP hydrodynamic diameters were stable in both PBS and water over two weeks (Figure 5-1E).

The 3D printed microfluidic nanoprecipitation device used in this study has a very high throughput, and there are only a small number of parameters that affect the nanoformulation physicochemical characteristics. By optimization of organic and aqueous phases' flow rates, highly reproducible monodispersed formulations were obtained. The GSK3i nanoformulation was optimised using a hydrophobic ion pairing strategy. Hydrophobic ion complexation enables efficient loading of challenging small molecules within polymeric NPs and also improve drug release behaviour [31]. This strategy is increasingly being used by pharmaceutical companies to improve the loading, stability and release profile of low molecular weight therapeutics, and foster their clinical application [25,32]. The amount of loaded SB415286 into the PEG-PLGA NPs was quantified for the optimum ratio of sodium deoxycholate and SB415286 (2/1 molar ratio), which yielded an acceptable loading of 2.6 ± 0.06 % (w/w) vs 1.8 ± 0.05 % without hydrophobic ion pairing.

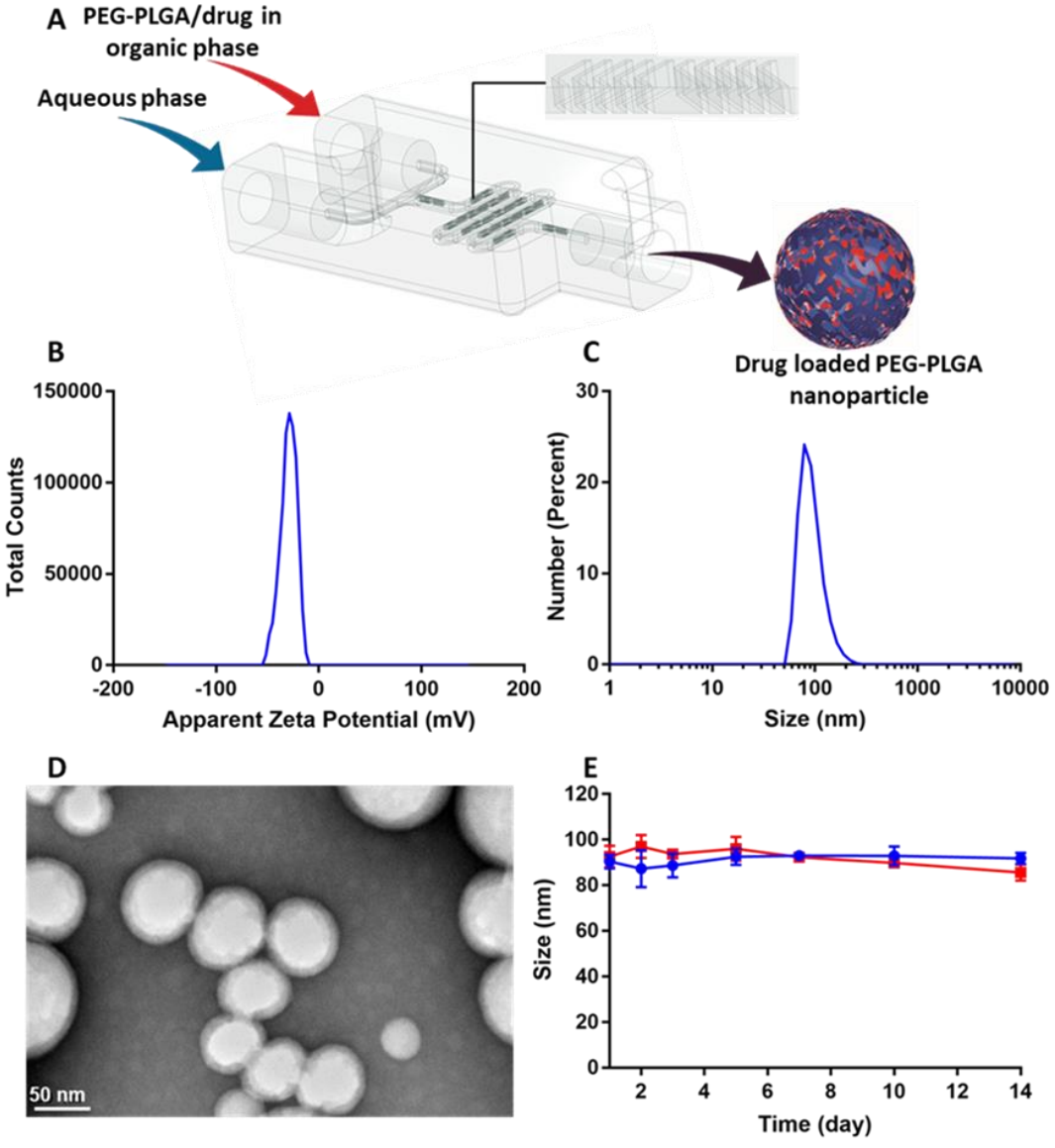

Figure 5-1 Preparation and physicochemical characterization of GSK3i NPs.
A) Schematic illustration of GSK3i nanoformulation within PEG-PLGA NPs using a 3D printed microfluidic nanoprecipitation device. Mixtures of PLGA, PEG-PLGA, GSK3i and sodium deoxycholate in acetonitrile are introduced via one inlet and rapidly mixed in a herringbone structured microfluidic channel with Milli-Q® water introduced via the other inlet to nanoprecipitate the polymer/drug and form the GSK3i NPs. B) Zeta potential in Milli-Q® and C) hydrodynamic diameter of a typical GSK3i nanoformulation. D) Morphology by transmission electron microscopy of a typical GSK3i nanoformulation (scale bar 50 nm). E) Evolution of the hydrodynamic diameter of a GSK3i nanoformulation over two weeks in water and PBS. The data are representative of at least three independent batches of preparation.

5.3.2 GSK3i NPs efficiently inhibit PD-1 receptor and retain functionality

To determine the efficacy of the GSK3i nanoformulation to inhibit the PD-1 expression of CAR-T cells, LGR5 targeted CAR-T cells were co-cultured with LIM1215 cancer cells. To validate the co-culture of LIM1215 and LGR5 specific CAR-T cells as a suitable model to investigate the efficacy of the GSK3i NPs to reduce PD-1 expression, the antigen specific overexpression of PD-1 receptors following co-culture was first confirmed. PD-1 expression by imaging flow cytometry analysis revealed that the PD-1 fluorescence intensity of CAR-T cells increased 1.6 fold (Figure 5-2-A) and that the percentage of basal PD-1$^+$ pan T-cells increased from 28.9 % to 43.4 % in the CAR-T cell/ LIM1215 co-culture. In contrast, the expression levels of the PD-1 receptor in untransduced T-cells remained unchanged after stimulation with LIM1215 cells. These results indicate that the LGR5 expressing LIM1215 cells efficiently and specifically activated the LGR5 targeted CAR-T cells leading to substantial upregulation of the expression of PD-1 receptors.

Next, the efficacy of the GSK3i nanoformulation in inhibiting PD-1 expression was determined. Treatment with the GSK3i NPs (20µM) significantly reduced PD-1 expression in the antigen activated CD3$^+$CAR-T cells compared to the no treatment control group, yielding expression levels close to basal level (36 % vs 28.9%) of PD-1$^+$ cells (Figure 5-2-B). Inhibition of CAR T cells PD-1 expression by the GSK3i nanoformulation was comparable to that yielded by the free GSK3i, demonstrating that the chemical design of the nanoformulation did not affect the activity of the GSK3i. Interestingly, the reduction of PD-1 expression by the GSK3i NPs and free GSK3i was more significant in CD4$^+$ T-cells (Figure 5-2-C) and we did not observe a significant change in PD-1 expression for CD8$^+$ T-cells (Figure 5-2-D).

Further assessment confirmed that PD-1 upregulation was vastly higher for CD4$^+$ CAR T-cells after stimulation by LIM1215 compared to pan T-cell (gated as CD3$^+$) population. No PD-1 upregulation was measured for the CD8$^+$ cells (Figure 5-2-B, C, D). These

results validates that the inhibition of PD-1 expression down stream of GSK3 inhibition only occurs when PD-1 is overexpressed as a consequence of antigen specific stimulation. While previous studies describe the effects of GSK3i induced PD-1 inhibition of antigen specific activated $CD8^+$ T-cells, the effect on $CD4^+$ cells was not assessed *in vitro* [12,33].

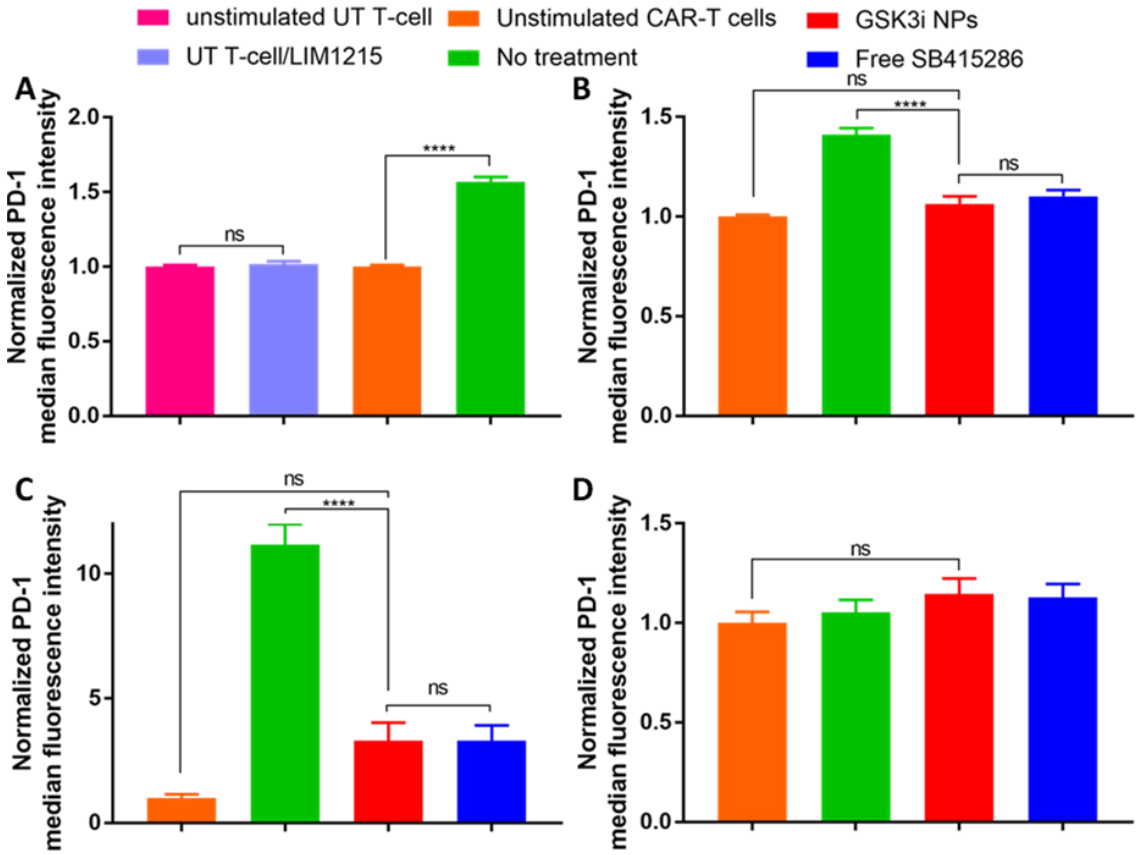

Figure 5-2 GSK3i NP are functional and efficiently inhibit PD-1 receptor expression.
A) PD-1 median fluorescent intensities of LGR5 specific CAR-T cells and untransduced (UT) T-cells mono-culture (unstimulated) and co-cultured with LIM1215. Effect of treatment on PD-1 fluorescent intensities of (B) $CD3^+$, (C) $CD4^+$ and (D) $CD8^+$ LGR5 specific CAR-T cells mono-culture and co-cultured with LIM1215, after two days treatment with 20 µM free SB415286, 20 µM GSK3i NPs and untreated. The experiments were repeated at least two times. The data was analysed by one-way ANOVA and Tukey post hoc test; *P<0.05, **P < 0.01, ***P ≤ 0.001 and ****P ≤ 0.0001 and ns indicates no significant.

Previous studies demonstrate that GSK3 inhibition activates the Wnt/β-catenin signaling pathway. While GSK3 constitutively controls β-catenin at a low levels by its degradation, GSK3 inhibition stabilizes β-catenin, which can be translocated into the nucleus and activate gene transcription [34,35]. This regulation is also involved in the regulation of PD-1 expression. GSK3 inhibition can increase transcription of Wnt/β-catenin regulated T-bet gene, which reduces PD-1 expression [12]. To confirm the functionality of the GSK3i NPs to regulate the Wnt/β-catenin signalling pathway, reporter HEK293T cells expressing the Wnt inducible NanoLuc luciferase were used. Wnt activity increased 193.4

± 1.7 times after treatment with GSK3i NPs and 147.6 ± 5.9 times in the case of the free SB415286 GSK3i (Figure 5-3-A), further validating the activity of SB415286 loaded within the nanoformulation. This data also confirms the activity of GSK3i to regulate the Wnt/β-catenin signalling pathway.

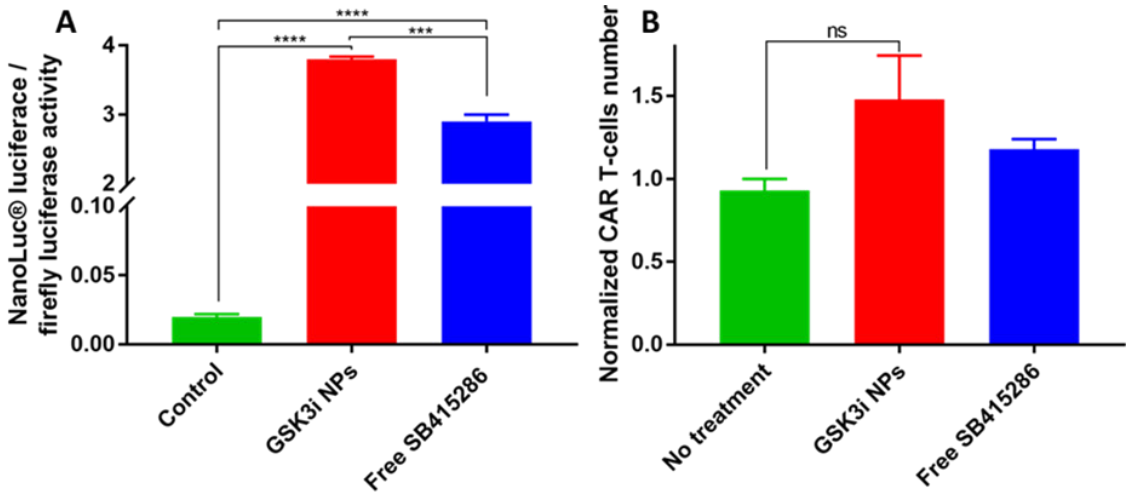

Figure 5-3 GSK3i NPs induce Wnt/β catenin pathway and enhance T-cell proliferation.
A) Ratio of luminescence of NanoLuc® luciferase/firefly luciferase (Nluc/Fluc) in HEK293T reporter cells treated by 20 µM GSK3i NPs or free SB415286 and normalized to non-treated cells (N=3). B) Normalized number of viable CAR-T cell, two days after stimulation by LIM1215 cells and treatment with 20 µM GSK3i NPs or free SB415286 GSK3i as determined by the trypan blue exclusion assay. The experiments were repeated at least two times. The data was analysed by one-way ANOVA and Tukey post hoc test; *P<0.05, **P < 0.01, ***P ≤ 0.001 and ****P ≤ 0.0001 and ns indicates not significant.

Treatment with GSK3i NPs or with the free SB415286 GSK3i resulted in 1.59 fold and 1.27 fold increase in viable CAR-T cell number compared to the no treatment control group, respectively (Figure 5-3-B). This substantial increase in CAR-T cell number suggests that treatment with GSK3i NPs enhanced the proliferation of CAR-T cells. This observation is consistent with a previous study by Sengupta *et al.*, where a loss of viability in IL13CAR-T cells was measured upon antigen specific activation. However, addition of IL-2 and the SB216763 GSK3i improved the survival of the CAR T-cells [13]. Interestingly, in our study the GSK3i nanoformulation not only prevented the viability loss of CAR-T cells but also enhanced their proliferation.

PD-1 inhibition is associated with higher T-cell cytotoxicity [36,37]. The SB415286 GSK3i efficiently reduced the expression of PD-1 receptors and restored the activity of T-cells in previous studies using melanoma mouse tumour model and clearing viral infection [12,38]. GSK3 inhibition was shown in these studies to be as effective as aPD-1 in inhibiting PD-1 receptor expression and delaying tumour's growth. Moreover, Taylor

et al., determined that GSK3 inhibition substitutes for the activation of CD28 co-stimulatory signal, a second signal required for full activation of T-cells and PD-1 blockade by aPD-1 [39]. This is due to the central role of GSK3 in priming CD28.

Altogether, our biological data validates the chemical design of the GSK3i PEG-PLGA nanoformulation as its biological activity was either comparable or higher than that of the free GSK3i. This highlights the benefit of the combination of hydrophobic ion pairing and microfluidic nanoprecipitation that yield acceptable loading of the SB415286 GSK3i within the nanocarriers without chemical modification. This can be contrasted to previous reports of GSK3i nanoformulations. For example, silicasome delivery of the AZD1080 GSK3i successfully mitigated the toxicity of the free GSK3i in several preclinical tumour models, however, the free GSK3i was shown to be more efficient than the silicasome formulation in inhibiting the PD-1 gene expression of T-cells *in vitro* [16]. Similarly, the 6-bromoindirubin-3′-oxime GSK3i loaded within PEGylated polycaprolactone nanocarriers improved the pharmacokinetic and toxicity of the GSK3i for bone osteogenesis. But although the nanocarriers reduced the toxicity compared to the free drug, the induction of Wnt signalling was decreased in a luciferase assay [40].

5.3.3 Effect of the GSK3i NPs on the CAR T-cells phenotypes

Limited differentiation of T-cells and augmentation of memory T-cells is controlled by the Wnt/β-catenin pathway, which is inhibited by GSK3. Therefore, GSK3 inhibition was shown to increase the activity of Wnt/β-catenin pathway and induce memory phenotype (Tcm and/or Tem) in both $CD4^+$ and $CD8^+$ T-cells, which is critical in providing long-lasting anti-tumour immune response [41–45]. To determine if lower exhaustion of T-cells by PD-1 inhibition can lead to the formation of memory T-cells, which are critical for anti-tumour T-cell activity, the T-cell phenotype changes were assessed following CAR-T cell/cancer cell co-culture, six days after treatment. The total population of $CD4^+$ and $CD8^+$ T-cells remained unchanged after treatment and the majority of the CAR-T cell populations were Tem with only a very small Tn population. Activation of the CAR-T cells by cancer cells expressing the LGR5 CAR target reduced the Teff population and the cells acquired a memory phenotype with increases in Tem and Tcm for both $CD4^+$ and $CD8^+$ cells (Figure 5-4-A, B). Treatment by GSK3i NPs resulted in a further shift to the memory phenotype, however, only the Tcm of $CD4^+$ and $CD8^+$ T-cells, but not Tem, increased compared to untreated cells. The Tcm $CD4^+$ T-cell population increased from 9.14 % (untreated) to 19.3 %, upon treatment with the GSK3i nanoformulation, while

$CD8^+$ Tcm increased from 18.1 % (untreated group) to 22.8 % in the GSK3i NPs treated group. The modified phenotype of CAR-T cells treated by the GSK3i nanoformulation was also associated with increased ratio of Tcm/Teff, which is a predictive marker of anti-tumour immune activity [45] (table 5-1). Treatment with the free SB415286 GSK3i showed a similar shift in Tcm. The $CD4^+$ Tem changed to 76.3 % from 85.4 % (untreated). In $CD8^+$ T-cells, the population of Tem did not change after GSK3i NPs treatment. The effect of treatment on Tn and Teff was not significant.

Table 5-1 Effect of GSK3 inhibition on the ratios of Tcm/Teff cells.

	$CD4^+$ T-cells	$CD8^+$ T-cells
No treatment	2.59	2.60
GSK3i NPs	8.35	9.42
Free SB415286	4.49	7.72

These findings corroborate with previous studies, where GSK3 inhibition functioning via the Wnt/ β-catenin pathway induced memory phenotype [41–44]. Likewise, Sengupta *et al.,* observed that GSK3 inhibition increased the population of Tem $CD8^+$ CAR-T cells, and that as a result the immune system rejected tumour re-challenge in a mouse model of glioblastoma [13]. This highlights that formation of memory T-cells is critical in the anti-tumour activity of T-cells to induce rapid and efficient response against re-exposure to the tumour antigen. However, in our study the memory induction was more significant in Tcm. Previous studies have demonstrated the superiority of Tcm in providing persistent anti-tumour immunity compared to Teff and Tcm/Teff ratio has been proposed as a predictive marker of the efficacy of the anti-tumour immune response [45]. The GSK3 inhibition induced shift towards anti-tumour memory T-cells observed in this study further establishes the GSK3i nanoformulation as a promising immunotherapy alternative to PD-1 antibody strategies.

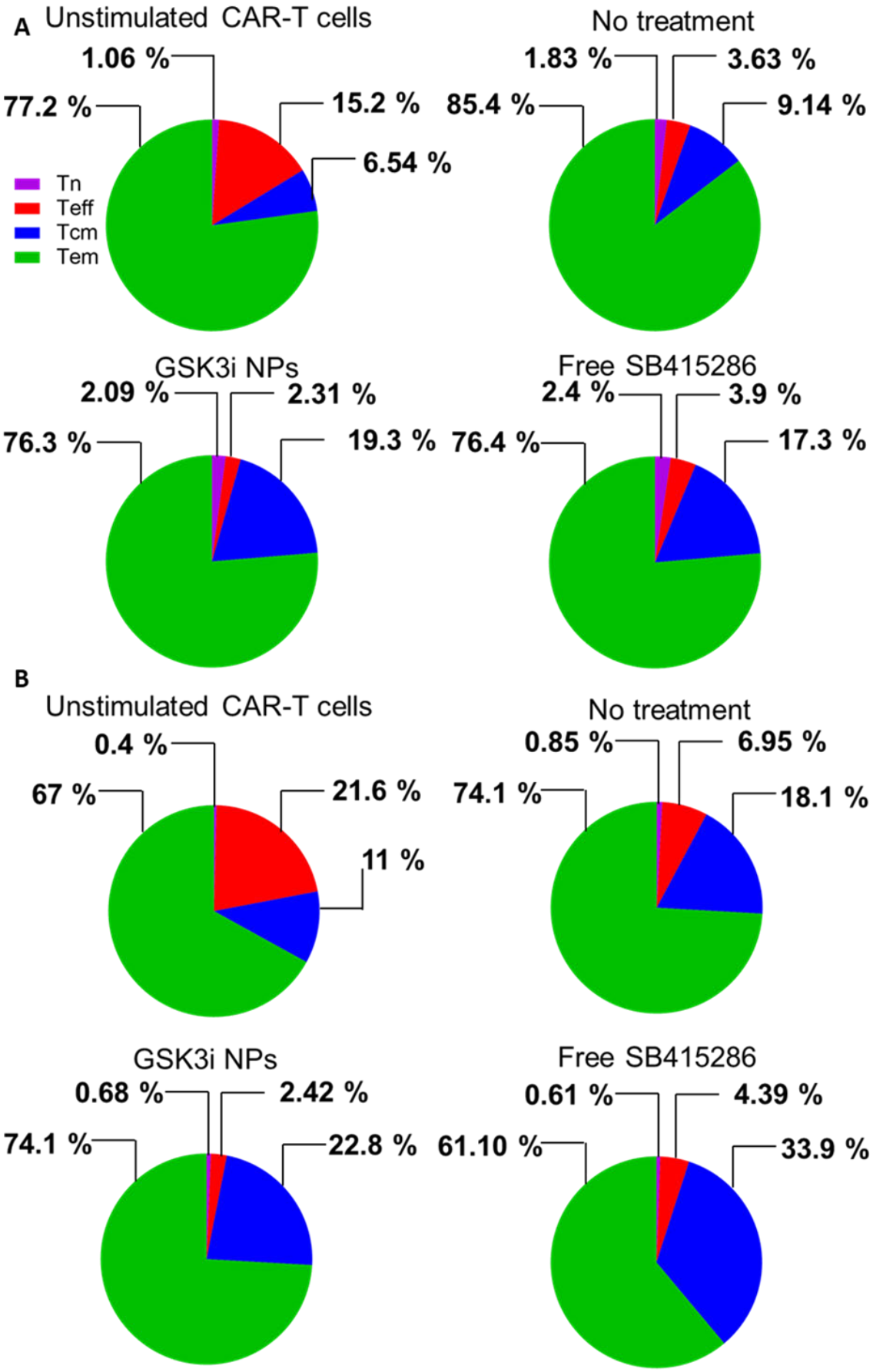

Figure 5-4 GSK3 inhibition induced changes on CAR T-cell phenotype.

Percentages of LGR5 targeted CAR-T cells phenotypes for A) $CD4^+$ population and B) $CD8^+$ based on naïve T-cells (Tn), effector T-cells (Teff), central memory T-cells (Tcm) and effector memory T-cells, six days after CAR-T cells monoculture (unstimulated), and for CAR-T cells co-culture with LIM1215 cells and treatment with 20 µM free SB415286 , 20 µM GSK3i NPs and untreated. The percentages of each population are shown as representative of experiments after gating based on fluorescence intensity of CCR7 and CD45RO markers.

5.4 Conclusion

In conclusion, we have developed a simple and reproducible GSK3i nanoformulation based on PEG-PLGA nanoparticles incorporating the SB415286 GSK3i by hydrophobic ion complexation and nanoprecipitation in a microfluidic device. The biological activity of the GSK3i nanoformulation was assessed in an *in vitro* model of CAR-T cells activated by colorectal cancer cells expressing the CAR LGR5 target. GSK3 inhibition with the nanoformulation efficiently reduced the expression of PD-1 receptors in CAR-T cells, increased T-cell proliferation and induced memory phenotype. On the bases of these results, the GSK3i nanoformulation is a promising candidate for improving the biodistribution of the GSK3i *in vivo,* increasing its anti-tumour response, and mitigating its off-target toxicity.

5.5 References

[1] M. Bersanelli, S. Buti, From targeting the tumor to targeting the immune system: Transversal challenges in oncology with the inhibition of the PD-1/PD-L1 axis, World J. Clin. Oncol. 8 (2017) 37. https://doi.org/10.5306/wjco.v8.i1.37.

[2] Y. Jiang, X. Zhao, J. Fu, H. Wang, Progress and Challenges in Precise Treatment of Tumors With PD-1/PD-L1 Blockade, Front. Immunol. 11 (2020) 339. https://doi.org/10.3389/fimmu.2020.00339.

[3] R.M. Wong, R.B. Cameron, Immune Checkpoint Blockade and Adaptive Immune Resistance in Cancer, in: Immunother. Reality, Ideas, Futur., InTech, Rijeka, 2017: pp. 47–61.

[4] M.A. Postow, M.K. Callahan, J.D. Wolchok, Immune checkpoint blockade in cancer therapy, J. Clin. Oncol. 33 (2015) 1974. https://doi.org/10.1200/JCO.2014.59.4358.

[5] S.P. Arlauckas, C.S. Garris, R.H. Kohler, M. Kitaoka, M.F. Cuccarese, K.S. Yang, M.A. Miller, J.C. Carlson, G.J. Freeman, R.M. Anthony, R. Weissleder, M.J. Pittet, In vivo imaging reveals a tumor-associated macrophage-mediated resistance pathway in anti-PD-1 therapy, Sci. Transl. Med. 9 (2017) eaal3604. https://doi.org/10.1126/scitranslmed.aal3604.

[6] E. Doevendans, H. Schellekens, Immunogenicity of Innovative and Biosimilar Monoclonal Antibodies, Antibodies. 8 (2019) 21. https://doi.org/10.3390/antib8010021.

[7] K. Li, H. Tian, Development of small-molecule immune checkpoint inhibitors of PD-1/PD-L1 as a new therapeutic strategy for tumour immunotherapy, J. Drug Target. 27 (2019) 244–256. https://doi.org/10.1080/1061186X.2018.1440400.

[8] L. Skalniak, K.M. Zak, K. Guzik, K. Magiera, B. Musielak, M. Pachota, B. Szelazek, J. Kocik, P. Grudnik, M. Tomala, S. Krzanik, K. Pyrc, A. Dömling, G. Dubin, T.A. Holak, Small-molecule inhibitors of PD-1/PD-L1 immune checkpoint alleviate the PD-L1-induced exhaustion of T-cells, Oncotarget. 8 (2017) 72167. https://doi.org/10.18632/oncotarget.20050.

[9] P. Sasikumar, R. Shrimali, S. Adurthi, R. Ramachandra, L. Satyam, A. Dhudashiya, D. Samiulla, K.B. Sunilkumar, M. Ramachandra, A novel peptide

therapeutic targeting PD1 immune checkpoint with equipotent antagonism of both ligands and a potential for better management of immune-related adverse events, J. Immunother. Cancer. 1 (2013) O24. https://doi.org/10.1186/2051-1426-1-s1-o24.

[10] I. Sahin, A. Eturi, A. De Souza, S. Pamarthy, F. Tavora, F.J. Giles, B.A. Carneiro, Glycogen synthase kinase-3 beta inhibitors as novel cancer treatments and modulators of antitumor immune responses, Cancer Biol. Ther. 20 (2019) 1047–1056. https://doi.org/10.1080/15384047.2019.1595283.

[11] Q. Wu, L. Jiang, S. cheng Li, Q. jun He, B. Yang, J. Cao, Small molecule inhibitors targeting the PD-1/PD-L1 signaling pathway, Acta Pharmacol. Sin. 42 (2021) 1–9. https://doi.org/10.1038/s41401-020-0366-x.

[12] A. Taylor, J.A. Harker, K. Chanthong, P.G. Stevenson, E.I. Zuniga, C.E. Rudd, Glycogen Synthase Kinase 3 Inactivation Drives T-bet-Mediated Downregulation of Co-receptor PD-to Enhance CD8+ Cytolytic T Cell Responses, Immunity. 44 (2016) 274–286. https://doi.org/10.1016/j.immuni.2016.01.018.

[13] S. Sengupta, S.C. Katz, S. Sengupta, P. Sampath, Glycogen synthase kinase 3 inhibition lowers PD-1 expression, promotes long-term survival and memory generation in antigen-specific CAR-T cells, Cancer Lett. 433 (2018) 131–139. https://doi.org/10.1016/j.canlet.2018.06.035.

[14] S. Lim, J. Park, M.K. Shim, W. Um, H.Y. Yoon, J.H. Ryu, D.K. Lim, K. Kim, Recent advances and challenges of repurposing nanoparticle-based drug delivery systems to enhance cancer immunotherapy, Theranostics. 9 (2019) 7906–7923. https://doi.org/10.7150/thno.38425.

[15] H. Eldar-Finkelman, A. Martinez, GSK-3 Inhibitors: Preclinical and Clinical Focus on CNS, Front. Mol. Neurosci. 4 (2011) 32. https://doi.org/10.3389/fnmol.2011.00032.

[16] S.D. Allen, X. Liu, J. Jiang, Y.P. Liao, C.H. Chang, A.E. Nel, H. Meng, Immune Checkpoint Inhibition in Syngeneic Mouse Cancer Models by a Silicasome Nanocarrier Delivering a GSK3 Inhibitor, Biomaterials. 269 (2021) 120635. https://doi.org/10.1016/j.biomaterials.2020.120635.

[17] F. Danhier, E. Ansorena, J.M. Silva, R. Coco, A. Le Breton, V. Préat, PLGA-based nanoparticles: An overview of biomedical applications, J. Control. Release. 161 (2012) 505–522. https://doi.org/10.1016/j.jconrel.2012.01.043.

[18] F.S.T. Mirakabad, K. Nejati-Koshki, A. Akbarzadeh, M.R. Yamchi, M. Milani, N. Zarghami, V. Zeighamian, A. Rahimzadeh, S. Alimohammadi, Y. Hanifehpour, S.W. Joo, PLGA-based nanoparticles as cancer drug delivery systems, Asian Pacific J. Cancer Prev. 15 (2014) 517–535. https://doi.org/10.7314/APJCP.2014.15.2.517.

[19] J. Ghitman, E.I. Biru, R. Stan, H. Iovu, Review of hybrid PLGA nanoparticles: Future of smart drug delivery and theranostics medicine, Mater. Des. 193 (2020) 108805. https://doi.org/10.1016/j.matdes.2020.108805.

[20] A. Beletsi, Z. Panagi, K. Avgoustakis, Biodistribution properties of nanoparticles based on mixtures of PLGA with PLGA-PEG diblock copolymers, Int. J. Pharm. 298 (2005) 233–241. https://doi.org/10.1016/j.ijpharm.2005.03.024.

[21] N. Cheraga, N.C. Sun, X.X. Huang, Z. Ye, Q.R. Xiao, N.P. Huang, Optimized rapamycin-loaded PEGylated PLGA nanoparticles: Preparation, characterization and pharmacokinetics study, J. Drug Deliv. Sci. Technol. 61 (2021) 102144. https://doi.org/10.1016/j.jddst.2020.102144.

[22] X. Li, X. Jiang, Microfluidics for producing poly (lactic-co-glycolic acid)-based pharmaceutical nanoparticles, Adv. Drug Deliv. Rev. 128 (2018) 101–114. https://doi.org/10.1016/j.addr.2017.12.015.

[23] Y. Kim, B. Lee Chung, M. Ma, W.J.M. Mulder, Z.A. Fayad, O.C. Farokhzad, R. Langer, Mass production and size control of lipid-polymer hybrid nanoparticles through controlled microvortices, Nano Lett. 12 (2012) 3587–3591. https://doi.org/10.1021/nl301253v.

[24] J. Sun, Y. Xianyu, M. Li, W. Liu, L. Zhang, D. Liu, C. Liu, G. Hu, X. Jiang, A microfluidic origami chip for synthesis of functionalized polymeric nanoparticles, Nanoscale. 5 (2013) 5262–5265. https://doi.org/10.1039/c3nr01289a.

[25] S. Ashton, Y.H. Song, J. Nolan, E. Cadogan, J. Murray, R. Odedra, J. Foster, P.A. Hall, S. Low, P. Taylor, R. Ellston, U.M. Polanska, J. Wilson, C. Howes, A. Smith, R.J.A. Goodwin, J.G. Swales, N. Strittmatter, Z. Takáts, A. Nilsson, P. Andren, D. Trueman, M.

Walker, C.L. Reimer, G. Troiano, D. Parsons, D. De Witt, M. Ashford, J. Hrkach, S. Zale, P.J. Jewsbury, S.T. Barry, Aurora kinase inhibitor nanoparticles target tumors with favorable therapeutic index in vivo, Sci. Transl. Med. 8 (2016) 325ra17. https://doi.org/10.1126/scitranslmed.aad2355.

[26] K.D. Ristroph, R.K. Prud'homme, Hydrophobic ion pairing: Encapsulating small molecules, peptides, and proteins into nanocarriers, Nanoscale Adv. 1 (2019) 4207–4237. https://doi.org/10.1039/c9na00308h.

[27] M. Ichinose, N. Suzuki, T. Wang, J.A. Wright, T.R.M. Lannagan, L. Vrbanac, H. Kobayashi, K.A. Gieniec, J.Q. Ng, Y. Hayakawa, P. García-Gallastegui, E.M. Monsalve, S.R. Bauer, J. Laborda, J.J. García-Ramírez, G. Ibarretxe, D.L. Worthley, S.L. Woods, Stromal DLK1 promotes proliferation and inhibits differentiation of the intestinal epithelium during development, Am. J. Physiol. - Gastrointest. Liver Physiol. 320 (2021) G506–G520. https://doi.org/10.1152/AJPGI.00445.2020.

[28] F. Walker, H.H. Zhang, A. Odorizzi, A.W. Burgess, LGR5 is a negative regulator of tumourigenicity, antagonizes wnt signalling and regulates cell adhesion in colorectal cancer cell lines, PLoS One. 6 (2011) e22733. https://doi.org/10.1371/journal.pone.0022733.

[29] Y. Jiang, W. Li, X. He, H. Zhang, F. Jiang, Z. Chen, Lgr5 expression is a valuable prognostic factor for colorectal cancer: Evidence from a meta-analysis, BMC Cancer. 16 (2016) 1–9. https://doi.org/10.1186/s12885-015-1986-2.

[30] M. Yang, J. Li, P. Gu, X. Fan, The application of nanoparticles in cancer immunotherapy: Targeting tumor microenvironment, Bioact. Mater. 6 (2021) 1973–1987. https://doi.org/10.1016/j.bioactmat.2020.12.010.

[31] J. Liu, Y. Xu, Z. Liu, H. Ren, Z. Meng, K. Liu, Z. Liu, J. Yong, Y. Wang, X. Li, A modified hydrophobic ion-pairing complex strategy for long-term peptide delivery with high drug encapsulation and reduced burst release from PLGA microspheres, Eur. J. Pharm. Biopharm. 144 (2019) 217–229. https://doi.org/10.1016/j.ejpb.2019.09.022.

[32] Y.H. Song, E. Shin, H. Wang, J. Nolan, S. Low, D. Parsons, S. Zale, S. Ashton, M. Ashford, M. Ali, D. Thrasher, N. Boylan, G. Troiano, A novel in situ hydrophobic ion paring (HIP) formulation strategy for clinical product selection of a nanoparticle drug

delivery system, J. Control. Release. 229 (2016) 106–119. https://doi.org/10.1016/j.jconrel.2016.03.026.

[33] A. Taylor, C.E. Rudd, Glycogen synthase kinase 3 (GSK-3) controls T-cell motility and interactions with antigen presenting cells, BMC Res. Notes. 13 (2020) 1–7. https://doi.org/10.1186/s13104-020-04971-0.

[34] J. Huang, X. Guo, W. Li, H. Zhang, Activation of Wnt/β-catenin signalling via GSK3 inhibitors direct differentiation of human adipose stem cells into functional hepatocytes, Sci. Rep. 7 (2017) 1–12. https://doi.org/10.1038/srep40716.

[35] D. Wu, W. Pan, GSK3: a multifaceted kinase in Wnt signaling, Trends Biochem. Sci. 35 (2010) 161–168. https://doi.org/10.1016/j.tibs.2009.10.002.

[36] R. Garcia de Moura, L.P. Covre, C.H. Fantecelle, V.A.T. Gajardo, C.B. Cunha, L.L. Stringari, A.T. Belew, C.B. Daniel, S.V. Von Zeidler, C.E. Tadokoro, H.L. de Matos Guedes, R.L. Zanotti, D. Mosser, A. Falqueto, A.N. Akbar, D.C.O. Gomes, PD-1 Blockade Modulates Functional Activities of Exhausted-Like T Cell in Patients With Cutaneous Leishmaniasis, Front. Immunol. 12 (2021) 245. https://doi.org/10.3389/fimmu.2021.632667.

[37] S. Rafiq, O.O. Yeku, H.J. Jackson, T.J. Purdon, D.G. van Leeuwen, D.J. Drakes, M. Song, M.M. Miele, Z. Li, P. Wang, S. Yan, J. Xiang, X. Ma, V.E. Seshan, R.C. Hendrickson, C. Liu, R.J. Brentjens, Targeted delivery of a PD-1-blocking scFV by CAR-T cells enhances anti-tumor efficacy in vivo, Nat. Biotechnol. 36 (2018) 847–856. https://doi.org/10.1038/nbt.4195.

[38] A. Taylor, D. Rothstein, C.E. Rudd, Small-molecule inhibition of pd-1 transcription is an effective alternative to antibody blockade in cancer therapy, Cancer Res. 78 (2018) 706–717. https://doi.org/10.1158/0008-5472.CAN-17-0491.

[39] A. Taylor, C.E. Rudd, Glycogen synthase kinase 3 inactivation compensates for the lack of CD28 in the priming of CD8+ cytotoxic T-cells: Implications for anti-PD-1 immunotherapy, Front. Immunol. 8 (2017) 1653. https://doi.org/10.3389/fimmu.2017.01653.

[40] E. Scarpa, A.A. Janeczek, A. Hailes, M.C. de Andrés, A. De Grazia, R.O. Oreffo, T.A. Newman, N.D. Evans, Polymersome nanoparticles for delivery of Wnt-activating

small molecules, Nanomedicine Nanotechnology, Biol. Med. 14 (2018) 1267–1277. https://doi.org/10.1016/j.nano.2018.02.014.

[41] H. Kared, S.W. Tan, M.C. Lau, M. Chevrier, C. Tan, W. How, G. Wong, M. Strickland, B. Malleret, A. Amoah, K. Pilipow, V. Zanon, N.M. Govern, J. Lum, J.M. Chen, B. Lee, M.C. Florian, H. Geiger, F. Ginhoux, E. Ruiz-Mateos, T. Fulop, R. Rajasuriar, A. Kamarulzaman, T.P. Ng, E. Lugli, A. Larbi, Immunological history governs human stem cell memory CD4 heterogeneity via the Wnt signaling pathway, Nat. Commun. 11 (2020) 1–17. https://doi.org/10.1038/s41467-020-14442-6.

[42] M.A. Forget, Y. Huon, A. Reuben, C. Grange, M. Liberman, J. Martin, A.M. Mes-Masson, N. Arbour, R. Lapointe, Stimulation of Wnt/ß-Catenin pathway in human CD8+ T lymphocytes from blood and lung tumors leads to a shared young/memory phenotype, PLoS One. (2012) e41074. https://doi.org/10.1371/journal.pone.0041074.

[43] G. Jeannet, C. Boudousquié, N. Gardiol, J. Kang, J. Huelsken, W. Held, Essential role of the Wnt pathway effector Tcf-1 for the establishment of functional CD8 T cell memory, Proc. Natl. Acad. Sci. U. S. A. 107 (2010) 9777–9782. https://doi.org/10.1073/pnas.0914127107.

[44] M. Mavigner, M. Zanoni, G.K. Tharp, J. Habib, C.R. Mattingly, M. Lichterfeld, M.T. Nega, T.H. Vanderford, S.E. Bosinger, A. Chahroudi, Pharmacological modulation of the Wnt/β-catenin pathway inhibits proliferation and promotes differentiation of long-lived memory CD4+ T cells in antiretroviral therapy-suppressed simian immunodeficiency virus-infected macaques, J. Virol. 94 (2019) e01094-19.

[45] Q. Liu, Z. Sun, L. Chen, Memory T cells: strategies for optimizing tumor immunotherapy, Protein Cell. 11 (2020) 549–564. https://doi.org/10.1007/s13238-020-00707-9.

Chapter 6

Microfluidic Nanoprecipitation Combined with Hydrophobic Ion Pairing Enables the Preparation of High Performance Indocyanine Green Highly Tuneable Nanoformulations

6 Microfluidic nanoprecipitation combined with hydrophobic ion pairing enables the preparation of high performance indocyanine green highly tuneable nanoformulations

6.1 Introduction

Image guided surgery by near infrared (NIR) fluorescence is increasingly used clinically, including to assist in the resection of tumours and in sentinel lymph node (SLN) mapping/biopsy procedures [1]. As their excitation/emission are within the tissue optical window of 780-1700 nm, NIR dyes display low tissue scattering, high signal to background noise and deep tissue penetration [2,3]. Indocyanine green (ICG) is a NIR dye broadly used for image guided surgery of different cancer types, including but not limited to gastric, breast and head and neck cancers. ICG has low toxicity and is approved by the United Sates Food and Drug Administrative (FDA) and the European medicines agency (EMA) [3]. For SLN biopsy procedure, an ICG aqueous solution is injected in the peritumoural region by the intradermal or subcutaneous route. ICG rapidly drains to the SLNs, which can thus be detected by a charge-coupled device (CCD) camera equipped with light-emitting diodes (LEDs) and NIR-sensitive image intensifier, allowing the surgeon to resect the SLNs [4].

However, the aqueous stability of ICG is very low and at high concentrations, it loses its fluorescence by aggregation-caused quenching due to inter and/or intra molecular attractions [5,6]. In addition, ICG has a short half-life *in vivo* (2-4 min) with low retention in the lymphatic system [5,6]. It can be difficult to distinguish SLNs from nodes of higher echelons (downstream LNs), due to the rapid distribution of ICG from SLN to other LNs.

In this regard, ICG nanoformulation has been investigated to increase the ICG optical properties, aqueous stability and improve its biodistribution for both diagnostic and therapeutic (e.g. photodynamic and photothermal therapies) purposes [7,8]. Several organic and inorganic nanoparticles (NPs), including liposomes, polymeric NPs, polypeptide micelles, silica NPs, gold NPs, iron oxide NPs and hybrid NPs have been employed in previous studies for the nanoformulation of ICG [9–13]. The majority of these studies have focused NPs on therapeutic application; and only a surprising small number of studies have investigated diagnostic application of ICG nanoformulations, including SLN biopsies. The improved optical properties of liposomal ICG led to higher

fluorescence intensity in the popliteal LNs of mice and improved imaging of lymphatic drainage 6 minutes after injection compared to free ICG [14]. In another study, the fluorescence of targeted and non-targeted ICG liposomes detected in the SLNs of mice over 18 h was associated with a rapid reduction of fluorescence after a few hours [15]. Also, in a study ICG was encapsulated in H-ferritin nano-cages for image guided cancer surgery, however, the nano-formulation lost 60 % of its fluorescence after about 13 h, when the fluorescence of free ICG became undetectable [16]. Wei et al., loaded ICG within tumour targeted poly(ethylene glycol)-b-poly(lactide-co-glycolide) (PEG-PLGA) NPs and observed increased ICG fluorescence in the SLNs of mice up to 24 h compared to free ICG [17]. However, larger animal models are greatly superior model of the human lymphatic system [18]. In addition, some other studies have reported the difficulty of loading hydrophilic ICG molecule into polymeric NPs [19–22]

Previous studies have investigated the complexation of ICG with a cationic ion pair to improve the loading and stability of ICG within nanoformulation, which also provides a simpler path to clinical use compared to more complex chemical modification of the dye itself [20,23]. In hydrophobic ion pairing, the counter ion shields the ionic charge of the molecule and increases its hydrophobicity [23]. This approach was used previously to pair ICG with poly(ethylenimine) and improving the loading of ICG in PEG-PLGA and silica NPs, as well as for complexation with tetrabutylammonium iodide, tetraoctylammonium chloride, and tetradodecylammonium chloride and loading in polystyrene micelles [20,24–26].

Building on these previous reports, we endeavoured to develop ICG nanoformulation with well-controlled physicochemical features and excellent optical properties. To this end, we designed a high throughput 3D printed microfluidic nanoprecipitation device to reliably prepare highly monodispersed PEG-PLGA NPs over a range of size suitable for image-guided surgical procedures [27,28]. A proof-of-concept study was performed in a large animal swine model to assess the potential of the ICG nanoformulation in enabling long term imaging of cervical sentinel lymph nodes. The preliminary data suggest the feasibility of differentiating SLNs from higher echelon LNs, and to image SLNs up to 10 days post interstitial injection.

6.2 Materials and method

6.2.1 Materials

PLGA (5-10 KDa) and methoxy-PEG-PLGA (mPEG-PLGA) (2-15 KDa) were purchased from PoliSciTech (USA). Acetonitrile, ICG (Cardiogreen), tetraoctylammonium bromide (TOAB), trehalose were obtained from Sigma Aldrich (USA).

6.2.2 PEG-PLGA NPs preparation

A 3D printed microfluidic nanoprecipitation device was fabricated to produce the PEG-PLGA NPs. The chip was designed using the Autodesk Inventor® software and printed with a MiiCraft 3D printer (Rays Optics, Canada) using the Master Mold resin (Creative CADworks, Canada). The device is designed with two inlets used to introduce two miscible phases that are merged in a herringbone structured mixing channel (height of 1.1 mm, width of 0.6 mm) where the polymer/dye mixture is rapidly nanoprecipitated to form the NPs. The mixing channel consists of 13 mixing herringbone units (two groups of asymmetrical grooves) with vertices against the direction of flow. The microfluidic channel was imaged by a Nikon SMZ25 stereo microscope (Nikon, Japan) and is illustrated in Figure 6-1-A, B.

The 3D printed microfluidic device was used to prepare and optimize PEG-PLGA NPs. 5 mg/mL polymer mixture comprising of 50% PLGA and 50% mPEG-PLGA in acetonitrile was introduced via one inlet and Milli-Q® water used as the aqueous phase was introduced by the other inlet (Figure 6-1-C). The flow rate of each phase was controlled by syringe pumps (Chemyx fusion 200) and the solutions were introduced using thermoplastic ethyl vinyl acetate microbore microfluidic tubing (0.020"ID x 0.060"OD) (Coleparmer, USA). To modulate the size of the PEG-PLGA NPs, various flow rates ranging from total flow rate (TFR) of 2 to 18 mL/min were used to nanoprecipitate the polymer. The NPs were collected from the outlet and the hydrodynamic size of the NPs was measured by dynamic light scattering with a Zetasizer 3000 HS (Malvern Instruments Ltd, UK).

6.2.3 Preparation of ICG loaded PEG-PLGA NPs

ICG loaded PEG-PLGA NPs (ICG NPs) were prepared by nanoprecipitation within the 3D printed microfluidic device. Hydrophobic ion pairing was used to increase the loading of ICG into the PEG-PLGA NPs and TOAB was employed as the counter-ion. The

polymer mixture consisted of 5 mg/mL 50 % PLGA and 50 % mPEG-PLGA in acetonitrile. ICG (at 5 % (w/w) of the polymer mixture) and TOAB solutions in acetonitrile were premixed at a 1/1 molar ratio, and subsequently added to the polymer mixture to make the organic phase. The organic phase and Milli-Q® water were introduced within the device at specific flow rates (1/3, 1/8 and 3/15 mL/min) used to prepare large, middle and small sized ICG PEG-PLGA NPs, respectively. The nanoprecipitated ICG NPs were washed using Amicon® Ultra-4 Centrifugal Filters (10 KD, Merck millipore, USA) and used for *in vitro* analyses.

For nanoformulations used in the *in vivo* experiments, the ICG NPs were prepared under aseptic conditions. The nanoprecipitated ICG NPs were redispersed in Milli-Q® water containing 5 % (w/v) trehalose, then frozen at -20°C which was followed by freeze drying using a Modulyo® freeze dryer (Thermo Fisher Scientific Inc., USA).

6.2.4 Physicochemical characterisation of ICG NPs

ICG NPs were dispersed in Milli-Q® water for hydrodynamic size and zeta potential measurements by the Zetasizer 3000 HS. JEOL JEM-2100F-HR transmission electron microscope (TEM) (Jeol, Japan) was also used to image the ICG NPs' morphology and confirm their size after negative staining with 2% phosphotungstic acid.

The drug loading of ICG NP was determined using the following equation. $\text{Drug loading } (\%) = \frac{\text{Mass of loaded ICG}}{\text{Mass of ICG NPs}} \times 100$ To determine the mass of loaded ICG, the ICG NPs were dissolved with acetonitrile and the ICG fluorescence was measured by fluorescence spectrophotometry. Free ICG dilutions were used to prepare the standard curve needed to quantify the mass of loaded ICG. The mass of ICG NPs was measured after lyophilisation of NPs as described above.

The encapsulation efficiency of ICG NP was determined by the following equation. $\text{Encapsulation efficiency}(\%) = \frac{(\text{Initial mass of ICG} - \text{mass of ICG in filtrate})}{\text{Initial mass of ICG}} \times 100.$ To measure the mass of ICG not loaded within the PEG-PLGA during the nanoprecipitation, the eluted ICG NP solution was centrifuged using an Amicon® Ultra-4 Centrifugal Filter, and the fluorescence of ICG in the filtrate of the sample quantified by fluorescence spectrophotometry.

6.2.5 ICG NP's fluorescence properties

ICG fluorescence was measured using a Cary Eclipse Fluorescence Spectrophotometer (Agilent, USA). The sample was excited at 783 nm and the fluorescence emission spectrum was recorded between 790-850 nm. To measure the fluorescence, the sample was diluted in Milli-Q® water to obtain linear curve of fluorescence intensity versus ICG concentration and exclude the scattering effect of the NPs. The slope of fluorescence versus ICG concentrations was determined by GraphPad Prism 7 (GraphPad Software, Inc., USA), as an intrinsic fluorescence of the formulation. Fluorescence per particle was estimated by dividing the fluoresce value to the number of NPs in the sample. The number of NPs was estimated based on their size and mass.

To determine the relative quantum yield (QY) of the ICG NPs, the absorbance of five concentrations of ICG NPs and free ICG in water (ranging from 0.097 to 1.56 µg/mL) was measured using an Evolution 201 UV-Vis Spectrophotometer (ThermoFisher Scientific, USA). The absorbance was measured at 783 nm, which is the peak excitation wavelength of ICG. The concentration range was chosen to ensure absorbance values below 0.1 and prevent re-absorbance effects. The samples' fluorescence intensity spectrum was also recorded as described above and the integrated fluorescence intensity was calculated by GraphPad Prism 7. The graph of the integrated fluorescence intensity vs absorbance was plotted using the values of five concentrations for ICG NPs or free ICG to determine the slope of the plotted straight line. The QY of ICG NPs was determined using the following equation and relative to the QY of free ICG in water as a reference, which is previously reported to be 1.3 [29].

$$QYsample = QYreference \times \frac{Gradient\ of\ sample}{Gradient\ of\ reference}$$

To study the stability of the ICG NPs, samples of each formulation and free ICG in water (2.5 µg/mL) were stored at room temperature in the dark. At several time-points over two weeks, a sample of ICG NPs was first sonicated in a water bath sonicator and then filtered with an Amicon® Ultra-4 Centrifugal Filter 10 KD to remove the free/released ICG and redispersed in the same volume of water. The hydrodynamic size and fluorescence of the ICG NPs and free ICG were measured as described above.

To compare the fluorescence quenching of the free ICG in water with that of the NPs, the fluorescence of several concentrations of 60 nm sized ICG NPs (ICG NP-60) and free ICG in water ranging from 0.78 to 50 µg/mL were measured.

6.2.6 Mapping of lymphatic drainage in a large animal swine model

Animal experiments were performed according to a protocol approved by the Animal Ethics Committee of the South Australian Health and Medical Research Institute (SAHMRI). All animal work was performed on site at the SAHMRI preclinical imaging and research laboratory (PIRL) in compliance with "The Australian Code of Practice for the Care and Use of Animals for Scientific Purposes, NHMRC" and The Animal Welfare Act. Three female large white pigs (sus scrofa domesticus) weighing approximately 40-50 kg were obtained and maintained according to institutional standards. For the procedure, anaesthetic was administered intramuscularly (1 mg/kg Xylazil-100 and 10 mg/kg ketamine) and maintained via endotracheal intubation with 2% isoflurane. Heart rate, oxygen saturation and body temperature were monitored while under general anaesthetic. At the completion of each procedure, animals were humanely euthanized with a lethal overdose of barbiturate, prior to performing a neck dissection.

The ICG NPs uptake rate in the lymph nodes was investigated and compared to that of the free ICG. To this end, 1 mL ICG NP-60 or free ICG in sterile water (1 mg/mL) were injected into one side of the mammary tissue via three subcutaneous injections. The ICG or ICG NP-60 uptake rates in the draining inguinal LNs were determined by measuring the transdermal fluorescence. To assess the feasibility of using the ICG nanoformulation to identify cervical SLN(s), 1 mL ICG NP-60 (1 mg/mL) was injected into the tongue muscle in three injections. At two time-points, 4 h and 10 days after injection (N=1/time-point), the animals were euthanized and neck dissection was performed by a surgeon to excise the fluorescent LNs.

Fluorescence live imaging was performed using a Karl Storz Image1 S 4U Rubina camera system, which was generously loaned from Karl Storz Endoscopy Australia. The camera was paired with a 10 mm, 0˚ endoscope attachment and handheld throughout the dissection procedure to help guide the surgeon to draining lymphatic vessels and nodes. For lymphatic uptake and *ex vivo* imaging, a fixed field of view was maintained by mounting the camera and endoscope in a retort stand clamp. The *ex vivo* fluorescence of resected LNs were compared using a custom MATLAB script, which measured the mean

background-subtracted intensity from two opposing surfaces (e.g. inferior and superior sides) of each LN using the NIR/ICG ‘contrast’ mode.

6.2.7 Statistics

All *in vitro* experiments were repeated independently at least two times. All data were plotted using GraphPad Prism 7 (GraphPad Software, Inc., USA) and are presented as average ± standard error of mean.

6.3 Results and discussion

6.3.1 Size controllable preparation of PEG-PLGA NPs using a 3D printed microfluidic nanoprecipitation device

The mixing procedure is the most critical step in the preparation of monodispersed NPs [30]. Therefore, a mixing channel with staggered herringbone grooves was designed for efficient mixing by inducing chaotic advection, where micro-mixing occurs by directing the flow towards the transverse paths [30,31]. The herringbone structured microfluidic devices could be reliably fabricated by a 3D printer as confirmed by microscopy images of sections of the devices and herringbone mixing channels (Figure 6-1-B).

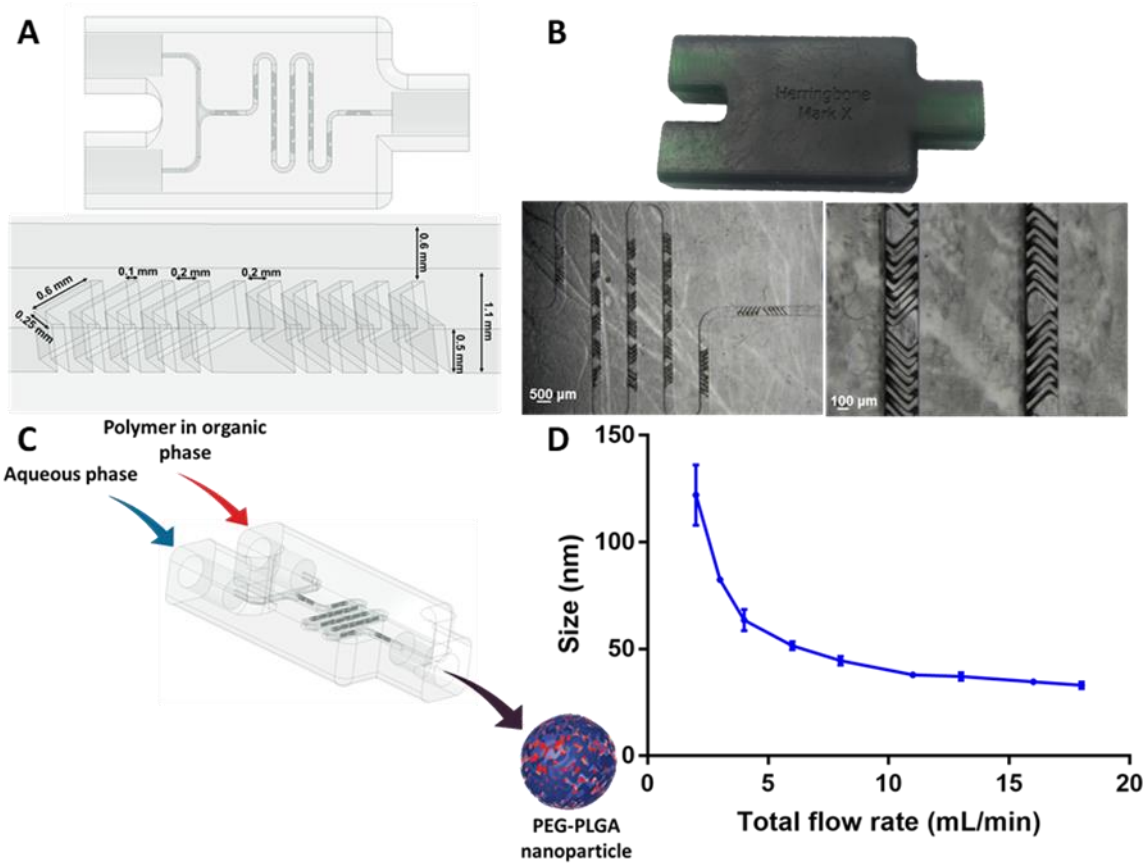

Figure 6-1 3D printed herringbone structured microfluidic nanoprecipitation devices for high throughput preparation of PEG-PLGA NPs.
A) Schematic illustration of the microfluidic device design and channels' dimensions. B) Images of a 3D printed microfluidic device and cross-section of the herringbone mixing channel. C) Graphical illustration of the nanoprecipitation of the PEG-PLGA NPs within the 3D printed microfluidic device. D) Effect of the total flow rate on the hydrodynamic diameter of the PEG-PLGA NPs.

Next, we investigated effect of the microfluidic nanoprecipitation device operating conditions on the physicochemical properties of the produced PEG-PLGA NPs. The device could easily and durably withstand total flow rate as high as 18 mL/min (note: no higher flow rate was tested). By increasing the total flow rate from 2 to 18 mL/min, the hydrodynamic size of NPs significantly decreased from 122 ± 10 nm to 33 ± 1 nm, demonstrating that the NPs' size is highly dependent on the flow rates (Figure 6-1-D). In this experiment, nine different TFR reproducibly resulted in nine distinct NP sizes, without changing polymer composition or concentration.

All PEG-PLGA NPs produced within the nanoprecipitation device were monodispersed with poly dispersity indexes (PDI) < 0.15, confirming the efficient and rapid mixing of the two phases within the mixing chamber. Nanoprecipitation is initiated by a nucleation step that occur at super-saturation of the polymer [32,33]. During this nucleation step, the concentration of the polymer drops below the super-saturation condition, which prevents

further nuclei formation. At this step, nucleus grow by associating more polymer until the concentration reaches the equilibrium saturation concentration. Rapid and efficient mixing is critical to achieve local super-saturation and therefore to control the nucleation and growth of the NPs in the nanoprecipitation process [33] as short mixing time favours homogenous and controlled nucleation. In agreement with some other reports on microfluidic nanoprecipitation [34], we observed that smaller NPs are generated at higher total flow rate. This is because higher flow rate are associated to shorter mixing time, and consequently, the nucleation step is favoured over the growth step, preventing the formation of larger NPs.

3D printing was used to fabricate a nanofabrication device with relatively large mixing channels, as opposed to the dimensions typically used for polydimethylsiloxane (PDMS) based microfluidic devices. The large mixing channels enabled the use of high flow rates, which is crucial for high throughput NP synthesis. Moreover, no clogging was observed in the device even for long operation, which is one of the limitations of PDMS based nanoprecipitation devices with narrow channels [35]. These results validate the feasibility of using 3D printing to prepare microfluidic nanoprecipitation devices that be reliably and reproducibly produce PEG-PLGA NPs with well-defined dimensions.

6.3.2 Microfluidic nanoformulation of ICG NPs by hydrophobic ion pairing

Previous reports showed difficulty of loading ICG within polymeric NPs due to it hydrophilicity [19,21,22]. We therefore decided to utilise the hydrophobic ion pairing strategy to increase the apparent hydrophobicity of the dye and its compatibility with the PLGA core. TOAB was used as a counter ion, which provides a positive charge to form an ionic complex with the negatively charged ICG under the experimental condition used in this study (Figure 6-2-A). Three organic/aqueous phase flow rates of 1/3, 1/8 and 3/15 mL/min were selected based on the operating condition optimisation experiments described above towards preparing ICG NPs within the targeted range of hydrodynamic diameters. It is well established that lymphatic drainage from the interstitial injection site and LN retention is strongly dependent on the size of the nanoparticles [36,37]. Formulations with hydrodynamic diameters larger than 100 nm are typically strongly retained at the injection site, due to the pore size limitation of lymphatic endothelial cells anchoring filaments and interstitium extracellular matrix [37]. The 3 tested flow conditions resulted in 99.9 ± 2.8 nm, 58.7 ± 1.7 nm and 42.4 ± 1.5 nm sized ICG NPs, respectively. The excellent monodispersity and spherical morphology of the

nanoformulations were confirmed by the dynamic light scattering and TEM measurements (Figure 6-2-B, C). These three ICG nanoformulations are referred to as ICG NP-45, ICG NP-60 and ICG NP-100. The three sizes of ICG NPs were therefore deemed suitable to investigate their physicochemical and optical properties in view of their potential application in SLN mapping procedures.

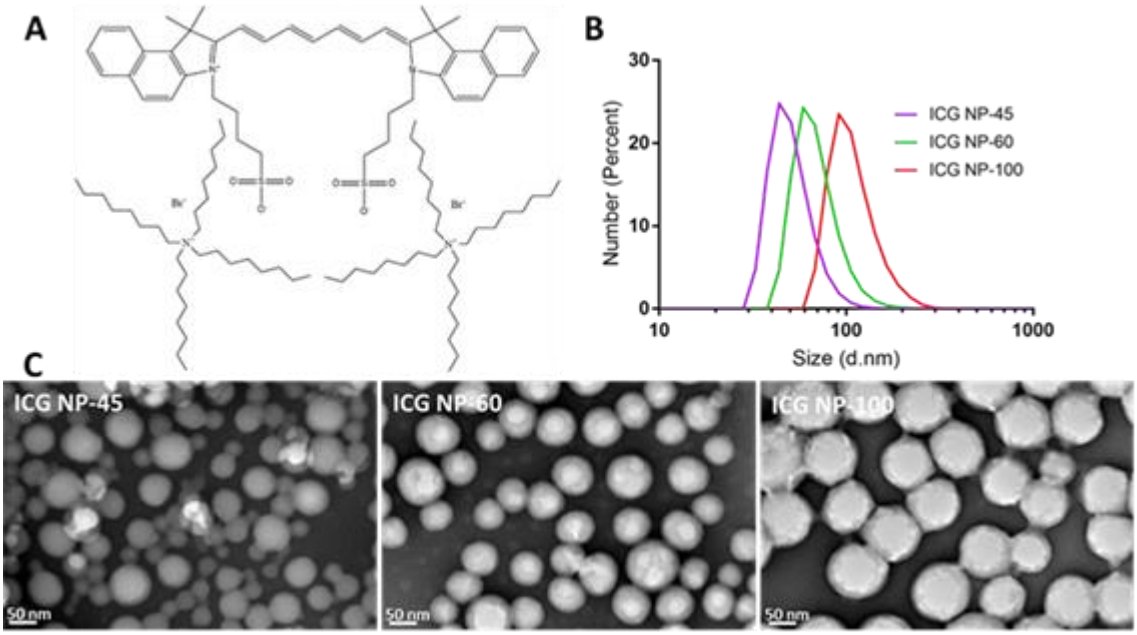

Figure 6-2 Physicochemical properties of ICG NPs prepared by hydrophobic ion pairing within the microfluidic device.
A) Molecular structure of ICG and TOAB used as the hydrophobic pairing agent. B) Hydrodynamic size distribution of the ICG NPs prepared with organic/aqueous phase flow rates of 1/3, 1/8 and 3/15 mL/min. C) Representative TEM images of ICG NP-45, ICG NP-60 and ICG NP-100 (left to right) after negative staining by phosphotungstic acid 2 %.

The details of ICG nanoformulation size, zeta potential, encapsulation efficiency and loading level for each nanoformulation are shown in table 6-1. The combination of the microfluidic nanoprecipitation and hydrophobic pairing of the ICG with TOAB at a 1:1 molar ratio yielded very high encapsulation efficiency (>99 %) and excellent loading levels (> 11%). This is significantly higher than efficiencies achieved in previous studies preparing ICG loaded PLGA NPs without employing a counter ion (<40 % encapsulation efficiency and <8 % loading) [19,21]. Increasing the molar ratio of TOAB to 2:1 decreased the optical properties of the ICG NPs. Our data is also in agreement with a previous report where tetraoctylammonium chloride (TOAC) was successfully used as the pairing agent and reported the molar ratio of 1/1 TOAC/ICG as being optimum [20].

Table 6-1 Physicochemical and optical properties of ICG NPs.

	Size (± SEM) (nm)	Zeta potential (± SEM) (mV)	Encapsulation efficiency (% ± SEM)	Drug loading (% ± SEM)	Intrinsic fluorescence (slope) [AU/(mg/mL)]	Quantum yield (% ± SEM
ICG (water)	-	-	-	-	3.9×10^5	1.3 [29]
ICG NP-45	42.4 ± 1.5	-26 ± 0.5	99.9 ± 0.04	11.1 ± 0.003	2.5×10^5	1.2 ± 0.3
ICG NP-60	58.7 ± 1.7	-24.5 ± 0.5	99.8 ± 0.07	11.1 ± 0.01	2.0×10^5	1.1 ± 0.2
ICG NP-100	99.9 ± 2.8	-19.9 ± 0.1	99.8 ± 0.10	11.1 ± 0.003	2.0×10^5	1.1 ± 0.1

To confirm the efficient encapsulation of ICG within the PEG-PLGA NPs, the fluorescence properties were characterised and compared to that of free ICG in water. The three tested ICG nanoformulation had similar fluorescence intensity at equivalent concentrations of loaded ICG. ICG NPs emitted fluorescence at the same wavelength as the free ICG in water and had a comparable spectrum shape (Figure 6-3-A). The fluorescence properties of the ICG NPs tabulated in table 6-1. Moreover, the intrinsic fluorescence of the ICG NPs, which is the slope of the fluorescence versus ICG concentration, was 0.52 (ICG NP-100 and ICG NP-60) and 0.63 (ICG NP-45) that of the free ICG, indicating a small decrease in the intrinsic fluorescence of ICG molecules encapsulated into the NPs (Figure 6-3-B). This decrease in fluorescence is likely caused by aggregation and consequent quenching of the ICG molecules upon loading within the PLGA core of the NPs. This is also illustrated by modest decreases in the QYs of the ICG nanoformulations compared to the free ICG in water. The relative QYs of the ICG NP-100, ICG NP-60 and ICG NP-45 were 1.12, 1.15 and 1.24 % respectively, compared to the reported QY of free ICG in water of 1.3 % [29]. The data shows that hydrophobic ion pairing of ICG with TOAC not only improved the loading of the dye within the PEG-PLGA nanoformulations but also protected it from significant aggregation and therefore preserves its optical properties. Reduced QYs typically result from ICG nanoformulation. For example, an ICG hyaluronan nanoformulation yielded five-fold decrease in the fluorescence intensity compared to ICG, although nanoformulation nevertheless improved fluorescence in the tumour compared to free ICG in an orthotopic model of pancreatic ductal adenocarcinoma [38]. Conversely, the intrinsic fluorescence of ICG loaded within vitamin E based NPs using TOAC as the counter ion was 0.036 of the free

ICG in water and the QY was 0.44 % relative to the free ICG (1.3 %) [20]. The improved optical properties of our ICG nanoformulation suggest a benefit of combining hydrophobic ion pairing and microfluidic nanoprecipitation, although the nanoparticle composition also likely plays a role in QY of nanoformulated ICG. In a similar approach, the SN38 chemotherapeutic agent was used to complex ICG by hydrophobic interactions, and their nanoassembly prevented the aggregation of ICG and yielded higher fluorescence compared to free ICG [39].

Further supporting the fact that the combination of hydrophobic ion pairing with microfluidic nanoprecipitation efficiently load ICG within the PLGA core of the nanoformulation, we observed that the ICG fluorescence per particle scaled linearly with the nanoformulation volume i.e. it scaled with the NP diameters (D) at a power of three (FL/NP = (2.46x10 -16)D3.028) (Figure 6-3-C). This confirm the homogeneous encapsulation of the ICG within the PLGA core rather than at the core-shell interface, which would have scaled with the NP diameter at the power of two (D2) [20].

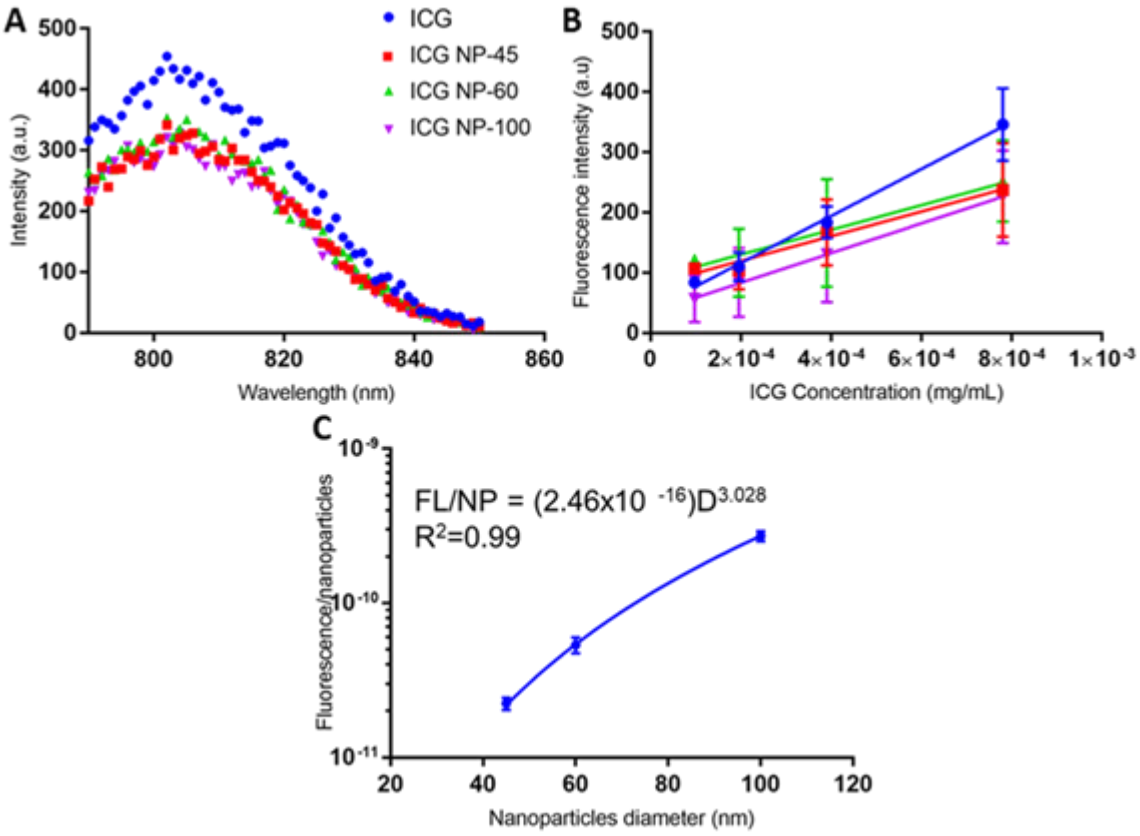

Figure 6-3 Optical properties of ICG PEG-PLGA nanoformulations.
A) Fluorescence spectrum of ICG NP-45, ICG NP-60, ICG NP-100 and free ICG in water at an equivalent ICG concentration of 0.78 µg/mL. B) Relationship between ICG concentration and fluorescence intensity

for the ICG nanoformulation and free ICG in water. C) Effect of the NPs' diameter on the fluorescence per NP.

In the next step, the stability of the ICG NPs were determined by measuring the evolution of the hydrodynamic size when stored in Milli-Q® water at room temperature (Figure 6-4-A). The measured changes in size after two weeks was less than 9, 1 and 10 % for ICG NP-100, ICG NP-60 and ICG NP-45, respectively, without any sign of aggregation. These measurements demonstrate the absence of aggregation and colloidal stability of the nanoformulations, as well as the absence of significant degradation in water over that time frame.

In parallel, the stability of the ICG fluorescence in the nanoformulation was investigated over two weeks. The free ICG lost more than 70 % of its fluorescence after 24 h storage in water, and the fluorescence decreased by more than 95 % after 48 h, which is in line with previously reported half-life of ICG in aqueous solutions at room temperature [24]. On the other hand, the formulation of ICG within the PEG-PLGA NPs by hydrophobic ion pairing and microfluidic nanoprecipitation dramatically increased the stability of ICG fluorescence, as all three formulations preserved almost half the fluorescence after one week (Figure 6-4-B). The fluorescence of ICG NP-100 decreased to 82.8 % after 24 h, and further decreased to 46.1 % at day seven, ultimately reaching 43.8 % of the initial fluorescence after two weeks. Likewise, the fluorescence of ICG NP-60 decreased to 87.8 % and 71.2 % after 24 h and 2 weeks, respectively. The fluorescence of ICG NP-45 decreased to 93.7 % after 24 h but there displayed significant decrease after two weeks, yielding only 28.5 % of the initial fluorescence. It should be noted that in this experiment, the ICG nanoformulations were sonicated and washed using Amicon® Ultra-4 Centrifugal Filters to remove free ICG, towards ensuring that the measured fluorescence was from ICG in the core of the NPs. Overall, these results demonstrates that the chemical design yielded low release of the ICG from the nanoformulation, and also increased the stability of the fluorescence in aqueous solution. As a result, substantial amount of fluorescence could be measured up to the two weeks of the study, with the ICG NP-60 formulation displaying over 70 % of its initial fluorescence. These results can also be compared to a previous report where ICG loaded lipid-PLGA NPs with diameters of 39, 68, and 119 nm were investigated as photothermal agent [21]. The fluorescence of the three nanoformulations remained above 60 % after four weeks while the free ICG reduced to 13.4 %. However, more than 90 % of the ICG was released from the NPs after three days. The correlation between ICG release profile and stability was not discussed in that study,

but Pansare et al. suggested that the non-uniform ICG encapsulation typically results when the dye is loaded from the aqueous phase, which may also explain the high burst release of ICG in that study [20].

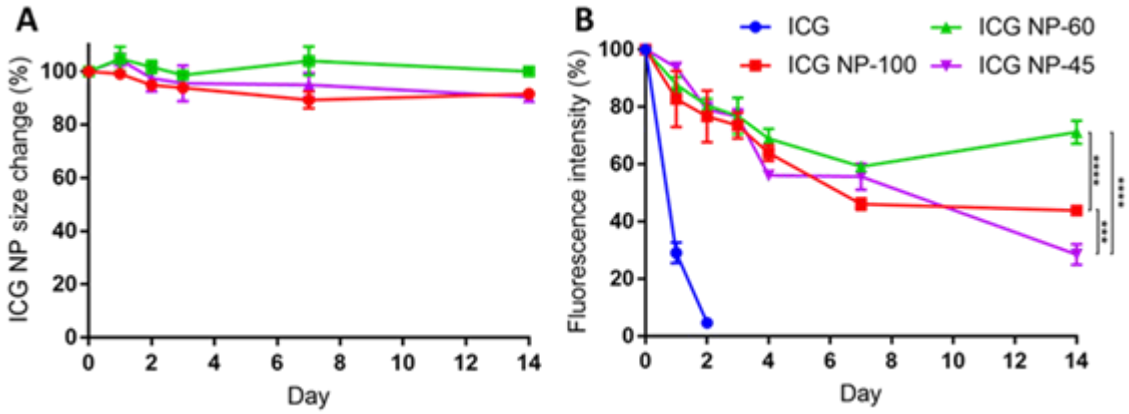

Figure 6-4 Stability of the ICG nanoformulations.
A) Evolution of the ICG NPs size and (B) fluorescence over two weeks of storage in water at room temperature in the dark. Statistical significance by two-way ANOVA with Tukey post hoc test is indicated *P<0.05, **P < 0.01, ***P ≤ 0.001 and ****P ≤ 0.0001 and ns indicates not significant.

Next, we sought to determine whether the ICG nanoformulations prevent quenching of ICG. To this end, the fluorescence of increasing concentrations of ICG NP-60, selected because of its best fluorescence stability, was measured (Figure 6-5-A) and compared to that of free ICG. The fluorescence of the nanoformulation increased with increase of the concentration of the ICG NP-60 formulation up to 10 µg/mL. However, further increase of the concentration resulted in decreased fluorescence. This pattern of fluorescence change vs concentration was comparable to that of the free ICG in water. The fluorescence spectrum was further evaluated to distinguish whether the observed decrease of fluorescence at increased ICG NP concentration is due to quenching of the ICG molecules or to scattering and adsorption of the fluorescence by the NPs at high concentrations. The fluorescence spectrum of the free ICG and ICG NP-60 at the concentrations of 0.78, 5 and 50 µg/mL were recorded (Figure 6-5-B). Increasing the concentration of free ICG from 5 to 50 µg/mL led to not only decrease in the fluorescence intensity, but also to a 15 nm red shift in the emission spectrum. This can be interpreted as aggregation-caused quenching, as aggregates emit at longer wavelengths than single ICG molecule [6,20]. On the other hand, increasing the concentration of the ICG NP-60 formulation from 5 to 50 µg/mL led to a similar decrease in the ICG fluorescence intensity but without any red shifting effect (Figure 6-5-C). This suggests different mechanisms,

and more specifically that the observed reduction of fluorescence at concentrations above 10 µg/mL is due to scattering/absorption at high NP concentration but not to ICG molecule aggregation-caused quenching. Note this issue is predominant in the *in vitro* setting but likely less so *in vivo* due to the presence of tissues' fat with significant light scattering and absorption.

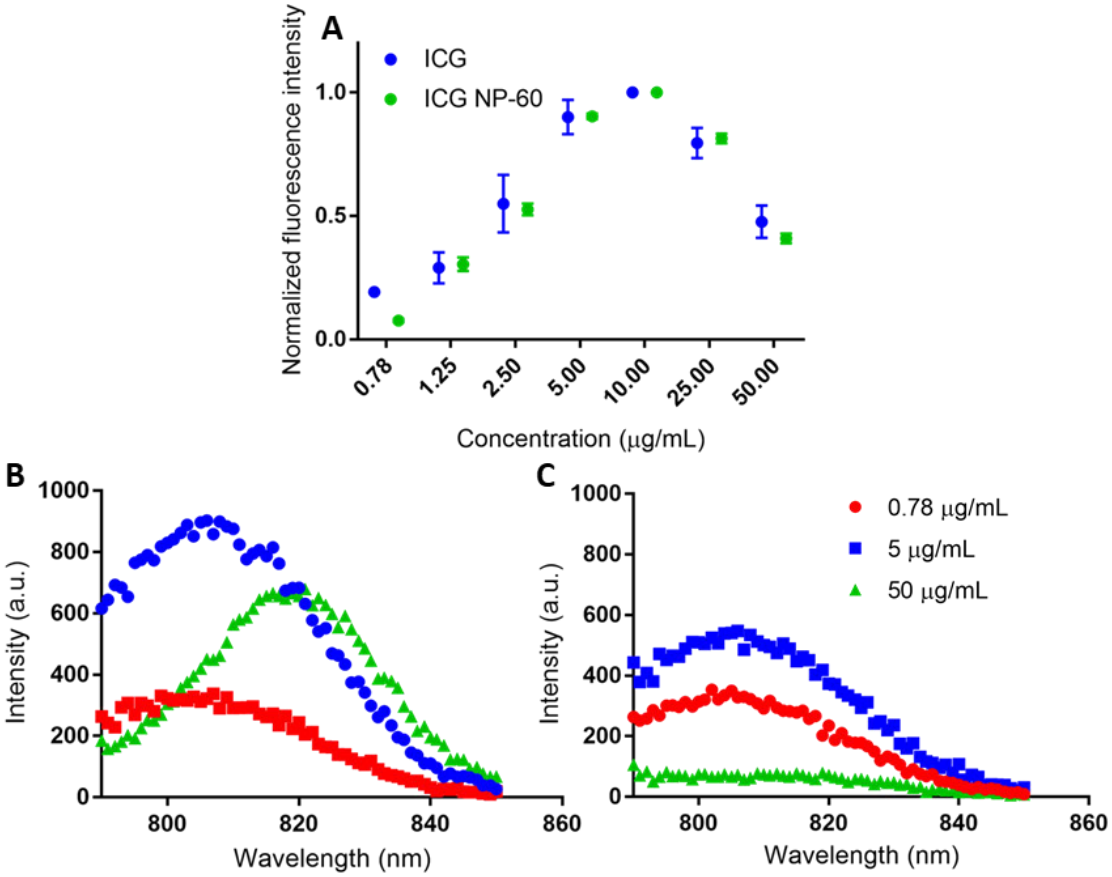

Figure 6-5 Relationship between ICG NP-60 concentration and fluorescence intensity.
A) Fluorescence intensity in water vs ICG NP-60 and free ICG concentrations. Representative fluorescence spectrum for (B) free ICG and (C) ICG NP-60 at concentrations of 0.78, 5 and 50 µg/mL.

6.3.3 ICG NP-60 efficiently retains ICG fluorescence for sentinel lymph node detection

Since ICG NP-60 had the highest fluorescence stability *in vitro*, we selected it to test the feasibility of using the ICG nanoformulation to identify SLNs in the large animal model via image guided surgery. First, we confirmed efficient uptake of the ICG NP-60 formulation in the inguinal LN of a pig after injection into the mammary tissue and compared it with free ICG. The fluorescence signal could be detected in the inguinal LN which directly drains from the mammary tissues less than a minute after injection of ICG

and ICG NP-60 (Figure 6-6-A). However, the uptake rate was initially slower for the ICG NP-60 compared to free ICG with a slope of 5.97 versus 8.54, respectively. In both case the fluorescence signal in the inguinal LNs reached a plateau. This result is not surprising as the lymphatic transport of biomolecules and nanoparticles is strongly influenced by their size.

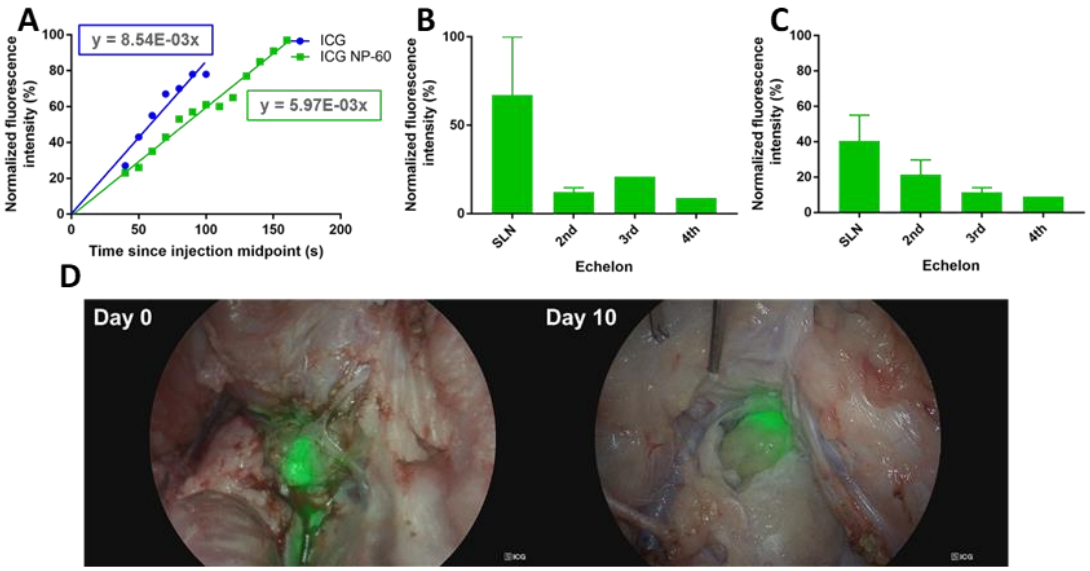

Figure 6-6 SLN mapping in a large animal swine model.
A) Uptake rates of ICG NP-60 and free ICG in inguinal lymph node after injection in the mammary tissue. Fluorescence of ICG NP-60 in SLN (defined as the first draining node in the regional basin) and higher echelons nodes at (B) day 0 (4 h) and (C) day 10 after injection in the tongue (N= 1/time-point). D) Representative intraoperative fluorescence images at days 0 and 10 of SLNs (shown in green) after injection of ICG NP-60 in the tongue.

Next, we evaluated the fluorescence of ICG NP-60 in cervical LNs, including the SLN defined as the first draining node(s) and other (2nd, 3rd and 4th) echelons LNs. To this end, the ICG formulation was injected in the tongue, which is used as a model of head and neck squamous cell carcinoma. 4 h after injection, the SLNs and higher echelons LNs were identified and excised based on their fluorescence and lymphatic drainage. There was no leakage of the ICG formulation out of lymphatic system. The *ex vivo* fluorescence measurement revealed that ICG NP-60 fluorescence in SLN was higher than that in the downstream echelons, e.g. it was 5.4 times higher in the first draining node than in the second echelon node (Figure 6-6-B). This is an interesting observation that suggest the feasibility of using the fluorescence intensity to differentiate between SLN(s) and higher echelon LNs (Figure 6-6-B), which could facilitate SLN biopsy procedures.

Next, the retention of the ICG NP-60 and associated fluorescence in the SLN 10 days after injection was then investigated. By day 10, while the fluorescence was still higher in the SLN compared to higher echelon nodes, the difference had decreased compared to the same day surgery (Figure 6-6-C). The fluorescence in the SLN was 1.9 times higher than in the second echelon node. The intraoperative images of the SLNs 4 h and 10 days after injection are shown in Figure 6-6-D. The observed persistence of the fluorescence in LNs after 10 days in the swine model validates that the ICG NP-60 formulation efficiently preserves the ICG fluorescence in a realistic *in vivo* setting.

To the best of our knowledge, the performance of ICG nanoformulations has not been investigated in SLN versus other higher echelon nodes in a large animal model. Although substantially more complex and expensive than murine studies, such swine studies are more relevant to the human anatomy and therefore informative about the potential of lymphotropic imaging agents. Although further studies are clearly warranted to fully establish the potential of the ICG nanoformulation, its excellent optical properties could address some of the challenges of current SLN biopsy procedures. ICG is commonly used concurrently with radionuclide tracers such as 99mTc to accurately facilitate intraoperative identification of SLNs from downstream LNs, where LNs that are both fluorescent and radioactive are considered to be SLNs [40,41]. This approach was recommended in the surgical consensus guideline on SLN biopsy of patients with oral cancers, which was published in 2019 [42]. This is due to the rapid spread of ICG to other LN and it is reported that number of presumed SLNs increases over time, which limits the diagnostic window [43].

In this regard, ICG nanoformulation such as ICG NP-60 could be beneficial by increasing the retention of the fluorescence within SLN(s), leading to higher fluorescence in SLNs compared to higher echelons nodes. However, ICG NP-60 did not preserve the preferential uptake in SLNs at the 10-day time-point, as compared to day 0. Towards further increasing the retention of the ICG nanoformulation, larger NPs such as ICG NP-100 should be investigated [44]. Due to the limitation of available pigs, we were not able to test this in the present study. In addition, functionalization of the nanoformulation with moieties with high binding affinity to lymphoid cells/tissues such as mannose and hyaluronic acid, is also a promising strategy to target SLNs more specifically [45,46], which would be a straightforward modification of the present ICG PEG-PLGA NPs.

6.4 Conclusions

We demonstrated a novel approach to the preparation of ICG nanoformulation based on the combined use of a high throughput microfluidic nanoprecipitation device and hydrophobic ion pairing. This approach enabled precise control over the physicochemical properties of the PEG-PLGA nanoparticles including their hydrodynamic diameter and yielded high performance ICG nanoformulation with excellent optical properties. Importantly, the ICG fluorescence was significantly preserved over two weeks, paving the way to innovative image guided surgical applications. A feasibility study was performed to explore the application of the ICG nanoformulation in sentinel lymph node mapping/biopsy procedures. The excellent stability translated into the possibility of detecting the fluorescence in cervical SLNs 10 days post administration in a large animal swine model. ICG nanoformulations prepared by the combination of microfluidic nanoprecipitation and hydrophobic ion pairing are promising towards broadening the applications of ICG in imaging guided surgery and warrant further investigation.

6.5 References

[1] S.L. Gibbs, Near infrared fluorescence for image-guided surgery., Quant. Imaging Med. Surg. 2 (2012) 177–187. https://doi.org/10.3978/j.issn.2223-4292.2012.09.04.

[2] H.C. Zeng, J.L. Hu, J.W. Bai, G.J. Zhang, Detection of Sentinel Lymph Nodes with Near-Infrared Imaging in Malignancies, Mol. Imaging Biol. 21 (2019) 219–227. https://doi.org/10.1007/s11307-018-1237-4.

[3] Y. Liu, Q. Jia, J. Zhou, Recent Advance in Near-Infrared (NIR) Imaging Probes for Cancer Theranostics, Adv. Ther. 1 (2018) 1800055.

[4] K. Polom, D. Murawa, Y.S. Rho, P. Nowaczyk, M. Hünerbein, P. Murawa, Current trends and emerging future of indocyanine green usage in surgery and oncology: A literature review, Cancer. 117 (2011) 4812–4822. https://doi.org/10.1002/cncr.26087.

[5] P. Liu, C. Yue, B. Shi, G. Gao, M. Li, B. Wang, Y. Ma, L. Cai, Dextran based sensitive theranostic nanoparticles for near-infrared imaging and photothermal therapy in vitro, Chem. Commun. 49 (2013) 6143–6145. https://doi.org/10.1039/c3cc43633k.

[6] V. Saxena, M. Sadoqi, J. Shao, Degradation kinetics of indocyanine green in aqueous solution, J. Pharm. Sci. 92 (2003) 2090-2097. https://doi.org/10.1002/jps.10470.

[7] Q. Dai, E. Ren, D. Xu, Y. Zeng, C. Chen, G. Liu, Indocyanine green-based nanodrugs: A portfolio strategy for precision medicine, Prog. Nat. Sci. Mater. Int. 30 (2020) 577–588. https://doi.org/10.1016/j.pnsc.2020.08.002.

[8] M. Sevieri, F. Silva, A. Bonizzi, L. Sitia, M. Truffi, S. Mazzucchelli, F. Corsi, Indocyanine Green Nanoparticles: Are They Compelling for Cancer Treatment?, Front. Chem. 8 (2020) 535. https://doi.org/10.3389/fchem.2020.00535.

[9] S. Ren, X. Cheng, M. Chen, C. Liu, P. Zhao, W. Huang, J. He, Z. Zhou, L. Miao, Hypotoxic and Rapidly Metabolic PEG-PCL-C3-ICG Nanoparticles for Fluorescence-Guided Photothermal/Photodynamic Therapy against OSCC, ACS Appl. Mater. Interfaces. 9 (2017) 31509–31518. https://doi.org/10.1021/acsami.7b09522.

[10] F. Shu, T. Yang, X. Zhang, W. Chen, K. Wu, J. Luo, X. Zhou, G. Liu, J. Lu, X. Mao, Hyaluronic acid modified covalent organic polymers for efficient targeted and

oxygen-evolved phototherapy, J. Nanobiotechnology. 19 (2021) 1–13. https://doi.org/10.1186/s12951-020-00735-x.

[11] Z. Chaudhary, G.M. Khan, M.M. Abeer, N. Pujara, B. Wan-Chi Tse, M.A. McGuckin, A. Popat, T. Kumeria, Efficient photoacoustic imaging using indocyanine green (ICG) loaded functionalized mesoporous silica nanoparticles, Biomater. Sci. 7 (2019) 5002–5015. https://doi.org/10.1039/c9bm00822e.

[12] X. Jiang, B. Du, Y. Huang, M. Yu, J. Zheng, Cancer Photothermal Therapy with ICG-Conjugated Gold Nanoclusters, Bioconjug. Chem. 31 (2020) 1522–1528. https://doi.org/10.1021/acs.bioconjchem.0c00172.

[13] C. Niu, Y. Xu, S. An, M. Zhang, Y. Hu, L. Wang, Q. Peng, Near-infrared induced phase-shifted ICG/Fe3O4 loaded PLGA nanoparticles for photothermal tumor ablation, Sci. Rep. 7 (2017) 1–10. https://doi.org/10.1038/s41598-017-06122-1.

[14] J.C. Kraft, R.J.Y. Ho, Interactions of indocyanine green and lipid in enhancing near-infrared fluorescence properties: The basis for near-infrared imaging in vivo, Biochemistry. 53 (2014) 1275–1283. https://doi.org/10.1021/bi500021j.

[15] H.S. Jeong, C.M. Lee, S.J. Cheong, E.M. Kim, H. Hwang, K.S. Na, S.T. Lim, M.H. Sohn, H.J. Jeong, The effect of mannosylation of liposome-encapsulated indocyanine green on imaging of sentinel lymph node, J. Liposome Res. 23 (2013) 291–297. https://doi.org/10.3109/08982104.2013.801488.

[16] L. Sitia, M. Sevieri, A. Bonizzi, R. Allevi, C. Morasso, D. Foschi, F. Corsi, S. Mazzucchelli, Development of Tumor-Targeted Indocyanine Green-Loaded Ferritin Nanoparticles for Intraoperative Detection of Cancers, ACS Omega. (2020). https://doi.org/10.1021/acsomega.0c00244.

[17] R. Wei, G. Jiang, M.Q. Lv, S. Tan, X. Wang, Y. Zhou, T. Cheng, X. Gao, X. Chen, W. Wang, C. Zou, F. Li, X. Ma, J. Hu, D. Ma, D. Luo, L. Xi, TMTP1-modified indocyanine green-loaded polymeric micelles for targeted imaging of cervical cancer and metastasis sentinel lymph node in vivo, Theranostics. 9 (2019) 7325–7344. https://doi.org/10.7150/thno.35346.

[18] T. Kurihara, S. Matsuda, Y. Nakamura, S. Suzuki, D. Fuchimoto, A. Onishi, K. Saeki, T. Nakagawa, R. Fujiwara, M. Kamata, J. Kuramoto, K. Kameyama, M. Sekino,

M. Kusakabe, T. Hayashida, H. Jinno, Y. Kitagawa, Establishment of a model of sentinel lymph node metastasis using immunodeficient swine, Sci. Rep. 9 (2019) 1–9. https://doi.org/10.1038/s41598-019-44171-w.

[19] M. Tayama, T. Inose, N. Yamauchi, K. Nakashima, M. Tokunaga, C. Kato, K. Gonda, Y. Kobayashi, Fabrication and fluorescence imaging properties of indocyanine green-loaded poly(lactic-co-glycolic acid) nanoparticles, Colloid Polym. Sci. (2021). https://doi.org/10.1007/s00396-021-04844-3.

[20] V.J. Pansare, W.J. Faenza, H. Lu, D.H. Adamson, Formulation of long-wavelength indocyanine green nanocarriers, J. Biomed. Opt. 22 (2017) 096007. https://doi.org/10.1117/1.jbo.22.9.096007.

[21] P. Zhao, M. Zheng, C. Yue, Z. Luo, P. Gong, G. Gao, Z. Sheng, C. Zheng, L. Cai, Improving drug accumulation and photothermal efficacy in tumor depending on size of ICG loaded lipid-polymer nanoparticles, Biomaterials. (2014). https://doi.org/10.1016/j.biomaterials.2014.04.019.

[22] R. Manchanda, A. Fernandez-Fernandez, A. Nagesetti, A.J. McGoron, Preparation and characterization of a polymeric (PLGA) nanoparticulate drug delivery system with simultaneous incorporation of chemotherapeutic and thermo-optical agents, Colloids Surfaces B Biointerfaces. (2010). https://doi.org/10.1016/j.colsurfb.2009.08.043.

[23] K.D. Ristroph, R.K. Prud'homme, Hydrophobic ion pairing: Encapsulating small molecules, peptides, and proteins into nanocarriers, Nanoscale Adv. 1 (2019) 4207–4237. https://doi.org/10.1039/c9na00308h.

[24] V.B. Rodriguez, S.M. Henry, A.S. Hoffman, P.S. Stayton, X. Li, S.H. Pun, Encapsulation and stabilization of indocyanine green within poly(styrene-alt-maleic anhydride) block-poly(styrene) micelles for near-infrared imaging, J. Biomed. Opt. 13 (2008) 014025. https://doi.org/10.1117/1.2834296.

[25] B. Quan, K. Choi, Y.H. Kim, K.W. Kang, D.S. Chung, Near infrared dye indocyanine green doped silica nanoparticles for biological imaging, Talanta. 99 (2012) 387–393. https://doi.org/10.1016/j.talanta.2012.05.069.

[26] W.H. Jian, T.W. Yu, C.J. Chen, W.C. Huang, H.C. Chiu, W.H. Chiang, Indocyanine Green-Encapsulated Hybrid Polymeric Nanomicelles for Photothermal Cancer Therapy, Langmuir. 31 (2015) 6202–6210. https://doi.org/10.1021/acs.langmuir.5b00963.

[27] X. Li, X. Jiang, Microfluidics for producing poly (lactic-co-glycolic acid)-based pharmaceutical nanoparticles, Adv. Drug Deliv. Rev. 128 (2018) 101–114. https://doi.org/10.1016/j.addr.2017.12.015.

[28] F. Danhier, E. Ansorena, J.M. Silva, R. Coco, A. Le Breton, V. Préat, PLGA-based nanoparticles: An overview of biomedical applications, J. Control. Release. 161 (2012) 505–522. https://doi.org/10.1016/j.jconrel.2012.01.043.

[29] W. Chen, R. Bardhan, M. Bartels, C. Perez-Torres, R.G. Pautler, N.J. Halas, A. Joshi, A molecularly targeted theranostic probe for ovarian cancer, Mol. Cancer Ther. 9 (2010) 1028–1038. https://doi.org/10.1158/1535-7163.MCT-09-0829.

[30] S.I. Hamdallah, R. Zoqlam, P. Erfle, M. Blyth, A.M. Alkilany, A. Dietzel, S. Qi, Microfluidics for pharmaceutical nanoparticle fabrication: The truth and the myth, Int. J. Pharm. 584 (2020) 119408. https://doi.org/10.1016/j.ijpharm.2020.119408.

[31] A.G. Hadjigeorgiou, A.G. Boudouvis, G. Kokkoris, Thorough computational analysis of the staggered herringbone micromixer reveals transport mechanisms and enables mixing efficiency-based improved design, Chem. Eng. J. 414 (2021) 128775. https://doi.org/10.1016/j.cej.2021.128775.

[32] T. Baby, Y. Liu, A.P.J. Middelberg, C.X. Zhao, Fundamental studies on throughput capacities of hydrodynamic flow-focusing microfluidics for producing monodisperse polymer nanoparticles, Chem. Eng. Sci. 169 (2017) 128–139. https://doi.org/10.1016/j.ces.2017.04.046.

[33] W.S. Saad, R.K. Prud'Homme, Principles of nanoparticle formation by flash nanoprecipitation, Nano Today. 11 (2016) 212–227. https://doi.org/10.1016/j.nantod.2016.04.006.

[34] E. Chiesa, R. Dorati, T. Modena, B. Conti, I. Genta, Multivariate analysis for the optimization of microfluidics-assisted nanoprecipitation method intended for the loading

of small hydrophilic drugs into PLGA nanoparticles, Int. J. Pharm. (2018). https://doi.org/10.1016/j.ijpharm.2017.11.044.

[35] S. Hassanpour-Tamrin, A. Sanati-Nezhad, A. Sen, A simple and low-cost approach for irreversible bonding of polymethylmethacrylate and polydimethylsiloxane at room temperature for high-pressure hybrid microfluidics, Sci. Rep. (2021). https://doi.org/10.1038/s41598-021-83011-8.

[36] D.A. Rao, M.L. Forrest, A.W.G. Alani, G.S. Kwon, J.R. Robinson, Biodegradable PLGA based nanoparticles for sustained regional lymphatic drug delivery, J. Pharm. Sci. 99 (2010) 2018–2031. https://doi.org/10.1002/jps.21970.

[37] G.P. Howard, G. Verma, X. Ke, W.M. Thayer, T. Hamerly, V.K. Baxter, J.E. Lee, R.R. Dinglasan, H.Q. Mao, Critical size limit of biodegradable nanoparticles for enhanced lymph node trafficking and paracortex penetration, Nano Res. 12 (2019) 837–844. https://doi.org/10.1007/s12274-019-2301-3.

[38] B. Qi, A.J. Crawford, N.E. Wojtynek, M.B. Holmes, J.J. Souchek, G. Almeida-Porada, Q.P. Ly, S.M. Cohen, M.A. Hollingsworth, A.M. Mohs, Indocyanine green loaded hyaluronan-derived nanoparticles for fluorescence-enhanced surgical imaging of pancreatic cancer, Nanomedicine Nanotechnology, Biol. Med. 14 (2018) 769–780. https://doi.org/10.1016/j.nano.2017.12.015.

[39] S. Hu, C. Dong, J. Wang, K. Liu, Q. Zhou, J. Xiang, Z. Zhou, F. Liu, Y. Shen, Assemblies of indocyanine green and chemotherapeutic drug to cure established tumors by synergistic chemo-photo therapy, J. Control. Release. 234 (2020) 250–259. https://doi.org/10.1016/j.jconrel.2020.05.018.

[40] N. Patel, M. Allen, K. Arianpour, R. Keidan, The utility of ICG fluorescence for sentinel lymph node identification in head and neck melanoma, Am. J. Otolaryngol. - Head Neck Med. Surg. 42 (2021) 103147. https://doi.org/10.1016/j.amjoto.2021.103147.

[41] A. Christensen, K. Juhl, B. Charabi, J. Mortensen, K. Kiss, A. Kjær, C. von Buchwald, Feasibility of Real-Time Near-Infrared Fluorescence Tracer Imaging in Sentinel Node Biopsy for Oral Cavity Cancer Patients, Ann. Surg. Oncol. 23 (2016) 565–572. https://doi.org/10.1245/s10434-015-4883-7.

[42] C. Schilling, S.J. Stoeckli, M.G. Vigili, R. de Bree, S.Y. Lai, J. Alvarez, A. Christensen, D.M. Cognetti, A.K. D'Cruz, B. Frerich, R. Garrel, N. Kohno, W.M. Klop, C. Kerawala, G. Lawson, J. McMahon, I. Sassoon, R.J. Shaw, J.F. Tvedskov, C. von Buchwald, M. McGurk, Surgical consensus guidelines on sentinel node biopsy (SNB) in patients with oral cancer, Head Neck. 41 (2019) 2655–2664. https://doi.org/10.1002/hed.25739.

[43] J. Yokoyama, Y. Hasegawa, M. Sugasawa, A. Shiotani, Y. Murakami, S. Ohba, N. Kohno, Long term-follow-up multicenter feasibility study of icg fluorescence-navigated sentinel node biopsy in oral cancer, Mol. Clin. Oncol. 13 (2020) 41. https://doi.org/10.3892/mco.2020.2111.

[44] Y.N. Zhang, J. Lazarovits, W. Poon, B. Ouyang, L.N.M. Nguyen, B.R. Kingston, W.C.W. Chan, Nanoparticle Size Influences Antigen Retention and Presentation in Lymph Node Follicles for Humoral Immunity, Nano Lett. 19 (2019) 7226–7235. https://doi.org/10.1021/acs.nanolett.9b02834.

[45] X. Ke, G.P. Howard, H. Tang, B. Cheng, M.T. Saung, J.L. Santos, H.Q. Mao, Physical and chemical profiles of nanoparticles for lymphatic targeting, Adv. Drug Deliv. Rev. 151 (2019) 72–93. https://doi.org/10.1016/j.addr.2019.09.005.

[46] O.J. Estudiante-Mariquez, A. Rodríguez-Galván, D. Ramírez-Hernández, F.F. Contreras-Torres, L.A. Medina, Technetium-Radiolabeled Mannose-Functionalized Gold Nanoparticles as Nanoprobes for Sentinel Lymph Node Detection, Molecules. 25 (2020) 1982. https://doi.org/10.3390/molecules25081982.

Chapter 7

Discussion of the Research Findings and Future Research Recommendations

7 Discussion of the research findings and future research recommendations

The research of this PhD thesis investigated the potential of nanomedicine to improve immune checkpoint inhibition for cancer immunotherapy, delivering new knowledge in the field as well as technological and methodological advancements.

Immune checkpoint inhibitors have changed the paradigm of cancer treatment since their first approval in 2011. Of particular importance are immune checkpoint antibodies inhibitors of the PD-1/PD-L1 pathway, as evidenced by their growing clinical use [1]. The United States' Medicare expenditure on the seven Food and Drug Administration (FDA) approved immune checkpoint antibodies increased by 1916 %, to more than five billion USD, from 2014 to 2019 [2]. Several immune checkpoint antibodies are also approved by the Australia's Therapeutic Goods Administration (TGA) for a variety of cancers [3]. For head and neck cancer squamous cell carcinoma (HNSCC), as an example, immune checkpoint antibodies have already changed the standard of care for recurrent and/or metastatic cancer patients. While such patients receive a standard of care multi-modal treatment including surgery, radiotherapy and chemotherapy, FDA approved PD-1 antibodies, such as pembrolizumab and nivolumab are now being utilised as a single or combination therapy after chemotherapy or even as a first line therapy [4].

Despite the outstanding success of immune checkpoint inhibitors, only a minority of patients respond to the therapy, while on the other hand a significant population of patients experience immune related adverse events (IRAEs) [4,5]. For example only 12.5 % of cancer patients response to therapy in the United States [2]. Also, IRAEs associated with ICIs are frequent and even life-threatening in rare occasions [6,7]. Therefore, to improve ICI therapies, it is necessary to address these limitations. Nanoparticles (NPs) modify the biodistribution of their biological payloads and their utilisation has been suggested as a way to improve the efficacy and toxicity profile of immune checkpoint therapies [8]. This core principle underpins the approaches used in this PhD research.

In developing the nanoformulations for this research, we considered from the onset key criteria towards clinical translation of nanomedicines. This included the use of the well-established and safe polymer poly(ethylene glycol)-b-poly(lactide-co-glycolide) (PEG-PLGA) [9] as a delivery system. In addition, to prepare the nanoformulations, we developed and implemented a custom-made 3D printed microfluidic nanoprecipitation

device, which enabled us to reproducibly prepare monodispersed PEG-PLGA NPs of different sizes. This approach is promising towards enabling formulation scale-up compared to conventional bulk mixing methods [10].

In the first part of this research project (chapter 3), we investigated the impact of PD-1 antibodies (aPD-1) conjugation to PEG-PLGA NPs (aPD-1 NPs) on aPD-1 biodistribution following intratumoural administration. This is an important significant knowledge gap as intratumoural administration of immunotherapeutics is gaining interest as an alternative to systemic injection. To conduct this study, we first developed and characterised an orthotopic murine model of head and neck cancer. Next, we observed that intratumoural injection of the aPD-1 nanoformulation significantly reduced the accumulation of aPD-1 in off-target organs and their blood circulation, whilst similar concentrations were retained in the tumour compared to free aPD-1 antibodies. In addition, compared to systemic administration of free aPD-1 antibodies, intratumoural injection of both aPD-1 and aPD-1 NPs led to significantly higher tumour bioavailability and lower biodistribution in off-target organs. *In vitro* biological assays confirmed that the conjugation of the aPD-1 to the PEG-PLGA NPs did not alter the activity of the antibodies in increasing the cytotoxicity of T-cells against head and neck cancer cells. These results address the knowledge gap regarding the biodistribution of intratumoural administration of aPD-1 nanoformulations. The data also supports the growing interest for local administration of immunotherapeutic agents and warrant further preclinical investigation towards reducing adverse effects associated with the off-target biodistribution of antibodies.

Of specific interest would be the investigation of the *in vivo* efficiency of the aPD-1 nanoformulation using the orthotopic mouse model developed in this project for the biodistribution study. However, as some of the ICIs' adverse effects occur over a fairly long time-frame, mouse models are limited in their ability to investigate potential side effects of ICIs. The use of larger animal models to study the toxicity of aPD-1 NPs may therefore provide better insight about the benefit of nanoformulation in reducing off-target toxicity. Furthermore, as the antigen binding fragment (Fab) of antibodies have been shown to be as effective as full antibody inhibitors, a biodistribution study of NPs conjugated to the Fab may be an interesting approach towards reducing the side effects caused by Fc region immunogenicity. In line with this approach, biodistribution studies

of local administration of PD-1/PD-L1 targeting peptides or small molecules may also be informative and can be compared to the biodistribution of aPD-1 NPs.

In the second part of the research project (chapter 4), the combination of 3D microfluidic nanoprecipitation and hydrophobic ion pairing was investigated towards the development of a nanoformulation of an indoleamine 2,3-dioxygenase (IDO) inhibitor (IDOi) (navoximod) within PEG-PLGA NPs (IDOi NPs). Hydrophobic ion pairing efficiently overcame the difficulty of loading navoximod into PEG-PLGA NPs. This approach was successfully integrated into a microfluidic based 3D printed nanoprecipitation device, leading to the development of a reproducible and well-characterised IDOi nanoformulation. The IDOi nanoformulation efficiently inhibited the IDO enzyme in head and neck cancer cells and was shown to be able both as single therapy and in combination with aPD-1 to enhance the cytotoxicity of T-cells against head and neck cancer cells. The administration of high dose of oral navoximod, which has a low oral bioavailability is associated with significant adverse effects. Pending further preclinical and clinical investigation, IDOi nanoformulation could potentially reduce such adverse effects. Also, this approach may overcome the resistance to aPD-1 therapy associated with the overexpression of IDO.

Although the navoximod nanoformulation showed an acceptable drug release profile, one of the limitations of this study was that the impact of hydrophobic ion pairing on the drug release was not investigated. To improve the drug release profile, it is suggested that other counter ions, in addition to sodium deoxycholate, be tested in future studies to find the best compromise between loading efficiency and burst release of the drug from the nanoparticles.

Based on the promising *in vitro* assessment of the IDOi nanoformulation, further experimental work is underway to test its efficacy as a single therapy and IDOi NP/ aPD-1 combination therapy in the orthotopic mouse model of head and neck cancer. In addition, since radiotherapy and immunotherapy can synergistically produce anti-tumour effects, the experimental design will investigate if IDOi NP/ aPD-1 therapy can improve the efficacy of radiotherapy in a mouse model of head and neck cancer. This comprehensive preclinical study will shed light on the potential of IDOi nanoformulation. As discussed above, the nanoformulation of small molecule IDOi within nanoparticles could pave the way to more efficient and/or safer immunotherapy based on intratumoural

administration. Further studies are warranted to investigate the therapeutic benefits and side-effect profile of intratumoural administration.

Next, as an alternative to PD-1 antibody, we endeavoured to reformulate a small molecule inhibitor of PD-1 expression (chapter 5). Specifically, we developed a delivery system for the glycogen synthase kinase 3 (GSK3) inhibitor (GSK3i), SB415286, by loading into the PEG-PLGA NPs (GSK3i NP) using a hydrophobic counter ion. As a proof-of-concept, we demonstrated that GSK3i NPs efficiently inhibited the expression of PD-1 receptor in chimeric antigen receptor (CAR) T-cells *in vitro*. This approach showed promising anti-tumour effects by preventing T-cell viability loss after antigen specific stimulation by cancer cells and shifted the T-cells towards the central memory phenotype, which potentially can provide long-lasting anti-tumour responses.

Due to the limitation of CAR-T cells availability, only a proof of concept study was conducted to determine the biological efficacy of GSK3i, which is the main limitation of this study. A more comprehensive study is recommended in the future to confirm the results observed in this work.

In vitro co-culture studies are routinely used for the initial assessment of CAR-T cells function, but are limited. Due to the inherent complexities of the immune system and the involvement of several immune cells and signalling pathways, it is not possible to simulate the *in vivo* environment by conventional cell culture models. In our study we observed limited PD-1 expression of CAR-T cells by *in vitro* activation. Further efficacy studies of GSK3i NPs in more clinically relevant *in vitro* models, such as organoids, and eventually in relevant animal preclinical models are recommended.

In the last part of the thesis (chapter 6), building on approaches used in chapters 4 and 5, we employed the hydrophobic ion pairing within the microfluidic nanoprecipitation device to formulate the indocyanine green (ICG) fluorescent dye into PEG-PLGA NPs (ICG NPs). We successfully developed three sizes of ICG NPs (45, 60 and 100 nm), all with improved ICG optical stability and prevented the aggregation-caused quenching of ICG. The simple but efficient formulations of ICG within PEG-PLGA nanoparticles, led to a collaboration with Ferronova Pty Ltd. This enabled us to conduct a preliminary large animal study aimed at investigating the application of 60 nm sized ICG NPs for image guided surgery, i.e. intraoperative identification of sentinel lymph nodes. We demonstrated that ICG NPs are efficiently and rapidly taken up by sentinel lymph node(s)

after interstitial injection and resulted in higher fluorescence in sentinel lymph nodes compared to higher echelon nodes. This could improve the intraoperative application of ICG for detection of sentinel lymph nodes. Also, the fluorescence of the ICG NPs was detectable in lymph nodes over a relatively long time (10 days). However, the preferential retention of the ICG NPs in the sentinel lymph nodes was less significant compared to the short term situation.

Further investigation of the ICG nanoformulation in the swine model is recommended to confirm and broaden the results observed in our pilot study. Since only a limited number of swine could be used (due to ethical and cost limitations) during this study, only one size of the ICG nanoformulations was investigated *in vivo*, which was the nanoformulation with the best *in vitro* stability. It is recommended to investigate the application of other sizes of ICG nanoformulations for the detection of sentinel lymph nodes using this large animal model.

Moreover, evaluation of other sizes of ICG NPs, particularly ICG NP-100 is suggested as it may be beneficial towards enhancing the retention in sentinel lymph nodes over a long time. A promising outcome of this research will pave the way to use porcine tumour models to evaluate the preferential uptake of ICG NPs into tumour draining lymph nodes versus non-tumour draining lymph nodes. ICG NPs can be further targeted to the tumour draining lymph nodes by conjugating tumour targeting small molecules to the PEG-PLGA NPs.

The body of knowledge produced during this PhD thesis provides new insights into the potential of nanomedicine-based drug delivery systems to improve immune checkpoint inhibition. More specifically, the following outcomes are notable from this PhD thesis:

- Lower biodistribution of aPD-1, when conjugated to PEG-PLGA vs free antibodies in off-target organs was determined following intratumoural injection.
- Higher bioavailabilities of aPD-1 antibodies in tumour and tumour draining lymph nodes and reduced off-target biodistribution by intratumoural administration of aPD-1 nanoformulation and free antibodies was determined compared to systemic administration of free aPD-1.

- Significant improvement of navoximod loading into the PEG-PLGA NPs was achieved by hydrophobic ion pairing.
- Efficient induction of anti-tumour immune responses by the navoximod nanoformulation in synergy with PD-1 antibodies.
- Highly monodispersed synthesis of SB415286 GSK3 inhibitor nanoformulation could be reliably prepared.
- Efficient inhibition of PD-1 receptors' expression, prevention of viability loss and induction of memory phenotype in CAR T-cells was achieved using the SB415286 GSK3 inhibitor nanoformulation.
- Development of an ICG nanoformulation with precise control over physico-chemical properties.
- Improved stability of ICG in the aqueous environment and preservation of its optical properties by nanoformulation within PEG-PLGA nanoparticles and hydrophobic ion pairing.
- Demonstration of the feasibility of detecting sentinel lymph nodes using the ICG nanoformulation both shortly after injection and up to 10 days in a swine model.

In conclusion, this PhD research project established a simple and easily scalable preparation method for ICI nanoformulation. Moreover, it contributed to address the knowledge gap on the biodistribution of intratumourally administered aPD-1 nanoformulation. This thesis outcome warrants further investigation to potentially: 1) improve the toxicity of aPD-1 by intratumoural administration of aPD-1 NPs, 2) improve the delivery and formulation of IDOi by IDOi NPs, and mitigate the resistance to aPD-1 therapy, 3) enhance the delivery of GSK3i by GSK3i NPs, to improve PD-1 inhibition, 4) improve the accuracy and application of ICG for image guided surgery for detection of sentinel lymph nodes.

The nanoformulation strategies utilised and the body of knowledge generated in this thesis, can hopefully serve the research community and be applied to other therapeutic and diagnostic agents, eventually leading to improved cancer therapy outcomes.

7.1 References

[1] J. Gill, V. Prasad, A reality check of the accelerated approval of immune-checkpoint inhibitors, Nat. Rev. Clin. Oncol. 16 (2019) 656–658. https://doi.org/10.1038/s41571-019-0260-y.

[2] P. Puri, D. Cortese, S. Baliga, A time series analysis of immune checkpoint inhibitor use in the United States Medicare population: 2014–2019, J. Dermatolog. Treat. (2021) 1–9. https://doi.org/10.1080/09546634.2021.1962002.

[3] L. Ardolino, A. Joshua, Immune checkpoint inhibitors in malignancy, Aust. Prescr. 42 (2019) 62–67. https://doi.org/10.18773/austprescr.2019.012.

[4] S.E. Green, M.G. McCusker, R. Mehra, Emerging immune checkpoint inhibitors for the treatment of head and neck cancers, Expert Opin. Emerg. Drugs. 25 (2020) 501–514.

[5] Y. Jiang, X. Zhao, J. Fu, H. Wang, Progress and Challenges in Precise Treatment of Tumors With PD-1/PD-L1 Blockade, Front. Immunol. 11 (2020) 339. https://doi.org/10.3389/fimmu.2020.00339.

[6] D.Y. Wang, J.-E. Salem, J. V. Cohen, S. Chandra, C. Menzer, F. Ye, S. Zhao, S. Das, K.E. Beckermann, L. Ha, W.K. Rathmell, K.K. Ancell, J.M. Balko, C. Bowman, E.J. Davis, D.D. Chism, L. Horn, G. V. Long, M.S. Carlino, B. Lebrun-Vignes, Z. Eroglu, J.C. Hassel, A.M. Menzies, J.A. Sosman, R.J. Sullivan, J.J. Moslehi, D.B. Johnson, Fatal Toxic Effects Associated With Immune Checkpoint Inhibitors, JAMA Oncol. 4 (2018) 1721–1728. https://doi.org/10.1001/jamaoncol.2018.3923.

[7] M.A. Postow, R. Sidlow, M.D. Hellmann, Immune-related adverse events associated with immune checkpoint blockade, N. Engl. J. Med. 378 (2018) 158–168.

[8] M.J. Sanaei, A. Pourbagheri-Sigaroodi, V. Kaveh, S.A. Sheikholeslami, S. Salari, D. Bashash, The application of nano-medicine to overcome the challenges related to immune checkpoint blockades in cancer immunotherapy: Recent advances and opportunities, Crit. Rev. Oncol. Hematol. 157 (2021) 103160. https://doi.org/10.1016/j.critrevonc.2020.103160.

[9] H.A. Almoustafa, M.A. Alshawsh, Z. Chik, Technical aspects of preparing PEG-PLGA nanoparticles as carrier for chemotherapeutic agents by nanoprecipitation method, Int. J. Pharm. 533 (2017) 275–284. https://doi.org/10.1016/j.ijpharm.2017.09.054.

[10] J.P. Martins, G. Torrieri, H.A. Santos, The importance of microfluidics for the preparation of nanoparticles as advanced drug delivery systems, Expert Opin. Drug Deliv. 15 (2018) 469–479. https://doi.org/10.1080/17425247.2018.1446936.